LBNL-38884
UC-413

ERNEST ORLANDO LAWRENCE BERKELEY NATIONAL LABORATORY

Multifragmentation in Intermediate Energy ^{129}Xe-Induced Heavy-Ion Reactions

K. Tso
Nuclear Science Division

May 1996
Ph.D. Thesis

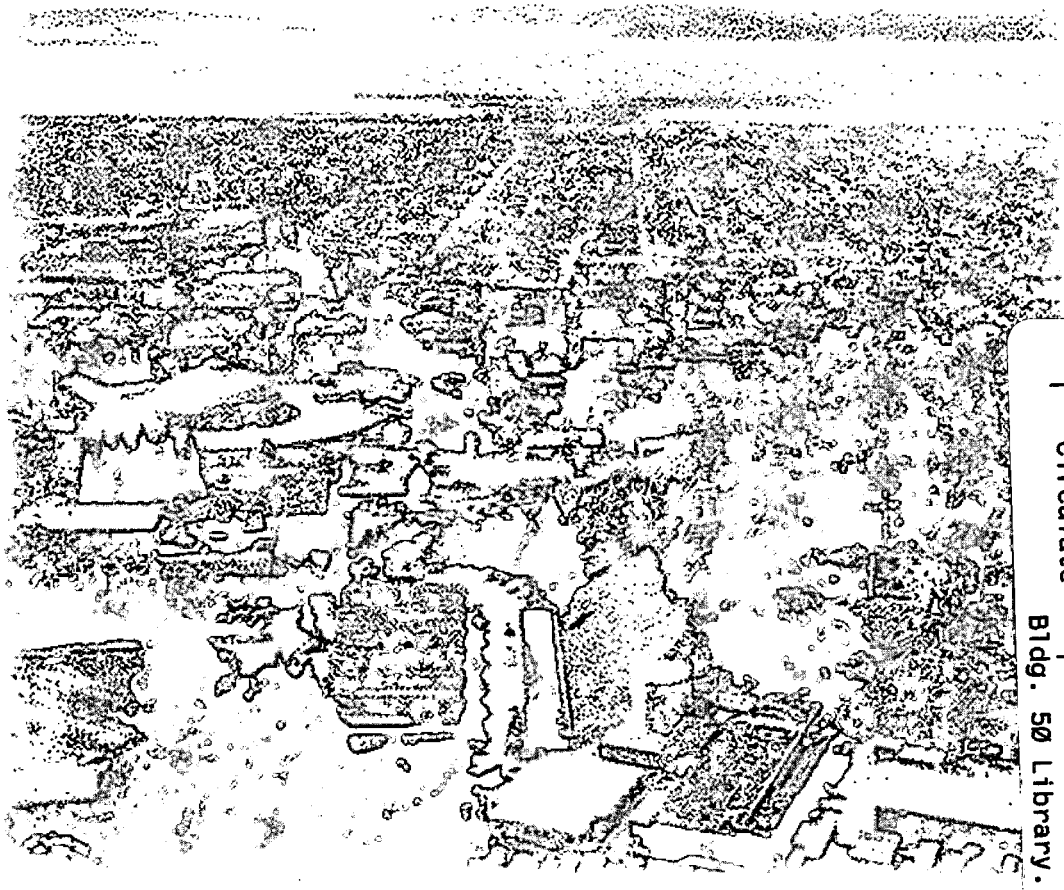

REFERENCE COPY
Does Not
Circulate
Bldg. 50 Library.
LBNL-38884
Copy 1

DISCLAIMER

This document was prepared as an account of work sponsored by the United States Government. While this document is believed to contain correct information, neither the United States Government nor any agency thereof, nor the Regents of the University of California, nor any of their employees, makes any warranty, express or implied, or assumes any legal responsibility for the accuracy, completeness, or usefulness of any information, apparatus, product, or process disclosed, or represents that its use would not infringe privately owned rights. Reference herein to any specific commercial product, process, or service by its trade name, trademark, manufacturer, or otherwise, does not necessarily constitute or imply its endorsement, recommendation, or favoring by the United States Government or any agency thereof, or the Regents of the University of California. The views and opinions of authors expressed herein do not necessarily state or reflect those of the United States Government or any agency thereof or the Regents of the University of California.

LBNL-38884
UC-413

Multifragmentation in Intermediate Energy ^{129}Xe-Induced Heavy-Ion Reactions

Kin Tso

Department of Chemistry
University of California, Berkeley

Nuclear Science Division
Lawrence Berkeley National Laboratory
Berkeley, California 94720, USA

May 1996

This work was supported in part by the Director, Office of Energy Research, Office of High Energy and Nuclear Physics, Division of High Energy Physics, of the U.S. Department of Energy under Contract No. DE-AC03-76SF00098.

Recycled Paper

Multifragmentation in Intermediate Energy ^{129}Xe–Induced Heavy–Ion Reactions

by

Kin Tso

B.S. (University of St. Thomas) 1990

A dissertation submitted in partial satisfaction of the
requirements for the degree of

Doctor of Philosophy

in

Chemistry

in the

GRADUATE DIVISION

of the

UNIVERSITY of CALIFORNIA, BERKELEY

Committee in charge:

Professor Luciano G. Moretto, Chair
Professor Darleane C. Hoffman
Professor Stanley G. Prussin

1996

Abstract

Multifragmentation in Intermediate Energy ^{129}Xe–Induced Heavy–Ion Reactions

by

Kin Tso

Doctor of Philosophy in Chemistry

University of California at Berkeley

Professor Luciano G. Moretto, Chair

The ^{129}Xe–induced reactions on ^{nat}Cu, ^{89}Y, ^{165}Ho, and ^{197}Au at bombarding energies of $E/A = 40$ & 60 MeV have been studied theoretically and experimentally in order to establish the underlying mechanism of multifragmentation at intermediate energy heavy–ion collisions.

Nuclear disks formed in central heavy–ion collisions, as simulated by means of Boltzmann–like kinetic equations, break up into several fragments due to a new kind of Rayleigh–like surface instability. A sheet of liquid, stable in the limit of non-interacting surfaces, is shown to become unstable due to surface–surface interactions. The onset of this instability is determined analytically. A thin bubble behaves like a sheet and is susceptible to the surface instability through the "crispation" mode (modulated thickness). The Coulomb effects associated with the depletion of charges in the central cavity of nuclear bubbles are investigated. The onset of Coulomb instability is demonstrated for perturbations of the "radial" mode (constant thickness).

Experimental intermediate–mass–fragment multiplicity distributions for the

^{129}Xe–induced reactions are shown to be binomial at each transverse energy. From these distributions, independent of the specific target, an elementary binary decay probability p can be extracted that has a thermal dependence. Thus it is inferred that multifragmentation is reducible to a combination of nearly independent emission processes. If sequential decay is assumed, the increase of p with transverse energy implies a contraction of the emission time scale. The sensitivity of p to the lower Z threshold in the definition of intermediate–mass–fragments points to a physical significance. Poisson simulations of the particle multiplicities show that the weak auto–correlation between the fragment multiplicity and the transverse energy does not distort a Poisson distribution into a binomial distribution. The effect of device efficiency on the experimental results has also been studied.

A strong thermal signature is found in the charge distributions associated with multifragmentation from these ^{129}Xe–induced reactions. The n–fold charge distributions are reducible to the 1–fold charge distributions through a simple scaling factor e^{-cnZ} that is dictated by fold number and charge conservation. Experimentally, c starts from zero at low values of the transverse energy and reaches a saturation value at high transverse energy. In a liquid–gas phase diagram, $c = 0$ for the saturated vapor, while $c > 0$ for the unsaturated vapor. It is suggested that in the $c \approx 0$ regime the source evaporates down to a sizable remnant, while for $c > 0$ the source vaporizes completely. Percolation and nuclear evaporation calculations of finite systems portray a behavior similar to that observed experimentally.

Contents

List of Figures vi

List of Tables x

1 Introduction 1
- 1.1 Complex Fragment Emission in Low Energy Reactions 4
- 1.2 Multifragmentation in Intermediate Energy Reactions 5
  - 1.2.1 Theoretical Approach 6
    - 1.2.1.1 Statistical Theories 6
    - 1.2.1.2 Dynamical Theories 17
    - 1.2.1.3 Dynamical–Statistical Theories 22
  - 1.2.2 Experimental Investigation 23
- 1.3 Goal of Project 26

2 Surface and Coulomb Instabilities 29
- 2.1 Boltzmann–Like Equations and Simulations 29
- 2.2 Formation and Fragmentation of Nuclear Disks 34
  - 2.2.1 Disk Formation in BNV Calculations 35
  - 2.2.2 Disk Fragmentation and Surface Instability 40
  - 2.2.3 Metastability of a Sheet of Liquid 43
  - 2.2.4 New Rayleigh Instability of a Sheet of Liquid 44
- 2.3 Stability of Nuclear Bubbles 47
  - 2.3.1 Radial Monopole Oscillations and Coulomb Bubbles 52
  - 2.3.2 Higher Order Perturbations and Coulomb Instability 62
  - 2.3.3 Proximity Effects and Surface Instability 70

3 Experimental Method 76
- 3.1 Experimental Setup 76
  - 3.1.1 Beams and Targets 78
  - 3.1.2 MSU Miniball Phoswich Array 80
  - 3.1.3 LBL Si–Si–Pl Array 85

3.1.4 Data Acquisition Electronics 87
3.1.4.1 MSU Miniball Array 89
3.1.4.2 LBL Si–Si–Pl Array 90
3.2 Calibrations 90
3.2.1 Position Calibration and Resolution 91
3.2.2 Energy Calibration and Resolution 93
3.2.3 Particle Identification and Resolution 101

4 Excitation Functions **106**
4.1 Transverse Energy 107
4.2 Binomial Reducibility and Thermal Scaling of multifragment Emission Probability 113
4.3 General Interpretation of Reducibility 126
4.4 Sequential Interpretation of p and m 130
4.5 Auto–Correlation Effects 134
4.5.1 Poisson Simulations 137
4.5.2 Event–to–Event Fluctuations 139
4.6 Efficiency Effect on Binomial Parameters 149
4.7 Target Independence 156

5 Charge Distributions **168**
5.1 Reducibility and Thermal Scaling 169
5.1.1 Extraction of c 170
5.1.2 Other Methods of c Extraction 174
5.1.3 Origin and Interpretation of c 178
5.2 Transverse Energy Dependence of c 182
5.3 $Z_{threshold}$ effect on the extraction of c 191
5.4 Target Independence 198

6 Conclusion **201**
6.1 Theoretical Approach 201
6.2 Experimental Investigation 203
6.2.1 Excitation Functions 204
6.2.2 Charge Distributions 207

A Energy Calculations **209**
A.1 Nuclear Disks 209
A.1.1 Surface Energy 211
A.1.2 Proximity Energy 212
A.1.3 Overall Energy 214
A.2 Nuclear Bubbles 214
A.2.1 Reference Energy State 216
A.2.2 Surface Energy 218

A.2.3 Coulomb Energy 220
A.2.4 Proximity Energy 221

Bibliography **224**

List of Figures

1.1 Figure illustrating the approximate domains of heavy–ion reaction mechanisms 2
1.2 Results of the microcanonical calculation by Gross et al. for ^{131}Xe . . 12
1.3 BNV calculations of the reaction ^{129}Xe + ^{197}Au at $E/A = 60$ MeV for several different impact parameters b 19

2.1 BNV calculations for head–on collision (impact parameter = 0) of the reaction ^{129}Xe + ^{197}Au at $E/A = 40$ MeV 36
2.2 Same as Figure 2.1 for $E/A = 60$ MeV 37
2.3 Same as Figure 2.1 for $E/A = 75$ MeV 38
2.4 Central density of the colliding system as a function of time 40
2.5 Density profiles of nuclear disks along the beam axis (R_z) and the plane perpendicular to the beam axis (R_{xy}) at time = 120 fm/c 41
2.6 Schematic illustration of the perturbation of a thin sheet of liquid. . . 45
2.7 Schematic diagrams for perturbations of the radial mode 50
2.8 Schematic diagrams for perturbations of the crispation mode 51
2.9 Surface and Coulomb energies of bubbles subjected to monopole oscillations 54
2.10 Total energy of Coulomb bubbles as a function of P for several values of fissility parameter X 57
2.11 Pressure effect on the stability of Coulomb bubbles 61
2.12 Surface and Coulomb energies for bubbles subjected to higher order perturbations 64
2.13 Boundary conditions of Coulomb instability for nuclear bubbles . . . 67
2.14 Same as Figure 2.13 including configurations of Coulomb bubbles . . 69
2.15 Same as Figure 2.14 including the pressure effect 71

2.16 Proximity effects on the stability of nuclear bubbles 74

3.1 Photograph of the multidetector configuration 77
3.2 Isometric view of the Miniball target insertion mechanism. 81
3.3 Artist's perspective of the assembly structure of the Miniball 81
3.4 Half–plane section of the Miniball Array 82
3.5 Schematic of phoswich assembly of a Miniball detector. 82
3.6 Timing and widths of the fast, slow and tail gates of the Miniball phoswich detector signal. 84
3.7 Exploded view of the Si–Si(Li)–Pl Array telescope 86
3.8 Schematic electronic diagram for the multidetector system 88
3.9 Raw position spectra for a 300 μm Si and a 5 mm Si(Li) detector . . 92
3.10 Calibrated X and Y positions for a LBL telescope 94
3.11 Energy spectrum of a 5 mm and a 300 μm silicon detector exposed to a triplet beam of ^{129}Xe, ^{86}Kr and ^{43}Ca ions 97
3.12 Light output of a Plastic Scintillator as a function of energy for some representative ions 100
3.13 Density plot of E versus ΔE for one of the LBL telescopes 102
3.14 E versus ΔE plots for a Miniball detector 102
3.15 Particle identification spectra for a LBL Si–Si(Li)–Pl telescope and a MSU Miniball detector 104

4.1 Transverse energy E_t distributions for the ^{129}Xe–induced reactions . . 109
4.2 The available energy in the center–of–mass frame E_{cm} as a function of the upper limit of E_t for the ^{129}Xe–induced reactions 111
4.3 Correlation between E_t and E^* determined from the source velocity . 112
4.4 The probability P_n to emit n intermediate mass fragments as a function of E_t for the reaction ^{129}Xe + ^{197}Au 114
4.5 The natural logarithm of the ratio of the n–fold to the 2–fold probability as a function of ${E_t}^{-1/2}$ for the reaction ^{129}Xe + ^{197}Au 115
4.6 The extracted values of m and p as a function of E_t for the reaction ^{129}Xe + ^{197}Au 118
4.7 A comparison between the experimental probability and the calculated probability to emit n intermediate mass fragments for the reaction ^{129}Xe + ^{197}Au 119
4.8 Arrhenius plots for the reaction ^{129}Xe + ^{197}Au 121

4.9 Same as Figure 4.8 but the data with E_t less than 700 MeV are not shown 122
4.10 Same as Figure 4.8 but the values of $1/p$ are extracted "differentially" using Equation 4.14 124
4.11 Same as Figure 4.8 but the values of $1/p$ are extracted "independently" using Equation 4.17 125
4.12 The probability P_n and the extracted values of $1/p$ for the reaction ^{129}Xe + ^{197}Au with different values of the lower threshold in the definition of IMF 128
4.13 Same as Figure 4.12 but for bombarding energy at $E/A = 60$ MeV . 129
4.14 The extracted values of m as a function of E_t for different values of $Z_{threshold}$ for the reaction ^{129}Xe + ^{197}Au 133
4.15 The products of m and $Z_{threshold}$ as a function of E_t for different values of $Z_{threshold}$ for the reaction ^{129}Xe + ^{197}Au 135
4.16 Inputs for the Poisson simulations 138
4.17 Results from the Poisson simulations using the experimental inputs for the N_{IMF} and N_{LCP} distributions 142
4.18 Same as Figure 4.17 but E_t^m is calculated from charged particles only 145
4.19 The probability P_n, the extracted values of p and m for the N_{LCP} distribution generated from the Poisson simulation 146
4.20 Results for the N_{LCP} distribution generated from the Poisson simulation using the linear input 148
4.21 Geometrical acceptance of the device (Miniball + Array) as a function of θ and ϕ 151
4.22 The probability P_n of detecting n IMFs by using all, 1/2 and 1/3 of Miniball detectors is shown as a function of E_t for the reaction ^{129}Xe + ^{197}Au 153
4.23 The values of p and m extracted from the N_{IMF} distributions shown in Figure 4.22 154
4.24 The Arrhenius plot for the data shown in Figure 4.22 155
4.25 The probability P_n to emit n intermediate mass fragments as a function of E_t for the ^{129}Xe–induced reactions on different targets 157
4.26 The values of $\langle N_{IMF} \rangle$ and σ^2 extracted from the N_{IMF} distributions for the ^{129}Xe–induced reactions on different targets 158
4.27 Arrhenius plots for the ^{129}Xe–induced reactions on different targets . 160

4.28 Schematic illustrations of the incomplete fusion and fireball models. . 161
4.29 The source velocity calculated from the incomplete fusion model . . . 163
4.30 The values of $\langle n \rangle$ and σ^2 extracted from the N_{IMF} distribution gated on θ for the ^{129}Xe–induced reactions on different targets 166

5.1 The n–fold charge distributions $P_n(Z)$ of intermediate mass fragments for the reaction ^{129}Xe + ^{197}Au at selected values of E_t and n 171
5.2 The exponential fit parameter α_n as a function of $1/\sqrt{E_t}$ for the reaction ^{129}Xe + ^{197}Au 173
5.3 The "reduced" charge distributions for the same cuts on E_t and n as Figure 5.1 175
5.4 The natural logarithm of the ratio $P_n(Z)/P_{n+1}(Z)$ is plotted as a function of Z for the charge distributions shown in Figure 5.1 177
5.5 An illustration of the reducibility of charge distributions for the reaction ^{129}Xe + ^{197}Au 183
5.6 The coefficient c extracted by the χ^2 method and from the ratio of $P_n(Z)/P_{n+1}(Z)$ as a function of E_t for the reaction ^{129}Xe + ^{197}Au . . 184
5.7 The extracted values of c and cZ_o as a function of the percentage of bonds broken (p_b) from the percolation calculations 186
5.8 The extracted values of c and cZ_o as a function of the excitation energy from the evaporation calculations 189
5.9 Liquid–gas phase diagram 190
5.10 The coefficient c extracted from the charge distributions associated with different values of N_{IMF} and $Z_{threshold}$ is plotted as a function of E_t for the reaction ^{129}Xe + ^{197}Au 194
5.11 The corrected coefficient c_o extracted from the charge distributions associated with different values of N_{IMF} and $Z_{threshold}$ is plotted as a function of E_t for the reaction ^{129}Xe + ^{197}Au 196
5.12 The coefficients c and c_o as a function of N_{IMF} for the reaction ^{129}Xe + ^{197}Au 197
5.13 The coefficient c as a function of E_t for the ^{129}Xe-induced reactions on four targets 199

List of Tables

2.1 Coefficients A, B and σ extracted for three different values of K. . . . 30

3.1 Excitation energy (MeV) available in the center–of–mass system. . . . 78
3.2 Ion and molecular beams for detector calibrations. 79
3.3 Thickness of Targets. 80

5.1 Coefficient c extracted by three different procedures. 178

A.1 Definition of symbols for energy calculations of a sheet of fluid. 210
A.2 Definition of symbols for energy calculations of nuclear bubbles. . . . 216

Acknowledgements

This thesis is the fruit of God working through many people in my life. Personally and professionally, they have helped me pass through graduate school at Berkeley. I would like to take this opportunity to recognize their contributions.

I owe the most thanks for my achievement and success to my thesis advisor, Professor Luciano Moretto, who had significant impact on me during my endeavors in graduate school. He taught me how to relate the nature of physics to complicated mathematics. His simple visualization and physical insight of complex problems have constantly been a source of inspiration, and his guidance was instrumental in the formulation of this material. I am also grateful to him for his enduring patience in teaching me English and improving my writing skills.

I would like to express my gratitude to Dr. Gordon Wozniak for his professional, supervisory, and personal input during various phases of my work. His thoroughness and perseverance have shown me what an experimentalist should strive to be. His technical knowledge and expert advice made significant contributions to the success of my thesis experiments, and I could always count on his help when things were not going smoothly.

It has been a privilege and a wonderful opportunity to work closely with Dr. Larry Phair during the past two years. I am grateful to him for his example of integrity, for his willingess to share his knowledge with me, and for his patience in teaching me many new skills in data analysis. On a personal level, I greatly appreciate his friendship and companionship on morning rides to the lab.

In addition, I would like to mention Dr. Nicola Colonna and Dr. Wojtek Skulski, who played important roles and made invaluable contributions during the early stages of this project. Thanks also goes to the rest of the members of the

Moretto/Wozniak group for providing a comfortable and enjoyable research environment. I would also like to acknowledge my collaborators at the National Superconducting Cyclotron Laboratory for assisting me with experimental setup and data collection.

Many of my friends have supported me during my graduate career. I am especially thankful to Alfred Ho, Wing Lau and Rita Hui for their gentle encouragement and their confidence in me. Many thanks go to the friends at the El Cerrito Chinese Christian Church for their prayers. But most of all, I am indebted to my parents, Sze Wo and Sin Mei, and my sister Jenny for their unfailing love and care during these years. This work could not have been completed without their unconditional support.

Chapter 1

Introduction

Heavy–ion collisions have been commonly used to study the formation and the decay of highly excited nuclear systems. In particular, the emission of complex fragments ($Z \geq 3$) has been a subject of great interest, since the emitted fragments may bear information about the system before decay. Experimentally, the emission of complex fragments (CF) or intermediate mass fragments (IMF) has been observed pervasively in heavy–ion reactions over a large range of bombarding energies and combinations of projectile and target [Kort 73, Goss 77, Meye 80, Bord 84, Sobo 84, McMa 85, Char 88a, Char 88b, More 88, Guer 89, Gutb 89, Gros 90, Bowm 91, Bowm 92, More 93, Rous 93, Peas 94, Tso 95].

Figure 1.1 shows a schematic representation of the evolution of the heavy–ion reaction mechanism with bombarding energy and impact parameter b. It essentially illustrates the formation of different emission sources in the various regimes of heavy–ion collisions. When two heavy nuclei collide with each other at low bombarding energies, they fuse together to form a hot transient object known as compound nucleus (CN). In other words, the nuclei stop each other and the translational kinetic energy is transformed into randomized microscopic motion. Sometimes, a

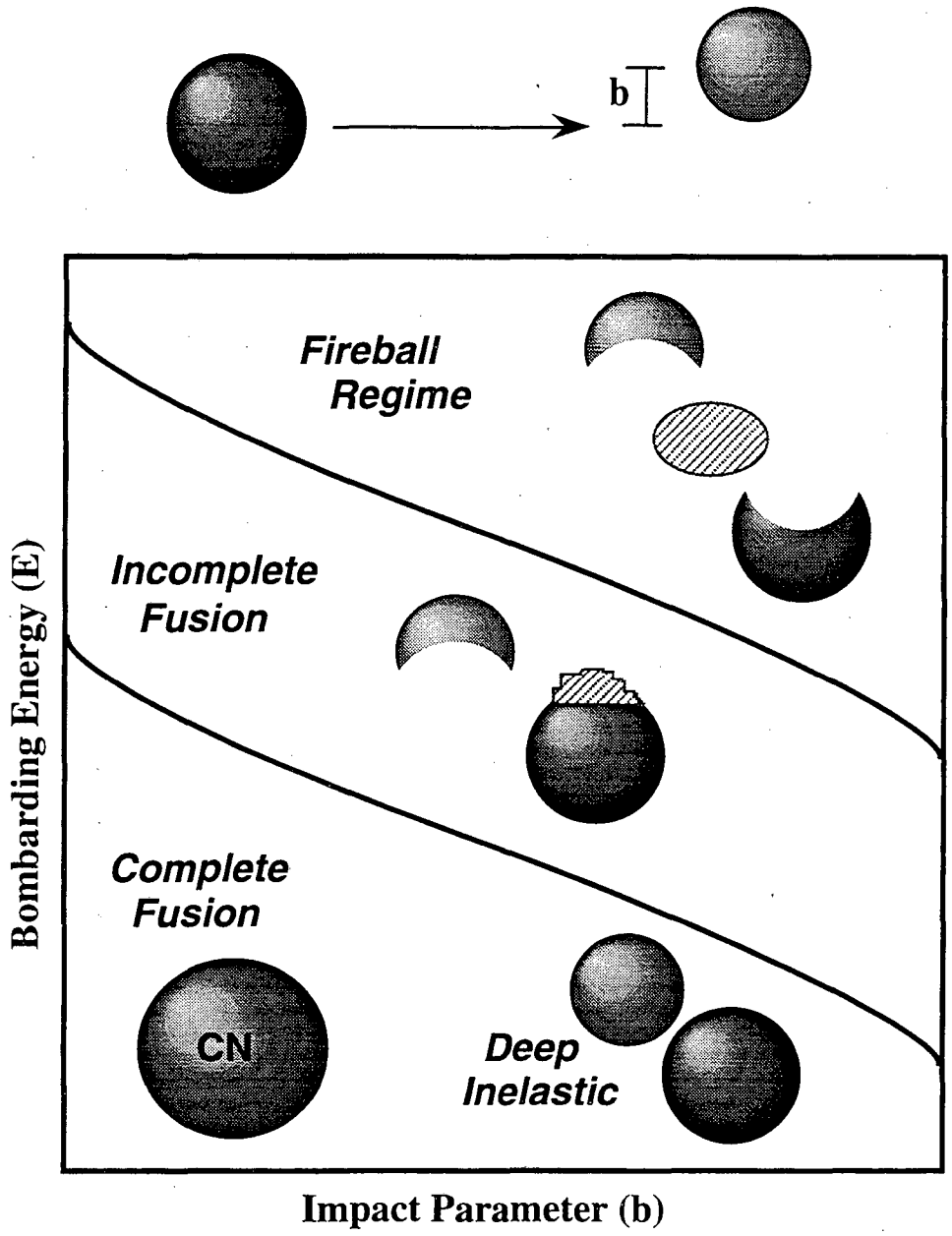

Figure 1.1 : A schematic representation of the evolution of the heavy–ion reaction mechanism with bombarding energy and impact parameter b. The different regimes are (a) complete fusion plus deep inelastic collision, (b) incomplete fusion, and (c) the fireball regime.

dinuclear transient system may be formed when the two nuclei just barely touch each other in a "deep–inelastic" collision [Schr 77, More 81] at large impact parameters. At higher bombarding energies, the probability of complete fusion decreases, since the collision occurs at such a high speed that only a piece of the smaller nucleus is absorbed by the larger nucleus. This is the incomplete fusion regime [Char 88a, Char 88b, Colo 89, Bowm 89, Hano 93], and the excited incomplete fusion product becomes a source of complex fragment emission. At even higher energies, the colliding system is divided into three pieces: the projectile spectator, the target spectator, and the "fireball" that arises from the overlapping region of the target and the projectile. In this fireball picture [Goss 77, West 76], the spectators are the emission sources of complex fragments, while the fireball, with thermal energy much larger than the nuclear binding energy, is likely to disintegrate completely into nucleons.

Although the formation of these excited emission sources of complex fragments is of great interest, the focus of this work is not on the dynamics of their formation, but rather the mechanism of their subsequent decay. A brief review is given in section 1.1 for the binary decay processes associated with complex fragment emission in the low energy regime ($E/A \leq 30$ MeV). These decay processes have been studied extensively, and their binary nature has also been confirmed by experiments [More 88]. The picture becomes less clear for complex fragment emissions at higher bombarding energies. The binary nature of the decay disappears and several experiments have shown the formation of many fragments [More 93] after the collision of two heavy nuclei at intermediate energies ($30 \leq E/A \leq 100$ MeV). This process of multifragment emission, also known as multifragmentation, is the theme of this thesis. A brief summary of the theoretical studies and the experimental investigations to understand multifragmentation is given in section 1.2, and the goal of this thesis is presented in section 1.3.

1.1 Complex Fragment Emission in Low Energy Reactions

In the low energy regime ($E/A < 30$ MeV), complex fragments are produced as the binary products of "deep–inelastic" and compound nucleus decay processes [Kauf 59, Gali 70, More 75, Schr 77, More 81]. In a "deep–inelastic" collision at relatively large impact parameters, the two nuclei just barely touch each other to form a transient dinuclear system which eventually separates. The properties of the decay products depend strongly on the exchange of nucleons during the interaction between the two nuclei. In general, these binary decay products resemble either the target or the projectile.

On the other hand, the decay of a compound nucleus is statistical in nature, and the underlying mechanism for the production of complex fragments is well understood. At relatively low excitation energies, the statistical decay of a compound nucleus occurs in the form of particle evaporation and of fission [Weis 37, Bohr 39]. In the first case, very light particles are emitted (neutrons, protons and alpha particles); in the second case, sizable fragments of approximately half the mass of the compound nucleus are observed. At higher bombarding energies, the emission of intermediate mass fragments associated with higher barriers becomes more probable. Consequently, the binary statistical decay of compound nuclei produces complex fragments that cover the entire range of mass–asymmetry [More 72, More 75, Sobo 83, More 88]. Unlike the projectile–like or target–like fragments observed in deep–inelastic collisions, complex fragments associated with compound nucleus decays bear no obvious genetic relationship to either the target or the projectile.

In this low energy regime, two sources of compound nuclei have been established: complete fusion and incomplete fusion. At very low energies ($E/A <$ 10 MeV), only complete fusion is observed [Birk 83]. However, as the bombard-

ing energy increases ($E/A > 10$ MeV), the probability of complete fusion decreases especially when the overlap of the two nuclei is not complete at relatively large impact parameters. The incomplete fusion sets in when the collision occurs with such speed that only a piece of the smaller nucleus is absorbed by the larger nucleus [Char 88a, Char 88b, Colo 89, Hano 93]. Still, the product of the incomplete fusion can relax into a hot compound nucleus.

1.2 Multifragmentation in Intermediate Energy Reactions

In the 1980's heavy–ion beams became available in the previously unexplored intermediate energy region. At intermediate bombarding energies (30 MeV $< E/A <$ 100 MeV), a transient nuclear system with an excitation energy comparable to its binding energy is formed and may eventually break up into many fragments. Indeed, evidence for such a multifragmentation scenario has been established in numerous experiments involving a wide range of excitation energies and reactions [Guer 89, Gutb 89, Gros 90, More 93]. However, the underlying mechanism of this multifragment emission process remains an unresolved puzzle. For instance, it is still unclear whether multifragmentation exists as a distinct simultaneous break up process, or if it is reducible to a sequence of binary decays similar to those observed at lower energy reactions. The issue whether the decay is driven by dynamics or statistics is also hotly debated theoretically, and is the object of intense experimental studies [Aich 91, Bord 92, Baug 93, Bowm 93, Ethv 93, Fox 93, Sang 93, Abou 94, Glas 94, Ller 94, Louv 94, Scha 94].

1.2.1 Theoretical Approach

Multifragmentation has stimulated theorists to put forth a variety of theories ranging from statistical to dynamical models. Statistical theories begin at the disassembly stage where the transient nuclear system is assumed to have attained equilibrium prior to its decay. These models have been successful in describing the equilibrium features of fragments emitted from equilibrated systems characterized by some conserved quantities such as the total mass (charge), the excitation energy, and the angular momentum. Some of these models assume a sequential approach while others portray a simultaneous break up. Dynamical theories, on the other hand, are designed to describe the entire evolution of the reaction from collision to fragmentation. Therefore, they are often used to account for the pre–equilibrium emission of light particles and other entrance channel effects observed in these reactions. These models have also demonstrated instabilities associated with the transient nuclear system. A brief description of the commonly used models is given in the following section.

1.2.1.1 Statistical Theories

Generally, statistical models can be classified as either "sequential" or "simultaneous". The former treats multifragmentation as a result of sequential emission of fragments; the latter describes a simultaneous break–up into many fragments. The sequential model is essentially an extension of the well established binary compound nucleus decay. The simultaneous models, on the other hand, study the probabilities of multifragment configurations under various conditions and assumptions about the system's equilibrium. In a different approach, the percolation model (with no time aspect) is used to explore phase transitions in highly excited nuclear systems.

A. Sequential Binary Decay When the excitation energy of a nuclear system is large enough, the primary binary–decay products, either from direct reactions or compound nucleus decays, may also be very excited and subjected to further binary decays. In this way, the process of multifragment production is reduced to a sequence of binary decays [More 88]. This is a very common process observed in low and intermediate energies heavy–ion reactions [Olmi 87, More 88, Bord 90, Toke 92]. At rather low energies, the excited projectile–like or target–like fragments produced in direct reactions such as deep–inelastic collisions may have a significant probability of further decay [Olmi 87, Bord 90, Toke 92]. Similarly, the binary–decay products of completely fused nuclei may also be sufficiently excited to break up into additional fragments. When incomplete fusion sets in at intermediate energies, the resulting incomplete fusion product can also relax to a compound nucleus and undergo further statistical decay [More 88]. At higher energies, the picture stays unchanged even though the resulting decay chains can become very long.

This process of sequential–binary decay relies on the formation of an initial compound nucleus. From the mass (charge), the excitation energy, and the angular momentum of this compound nucleus, the probability of decaying into two fragments with a given partition of excitation energy and angular momentum can be derived. This branching is continued until all the fragments can no longer decay. At each stage, the decay process is controlled by the compound nucleus branching ratios [More 88]. This simple picture however is bound by two main physical limitations. Like other statistical models, the system is assumed to have attained equilibrium prior to its decay. In a sequential model, equilibrium is required not only for the initial compound nucleus, but also for the subsequent intermediate relaxed systems. Therefore, the decay chain may be interrupted when the system fails to form a compound nucleus at a certain stage. In other words, the dynamics may lead the system to a different

state even before it fully relaxes.

The other limitation has to do with the interaction between sequential decays. When two sequential binary decays occur very close in space–time, their interactions are strong as if the fragments had been formed simultaneously. However, the essence of "sequentiality" should be the binary nature at each stage of emission rather than the emission time scale. For example, the interaction between two successive emissions with very short separation time may be strong enough to perturb the collective degrees of freedom such as the angular distributions. The intrinsic degrees of freedom that determine the level densities may not be disturbed seriously, and hence the corresponding decay probabilities may preserve their binary nature. In this case, the branching ratios of the multifragment events may still be binary, while the angular distributions are substantially perturbed. Therefore, the excitation functions of n–fold events, which are sensitive indicators of the statistical nature of the branching ratios, rather than the emission time scale should be examined in order to establish the binarity and thus the sequentiality of a reaction. In fact, it is simply a matter of semantics to argue that when the times become short, sequential becomes the same as simultaneous. A clear distinction then becomes unavailable when the criteria is based on the emission time scale only.

B. Simultaneous Multifragmentation The simultaneous model has several versions which depend upon the specific kind of equilibrium being assumed in each model. For example, fragment formation in a liquid–vapor equilibrium model is related to vapor condensation near the critical point. In other models, Coulomb interactions, nuclear masses, and level densities are incorporated; an ad–hoc critical volume is postulated in which fragments are assumed to attain chemical and physical equilibrium. In a somewhat different approach, nuclei are assumed to break up on impact

and shatter like a piece of brittle material, and the resulting mass distribution is described with a statistical ansatz.

Liquid–Vapor Equilibrium The success of the Liquid Drop Model in describing the macroscopic properties of nuclear system reflects the similarity between nuclear matter and ordinary fluids. If the Coulomb interaction is neglected for the moment, nuclear matter bound by nuclear forces with long–range attraction and short–range repulsion, behaves just like a Van der Waals gas. In fact, Fermi–Thomas [Barr 80, Barr 81] and Hartree–Fock [Saue 76, Lamb 81] calculations for nuclear matter produce isotherms that are quite similar to those of the Van der Waals equation. This similarity suggests that nuclear matter should be able to undergo a liquid–gas phase transition as observed in an ordinary fluid. In this spirit, much effort has been put forth to relate the occurrence of nuclear multifragmentation to the spectacular phenomenon of critical opalescence observed in an ordinary fluid at the critical point.

The probability $P(A)$ for a cluster of A particles to exist in equilibrium with other clusters in a fluid is given by [More 93]:

$$P(A) \propto A^{-\tau} \cdot e^{-\frac{\gamma}{T}A^{2/3}} \cdot e^{\frac{(\mu-\mu_L)}{T}A}. \tag{1.1}$$

The first term $A^{-\tau}$ arises from the energy independent statistical weight of a cluster size A, and τ is a critical exponent that depends on the dimensionality of the cluster. The second term accounts for the temperature dependence of the surface energy associated with cluster formation; γ and T are the surface energy coefficient and temperature respectively. This surface term favors the formation of clusters at high temperatures since the surface energy coefficient decreases with increasing temperature. The third term describes the chemical potential difference between the gas and the liquid phase; μ and μ_L are the chemical potential of a particle in the gas and

the liquid phase respectively. When $\mu < \mu_L$ for a stable gas phase, the exponent of this chemical potential term becomes negative and the formation of large clusters is suppressed. On the other hand, when $\mu > \mu_L$, the liquid phase becomes stable and the probability of cluster formation increases with the size A.

At the critical point, there is no distinction between the two phases and $\mu = \mu_L$; the densities of the liquid and gas are equal and thus $\gamma = 0$. Therefore, both the surface and the chemical potential terms of Equation 1.1 are reduced to 1 in this limit. The distribution of cluster size at the critical point then follows a power–law:

$$P(A) \propto A^{-\tau}. \tag{1.2}$$

This power–law distribution has been identified in a variety of inclusive nuclear experiments, and has lead to the claim that multifragmentation can be pictured as formation of nuclear droplets via vapor condensation near the critical temperature [Finn 82, Chit 83, Mahi 88, Trau 93]. However, several investigations have shown that the power–law dependence is not a unique signature of liquid–gas phase transition, but rather a generic feature associated with statistical equilibrium models [Hufn 86, Lync 87, More 88, Aich 91]. For example, a power–law dependence has also been observed in the fragment mass distributions obtained from chemical equilibrium models [Rand 81, Gros 82, Bond 85b] and percolation models [Baue 85, Baue 86]. Besides nuclear matter, similar power laws have also been observed for collision debris of stones and for the distribution of asteroids in the planetary system [Hufn 86].

Chemical Equilibrium The above liquid–vapor equilibrium model essentially describes the phenomenon of critical opalescence in a neutral fluid. This has raised questions concerning its applicability to finite systems of charged nuclei. Other chemical equilibrium models have thus been developed to incorporate Coulomb

interactions, nuclear masses, and level densities. These models assume that the reaction dynamics drives the system to a simple geometric configuration, within which statistical equilibrium is established with respect to the "fragmentation" degrees of freedom. In particular, spherical fragments are randomly distributed inside a sphere. The "freeze out" volume of the sphere is preassigned arbitrarily and the fragments are separated by a minimum distance that is also arbitrarily chosen. The statistical weight of each possible fragmentation configuration can then be evaluated using the microcanonical ensemble [Gros 86, Gros 87], canonical ensemble [Bond 85b, Bond 85a], and grand canonical ensemble [Rand 81] formalisms of statistical mechanics.

As an example, Figure 1.2 shows the results of the microcanonical calculation [Gros 87] for ^{131}Xe. In this approach, the statistical weight for each configuration of fragments inside the sphere is evaluated microcanonically by distributing the available energy using the internal and collective degrees of freedom. The relative yields of decays of ^{131}Xe into different final channels are plotted as a function of excitation energy E^* on the top panel of Figure 1.2. The events are classified by the number of intermediate mass fragments (IMFs) with mass $A \geq 10$ in the final channels. More specifically, events with 0, 1 and 2 intermediate mass fragments are called vaporization (V), evaporation (E) and fission (F), respectively. Finally, multifragmentation (M) is used to describe events with 3 or more intermediate mass fragments. In this particular case for ^{131}Xe, the excitation energy is not high enough to produce vaporization of the system, and thus only three decay channels are observed. The decay is dominated by evaporation (E) of light charged particles until the excitation energy is sufficiently high (250 MeV) for fission (F) to set in. At still higher energies, multifragmentation (M) sets in and the cracking of the nucleus into three or more pieces becomes the dominant mode. To study the effect of the Coulomb interaction on the onset of multifragmentation, the calculation for ^{131}Xe was performed excluding the Coulomb

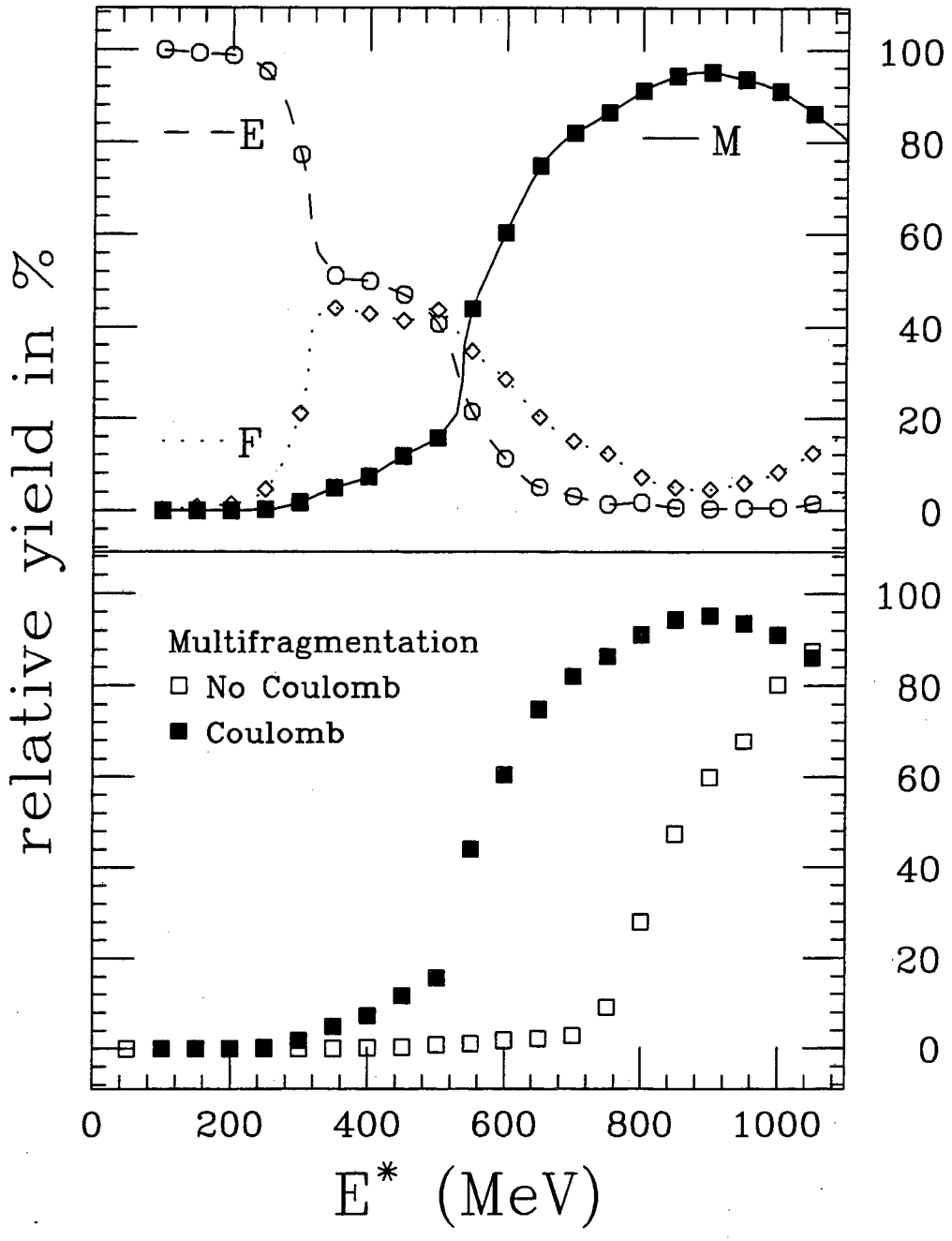

Figure 1.2 : Microcanonical calculation for ^{131}Xe. (Top) Calculated yields for the evaporation (E), fission (F), and multifragmentation (M) processes as a function of excitation energy. (Bottom) The multifragmentation yields with (solid squares) and without (open squares) the Coulomb interactions are compared.

interaction, and the resulting yield of multifragmentation is shown on the bottom panel of Figure 1.2. An increase in the excitation energy threshold (from 500 MeV to 700 MeV) for the onset of multifragmentation is clearly observed. This result suggests that the repulsive long range Coulomb interaction significantly enhances multifragmentation in this model.

The results of these models are very sensitive to the specific shape and size chosen for the "freeze out" configuration, from which the potential energy and thus the decay probabilities are calculated. For example, the overall Coulomb energy of the system is diminished significantly when the fragments are placed in an elongated rather than a spherical shaped container. If this shape degree of freedom is included in the model, the system will choose a stretched shape with the fragments infinitely far apart in order to minimize its energy. The conclusions regarding the significance of the Coulomb force are clearly incomplete, since the ad–hoc assumption made for the shape and volume of the "freeze out" configuration does not consider the effect of the Coulomb interaction. Indeed, major criticisms of these models have pointed at the arbitrary selection of these "freeze out" parameters that may not be well justified.

Nuclear Shattering In this model, multifragmentation results from the shattering of brittle nuclei under a sufficiently hard impact like two glass balls thrown at each other. The similarity between the resulting fragment mass distributions from nuclear multifragmentation and shattering of fragile material were first studied by Aichelin & Hufner [Aich 84a]. Empirically, the mass distribution of fragments generated from shattering was also found to approach a simple power–law dependence on the fragment size. In an attempt to derive such a distribution, Aichelin and Hufner assumed that all possible fragmentation configurations occur with equal probability. Sobotka & Moretto [Sobo 85] further showed that this approach is similar to Euler's

problem of number partition (i.e. the least biased breaking of an integer Z_o into n integers). An approximate solution of Euler's problem gives the following integer distribution:

$$P(n, Z) \propto e^{-\frac{nZ}{Z_o}}. \tag{1.3}$$

In the context of nuclear fragmentation, Z is the charge of an emitted fragment, n is the fragment multiplicity and Z_o is the total charge of the system. This approach, however, does not account for any kind of energy dependence and the above equation does not relate the charge distribution to other observables. A remedy suggested by Moretto et al. incorporated an energy dependence through the extra surface associated with fragment formation [More 86]. The charge distribution, evaluated with an additional constraint of a fixed amount of surface generated, has a similar functional form as the droplet size distribution in liquid–vapor equilibrium (Equation 1.1):

$$P(Z) = \frac{1}{exp[DZ + AZ^{2/3}] - 1}. \tag{1.4}$$

The constants D and A can be calculated for a system of fixed total charge and total energy (surface).

C. Percolation In a somewhat different approach, the percolation model is used to study the possibility of observing a second order phase transition of nuclear matter in multifragmentation [Baue 85, Camp 85, Baue 86, Camp 86, Desb 87, Baue 88]. In this model, the nucleus is treated as a lattice of nucleons connected by bonds. The probability to break a bond p_b is related to the excitation energy or temperature of the nucleus. When the nucleus is cold, the bond breaking probability is small and a large cluster extending throughout the lattice exists (percolating cluster). However, when the excitation energy of the system increases, the bond breaking probability increases accordingly. Eventually, the excitation energy and thus the bond breaking

probability reaches a critical value beyond which the percolating cluster no longer exists. The nucleus at this critical point (p_b^{crit}) breaks into many smaller clusters similar to those observed in nuclear multifragmentation.

The evolution from a large percolating cluster to a system of many fragments beyond a percolation threshold is similar to the behavior of systems undergoing liquid–gas phase transitions. In particular, the mass distribution of the clusters near the percolation threshold is given by a power–law consistent with the distribution of droplet size near the critical point in a liquid–vapor equilibrium. This observed similarity suggests that the percolation theory may be used to study phase transitions at criticality. One specific method that makes use of the percolation model is to search for observable quantities that behave in a qualitatively different way at the critical point. One of these quantities proposed by Campi [Camp 86] is the event–by–event moment of the fragment size distribution. The ith moment of the charge (mass) is defined as:

$$M_i = \sum Z^i, \tag{1.5}$$

where the sum is extended to all the fragments of the event except the largest one. The exclusion of the largest fragment is justified as an attempt to eliminate the "percolating" cluster. In other words, the heavy nuclear residue (when present) is associated with the "infinite" percolating cluster and the lighter fragments with the finite clusters. The percolation theory predicts that the ratio M_2/M_1 diverges at $p_b = p_b^{crit}$. The two branches identified in a scatter plot of $ln(M_2/M_1)$ vs p_b have been attributed to subcritical and supercritical events [Baue 88]. When the average value of M_2/M_1 is plotted as a function of p_b, a singularity is thus observed at $p_b = p_b^{crit}$ indicating a second order phase transition. However, theories of phase transitions are generally formulated for practically infinite systems. When the size of the system

decreases, a broad maximum instead of a singularity is observed due to the finite size effect. This illustrates how the signals of the critical behavior in a large system are smoothed when decreasing the size [Baue 88].

In a similar approach, combinations of moments have been studied. For example, an interesting combination of moments, γ_2, is given by

$$\gamma_2 = \frac{M_2 M_0}{M_1^2} = \frac{\sigma^2}{\langle Z \rangle^2} + 1, \tag{1.6}$$

where σ^2 is the variance and $\langle Z \rangle$ is the average charge of fragments in the event. When γ_2 is plotted versus the bond breaking probability p_b, $\gamma_2 = 1$ for $p_b = 0$ and $p_b = 1$, while it goes to infinity at criticality ($p_b = p_b^{crit}$). This singularity at p_b^{crit} reflects the large fluctuations (σ^2) in the fragment size distributions near the critical point. On the other hand, the value of γ_2 approaches 1 when the fluctuation in the fragment size is minimized as the system disassembles completely into nucleons at large p_b. Similarly, when the bond breaking probability is small and the heavy residue is dropped as the percolating cluster, the size fluctuation becomes minimal for the light evaporated particles, and γ_2 approaches 1.

The above result shows that the observed singularity near the critical bond breaking probability p_b^{crit} can be used to observe and verify second order phase transitions in nuclear multifragmentations. In practice, a variable strongly correlated with p_b like the excitation energy, or the total charge particle multiplicity is used in the above analysis. Sometimes, one uses the number of nucleons bound in clusters Z_{bound} that may go as $1/p_b$. The charge (mass) of the largest detected fragment Z_{max} has also been used as a measure of p_b, but it is more vulnerable to the experimental detection efficiency, since the heaviest fragment generally has a very small velocity in the laboratory frame.

1.2.1.2 Dynamical Theories

The dynamical descriptions of energetic heavy–ion collisions are generally based on one–body transport models, which are designed to describe the entire evolution of the reaction from collision to fragmentation. In the low energy regime, where the Pauli blocking effectively hinders the two–body collisions, the interaction of nucleons is dominated by the nuclear mean field. This characteristic feature of relatively cold nuclear systems is reflected in the rather long mean free path for the individual nucleons. At these energies, self–consistent theories of the nuclear mean field such as Time–Dependent Hartree–Fock (TDHF) calculations have been successful in describing fusion reactions and deep–inelastic scatterings [Davi 78, Nege 82]. On the other hand, pure kinetic models such as the Vlasov equation serves as another basis for describing heavy–ion reactions. The following expression for the Vlasov equation describes the propagation of the phase space distribution function $f(r,p,t)$ under the influence of the mean field U:

$$\frac{\partial f}{\partial t} + \frac{p}{m}\nabla_r f - \nabla_r U \cdot \nabla_p f = 0. \tag{1.7}$$

In a semi–classical approach, the phase space distribution function $f(r,p,t)$ is viewed as an ensemble of pseudoparticles moving along the classical trajectories in a potential dominated by the nuclear mean field U.

At higher energies, however, a larger domain of the available phase space becomes accessible to the scattered nucleons, and the two–body collisions (residual interactions) can no longer be neglected. The Pauli blocking becomes less effective as evidenced by a shortening of the mean free path for the individual nucleons. As a result, application of TDHF could become problematic at these energies. On the one hand, the requirement that the time scale for the mean field evolution is long compared with the time scale of the collisions may no longer be valid. On the other hand, the

enormous mathematical complexity involved in quantum corrections to the mean field theory by a collision integral is very difficult to carry out numerically. Similarly, the collisionless Vlasov equation fails to account for the non–negligible contributions from the two–body collisions. To account for the nucleon–nucleon collisions, the Vlasov equation has been augmented with a Pauli blocked collision term $D_t^{coll} f(r,p,t)$ of the Boltzmann form:

$$\frac{\partial f}{\partial t} + \frac{p}{m}\nabla_r f - \nabla_r U \cdot \nabla_p f = D_t^{coll} f(r,p,t). \tag{1.8}$$

Such an approach was first proposed by Nordheim [Nord 28] for the treatment of an electronic gas in solids and later taken by Uehling and Uhlenback [Uehl 33]. More recently, this general method has been adapted to nuclear dynamics. A series of microscopic dynamical theories, differing in ingredients and methods of solution, have been evolved along this semi–classical line [Bert 88, Bona 89, Schu 89, Bona 90b, Bona 90a]. They are variously labeled as the Boltzmann–Uehling–Uhlenbeck (BUU), Vlasov–Uehling–Uhlenback (VUU), and Boltzmann–Nordheim–Vlasov (BNV) equations, to indicate that a Pauli blocked Boltzmann collision term has been added to the Vlasov equation. An example illustrating the onset of multifragmentation in the BNV model calculations is shown in Figure 1.3 for the reaction ^{129}Xe + ^{197}Au at E/A=60 MeV. Computer simulations of heavy–ion collisions based on these kinetic equations will be discussed in some detail in Chapter 2.

In these dynamical models, the dynamics becomes dominant and drives the system into regions of instabilities that lead to multifragmentation. One instability that may play an important role in multifragmentation is the spinodal instability. This instability develops when a system of homogeneous fluid enters into a region of negative pressure, which leads to its breaking up into droplets of denser liquid embedded in a lower density vapor. In the case of heavy–ion reactions at intermediate

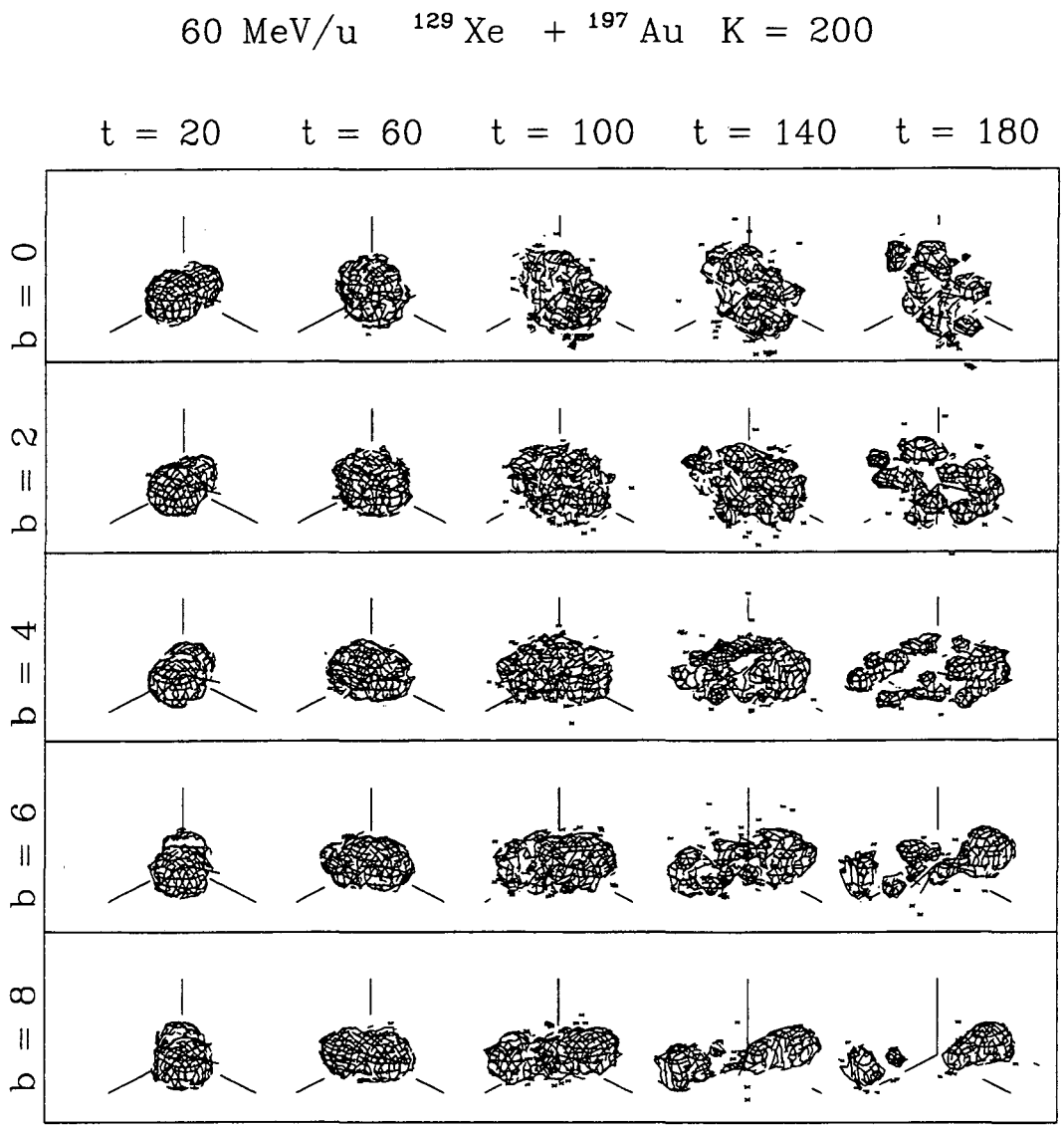

Figure 1.3 : BNV calculations of the time evolution of the reaction ^{129}Xe + ^{197}Au at $E/A = 60$ MeV for several different impact parameters b. The calculations were performed with an incompressibility coefficient of $K = 200$ MeV. Each row contains a different impact parameter and each column a different time step in units of fm/c.

energies, violent collisions may lead initially to a hot, compressed system of nuclear matter. This compressed system expands until the density is so low that the super-cooled system reaches the spinodal region of negative pressure, where instabilities with respect to density fluctuations can cause prompt multifragmentation. Since the spinodal instability can occur in an infinite system, it is often called a bulk, or volume instability.

Another class of instabilities has to do with the presence of a surface endowed with surface tension in finite nuclei. These instabilities of the Rayleigh kind [Rayl 64] have been observed in the BNV calculations of heavy–ion collisions at intermediate energies [More 92]. In a head–on collision, a "disk" develops due to the side–squeezing of nearly incompressible nuclear matter. The thickness of the disk decreases while the diameter increases monotonically with increasing bombarding energy. When it becomes sufficiently thin, it breaks up into several fragments. This disk fragmentation has been analyzed in terms of the new Rayleigh–like surface instability, in which the proximity force plays an essential role. Ordinarily, a disk is at most metastable due to the energy barrier associated with the increase in the surface area of a modulated disk. This barrier prevents the system to escape from the high surface energy of a disk by breaking up into a number of spherical fragments with less overall surface. When the disk becomes thin enough, the proximity potential due to the surface–surface interaction is sufficient to overcome the sharp surface barrier and trigger the surface instability, which causes the breaking of the thin disk into several fragments.

In addition to nuclear disks, other exotic shapes such as bubbles have also been observed in the Boltzmann–like calculations [Baue 92]. A bubble behaves much like a sheet, and is susceptible to the surface instability when its thickness is of the order of the proximity interaction range. However, the Coulomb energy has not been incorporated in the above discussion on the surface instability. For compact

shaped nuclear disks, the Coulomb contribution to the deformation energy may be small compared to the surface and proximity contributions. In the case of a nuclear bubble, the depletion of charges in the central cavity reduces the Coulomb energy significantly and this Coulomb effect should not be neglected. In Chapter 2, the Rayleigh–like surface instability and the effect of the Coulomb energy on the stability of nuclear bubbles will be discussed in detail.

The main drawback of these dynamical theories is that they are equations for the average one–body distribution function. They neglect fluctuations and correlations apart from incoherent two–body scatterings and Pauli principle correlations. Although some of the simulation results have shown that the algorithmic noise is sufficient to trigger instabilities and to break symmetries, the subsequent results are unphysical and are probably machine dependent [More 92]. There are generally many different final channels available in typical nuclear collisions at intermediate energies, and the actual fluctuations can be important in dictating the evolution of the system in a region of instability. Theoretical efforts have thus been made to introduce truly physical fluctuations based on the theory by Ayik and Gregoire [Ayik 88, Ayik 90]. To be more specific, the time dependent field is decomposed into an average part (mean field) and a fluctuating part in the spirit of the Langevin approach [Rand 90, Burg 91, Chom 91, Sura 92].

The above discussion suggests that the algorithmic noise is good only to show the underlying instabilities but not to generate realistic results. However, truly physical fluctuations are not necessary for some instabilities whose onset is independent of the noise that triggers them. One simple example is the Rayleigh instability of a cylinder of liquid [Rayl 64]. Rayleigh showed that a cylinder of fluid is unstable with respect to perturbations of wavelength $\lambda \geq 2\pi R$, and that the growth is fastest for $\lambda = 9.11R$, where R is the radius of the cylinder. This maximum instability at

$\lambda = 9.11R$ dominates exponentially in time over all the other wavelengths and thus determines the size of the droplets. As a result, the breaking up of the cylinder into droplets is practically independent of the noise that triggers the instability. In addition, manifestation of instabilites of the resonant type is also independent of the noise. For instance, a violin string struck by a bow sets up a stick–slip instability that always produces the same note, independently of the violinist. Of all the frequencies contained in the noise, only the resonant frequencies survive and have a chance to be amplified by the instability. The others are cancelled by negative interference.

1.2.1.3 Dynamical–Statistical Theories

Although the dynamical models such as the Boltzmann–like calculations can account for the pre–equilibrium emission of light particles and other entrance channel effects, they cannot always realistically describe the decay of hot nuclei at the late stages of the reaction, because they do not include physical fluctuations. In References [Snep 90, Colo 92a, Colo 92], this difficulty has been circumvented by coupling a dynamical calculation that describes the formation of the primary fragments, to a statistical model that simulates the decay of the excited fragments during the final stages. In practice, the excitation energy, the mass and the angular momentum of each primary fragment are extracted from the dynamical calculation and are used as input parameters for the subsequent statistical simulation. In such a hybrid model, it is essential to ensure equilibrium for the primary fragments before switching to a statistical calculation. Hence, the key problem in this dynamical–statistical coupling is the uncertainty in the determination of the "relaxation" time, the time at which energy relaxation (equilibrium) has occurred.

This practical limitation associated with a hybrid model has called for the development of a unified theory to incorporate both dynamics and statistics consis-

tently. In this direction, one schematic model has been developed by coupling statistical emission features to dynamical features associated with the density changes of the emitting source driven by the thermal pressure [Frie 90]. In this model, a dynamically expanding nucleus is allowed to evaporate particles of any size during its dynamical evolution. At low energies, the expansion features have little effect on fragmentation, but with increasing energy they provide dramatic effects. In particular, the model demonstrates that the evolution to a low density region is necessary for the onset of multifragmentation, indicating that dynamics may play an important role in this phenomenon.

1.2.2 Experimental Investigation

Many experiments were performed in the past decade trying to understand the mechanism and to characterize the source of multifragmentation. Most of the experimental conclusions rely strongly on comparisons with theoretical calculations. While the various models mentioned above may be sound in their essence, inevitable limitations make their applications to actual data somewhat problematic. Difficulties may occur for the theoretical variables or observables that cannot be accurately measured experimentally, and sometimes, different theories suggest different variables. Moreover, these models often contain adjustable parameters that are chosen to fit the experimental data and may not be well justified. As a result, bias associated with assumptions of individual models may be carried into the interpretations of the experimental data.

A less biased approach is to examine the data themselves and to search for signatures that may reveal the mechanism of the decay process. For example, the statistical origin of the α–induced fission probability P_f was demonstrated by

the presence of a thermal energy dependence $\left[ln(P_f) \propto 1/\sqrt{E^*}\right]$, where E^* is the excitation energy of the system [More 69]. The following derivation shows that this characteristic energy dependence is a generic attribute of statistical decay and is independent of any theoretical models.

In a statistical decay, the fission probability should be proportional to the level density of the system $\rho(E^*)$ at an excitation energy equal to the available energy minus the fission barrier:

$$P_f(E^*) \propto \rho(E^* - B_f). \tag{1.9}$$

For a Fermi gas level density,

$$P_f(E^*) \propto exp[2\sqrt{a(E^* - B_f)}], \tag{1.10}$$

where a is the level density parameter. For $E^* \gg B_f$ one obtains:

$$P_f(E^*) \propto e^{2\sqrt{aE^*}} e^{-B_f\sqrt{a/E^*}} \propto e^{-B_f/T}. \tag{1.11}$$

Therefore, the linear dependence observed in the plot of $P_f(E^*)$ versus $1/\sqrt{E^*}$ is empirical evidence for the statistical nature of α–induced fission [More 69].

In the fission studies, the focus is on the competition between the fission and neutron decay channels, but in principle this approach can be extended to multifragmentation, where the competition between decay channels of different IMF multiplicity becomes more interesting. If the hot nuclear system formed in a heavy–ion reaction decays statistically, it is conceivable that the multifragment decay is an extension of binary decay, and is governed by an average barrier B_n for n–fragment emission. Similarly, the n–fragment emission probability P_n should be proportional to the level density of the system $\rho(E^* - B_n)$, and for $E^* \gg B_n$, one obtains:

$$P_n(E^*) \propto e^{-B_n/T}. \tag{1.12}$$

This expression is similar to the above fission probability except that the fission barrier B_f is now replaced with an average barrier B_n for n–fragment emission. In the framework of the chemical equilibrium picture for a prompt multifragmentation, B_n can be considered as the potential energy of a n–body decay configuration. For a sequential picture, B_n is simply the sum of barriers $b_1, b_2, b_3, ..., b_n$ for the successive binary decays under the assumption that the temperature is nearly constant at all stages of emission. This result suggests that the linear dependence of $ln(P_n)$ with $1/\sqrt{E^*}$ is a generic attribute of statistical decay and it applies to both prompt and sequential multifragmentations governed by the statistics.

In the last several years, researchers have succeeded in isolating what appears to be true multifragmentation sources formed in reverse kinematics intermediate energy heavy–ion reactions [Blum 91, More 93a, Rous 93]. In these experiments, the excitation energy of the source E^* was estimated kinematically from the parallel source velocity assuming an incomplete fusion picture. To minimize the contamination from the pre–equilibrium emission of light charged particles, the source velocity was constructed on an event–by–event basis from the velocities and the masses of the detected fragments ($Z \geq 3$) only. The normalized probabilities $P(n)/P(2)$ for detecting n fragments were obtained as a function of this excitation energy E^*. These excitation functions were found to be independent of the specific target and even of the bombarding energy. At a given bombarding energy, the observed target independence is consistent with the picture of incomplete fusion, in which the source can be characterized by the amount of mass transferred from the target to the heavier projectile, and depends relatively little on the actual nature of the target. The bombarding energy independence also shows that once the excitation energy is determined from the source velocity, the probabilities for various decay channels are fixed no matter how the source is formed. This decoupling between the entrance and the exit channel

is a necessary condition for statistical decay.

A most remarkable result is that, at a given value of n, a linear dependence is observed when the natural logarithm of the above normalized probability $P(n)/P(2)$ for detecting n fragments is plotted as a function of $1/\sqrt{E^*}$ [More 93a]. Since nuclear temperature is proportional to $\sqrt{E^*}$ in the Fermi gas model, this linear dependence indicates a statistical energy dependence of the n–fragment emission probabilities. In other words, the dynamics of the reaction seems to be limited to the formation of a source, while the various fragment decay channels are dictated by the available phase space. However, it could not be decided by this approach whether the statistical emission is sequential or simultaneous.

In summary, the observed linear correlation between the logarithm of the fission probability and $1/\sqrt{E^*}$ is a powerful way to demonstrate the statistical nature of the fission reaction, and this has also been extended to multifragmentation. One merit of this approach is its direct experimental findings independent of any theoretical models. Essentially, an empirical conclusion is obtained by plotting the data in a particularly revealing way.

1.3 Goal of Project

At low ($E/A < 30$ MeV) bombarding energies, the binary nature of complex fragment productions associated with compound nucleus decays and deep–inelastic collisions has been studied extensively and is well understood. However, the origin of multifragmentation observed at at intermediate ($30 < E/A < 100$ MeV) bombarding energies is still a mystery. In particular the issue of dynamics versus statistics has been the subject of intense debate theoretically and experimentally. The goal of this thesis is to investigate the underlying mechanism of multifragmentation and to search

for signatures of dynamical or statistical effects. To this end, the reactions ^{129}Xe + ^{nat}Cu, ^{89}Y, ^{165}Ho, ^{197}Au at bombarding energies of E/A = 40 & 60 MeV have been studied theoretically and experimentally.

The heavy ^{129}Xe projectile is used to bring large amount of mass, angular momentum and excitation energy into the center–of–mass of the colliding nuclei in order to probe the onset of multifragmentation. Moreover, the choice of targets provides a variety of projectile–target combinations ranging from reverse to normal kinematic reactions, and covers a large range of excitation energies. In particular, the excitation energy per nucleon available in the center–of–mass system increases from 8.9 MeV for ^{nat}Cu (E/A = 40MeV) to 14.1 MeV for ^{197}Au (E/A = 60MeV).

Recent calculations of central heavy–ion collisions at intermediate energies performed by means of Boltzmann–like transport codes, have shown the formation of rather peculiar shapes, like bubbles, donuts and disks, which then proceed to break up into several fragments [Baue 92, Gros 92a, More 92]. These results suggest that multifragmentation may be due to the onset of static instabilities arised from the interplay of surface, proximity and Coulomb energies. In this spirit, the Boltzmann–Nordheim–Vlasov equation has been used to simulate the above ^{129}Xe-induced reactions. In particular, simulation results for central collisions have been studied in order to understand the underlying instabilities that trigger the onset of multifragmentation observed in these dynamical simulations.

In addition to these theoretical studies based on complicated simulation codes, the experimental data have also be examined to search for simple regularities. As mentioned in section 1.2.2, a linear dependence is observed when the natural logarithm of the relative probability of emitting n fragments is plotted as a function of $1/\sqrt{E^*}$ indicating a statistical behavior [More 93a]. This experimental study seems to relegate the role of dynamics to the formation of sources, which then proceed to decay

in an apparently statistical manner. However, it could not be decided whether the emission is sequential or simultaneous. Another relevant question that remains unanswered is the fundamental issue of reducibility: can multifragmentation be reduced to a combination of independent emissions of fragments? In this project, the above excitation function analysis has been extended to the ^{129}Xe-induced reactions with more complete measurements. In particular, excitation functions and charge distributions have been constructed and studied in order to verify empirically whether the probability for the emission of n fragments can be reduced to the emission probability of just one fragment.

Chapter 2

Surface and Coulomb Instabilities

In this chapter, the multifragment production observed in intermediate energy heavy–ion reactions is studied theoretically by analyzing the simulation results of Boltzmann–like transport codes. A brief description of these Boltzmann–like kinetic equations and their implementations in numerical calculations are given in section 2.1. These simulations of heavy–ion collisions have shown the formation of exotic shaped nuclei, like disks and bubbles [Baue 92, More 92]. Although disk, or bubble formation is of great interest, the main concern in this chapter is not the dynamics of their formation, but rather the mechanism of their fragmentation. Disk fragmentation and its relevance to the new Rayleigh–Like Surface Instability is discussed in section 2.2, and the Coulomb Instability of nuclear bubbles is studied in section 2.3.

2.1 Boltzmann–Like Equations and Simulations

Dynamical model calculations utilizing the Boltzmann–Nordheim–Vlasov (BNV), the Boltzmann–Uehling–Uhlenbeck (BUU) or the Vlasov–Uehling–Uhlenback (VUU) equations, have been widely used to simulate the evolution of heavy–ion collisions at intermediate energies [Gros 87, Bert 88, Schu 89, Bona 89, Bona 90a,

Bonà 90b, Aich 91]. The two fundamental ingredients of these kinetic equations are the self–consistent nuclear mean field U, and the two body nucleon–nucleon collisions (residual interactions). For example, the following expression for the BNV equation describes the propagation of the phase space distribution function $f(r,p,t)$ under the influence of the mean field U, and it also accounts for the nucleon–nucleon collisions by the collision integral D_t^{coll}:

$$\frac{\partial f}{\partial t} + \frac{p}{m}\nabla_r f - \nabla_r U \cdot \nabla_p f = D_t^{coll} f(r,p,t). \tag{2.1}$$

The mean field for a system of nucleons is given by the Coulomb interaction between protons, plus a nuclear potential approximated by a density dependent, Skyrme–like interaction of the following form:

$$U(\rho) = A\left(\frac{\rho}{\rho_o}\right) + B\left(\frac{\rho}{\rho_o}\right)^{\sigma}. \tag{2.2}$$

Here ρ and ρ_o are the local nucleon and normal nuclear densities respectively. The parameters A, B and σ are chosen such as to reproduce experimental binding energies and other saturation properties of nuclear matter. As an example, the values of A, B and σ for nuclear mean field of different "hardness" are listed in Table 2.1. The "hardness" of the nuclear equation of state is described by the adiabatic nuclear incompressibility coefficient K, which is defined in terms of these parameters A, B and σ:

$$K = 9\left(\frac{p_F^2}{3m} + A + \sigma B\right), \tag{2.3}$$

Table 2.1 : Coefficients A, B and σ extracted for three different values of K.

$K(MeV)$	A	B	σ
200	-356	303	7/6
380	-124	70.5	2
540	-98.8	46.3	26/9

where p_F and m are the Fermi momentum and mass of a nucleon respectively. The value of K ranges from 200 MeV (soft equation of state) to 540 MeV (hard equation of state), as is currently believed to be appropriate for nuclear matter. The above equation says that the incompressibility coefficient K depends not only on the fermi pressure associated with fermions, but it is also controlled by the details of the nucleon–nucleon interaction whose effects are contained in the paramters A, B and σ. In fact, the coefficient K is an input for the simulation to determine the values of A, B and σ from a parameter table (e.g. Table 2.1) for the construction of a mean field according to Equation 2.2. Finally, it is noted that the mean field is deterministic in a sense that a given initial distribution $f_o(r,p,t_o)$ produces a single dynamical history $f(r,p,t)$.

The collision integral, unlike the mean field, is stochastic, and it accounts for the evolution of the phase space distribution induced by the residual interaction,

$$\begin{aligned} D_t^{coll} f(r_1,p_1,t) &= \int dr_2 I(r_1,p_1,r_2,t), \\ I(r_1,p_1,t) &= \int dp_2 dp_3 dp_4 \delta(p_1+p_2-p_3-p_4)\delta(\epsilon_1+\epsilon_2-\epsilon_3-\epsilon_4)\sigma_{nn}^{eff} \cdot Pauli, \\ Pauli &= [(1-\bar{f}_1)(1-\bar{f}_2)f_3 f_4 - (1-\bar{f}_3)(1-\bar{f}_4)f_1 f_2], \end{aligned} \tag{2.4}$$

where ϵ_i and p_i are the single–particle energy and momentum respectively. The indexes 1, 2, 3 and 4 are used to label the quantities associated with two nucleons before and after they collide: $1 + 2 \rightarrow 3 + 4$. The two δ functions guarantee the momentum and energy conservation of the system. The effective nucleon–nucleon cross section is deduced from the energy dependent free cross section according to:

$$\sigma_{nn}^{eff} \equiv \left(\frac{d\sigma}{d\Omega}\right)_{nn}^{eff} = \left[\frac{d\sigma(E)}{d\Omega}\right]_{nn}^{free} [1 - Y(\rho)], \tag{2.5}$$

where $Y(\rho)$, a density scaling factor, accounts for the in–medium correction. $Y(\rho)$ is approximately equal to 0.5 at the normal density ρ_o and reach almost 0.1 for

$\rho = 1/2\rho_o$.

The Pauli Block factor consists of both a "gain" and a "loss" term:

$$\begin{array}{lll} gain\ \ term: & 3+4 \rightarrow 1+2 & (1-\bar{f}_1)(1-\bar{f}_2)f_3f_4, \\ loss\ \ term: & 1+2 \rightarrow 3+4 & (1-\bar{f}_3)(1-\bar{f}_4)f_1f_2. \end{array}$$

Here f_i is the phase space distribution and $\bar{f}_i$ is the corresponding occupation probabilitiy. This phase space occupation probabilitiy is simply the phase space distribution f_i divided by g/h^3, the maximal occupation allowed by quantum mechanics. In this case, the degeneracy factor g is 4 to account for the four possible states that are characterized by their spin (+ or −) and isospin (proton or neutron). To illustrate the implementation of this Pauli Blocking, the collision of two nucleons at initial states representated by 1 and 2 is considered. Then, what is the probability for this collision to occur and to produce final states 3 and 4? If the initial states 1 and 2 are highly occupied, the probability of collision is also increased and this is shown by the factor f_1f_2 in the loss term. On the other hand, when the final states 3 and 4 are largely occupied, their occupation probabilities become close to one. The factor $(1-\bar{f}_3)(1-\bar{f}_4)$ is small, and the collision into these final states becomes unlikely. In the limit when either of the final states is completely occupied, the collision becomes impossible and is said to be Pauli blocked.

In summary, this collision integral describes the change of states for two interacting particles during a collision with blocking factors forbidding collision leading to occupied states. The important roles of probability in governing these residual interactions reflect the stochastic nature of these collisions. In other words, a given initial distribution $f_o(r,p,t_o)$ may lead to many different dynamical evolutions of $f(r,p,t)$ as a result of the residual nucleon–nucleon collisions.

The simulation results presented in the following section are obtained with

the Boltzmann–Nordheim–Vlasov (BNV) model. To study the time evolution of the nuclear phase space distribution, the function $f(r,p,t)$ is decomposed as a superposition of coherent states:

$$f(r,p,t) = \sum_{n=1}^{A\times N} w(r_n,p_n)\cdot g_r[r - R(r_n,p_n,t)]\cdot g_p[p - P(r_n,p_n,t)], \qquad (2.6)$$

where $w(r_n,p_n)$ is the static coefficient for each contributing coherent state, and $g_r[r - R(r_n,p_n,t)]$, $g_p[p - P(r_n,p_n,t)]$ are the uncorrelated isotropic gaussians with frozen widths. The widths of these coherent states (gaussians) are obtained for their adequacy to give binding energies (mean field) and root mean square radii (surface diffuseness) as close as possible to the experimental values for nuclei being analyzed. In these numerical calculations, Equation 2.1 is solved by the *test particle* method [Bert 88, Bona 89, Bona 90a, Bona 90b]. In this approach, the gaussians (g_r,g_p) peak at (R,P) can be considered as pseudo particles or test particles with position R and momentum P at time t. Thus the explicit time dependence of the phase space distribution function $f(r,p,t)$ arises from the time dependence of $R(r_n,p_n,t)$ and $P(r_n,p_n,t)$. For the collision cross section, a system composed of A_P nucleons from the projectile and A_T nucleons from the target is described as an ensemble of $N(A_P+A_T)$ test particles that hit each other with a cross section σ_{nn}/N. Finally, a sufficiently large value of N is chosen to provide convergent results. It has been checked that $N = 40$ provides a good description of nuclear collisions, since doubling this number does not significantly change the dynamical evolution of the system. These results are thus stable in comparison to larger values of N which require substantially more computing time.

For the initial configuration, the test particles are assigned random positions in a sharp sphere of nuclear radius ($\sim A^{1/3}$). Momentum is also randomly assigned to each test particle within a local sphere in the momentum space of radius p_F. The

radius p_F is given by $p_F = (3\pi^2\rho)^{1/3}\hbar$, where ρ is the local density. Finally the momenta of these test particles in the projectile and target are boosted towards each other with their respective center–of–mass momenta determined from the incident energy, and the masses of the projectile and target. Once the initial condition (i.e. the value of $w(r_n, p_n)$) is fixed, Equation 2.1 is solved by following the trajectory of the phase space gaussian cells which play the role of a moving basis for the problem. The first moments of these gaussians $R(r_n, p_n, t)$ and $P(r_n, p_n, t)$, which contain all the time dependency, are solutions of the Hamilton equations:

$$\frac{dR}{dt} = \frac{P}{m} \quad and \quad \frac{dP}{dt} = -\int dr_n dp_n \nabla U g_r[r - R] g_p[p - P]. \tag{2.7}$$

For the sake of simplicity, the first order difference approach is used to solve the Hamilton equations for the evolution of momentum and position of each test particle, which actually has second order accuracy when the momentum is evaluated at time points half way between the times of the position determinations:

$$\begin{aligned} R(t_2) &= P(t_1 + 0.5\Delta t) \cdot \Delta t + R(t_1), \\ P(t_1 + 0.5\Delta t) &= -\nabla U(t_1)\Delta t + P(t_1 - 0.5\Delta t). \end{aligned} \tag{2.8}$$

2.2 Formation and Fragmentation of Nuclear Disks

Recent simulations of heavy–ion collisions with the Boltzmann–like kinetic equations have shown that under a variety of conditions, exotic shaped nuclei like disks and bubbles can be formed[Baue 92, More 92]. To investigate which reaction system, and at which bombarding energy one might expect to observe such exotic objects, extensive model calculations were performed for the reaction dynamics with the Boltzmann–Nordheim–Vlasov reaction model described in section 2.1. More specifically, the BNV model was used to simulate central collisions of ^{129}Xe–induced reac-

tions on ^{nat}Cu, ^{89}Y, ^{165}Ho and ^{197}Au targets at various bombarding energies (E/A = 40, 60, 75 MeV), and with different values of incompressibility coefficients K (200, 380, 540 MeV) to cover the range currently believed to be appropriate for nuclear matter (see Table 2.1). Central collisions are studied because they are the most violent and hence are most likely to decay through multifragmentation.

2.2.1 Disk Formation in BNV Calculations

One common interesting feature of the simulation results is that a "disk" develops during the collision process due to the side–squeezing of nearly incompressible nuclear matter. Moreover, the thickness of the disk decreases while the diameter increases monotonically with increasing bombarding energy. When it becomes sufficiently thin, it breaks up into several fragments of a size commensurate with the thickness of the disk. For the sake of illustration, the simulation results for head–on collisions of ^{129}Xe + ^{197}Au at two extreme values of K are shown as a function of bombarding energy in Figures 2.1 – 2.3. Both the front and side views of the colliding systems are shown in the rows for four different times at 20, 60, 120 and 180 fm/c (1 fm/c is simply the time that light needs to travel through a distance of 1 fm or 10^{-15}m in vacuum).

At the lowest bombarding energy of 40 MeV (Figure 2.1), the two colliding nuclei fuse together to form a "disk" shaped object at time = 180 fm/c for both values of K. To study the development of these disks in more detail, their central densities (radius < 3 fm) are also plotted as a function of time in Figure 2.4. In the beginning, the impact of the collision squeezes and compresses the fused nuclei to higher densities ($\rho > \rho_o$). A positive pressure associated with this higher density begins to build up in the system, which slows down the compression. Eventually, the system reaches its maximum density at which the pressure is sufficiently large

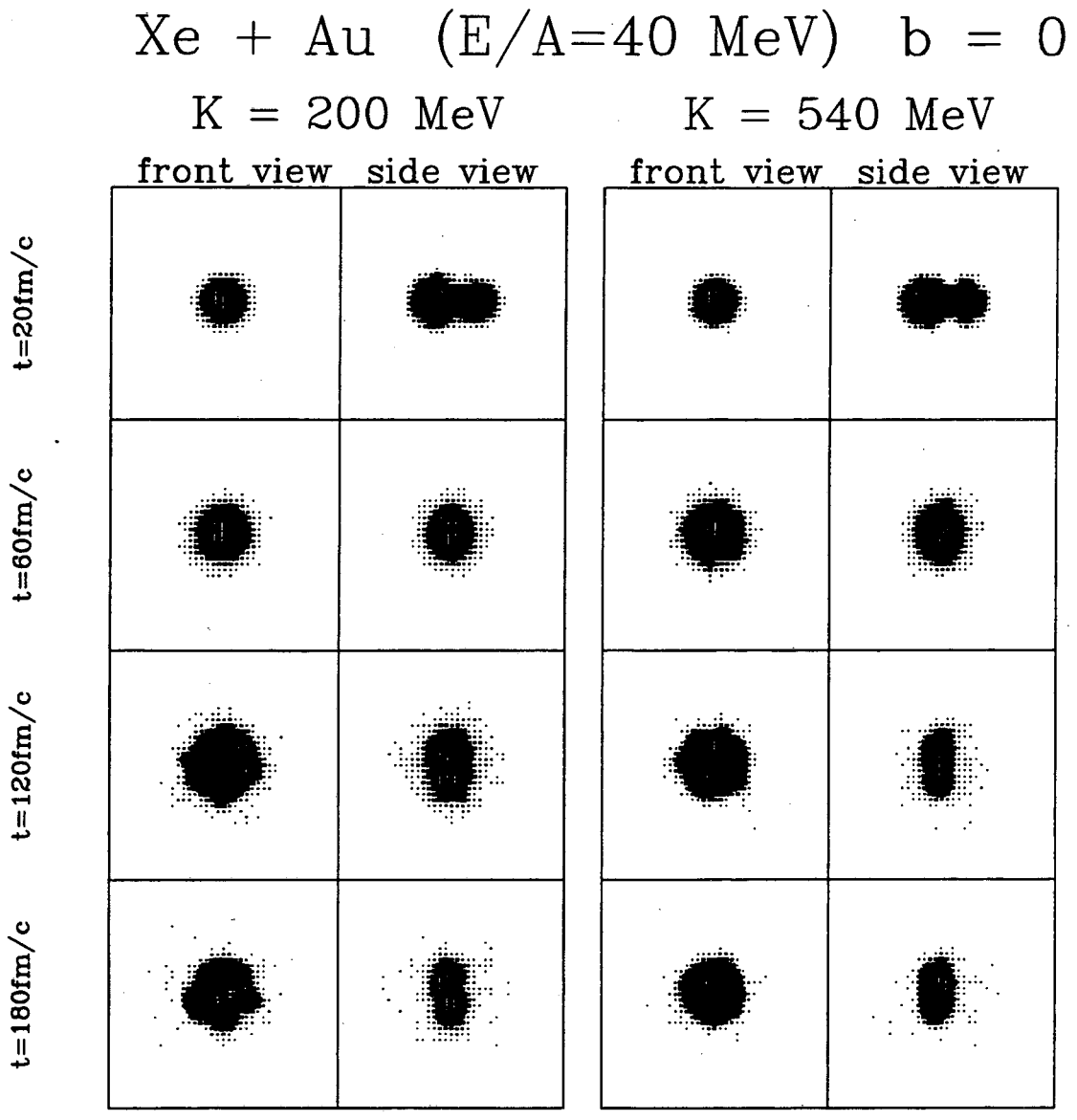

Figure 2.1 : BNV calculations for a head–on collision (impact parameter = 0) of the reaction ^{129}Xe + ^{197}Au at a bombarding energy of E/A = 40 MeV. Results at four indicated time steps are shown on four different rows. The front and side views of the colliding systems are given in columns 1 and 2, respectively, for a value of the incompressibility coefficient, K = 200 MeV. Similar views are shown in columns 3 and 4 for K = 540 MeV.

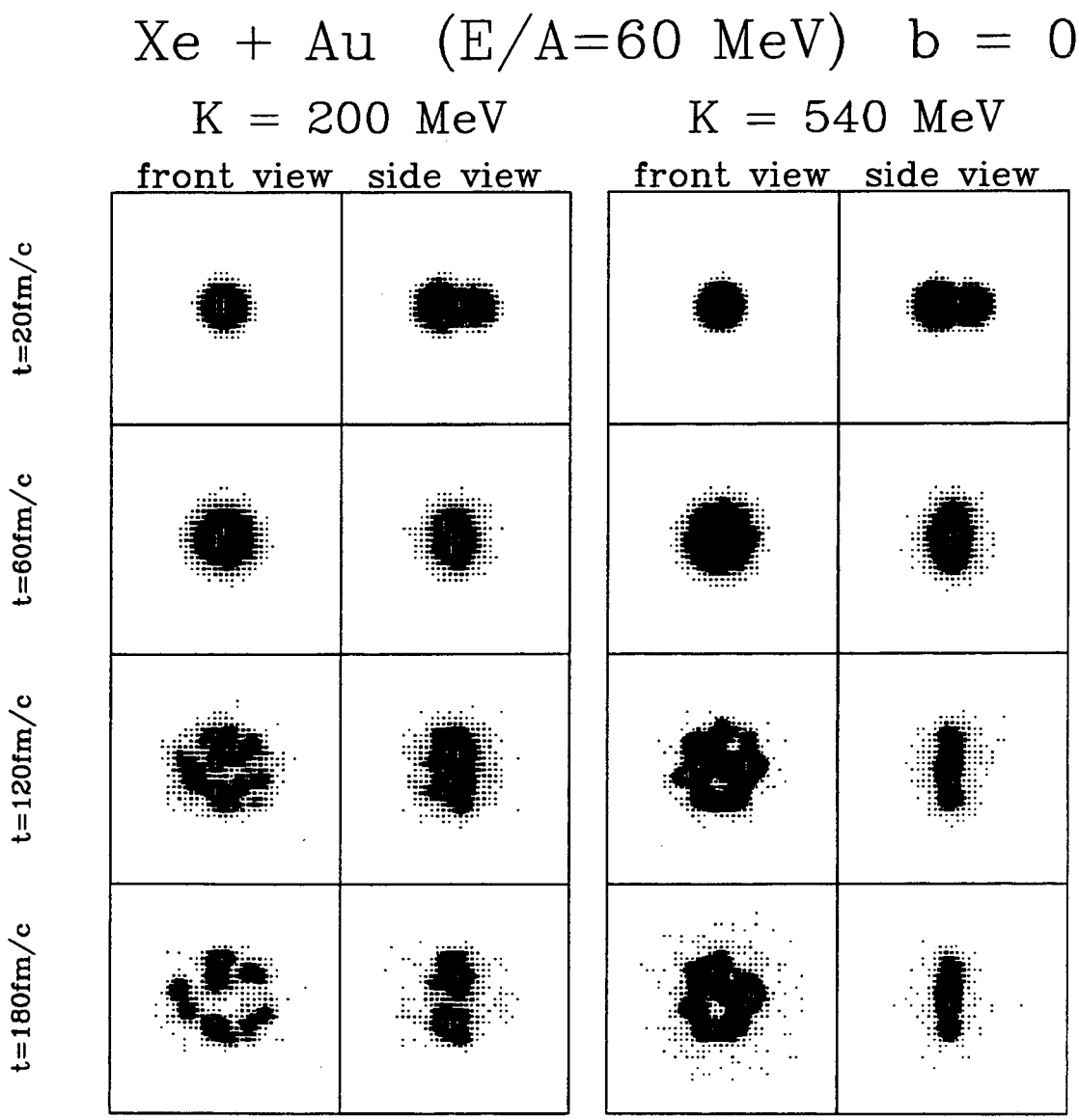

Figure 2.2 : Same as Figure 2.1 for the reaction ^{129}Xe + ^{197}Au at a bombarding energy of $E/A = 60$ MeV.

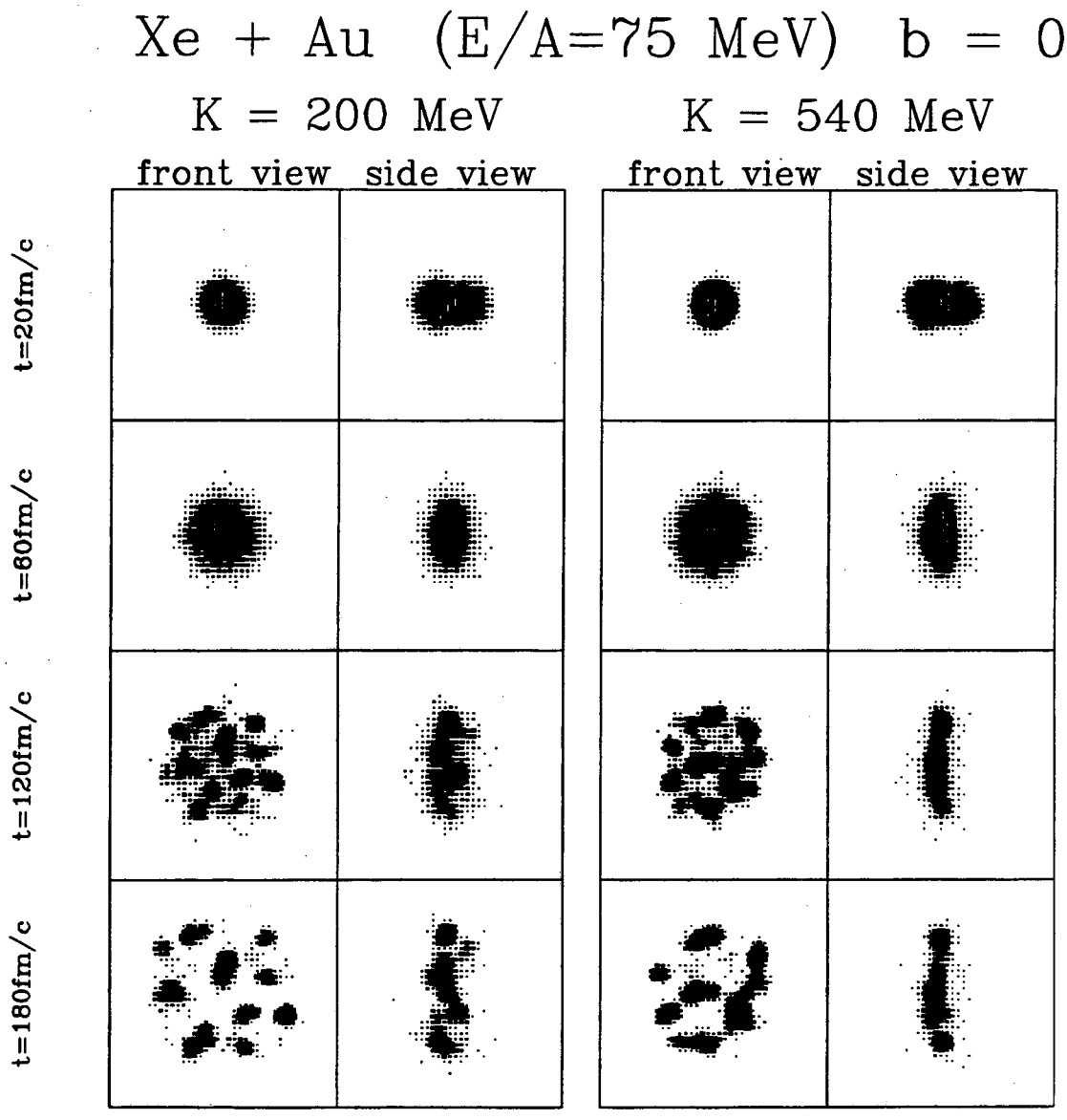

Figure 2.3 : Same as Figure 2.1 for the reaction ^{129}Xe + ^{197}Au at a bombarding energy of E/A = 75 MeV.

to stop the compression and the system begins to expand. In order to conserve energy, the expanding nuclear matter must acquire a radial velocity outwards. As the system expands, its density and thus the positive pressure decreases. When the system reaches the normal density corresponding to the lowest internal energy, the pressure vanishes, but the radial velocity drives the expansion further. The density is now lower than the normal nuclear density, the pressure becomes negative and the expansion is slowed down. This cycle continues until a normal nuclear density is restored at equilibrium or it may be interrupted if the system runs into a region of instability and breaks. For the simulation of ^{129}Xe + ^{197}Au reaction at $E/A =$ 40 MeV, the nuclear disks for both values of K do not break, and their densities indeed converge to nearly the normal density at the latter stage of their dynamical evolutions (t > 150 fm/c). However, the system governed by a "soft" equation of state ($K = 200$ MeV) tends to reach higher central densities during the compression stage but lower densities in the following expansion, as expected. On the other hand, the density oscillation observed in nuclear disks associated with the "hard" equation of state ($K = 540$ MeV) is minimal at later time steps (t > 100 fm/c).

As the bombarding energy is increased to 60 MeV (Figure 2.2), fragment formation occurs for $K = 200$ MeV in contrast to the high incompressibility case, where the thinner disk at $t = 180$fm/c is still well defined in spite of some mottlings. For the highest bombarding energy at $E/A = 75$ MeV, disk fragmentation is observed in both cases, but the disk for $K = 540$ MeV is much thinner and sharper. In the latter case, the mottling develops rapidly into a crown of fragments which gradually separate due to the mutual coulomb repulsion and the residual kinetic energy of the disk. In fact, the disk formed for $K = 200$ MeV is much fuzzier and the fragments seem to form within its thickness in a volume like process. This may be associated with the spinodal instability mentioned in Chapter 1. In other words, the system governed

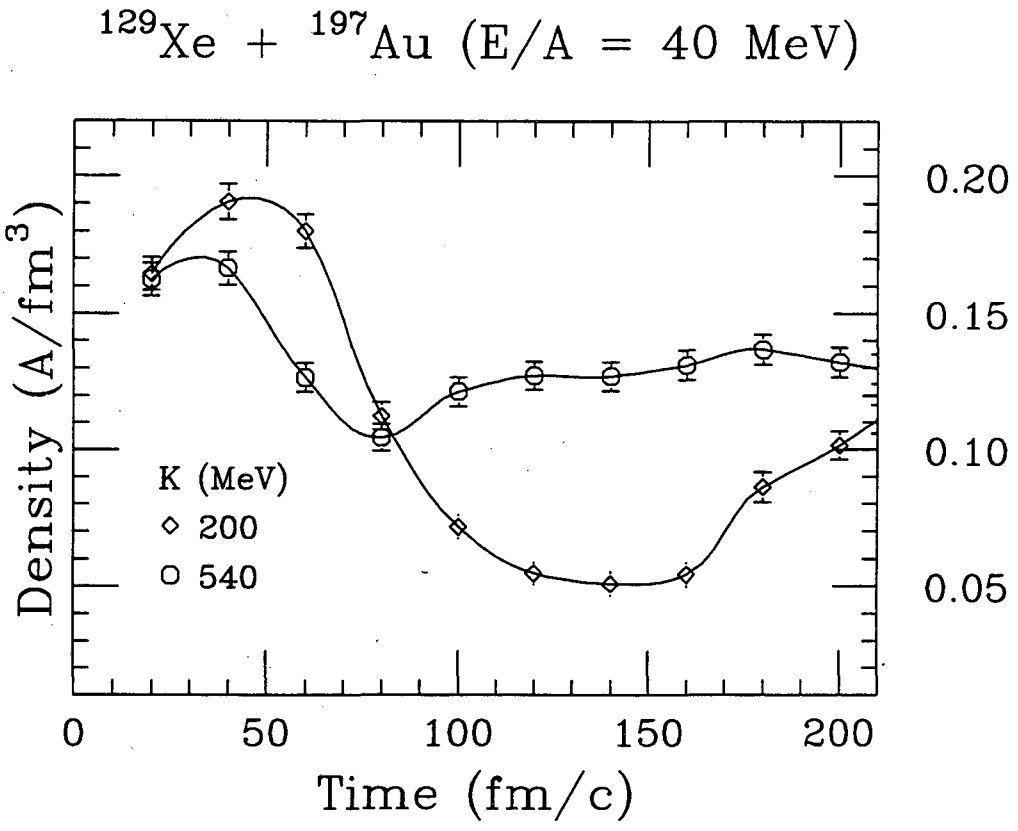

Figure 2.4 : Average central density ($r \leq 3fm$) of the colliding system as a function of time for the indicated values of the incompressibility coefficient K used in the BNV calculations.

by the "soft" equation of state may enter into a region of instability associated with a negative incompressibility during its expansion, and the system breaks into droplets of denser liquid (fragments) embedded in vapor (light particles). However, the effects of compression and expansion associated with the "hard" equation of state is rather weak. Then, what causes the thin disk to break?

2.2.2 Disk Fragmentation and Surface Instability

In the Liquid Drop Model, nuclei are treated as drops of nuclear matter, and their binding energies can be calculated as the sum of volume, surface and Coulomb energies. This macroscopic approach suggests that the energy, and thus the stability

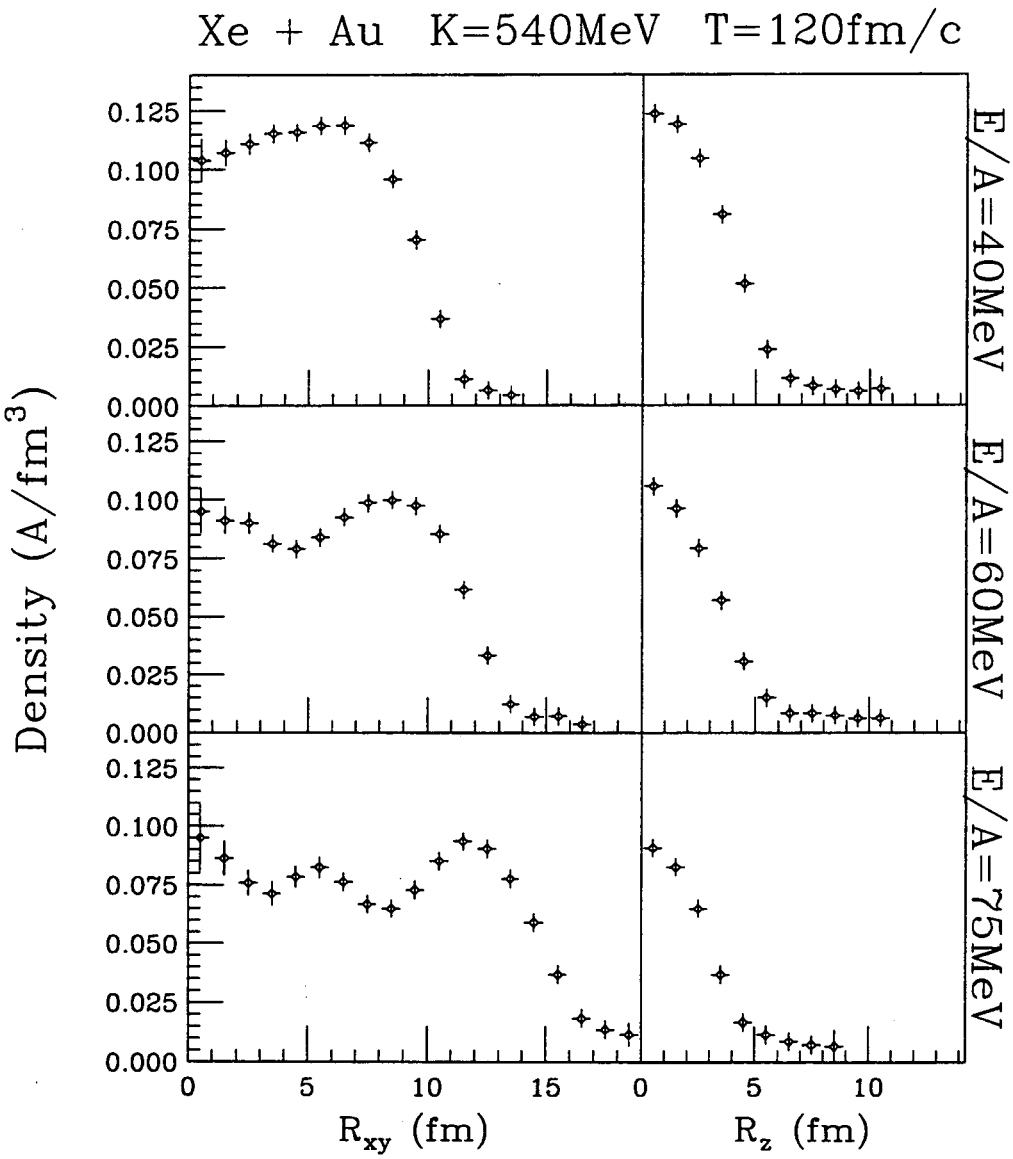

Figure 2.5 : Density profiles of nuclear disks along the beam axis (R_z) and the plane perpendicular to the beam axis (R_{xy}) at time = 120 fm/c. Disks are observed in the simulation results for head–on collisions of ^{129}Xe + ^{197}Au at the indicated bombarding energies and K = 540 MeV.

of a nuclear disk, depends significantly on the dimension of a disk.

To compare the dimension of the nuclear disks observed in the BNV calculations, their density profiles along the beam axis (z coordinate) and the plane perpendicular to the beam axis (xy plane) are plotted as a function of bombarding energy in Figure 2.5. These densities are extracted from the simulation results for the reaction ^{129}Xe + ^{197}Au with a "hard" equation of state ($K = 540$ MeV) at time = 120 fm/c. A well defined disk with a diameter $\sim$ 20 fm and a thickness $\sim$ 8 fm is observed for the system at $E/A = 40$ MeV (top panel). The disks become larger at higher energies (middle and bottom panel), but their density profiles are strongly modulated by surface oscillations, and the maxima of these oscillations seem to determine the positions of the fragments. Furthermore, the disks appear to be thinner even though the density profiles along the beam axis do not have a sharp fall off.

The above qualitative features associated with the disk dimension suggest that disk fragmentation is caused by a surface instability. More precisely, the system seems to escape from the high surface energy of a thin disk by breaking up into a number of spherical fragments with less overall surface. Thus, fragment formation in this picture depends solely on the presence of a surface energy term. (In the static limit, the BNV model reduces to a semi–classical approximation to the Hartree–Fock model, which can reproduce the nuclear masses throughout the periodic table and thus expresses a good surface energy.) This observed instability may be akin to the Rayleigh instability of a cylinder of liquid [Rayl 64]. The cylinder is unstable with respect to small perturbations of wavelength $\lambda \geq 2\pi R$, where R is the radius of the cylinder. But, is a disk of liquid, or more generally, a sheet of liquid, truly unstable?

2.2.3 Metastability of a Sheet of Liquid

For the sake of simplicity, a sheet of liquid instead of a finite disk is studied. On a sheet of thickness d, let us identify square tiles of side λ. A square tile can favorably collapse into a sphere of equivalent volume when the lateral surface area of the tile (top + bottom) is greater than the surface area of the sphere. The volume of the tile is simply $d\lambda^2$ and its surface area equals $2\lambda^2$. The radius (R_s) and the corresponding surface area (S_s) of the equivalent sphere can be expressed in terms of d and λ:

$$\begin{aligned} R_s &= \left(\frac{3V}{4\pi}\right)^{1/3} = \left(\frac{3d\lambda^2}{4\pi}\right)^{1/3}, \\ S_s &= 4\pi R_s^2 = 4\pi\left(\frac{3d\lambda^2}{4\pi}\right)^{2/3}. \end{aligned} \tag{2.9}$$

To determine the condition for the instability of this square tile, the ratio between the surface areas of the sphere and the square tile is evaluated,

$$\frac{S_s}{S} = \frac{(4\pi)^{1/3}(3d\lambda^2)^{2/3}}{2\lambda^2} = (2\pi)^{1/3}\left(\frac{3d}{2\lambda}\right)^{2/3}. \tag{2.10}$$

When this ratio is less than 1, the square tile becomes unstable with respect to the equivalent sphere and this occurs when,

$$\lambda \geq \sqrt{2\pi}(3d/2). \tag{2.11}$$

This surface instability seems to solve the puzzle of disk fragmentation observed in the BNV simulations. However, the above condition of instability is determined merely from the energy difference between the initial (square) and final (sphere) configurations. This derived instability condition (Equation 2.11) may actually refer to metastability only since there may be a barrier that prevents the sheet from reaching the more stable configurations. Indeed, the length of the sinusoid of a

modulated sheet increases with increasing amplitude of the modulation (Figure 2.6). Therefore, any modulation of finite wavelength λ increases the surface area of a sheet, regardless of its thickness. A second order approximation (see Appendix A) for the dimensionless surface energy increase is simply

$$\Delta E_s \approx \left(\frac{2\pi^2}{\lambda^2}\right) A^2, \tag{2.12}$$

where λ and A are the wavelength and the amplitude of the perturbation. The coefficient of A^2 is always positive, and this increase in energy clearly indicates the presence of a barrier for any perturbation of finite wavelength. So why do the disks observed in the BNV simulations develop what appears to be a genuine instability?

2.2.4 New Rayleigh Instability of a Sheet of Liquid

Thus far sharp surfaces (no surface diffuseness, no surface–surface interaction) have been assumed in the derivations. This assumption is reasonable for ordinary fluids because a sheet of liquid is sufficiently thick that the skin thickness of the surface (surface diffuseness) is negligible; the surface–surface interaction is also suppressed by the large separation distance between the two surfaces. However, nuclear surfaces are not sharp, and more importantly, the surface–surface interaction may not be negligible for a thin nuclear disk. In fact, nuclear surfaces interact with each other through an interaction of finite range known as the proximity force. A dimensionless proximity potential function $\Phi(s)$ is defined such that the proximity energy per unit area between two interacting surfaces separated at a distance s is $2\gamma\Phi(s)$, where γ is the surface energy coefficient [Bloc 77]. The dimensionless proximity energy (see Appendix A) of a sheet, subjected to a perturbation of wavelength λ and small amplitude A, is

$$E_p = \frac{2}{\lambda}\int_0^\lambda \Phi(s)dx \sim \frac{2P(\lambda)}{\lambda} + \frac{Q(\lambda)}{\lambda}A^2, \tag{2.13}$$

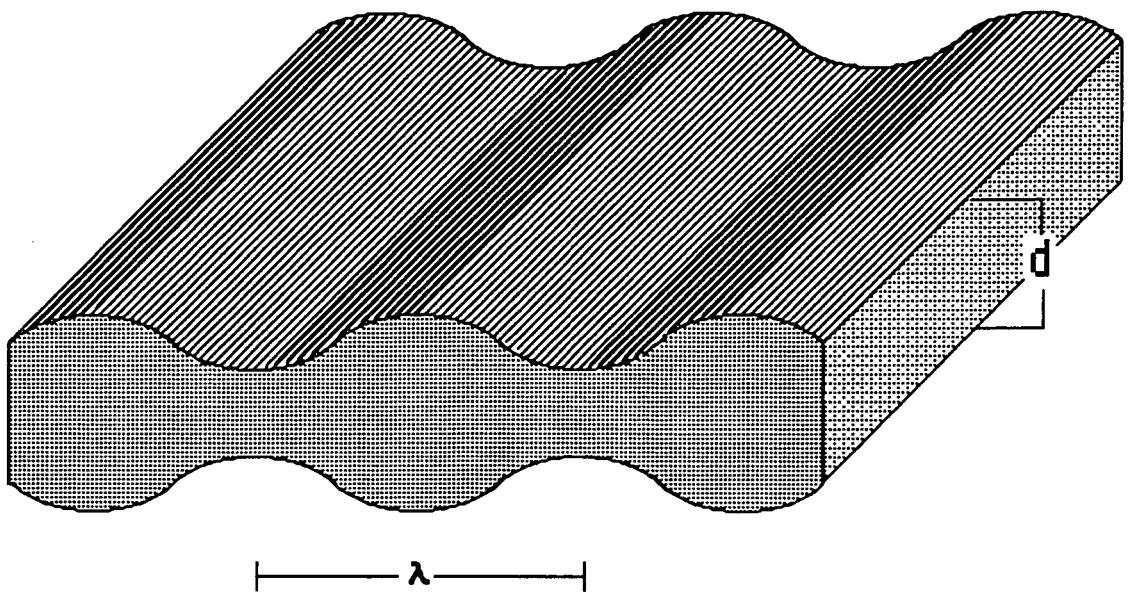

Figure 2.6 : Schematic illustration of the perturbation of a thin sheet of liquid.

where

$$P(\lambda) = \int_0^\lambda \Phi_0(x)dx \quad and \quad Q(\lambda) = \int_0^\lambda \Phi_2(x)dx, \tag{2.14}$$

with $s = d + 2Asinkx$, Φ_0 and Φ_2 being the zeroth and second order coefficients of the Taylor expansion of $\Phi(A, x)$ about $A = 0$, and $k = 2\pi/\lambda$. The proximity energy for the two surfaces of an unperturbed sheet can be derived by setting $A = 0$, and is simply equal to $2P(\lambda)/\lambda$. Thus, the change in proximity energy due to the perturbation is:

$$\Delta E_p \approx \frac{Q(\lambda)}{\lambda} A^2. \tag{2.15}$$

Therefore, the overall energy change of a modulated sheet can be calculated as the sum of a positive contribution from the surface energy (Equation 2.12), and a negative contribution from the proximity energy (Equation 2.15):

$$\Delta E = \Delta E_s + \Delta E_p = A^2 \left[\frac{2\pi^2}{\lambda^2} + \frac{Q(\lambda)}{\lambda} \right]. \tag{2.16}$$

When the coefficient of A^2 becomes zero or negative, the system becomes unstable, since the perturbation decreases the overall energy. In other words, a critical wavelength can be defined by equating this coefficient to zero:

$$2\pi^2 + \lambda_c Q(\lambda_c) = 0. \tag{2.17}$$

Any perturbation with $\lambda \geq \lambda_c$ will grow spontaneously and exponentially due to this surface instability, and thus cause the sheet to break up into smaller fragments. When the function derived from the Thomas–Fermi Nuclear Model is used for the proximity potential [Bloc 77], the following expression for λ_c is obtained:

$$\lambda_c = 1.1b \cdot e^{\frac{2d}{3b}}, \tag{2.18}$$

where b is the range of the proximity interaction and d is the thickness of the sheet.

When the thickness of a sheet becomes much greater than the range of the proximity interaction, the critical wavelength tends to infinity. This is just the trivial result for infinitely sharp surfaces. However, when the thickness of a sheet becomes comparable to the proximity range, the critical wavelength decreases rapidly. To observe this surface instability in a finite disk, the disk must then be thin enough to allow the critical wavelength to fit within its diameter. In fact, this is consistent with the observations in the BNV simulations. By studying the disks formed for K = 540 MeV, surface effects are isolated from those associated with compression and expansion. The disk formed at 40 MeV is relatively thick and it does not break. A thinner disk at 60 MeV shows some mottling, and eventually a thin disk at 75 MeV breaks up into many fragments. This interesting result says that the surface–surface interaction is essential to the sheet instability. In this sense, the sheet instability is a new kind of surface instability since the Rayleigh's cylinder instability can exist with pure surface tension and does not require the proximity interaction.

In summary, the results of these BNV calculations show that the surface instability should be pervasive in intermediate energy heavy–ion collisions. In the context of a nuclear disk, when the disk is thin enough, the proximity potential due to the surface–surface interaction is sufficient to overcome the sharp surface barrier to trigger the surface instability, which causes the breaking of the system into several fragments.

2.3 Stability of Nuclear Bubbles

Besides disks, bubble shaped nuclei have also been observed in the BUU calculations [Baue 92]. A bubble behaves much like a sheet, and is susceptible to the surface instability when its thickness is of the order of the proximity interaction range.

However, the Coulomb energy has not been incorporated in the above discussion on the surface instability. For compact shaped nuclear disks, the Coulomb contribution to the deformation energy may be small compared to the surface and proximity contributions. In the case of nuclear bubbles, the depletion of charges in the central cavity reduces the Coulomb energy significantly and this Coulomb effect should not be neglected. Moreover, a saturated vapor fills the cavity of an excited bubble ($T > 0$), and the vapor pressure would also affect the stable configuration of a bubble. These additional considerations have made the study of nuclear bubbles more complicated, but interesting. In fact, the stability of nuclear bubbles has been discussed in a variety of contexts [Wong 73, Wong 85]. Here the relevant degrees of freedom and the physical quantities that affect their stability are analyzed. The physical quantities that are considered are the Coulomb force, the surface tension, and the pressure difference across the walls of a bubble. The bubble degrees of freedom can be divided into two classes: the *radial modes* and the *crispation modes*. The distortions on the two surfaces of a bubble are in phase with each other for a radial mode of perturbation, and they are out of phase for a crispation mode.

Let us consider a nuclear bubble whose interior and exterior surfaces are distorted by small perturbations. The notations $R_1(\theta, \phi)$ and $R_2(\theta, \phi)$ are used to describe the interior and exterior radii of a perturbed bubble. The θ and ϕ dependence of R_1 and R_2 reflect the functional form of the perturbations on these surfaces. For the sake of simplicity, a kind of perturbation that preserves the azimuthal symmetry is studied so that the perturbed surfaces are functions of the polar angle θ only:

$$\begin{aligned} Exterior \quad Surface \qquad R_2 &= \langle R_2 \rangle \left[1 + A_2 P_n(cos\theta)\right], \\ Interior \quad Surface \qquad R_1 &= \langle R_1 \rangle \left[1 + A_1 P_n(cos\theta)\right]. \end{aligned} \tag{2.19}$$

Here $\langle R_1 \rangle, \langle R_2 \rangle$ are mean radii of the interior and exterior surfaces; A_1, A_2 are am-

plitudes of the perturbations and $P_n(cos\theta)$ is Legendre Polynomial of nth order:

$$P_n(\mu) = \frac{1}{2^n n!}\frac{d^n}{d\mu^n}\left(\mu^2 - 1\right)^n, \qquad where \quad \mu = cos\theta. \tag{2.20}$$

A perturbation of this kind is called the "Spheroidal Deformation". Expressions of Legendre Polynomials for $n = 0 - 4$ are shown below:

$$\begin{aligned}
P_0(cos\theta) &= 1, \\
P_1(cos\theta) &= cos\theta, \\
P_2(cos\theta) &= \frac{1}{2}(3cos^2\theta - 1), \\
P_3(cos\theta) &= \frac{1}{2}(5cos^3\theta - 3cos\theta), \\
P_4(cos\theta) &= \frac{1}{8}(35cos^4\theta - 30cos^2\theta + 3).
\end{aligned}$$

Since the perturbation of each surface is independent, the ratio of their amplitudes A_1/A_2 can be used to characterize the deformation. In the following derivations, this ratio is defined as the spheroidal deformation parameter $A \equiv A_1/A_2$. Schematic diagrams of perturbed bubbles are shown in Figure 2.7 for the radial mode. In these panels, slices through the center of these perturbed bubbles are shown for the indicated order of Legendre Polynomial perturbation. The two–dimensional geometric cross sections for the unperturbed and perturbed bubbles are represented by solid and dashed curves respectively. Their shape dependence reflects the functional form of the corresponding Legendre Polynomial. Since the distortions of the two surfaces are in phase with each other for a radial mode, $A > 0$, and the thickness is kept nearly constant throughout the bubble. Similar diagrams are shown in Figure 2.8 for the crispation mode. In this case, the distortions of the the two surfaces are out of phase with each other, then $A < 0$, and the perturbation modulates the thickness of the bubble's walls.

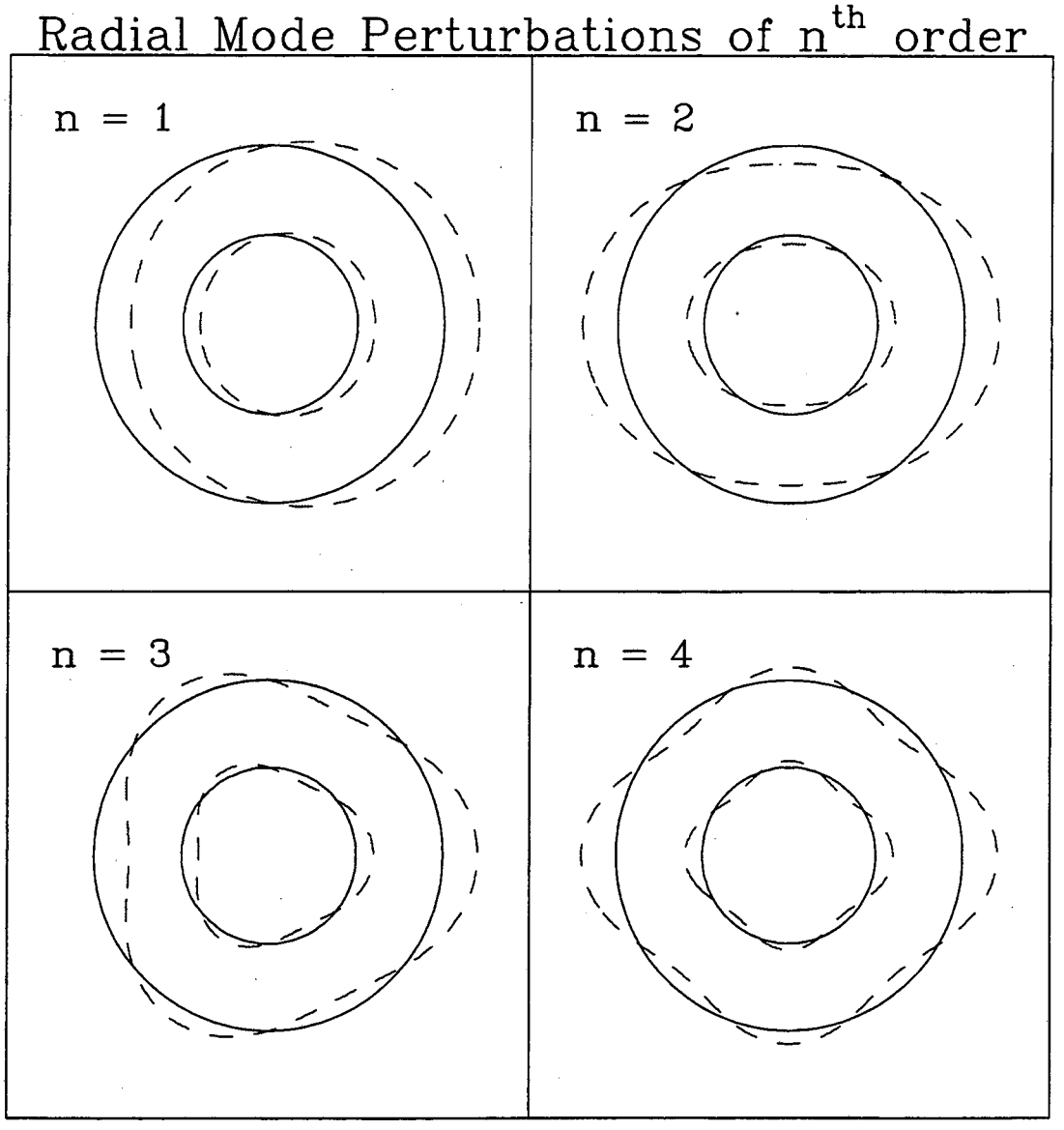

Figure 2.7 : Slices through the center of nuclear bubbles associated with perturbations of the radial mode for the indicated Legendre Polynomials. The two–dimensional geometric cross sections for the unperturbed and perturbed bubbles are represented by solid and dot–dashed curves respectively.

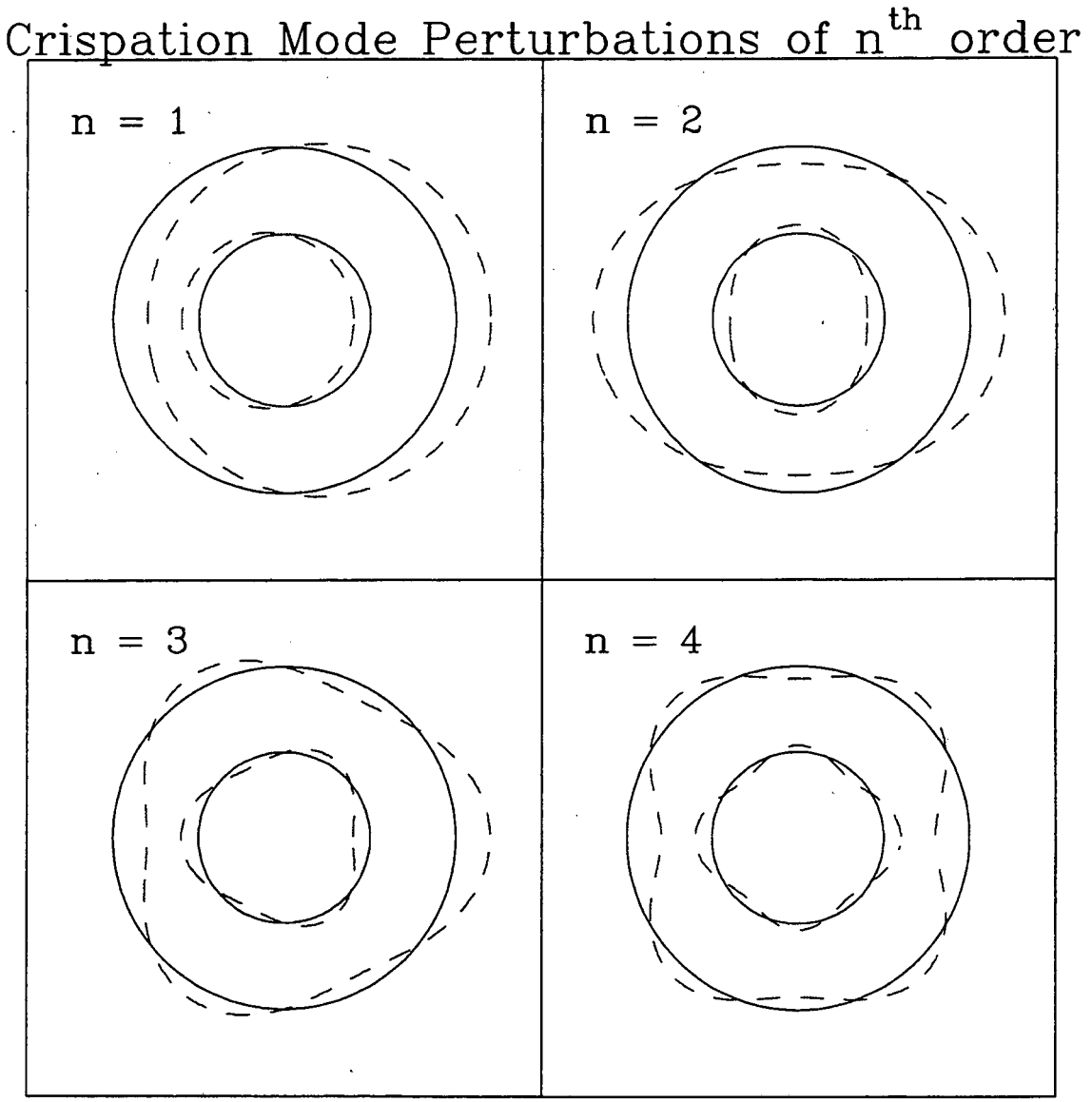

Figure 2.8 : Slices through the center of nuclear bubbles associated with perturbations of the crispation mode for the indicated Legendre Polynomials. The two-dimensional geometric cross sections for the unperturbed and perturbed bubbles are represented by solid and dot–dashed curves respectively.

2.3.1 Radial Monopole Oscillations and Coulomb Bubbles

The simpliest perturbation associated with the zeroth order Legendre Polynomial is considered. The appropriate expressions for the radii of the perturbed surfaces are:

$$\begin{aligned} R_2 &= \langle R_2 \rangle (1 + A_2) = R_{20}, \\ R_1 &= \langle R_1 \rangle (1 + A_1) = R_{10}. \end{aligned}$$

It is noticed that both the interior and exterior surfaces are spherical and are defined by their constant radii R_{10} and R_{20} respectively. Clearly, this perturbation is the most important bubble degree of freedom, which defines the bubble itself. In other words, it describes the expansion and contraction of a bubble under the constraint of volume conservation. This process is also known as monopole oscillation. Since both surfaces must either expand or contract in phase with each other in order to conserve volume, only the radial mode exists for this degree of freedom.

To describe a bubble formed at a given stage of expansion or contraction, a monopole oscillation parameter P defined as the ratio of the two radii R_{10}/R_{20} is introduced. As a bubble contracts, its interior surface (radius) must contract at a faster rate in order to conserve volume, and thus P becomes smaller. Eventually $P = 0$ when the cavity vanishes (R_{10} approaches 0), and the bubble is simply reduced to a sphere of equivalent volume. On the other extreme, as the interior surface (R_{10}) approaches the exterior surface (R_{20}) at the end of its expansion, P becomes close to 1, and this configuration describes an infinitely thin bubble under the condition of volume conservation. To determine the stabilities of these bubble configurations, their energies are calculated as a function of P.

Since volume is conserved during the oscillation, the relevant energies within the Liquid Drop Model are the shape dependent surface, and Coulomb energies. For

the sake of simplicity, the energy of an equivalent spherical nucleus is used as a reference energy state. Let R_0 be the radius of this equivalent sphere; its relation with R_{10} and R_{20} is derived from the constraint of volume conservation (i.e. $R_{20}^3 - R_{10}^3 = R_0^3$). Hence, R_{10} and R_{20} can be expressed in terms of R_0 and P:

$$\begin{aligned} R_{20} &= R_0(1-P^3)^{-1/3}, \\ R_{10} &= PR_{20} = R_0P(1-P^3)^{-1/3}. \end{aligned} \tag{2.21}$$

In the following derivation, the energies of various bubble configurations are expressed in terms of P and R_0 such that they can be compared readily.

The surface area S of a bubble is simply the sum of the two spherical surfaces:

$$\begin{aligned} S &= 4\pi\left(R_{10}^2 + R_{20}^2\right) \\ &= 4\pi R_0^2\left[P^2\left(1-P^3\right)^{-2/3} + \left(1-P^3\right)^{-2/3}\right] \\ &= 4\pi R_0^2\left(1-P^3\right)^{-2/3}\left(1+P^2\right). \end{aligned} \tag{2.22}$$

To calculate the corresponding surface energy, S is multiplied by a temperature dependent surface energy coefficient γ. Thus, the expression for the surface energy becomes:

$$\begin{aligned} E_s &= \gamma 4\pi R_0^2\left(1-P^3\right)^{-2/3}\left(1+P^2\right) \\ &= E_s^o\left(1-P^3\right)^{-2/3}\left(1+P^2\right). \end{aligned} \tag{2.23}$$

This derived surface energy is plotted as a function of P in Figure 2.9a. Here the energy unit $E_s^o = \gamma 4\pi R_0^2$ is the surface energy of the equivalent sphere. At the limit of $P = 0$, the bubble is reduced to the equivalent sphere, and E_s is indeed equal to E_s^o. As a bubble develops from a sphere and continues to grow with increasing P, its surface area and thus its surface energy is found to increase continuously and indefinitely.

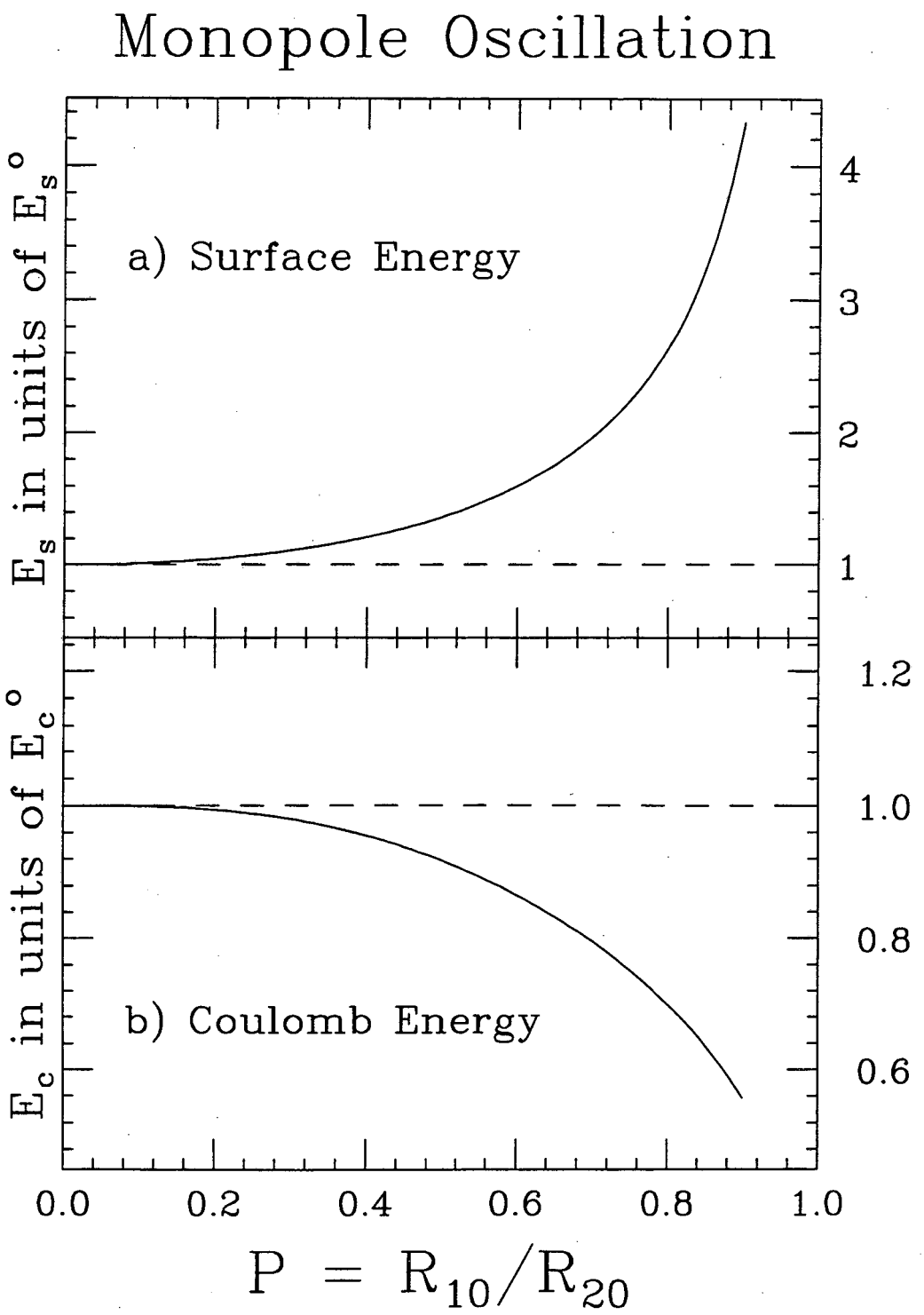

Figure 2.9 : Surface (a) and Coulomb energies (b) of bubbles subjected to monopole oscillations are calculated as a function of P according to Equations 2.23 and 2.24. The surface and Coulomb energies are expressed in units of E_s^o and E_c^o respectively.

To calculate the Coulomb energy of a charged bubble, its simple spherical symmetry is considered. Let us assume that a bubble with a uniform charge density distribution ρ_c has an interior radius R_{10} and an exterior radius r. The total amount of charge in this bubble is $q = (4/3)\pi\rho_c(r^3 - R_{10}^3)$. Now, consider an infinitely thin shell of thickness dr surrounding this bubble with the same charge density distribution. The volume of this thin shell is $dV = 4\pi r^2 dr$, and the charge is $dq = \rho_c dV = 4\pi r^2 \rho_c dr$. For the charge dq in this spherical shell, the charge q in the bubble can be treated as a charged particle q at the origin as far as their interaction is concerned. Therefore, the interaction energy between the bubble and this thin shell is $dE = (q/r)dq$. This is essentially the energy needed to bring the spherical shell from infinity to the surface of the charged bubble. By repeating this procedure, the exterior radius of the bubble can be expanded to reach R_{20}. The associated self–Coulomb energy of such a bubble is then the sum of the shell–bubble interaction energies of all stages:

$$\begin{aligned} E_c &= \int_{R_{10}}^{R_{20}} \frac{q\,dq}{r} \\ &= \frac{16}{3}\pi^2\rho_c^2 \int_{R_{10}}^{R_{20}} \left(r^4 - R_{10}^3 r\right) dr \\ &= \frac{16}{3}\pi^2\rho_c^2 \left[\frac{R_{20}^5}{5} - \frac{R_{10}^3 R_{20}^2}{2} + \frac{3R_{10}^5}{10}\right]. \end{aligned}$$

The constant charge density ρ_c can be replaced by $\frac{3Q}{4\pi(R_{20}^3 - R_{10}^3)}$, where Q is the total charge of the bubble. Then

$$\begin{aligned} E_c &= \frac{3Q^2}{5\left(R_{20}^3 - R_{10}^3\right)^2}\left[R_{20}^5 - \frac{5}{2}R_{10}^3 R_{20}^2 + \frac{3}{2}R_{10}^5\right] \\ &= E_c^o\left(1 - P^3\right)^{-5/3}\left(1 - \frac{5}{2}P^3 + \frac{3}{2}P^5\right). \end{aligned} \tag{2.24}$$

Similarly, this Coulomb energy is plotted as a function of P in Figure 2.9b, and the energy unit $E_c^o = 3Q^2/5R_0$ is the Coulomb energy of the equivalent sphere. At the limit $P = 0$, E_c is reduced to E_c^o for a spherical nucleus. On the other hand,

E_c becomes essentially zero for a very thin bubble when P approaches 1. In other words, as a bubble expands, the charges are brought farther apart due to the growing diameter of its central cavity, and the Coulomb energy decreases accordingly.

The above derivation suggests that the Coulomb energy, which favors configurations of large P, is indeed the driving force for the formation of a thin bubble; the surface energy however tends to reduce the size of the bubble's cavity, since it increases monotonically with P. It is thus possible that an interplay between the Coulomb and surface energies may generate a minimum energy point along the coordinate P. To search for such an energy minimum, the sum of the Coulomb and surface energies ($E = E_c + E_s$) is evaluated as a function of P. At this point, recall that E_c^o and E_s^o are related by the fissility parameter of a nucleus defined as $X \equiv 0.5(E_c^o/E_s^o)$. If $E^o \equiv E_s^o + E_c^o$, then

$$\begin{aligned} E_s^o &= E^o \frac{1}{1+2X}, \\ E_c^o &= E^o \frac{2X}{1+2X}. \end{aligned} \tag{2.25}$$

Therefore, the sum of the Coulomb and surface energies can be expressed in terms of E^o, P and X:

$$\begin{aligned} E &= E_c^o \left[\left(1-P^3\right)^{-5/3} \left(1 - \frac{5}{2}P^3 + \frac{3}{2}P^5\right) \right] + E_s^o \left[\left(1-P^3\right)^{-2/3} \left(1+P^2\right) \right] \\ &= \frac{E^o}{1+2X} \left(1-P^3\right)^{-2/3} \left[\left(1+P^2\right) + \frac{2X}{1-P^3} \left(1 - \frac{5}{2}P^3 + \frac{3}{2}P^5\right) \right]. \end{aligned} \tag{2.26}$$

Figure 2.10 plots this energy E as a function of P for a selected range of fissility parameters ($1.98 \leq X \leq 2.26$). A sharp rise in the energy E is observed for all the selected values of X in the early development of a bubble from an equivalent sphere. This reflects a tremendous increase in the surface area associated with the generation of an additional interior surface for a bubble. As a bubble continues to expand, its central cavity grows and the decrease in the Coulomb energy begins to

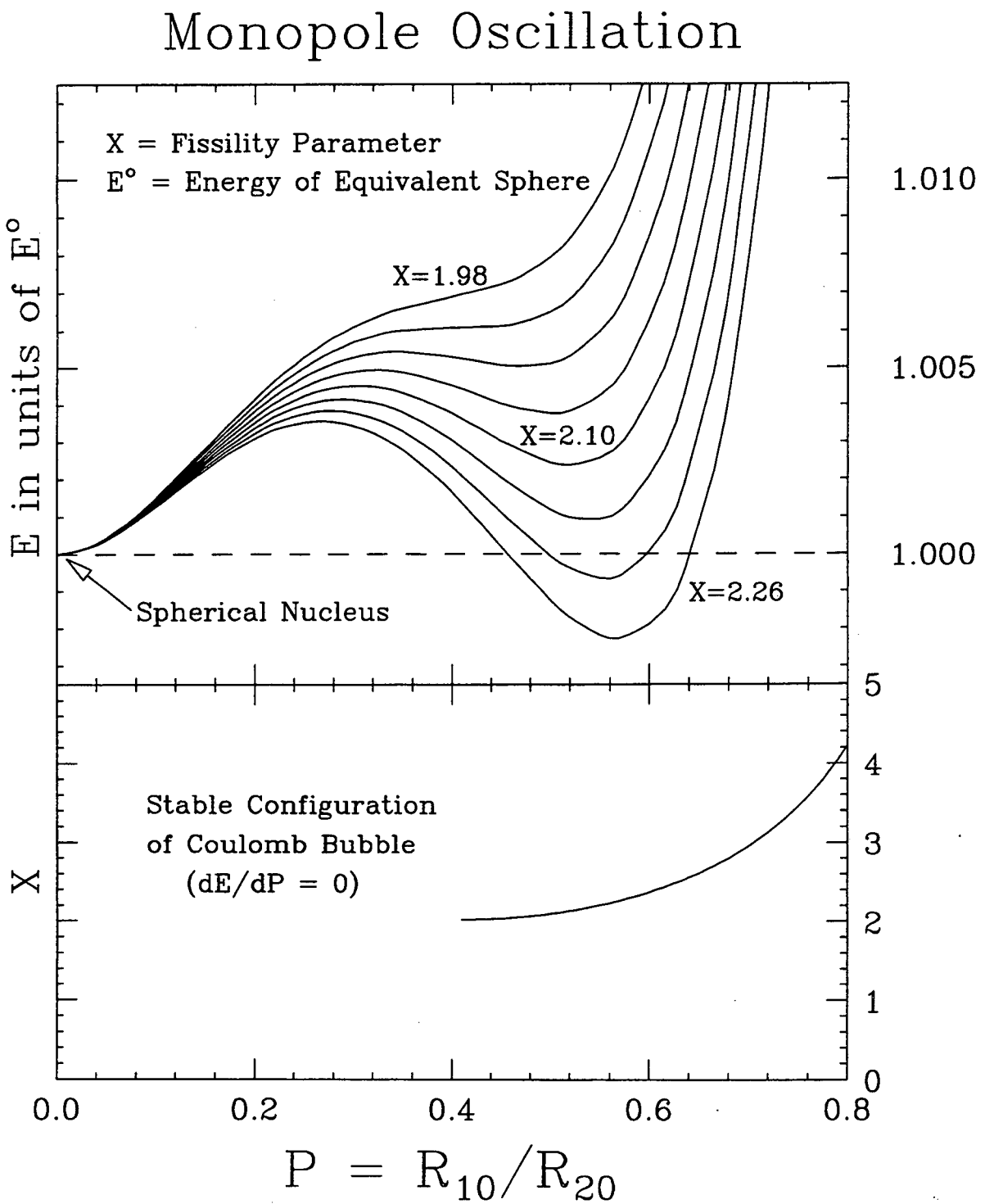

Figure 2.10 : (Top) Sum of the surface and the Coulomb energies of a nuclear bubble as a function of P calculated for the indicated values of fissility parameter X. (Bottom) Correlations between X and P for stable configurations of nuclear bubbles.

compensate for the gain in the surface energy. However, for small X, the contribution of the Coulomb energy is not large enough to completely offset the surface term. In this case, a minimum energy point does not exist and the energy of the bubble, dominated by the surface term, continues to grow as it expands. As the amount of charge stored in a bubble increases with X, the Coulomb contribution becomes more important and eventually when X reaches 2.02, it is sufficient to overcome the surface term and the energy curve begins to run downhills. However, a minimum is reached pretty soon, since the Coulomb energy levels off rapidly for a large thin bubble, whereas the surface energy continues to grow indefinitely. Eventually, the surface term takes over and the energy curve is running uphills for thin bubbles with large values of P. At a given fissility parameter X, the value of P that corresponds to the minimum energy state represents a stable configuration since bubbles of other dimensions will either expand or contract to attain this optimum configuration. Since the Coulomb energy is the driving force for the stability of these bubbles, they are called the "Coulomb bubbles". It is noticed that the minimum point at $P = 0.41$ for $X = 2.02$ is actually a secondary minimum since the energy of an equivalent spherical nucleus at $P = 0$ is even lower. As more charge is brought into the bubble with increasing X, the energy difference between the Coulomb bubble and the equivalent sphere becomes smaller. Indeed, for $X > 2.20$, the energy of the Coulomb bubble becomes an absolute minimum, and this bubble configuration is not only stable against monopole oscillations, but it is also more stable than the equivalent spherical nucleus.

The values of P for these Coulomb bubbles can be extracted by equating the first derivative of Equation 2.26 to zero; a positive second derivative is required to ensure that the extracted P corresponds to a minimum energy. The correlation between the optimum values of P and X for stable bubble configurations is plotted in Figure 2.10. This plot shows that the size of a Coulomb bubble increases with

the fissility parameter X. Intuitively this can be explained in terms of the driving force behind the expansion and contraction of a bubble. The two relevant forces are the Coulomb force and the surface tension. The Coulomb force tends to drive the bubble to expand, while the surface tension acts to contract the bubble. Thus a stable configuration is achieved only when these two forces balance each other. As the charge of a nuclear bubble increases with increasing X, the increased Coulomb force drives the bubble to grow to larger radii such that additional surfaces are generated to balance the increase of the Coulomb force. Consequently, a more heavily charged bubble becomes stable at a thinner configuration.

It is noticed that the threshold fissility parameter $X = 2.02$ (see Figure 2.10) for the formation of a Coulomb bubble is rather high and is impossible to attain for cold nuclei. However, one can reach higher excitation energies and temperatures in heavy–ion reactions. The surface tension is weakened with increasing temperature, and thus the surface energy coefficient becomes smaller. Therefore, the Coulomb contribution to the total energy becomes stronger at a higher temperature, and thus the fissility parameter X increases accordingly. Moreover, a saturated vapor fills the cavity of an excited bubble ($T > 0$). The vapor pressure is equal to the saturation pressure, which increases with temperature. At first sight, one would not expect a pressure acting upon the outer surface, which is facing the vacuum. However, this is not the case. The inner surface has an outgoing flux of evaporated particles, and an ingoing flux of vapor particles. At equilibrium the two fluxes are equal: they impart the same impulse to the surface, and thus contribute equally to the pressure. The outer surface, however has only the outgoing component, and thus feels a pressure equal to half of the inner pressure. A net outward pressure hence drives the cavity to grow even further.

The energy associated with this pressure is simply equal to the work done by

the system to generate a central cavity of saturated vapor from a solid sphere. Since the pressure of the saturated vapor depends solely on temperature and not volume, a constant pressure during the expansion is assumed. Thus, the required energy is simply a product of this constant pressure and the volume of the cavity,

$$E_{vap} = p\left(\frac{4}{3}\pi R_{10}^3\right) = pV_0\frac{R_{10}^3}{R_0^3}, \tag{2.27}$$

where V_0 is the volume of a bubble or an equivalent sphere. To compare this energy with the Coulomb and surface energies, E_{vap} is expressed in terms of E^o:

$$\begin{aligned} E_{vap} &= E_s^o\left[\left(\frac{pV_0}{E_s^o}\right)\frac{R_{10}^3}{R_0^3}\right] \\ &= E^o\frac{1}{1+2X}\left[P_v\frac{P^3}{1-P^3}\right]. \end{aligned} \tag{2.28}$$

Here $P_v \equiv pV_0/E_s^o$. Since work is done by the system during an expansion, the sign of of this energy E_{vap} should be negative. In other words, this outward pressure lowers the energy of a bubble with respect to that of an equivalent sphere. This effect is stronger with increasing P since more work is done for a thinner bubble with a larger cavity. As an illustration, Figure 2.11 shows the energy of a bubble as a function of P for $X = 2.26$ with $P_v = 0$ and 0.3 respectively. The energy curve for $P_v = 0$ (solid) is clearly lowered and shifted to the right when a pressure of $P_v = 0.3$ (dashed) is included in the energy calculation. It is noted that this energy shift is independent of the fissility parameter. Consequently, a secondary minimum may eventually become an absolute minimum at high enough pressure, and the threshold of X for a stable nuclear bubble is thus lowered. Moreover, the stronger pressure effect with increasing P drives the Coulomb bubble to a thinner configuration. These two effects are shown in the bottom panel of Figure 2.11 with a dashed line for $P_v = 0.3$.

Thus far, the Coulomb force has been shown to be the driving force for the formation of Coulomb bubbles that are stable against monople oscillations. For

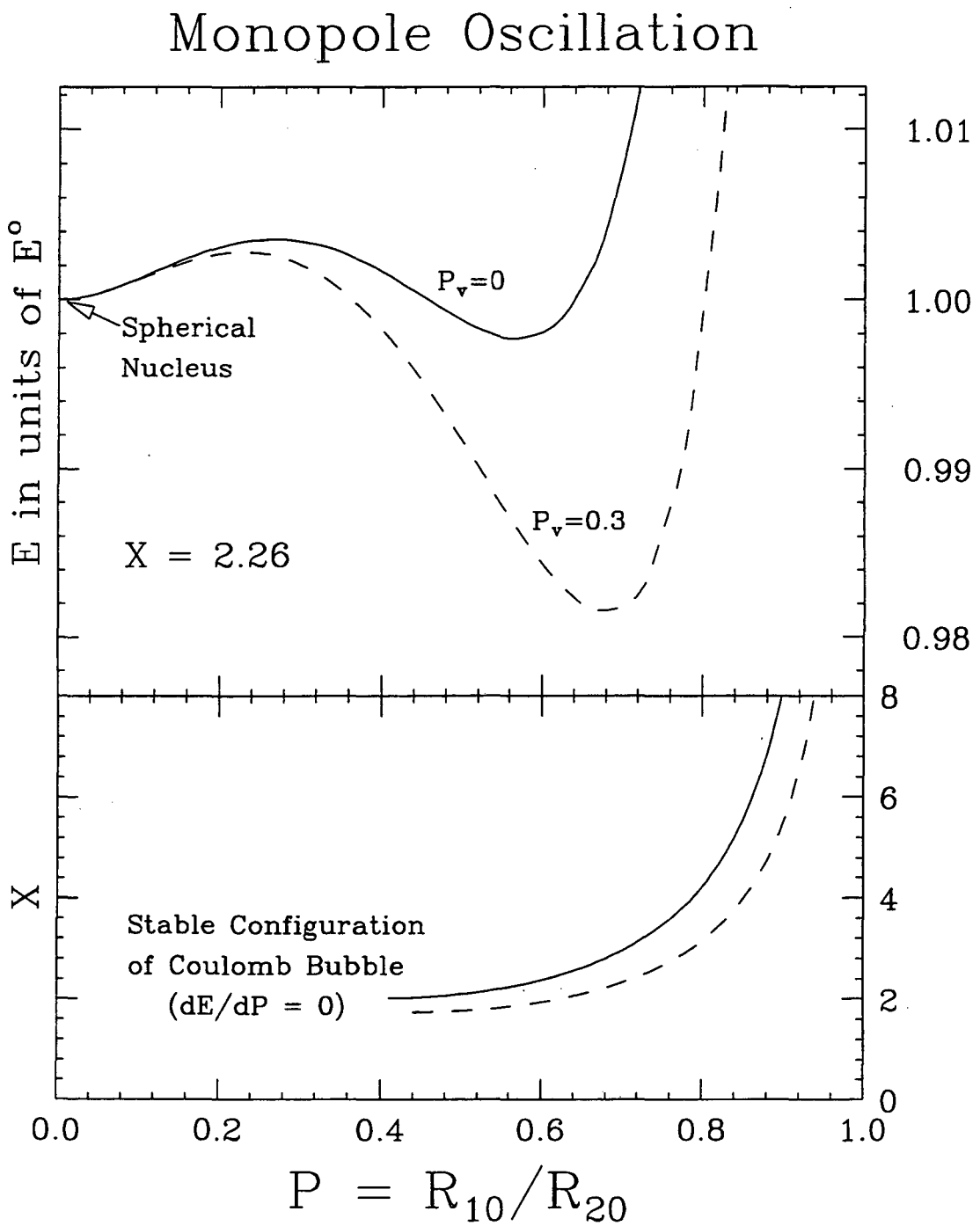

Figure 2.11 : (Top) Total energy including (dashed) and excluding (solid) the pressure effect as a function of P for a nuclear bubble with $X = 2.26$. (Bottom) Correlations between X and P for stable configurations of nuclear bubbles including (dashed) and excluding (solid) the pressure effect associated with the vapor in the central cavity.

Coulomb bubbles that are not heavily charged ($2.02 < X < 2.20$), they exist as excited states (secondary minimum) and may be formed at the expense of the system's excitation energy. On the other hand, the energies of Coulomb bubbles formed at higher fissility parameters ($X > 2.20$) are actually lower than the energy of an equivalent sphere. However, this stability of a bubble towards monopole oscillation is not a sufficient condition for the stability since there are higher order modes that must be checked.

2.3.2 Higher Order Perturbations and Coulomb Instability

The approach to calculate the energy of a nuclear bubble against higher order perturbations is similar to the above method used for a Coulomb bubble. The mathematics becomes more complicated, since the spherical symmetry of a Coulomb bubble does not exist for a perturbed bubble. However, in considering the stability of a nuclear bubble, one needs only to study the effect of small perturbation. Accordingly, one can expand various physical quantities in powers of A_1 and A_2, and retains only the leading terms (up to 2nd order). An outline of these calculations is given in Appendix A, and the results for the surface and Coulomb energies are shown below:

$$\begin{aligned}\frac{E_s}{E_s^o} &= \left[\left(1-P^3\right)^{-2/3}\left(1+P^2\right)\right] + \\ &\quad A_2^2\left[\left(1-P^3\right)^{-2/3}\left(1+A^2P^2\right)\frac{n^2+n-2}{2(2n+1)}\right],\end{aligned}$$

$$\begin{aligned}\frac{E_c}{E_c^o} &= \left[\left(1-P^3\right)^{-5/3}\left(1-\frac{5}{2}P^3+\frac{3}{2}P^5\right)\right] + \\ &\quad A_2^2\left[\frac{5}{2}(2n+1)P^3+5-5n-15AP^{n+3}+\frac{15}{2}A^2P^5\right]\frac{\left(1-P^3\right)^{-5/3}}{(2n+1)^2}. \quad (2.29)\end{aligned}$$

One simple limit to verify these derived equations is the case of a Coulomb bubble with $A_2 = 0$. Indeed, the expressions in the first brackets of the above equations are

identical to Equations 2.23 and 2.24 derived for the surface and Coulomb energies of a nuclear bubble. Therefore, the terms in the second bracket of these equations must account for the energy change associated with a perturbation described by the Legendre Polynomial of nth order. Equation 2.29 shows an A dependence for the Coulomb energy of a perturbed bubble indicating that the Coulomb perturbation energy is different for the radial and crispation modes even when other parameters are identical. On the other hand, an A^2 dependence is observed for the surface energy since the two modes differ only in the relative orientation of their surfaces, and this does not affect the surface area (energy).

Thus far, the value of A has been a free parameter in these calculations. It will be interesting to study a perturbation in which A_1 and A_2 are constrained to yield the least Coulomb energy. It will be shown later that this is indeed the most damaging perturbation as far as the stability is concerned. The coefficient of A_2^2 in the Coulomb energy expression is found to be minimized for $A = P^{n-2}$. In the following, the stability of a nuclear bubble is studied using this input for A, and the expressions for the change in the surface (ΔE_s) and Coulomb energies (ΔE_c) associated with the perturbation become:

$$\frac{\Delta E_s}{E_s^o} = A_2^2 \left[\left(1 - P^3\right)^{-2/3} \left(1 + P^{2n-2}\right) \frac{n^2 + n - 2}{2(2n+1)} \right], \tag{2.30}$$

$$\begin{aligned} \frac{\Delta E_c}{E_c^o} &= A_2^2 \left[5 - 5n + \frac{10n+5}{2} P^3 + \frac{45}{2} P^{2n+1} \right] \frac{(1-P^3)^{-5/3}}{(2n+1)^2} \qquad \textit{crispation mode,} \\ \frac{\Delta E_c}{E_c^o} &= A_2^2 \left[5 - 5n + \frac{10n+5}{2} P^3 - \frac{15}{2} P^{2n+1} \right] \frac{(1-P^3)^{-5/3}}{(2n+1)^2} \qquad \textit{radial mode.} \end{aligned}$$

The coefficients of A_2^2 of these perturbation energies are plotted in Figure 2.12 as a function of P for the indicated orders of Legendre Polynomials. These coefficients of the surface and Coulomb perturbation energies are expressed in units of E_s^o and E_c^o

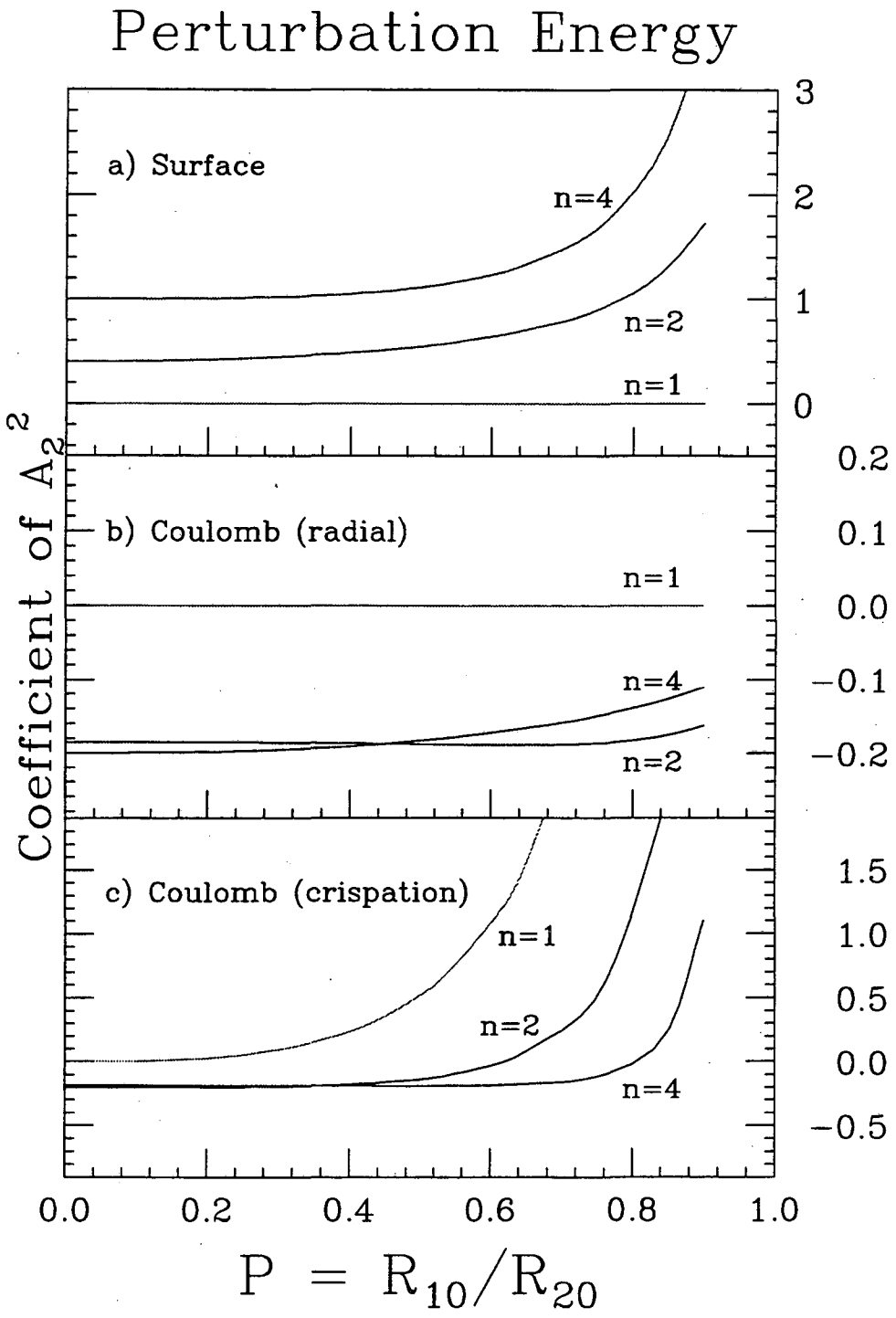

Figure 2.12 : Surface (a) and Coulomb energies (b,c) for the indicated higher order perturbations are calculated as a function of P according to Equation 2.30. The surface and Coulomb energy coefficients of A_2^2 are expressed in units of E_s^o and E_c^o respectively.

respectively. The Coulomb perturbation energies are shown to be different for the radial (Figure 2.12b) and crispation modes (Figure 2.12c) as expected.

Interestingly, the surface energy plot shows that a dipole oscillation ($n = 1$) does not affect the surface energy of the bubble at all. Intuitively, this is expected since Figure 2.7 shows that a radial dipole oscillation involves only the motion of the center–of–mass. In fact, the Coulomb perturbation energy is zero for such a radial dipole oscillation (Figure 2.12b). For the more interesting crispation dipole oscillation, it can be viewed as the motion of a negative sphere moving inside a larger sphere of positive charge (Figure 2.8). In this case, the coefficient of A_2^2 for the Coulomb energy becomes a positive increasing function of P, and thus a nuclear bubble is always stable with respect to a dipole perturbation of the crispation mode. When a neutral bubble is considered, this Coulomb barrier disappears, the inner sphere then moves freely until it bursts when it moves sufficiently outwards to touch the outer surface.

For higher order perturbations, the positive surface perturbation energy coefficient of Equation 2.30 suggests that any mode of distortion (radial & crispation) will increase the surface energy of a bubble. This effect becomes stronger for thinner bubbles and higher order perturbations as the perturbation energy increases with both P and n (Figure 2.12a). In the limit of $P = 0$, the surface perturbation energy is reduced to $\Delta E_s = A_2^2(n-1)(n+2)(4n+2)^{-1}E_s^o$, which agrees with Rayleigh's surface energy derivation [Rayl 64a] for higher multipole perturbations of a solid sphere. On the other hand, the Coulomb perturbation energy is negative when P is small, and it behaves rather differently for the radial and crispation modes when P becomes larger for thinner bubbles. In the case of a crispation mode, the positive terms of the Coulomb energy increase with P until they are sufficiently large that the Coulomb perturbation energy crosses the zero line and continues to grow (Figure 2.12c). This large Coulomb perturbation energy at large P is expected since it requires work to

clump charges of an infinitely thin bubble into local clusters. Mathematically, this effect is partly accounted for by the large positive coefficient of P^{2n+1} in Equation 2.30 for the crispation mode. For a radial mode of perturbation, the coefficient of P^{2n+1} is negative such that the overall increase in the Coulomb energy with P is not dramatic, and the Coulomb perturbation energy remains negative (Figure 2.12b) for thin bubbles with large values of P.

In summary, the surface perturbation energy is always positive while the Coulomb perturbation energy starts at negative values and may become positive at large values of P. This interplay between the Coulomb and surface perturbation energies implies the existence of a critical fissility parameter ($X_{critical}$) at a given P at which the positive surface energy balances the negative Coulomb energy. A bubble with $X > X_{critical}$ becomes sufficiently charged for the negative Coulomb energy to offset the positive surface term to produce a net perturbation energy that is negative. This is indeed the onset of the Coulomb instability since a negative perturbation energy drives the distortion to grow spontaneously and exponentially. On the other hand, when $X < X_{critical}$, the perturbation dominated by the positive surface energy increases the overall energy, and thus the nuclear bubble is stable at this configuration. In short the values of $X_{critical}$ defines the boundary condition for the Coulomb instability.

Values of $X_{critical}$ are extracted by equating the sum of the Coulomb and surface perturbation energies to zero. The extracted values of $X_{critical}$ are plotted as a function of P in Figure 2.13 for the indicated orders of Legendre Polynomial perturbations of the radial and crispation modes. Each curve essentially defines the boundary conditions of the bubble stability against perturbation of nth order Legendre Polynomial. It is noted that the same critical values are observed for the radial and crispation modes in the case of a solid sphere ($P = 0$), because the two modes are

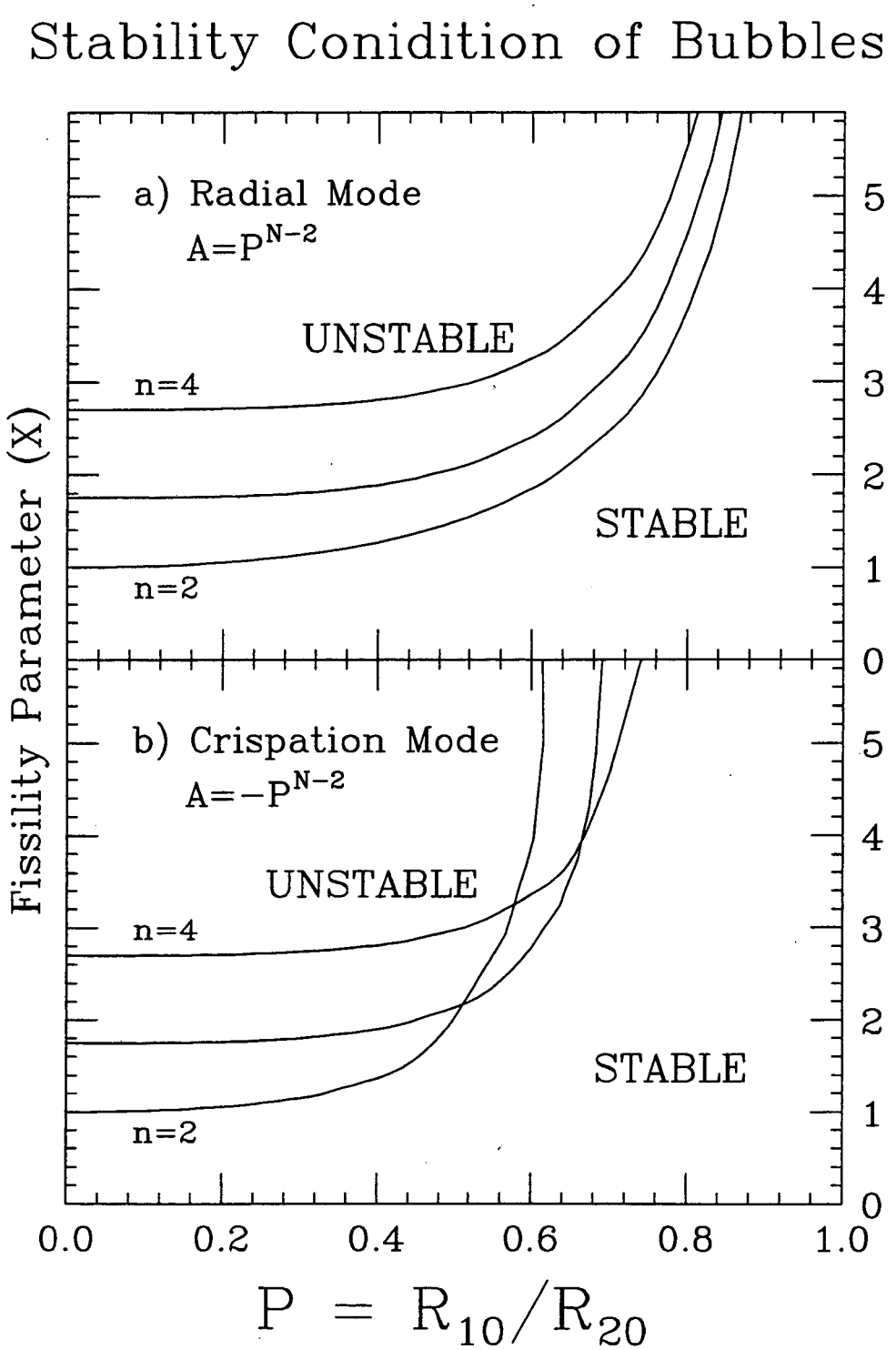

Figure 2.13 : Correlations between the critical values of P and X, which define the boundary conditions of bubble stability against the indicated higher order perturbations of radial (a) and crispation (b) modes.

indifferent. In this case, a solid sphere with $X < 1$ is stable against any mode of perturbations. At $X = 1$, the quadrupole mode for $n = 2$ becomes unstable, and this is the onset of the fission instability. As more charges are brought into the sphere with increasing values of X, the onset of instability occurs progressively for higher order modes. So, a highly charged sphere will not merely fission, but will break up into many fragments due to the instability of higher order modes. In other words, the perturbation modes are destabilized by the Coulomb interaction. This explains why the distortion $A = P^{n-2}$ with the least (most negative) Coulomb energy is the most damaging perturbation. Similarly, a nuclear bubble with $P > 0$ is stable unless it is sufficiently charged ($X > X_{critical}$) for the negative Coulomb perturbation energy to trigger the Coulomb instability. The fact that these critical fissility parameters increase with n for the radial mode implies that any bubble configuration that is stable against n^{th} order perturbation is also stable with respect to any higher order perturbation. Unlike the radial mode, the Coulomb perturbation energy of thin bubbles at large P becomes positive for the crispation mode. This is why some of the thin bubbles that are unstable against the radial mode (e.g. P > 0.8) are still stable against the crispation mode.

In considering the stability of a nuclear bubble, one must examine its stability against monopole oscillations and higher order perturbations simultaneously. To truly verify and search for a stable nuclear bubble, the configurations of Coulomb bubbles (bottom panel of Figure 2.10) that are stable against monopole oscillations are plotted in Figure 2.14 together with the values of $X_{critical}$ (Figure 2.13) that define the stability conditions for higher order perturbations. It can be seen that a relatively thick Coulomb bubble ($P < 0.5$) is unstable with respect to both the radial and crispation modes. On the other hand, thinner Coulomb bubbles with $P > 0.5$ become stable with respect to the perturbations of the crispation mode. However, these

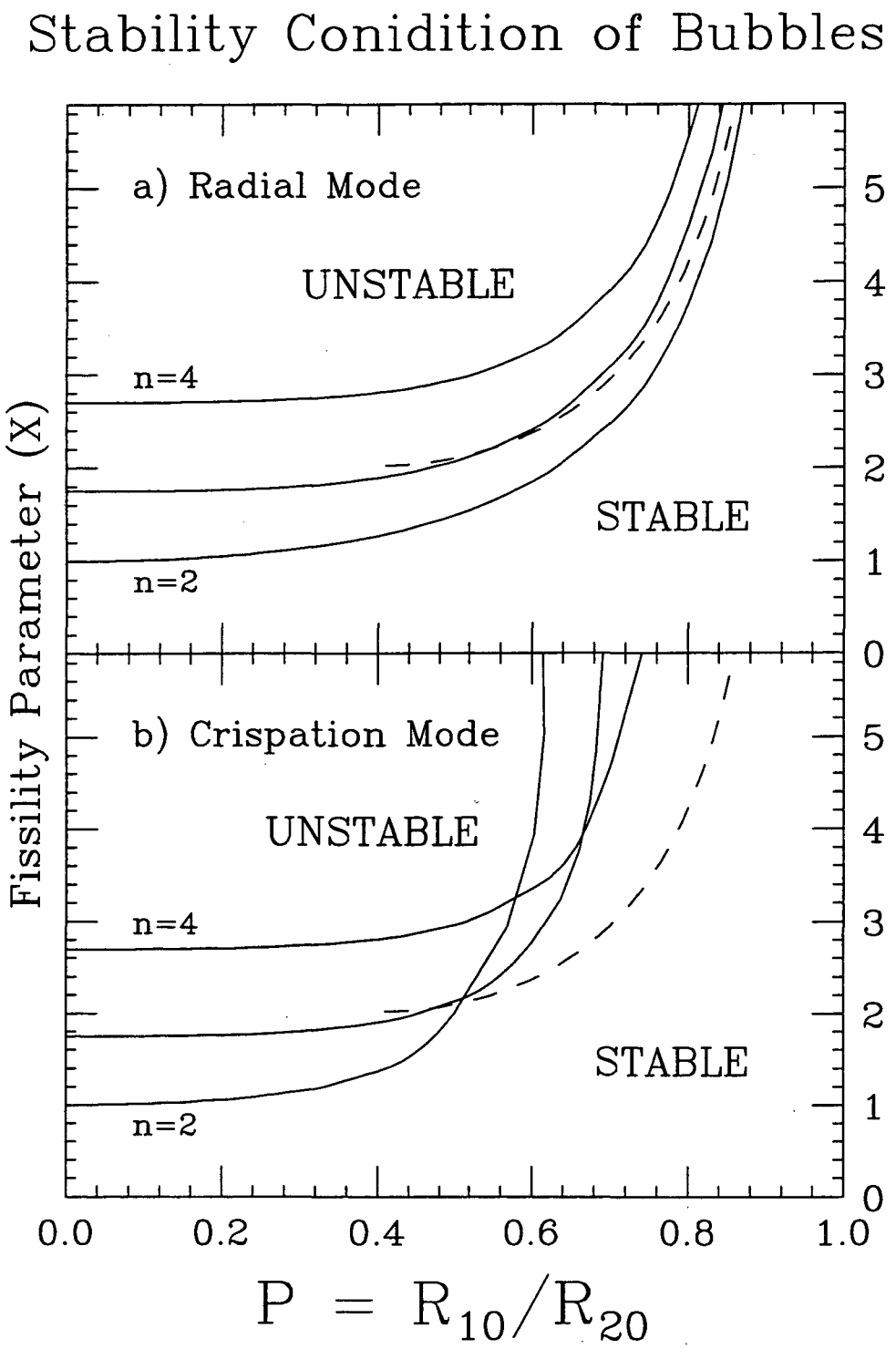

Figure 2.14 : Same as Figure 2.13 except that the stable configurations of Coulomb bubbles are also shown with dashed curves.

thin bubbles can not get away from the unstable region of the Coulomb instability for the radial mode. For example, the bubble at $X = 3$ is stable with respect to monopole oscillation but unstable against the radial quadrupole ($n = 2$) perturbation.

Consequently Coulomb bubbles are always unstable with respect to some higher order spheroidal deformations. In other words, there is always one kind or another deformation against which the bubble configuration is unstable. However, so far the effect of the pressure difference across the walls of an excited bubble has not been considered. Recall that the resulting pressure differential acts on the monopole mode by driving the Coulomb bubbles to thinner configurations. Since, only changes in volume of the bubble cavity will affect the energy associated with the vapor pressure, this pressure effect is minimal when the volume of a bubble's cavity is nearly unchanged in the case of higher order perturbations. Therefore, the correlations between P and $X_{critical}$ for the boundary conditions of the Coulomb instability associated with these higher order perturbations remain unaffected by the pressure. Consequently, a sufficiently large pressure may drive the Coulomb bubble to a thin enough configuration that is beyond the onset of quadrupole instability as shown in Figure 2.15. However, when a bubble becomes very thin, the surface–surface interaction may not be neglected and the proximity energy may play a significant role in determining its stability.

2.3.3 Proximity Effects and Surface Instability

It was mentioned in section 2.2.4 that a bubble behaves much like a sheet, and is subject to the surface instability. Therefore, a thin bubble that is safe from the Coulomb instability of both the radial and crispation modes may still be susceptible to the surface instability when its thickness is comparable to the range of the proximity interaction.

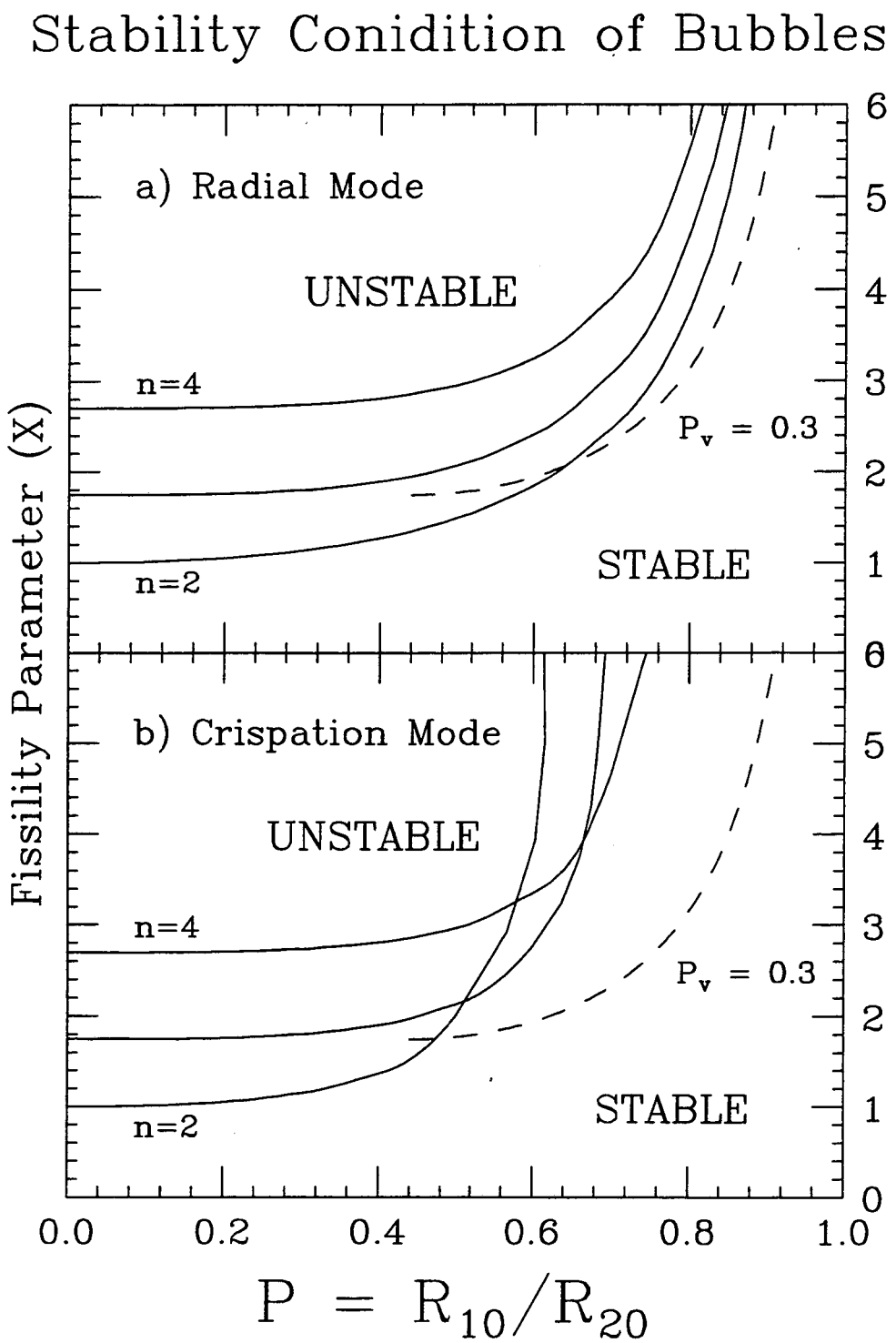

Figure 2.15 : Same as Figure 2.14 except that the stable configurations of Coulomb bubbles under the influence of the cavity pressure are shown with dashed curves for $P_v = 0.3$.

Recall that the proximity energy can be calculated from the integral of the dimensionless proximity potential $\Phi(s)$ over the area subjected to this surface–surface interaction:

$$E_p = \int 2\gamma\Phi(s)dA, \tag{2.31}$$

where $s = R_2 - R_1$ is the separation distance between the two interacting surfaces. In the case of a thin bubble, the surface element of the above integral can be approximated by the inner surface of the bubble:

$$dA = \sqrt{\left[R_1^4 sin^2\theta + R_1^2\left(\frac{dR_1}{d\phi}\right)^2 + R_1^2 sin^2\theta\left(\left(\frac{dR_1}{d\theta}\right)^2\right]}d\theta d\phi. \tag{2.32}$$

Similarly, the function derived from the Thomas–Fermi Nuclear Model is used for the proximity potential:

$$\Phi(s) = -4.5827e^{-\frac{4s}{3b}}.$$

Then, the corresponding proximity energy E_p is Taylor expanded with respect to a perturbation of small amplitude and only the leading terms in A_2^2 are retained. An outline of the derivation is given in Appendix A, and the coefficient of A_2^2 associated with the change in the proximity energy due to the perturbation is shown below:

$$\begin{aligned}\Delta E_p &= E_s^o P^2\left(1-P^3\right)^{-\frac{2}{3}}(-4.5827)e^{\frac{-4R_0}{3b}(1-P^3)^{-\frac{1}{3}}(1-P)}\left\{\left[\frac{A_2^2}{(2n+1)}\frac{8R_0}{3b}\frac{(1-PA^2)}{(1-P^3)^{1/3}}\right]\right.\\ &\left.+\frac{A_2^2A^2}{2n+1}\left[\frac{16R_0^2}{9b^2}\frac{\left(P-\frac{1}{A}\right)^2}{(1-P^3)^{2/3}}+\frac{16R_0}{3b}\frac{\left(P-\frac{1}{A}\right)}{(1-P^3)^{1/3}}+n^2+n-2\right]\right\}.\end{aligned}$$

Here R_0/b is a parameter used to account for the thickness dependence of the proximity interaction. In other words, the larger the ratio R_0/b, the thicker the bubble at a given P and the weaker the resulting proximity interaction. In fact, when R_0/b is small, the thickness of an equivalent bubble becomes comparable to b, and thus the system is more susceptible to the surface–surface interaction.

Figure 2.16 shows the effect of this proximity interaction on the stability of bubbles for an example of $R_0/b = 15$. For both the radial and crispation modes, the effect of the proximity interaction on relatively thick bubbles ($P < 0.55$) are minimal as expected. This effect becomes significant at thinner bubble configurations (large P) especially for the crispation mode, which involves thickening and thinning of the bubble's walls. The proximity energy is effective in offsetting the extra surface energy associated with the perturbation, and hence the value of $X_{critical}$ decreases at a given P. This result is similar to the proximity effect observed for a thin disk in section 2.2.2. Therefore, when the thickness of an expanding bubble becomes comparable to the range of the proximity interaction, it becomes susceptible to the surface instability and breaks up into several fragments. In fact, BNV calculations for very heavy systems at low bombarding energies show the formation of a thin bubble that seems to burst under the action of the surface instability.

In summary, exotic shaped nuclei such as "disks" and "bubbles" have been observed in dynamical calculations of intermediate energy heavy–ion collisions. For example, a "nuclear disk" develops during the collision process due to the side–squeezing of nearly incompressible nuclear matter. The subsequent decay of the disk into several smaller fragments has been analyzed in terms of the new Rayleigh–like surface instability, in which the proximity force plays an essential role. In these considerations, the effect of Coulomb energy has been neglected because of its limited contribution to the deformation energy of compact shaped nuclear disks. However, the contribution of Coulomb energy should not be ignored in the study of "nuclear bubbles", since the depletion of charges in the central cavity of nuclear bubbles reduces the Coulomb energy significantly. In fact the Coulomb energy is the driving force for the stability of "Coulomb" bubbles against monopole oscillations. The vapor pressure in the central cavity of an excited bubble provides an additional force that

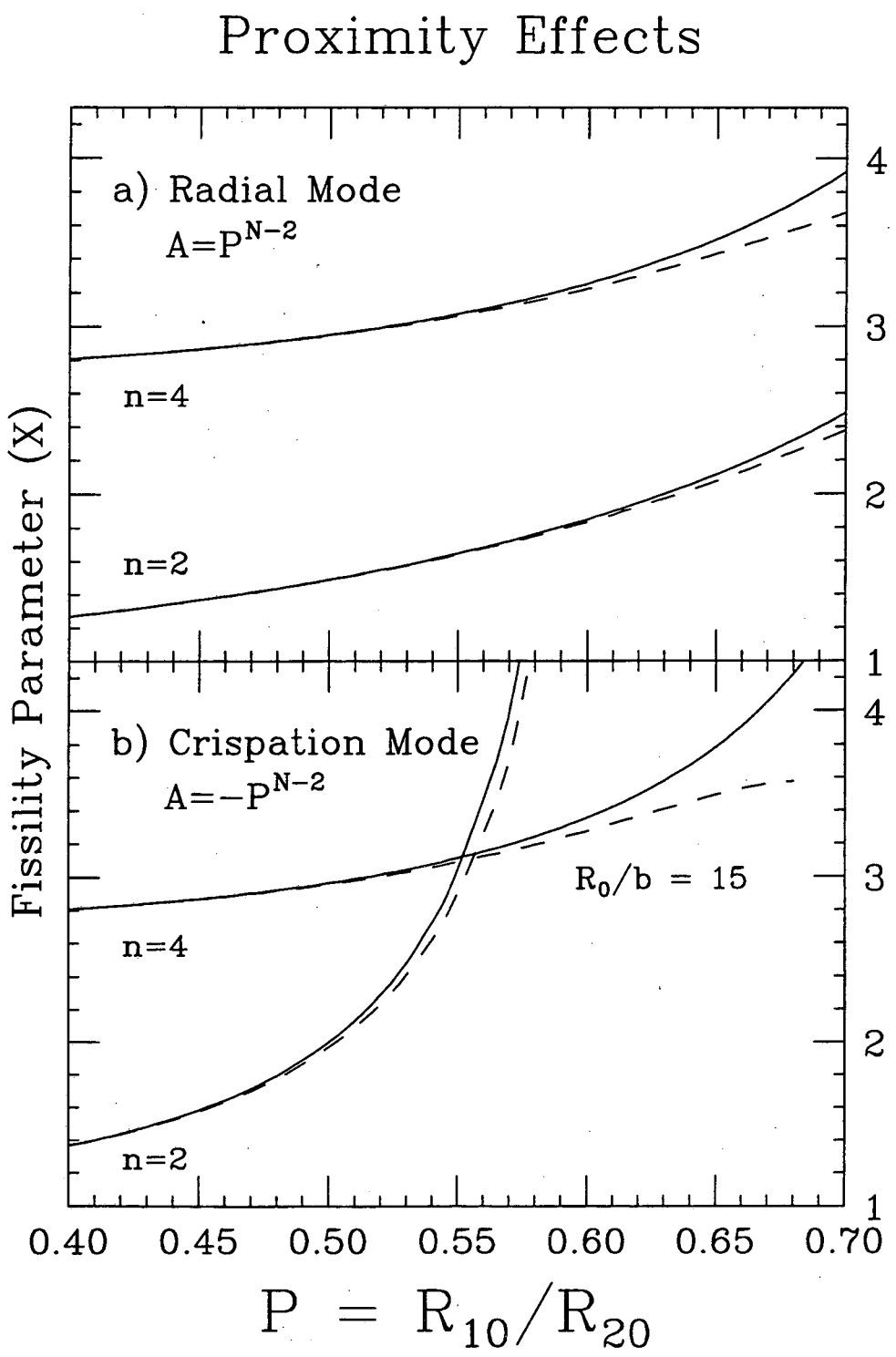

Figure 2.16 : Correlations between the critical values of P and X derived from energy considerations excluding (solid) and including (dashed) the proximity interaction.

drives the Coulomb bubbles to thinner configurations. These Coulomb bubbles however are susceptible to higher order perturbations. To be more precise, the Coulomb instability can be easily triggered by a perturbation of the radial mode when a bubble is thick. On the other hand, a thin Coulomb bubble behaves like a sheet and becomes susceptible to the surface instability via the crispation mode when its thickness is comparable to the range of the proximity interaction.

Chapter 3

Experimental Method

The experimental data presented in this thesis were obtained from the reactions ^{129}Xe + ^{nat}Cu, ^{89}Y, ^{165}Ho and ^{197}Au at bombarding energies of $E/A = 40$ & 60 MeV. The data were collected over a 192–hour running period (during June of 1992) at the National Superconducting Cyclotron Laboratory of Michigan State University. A detail description of the experimental setup is given in section 3.1. The techniques used to extract particle identification, position and energy are described in section 3.2.

3.1 Experimental Setup

To probe the onset of nuclear multifragmentation, the heavy ^{129}Xe projectile was used to bring large amount of mass, angular momentum and excitation energy into the center–of–mass of the colliding nuclei. The choice of targets provided a variety of projectile–target combinations ranging from reverse to normal kinematic reactions, and covered a large range of excitation energies. The excitation energy (MeV) available in the center–of–mass system is listed in Table 3.1 for the four targets at both bombarding energies.

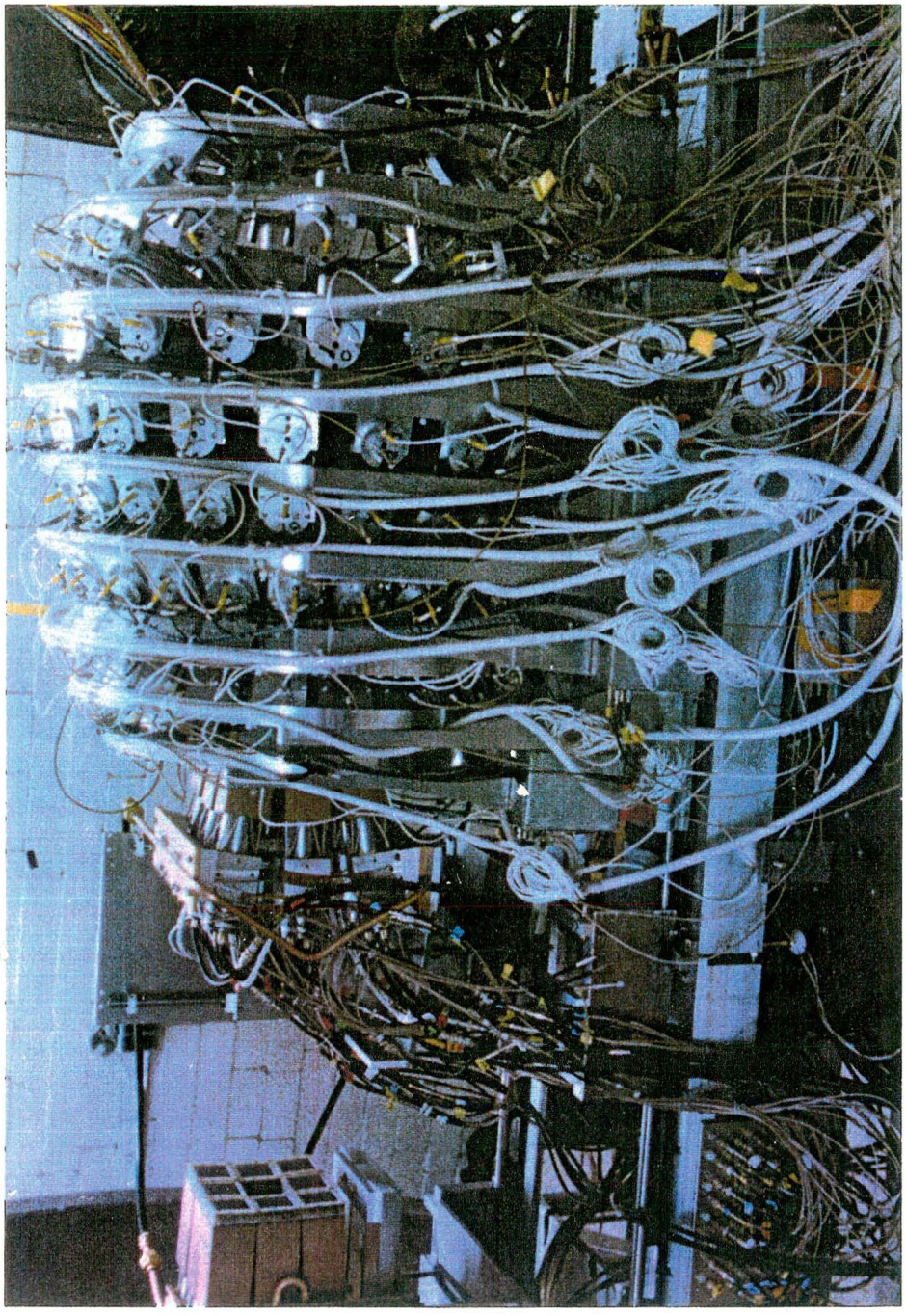

Figure 3.1 : Photograph of the detector configuration. The multidetector system couples the MSU Miniball Array and the LBL Si–Si(Li)–Plastic Array.

Table 3.1 : Excitation energy (MeV) available in the center–of–mass system.

Targets	$A_P + A_T$	$E/A = 40MeV$	$E/A = 60MeV$
Cu	193	1710 (MeV)	2600 (MeV)
Y	218	2100	3140
Ho	294	2900	4320
Au	326	3120	4600

Reaction products were detected with a multidetector system consisted of the MSU Miniball Array [deSo 90] and the LBL Si–Si(Li)–Plastic Array [Keho 92]. Photograph of the detector configuration is shown in Figure 3.1. Near complete coverage of the solid angle (89% of 4π) and good granularity of this combined detector system allowed simultaneous detection and identification of numerous and vastly different fragments over the entire emission phase space. The detector array was actively cooled and temperature stabilized in order to suppress radiation damage of the silicon detectors, to minimize scintillation efficiency variation of the phoswich detectors, and to remove heat generated by the photomultiplier voltage divider network. To prevent interactions of the beam and reaction products with atmospheric gas atoms, a vacuum of about 5×10^{-6} torr was maintained inside the scattering chamber by means of a cyro-pump and a turbo-pump.

3.1.1 Beams and Targets

40 and 60 MeV/nucleon ^{129}Xe beams were extracted from the K1200 cyclotron at the National Superconducting Cyclotron Laboratory. The ^{129}Xe ions were stripped to charge states of +26 and +30 for E/A = 40 and 60 MeV, respectively. The beam energy, with an estimated uncertainity of $\pm 1\%$, was determined from the cyclotron field and from the radial position at extraction. The beam was delivered

to the 92–inch scattering chamber with an intensity of about 10^7 particles per second and with a typical beam spot diameter of 3–4 mm.

Table 3.2 : Ion and molecular beams for detector calibrations.

Detectors	Calibration Beams	$< q/m >$	E/A (MeV)
LBL Silicon	$^{65}Cu^{+13}$, $^{55}Mn^{+11}$, $^{50}Cr^{+10}$	0.200	40
	$^{129}Xe^{+30}$, $^{86}Kr^{+20}$, $^{43}Ca^{+10}$	0.233	60
	$^{90}Zr^{+21}$, $^{60}Ni^{+14}$, $^{30}Si^{+7}$	0.234	60
	$^{16}O^{+4}$, $^{12}C^{+3}$	0.250	60
LBL Plastic	$^{4}HeH^{+}$	0.202	≤ 40
with 5 mm Si(Li)	H_2D^{+}	0.248	≤ 60
LBL Plastic and	$^{6}Li^{+}$, $^{4}HeD^{+}$	0.166	≤ 22
Miniball Phoswich	$^{18}O^{+3}$, $^{12}C^{+2}$	0.167	≤ 22

Besides the ^{129}Xe ion beams used for the data runs, other ion beams (see Table 3.2) at $E/A = 40$ and 60 MeV were used for the calibration of the LBL silicon detectors. Since the detected fragments had a large range of energy and mass, it was useful to calibrate each silicon detector with a number of calibration beams of different energies and masses. In order to minimize the time spent on calibrations, some of these ion beams were extracted simultaneously by combining them into a single triplet or quadruplet beam. This was feasible for those ion beams with the same charge–to–mass ratio (q/m) at all stages of the acceleration [McMa 86]. Molecular beams of $^{4}HeH^{+}$ and H_2D^{+} at $E/A = 40$ and 60 MeV respectively were also used to calibrate the LBL plastic scintillators. Aluminum degraders of various thickness (0.015 – 0.15 inch) were used to produce a range of beam energies and to split HeH and H_2D molecules into He, H and D ions. Similarly, these aluminum degraders were used with light ion beams ($^{18}O^{+3}$, $^{12}C^{+2}$, $^{6}Li^{+}$, $^{4}HeD^{+}$) at $E/A = 22$ MeV to produce more calibration points for the LBL Plastic and the MSU Miniball detectors.

The targets and the Miniball target insertion mechanism used in this exper-

iment are shown in Table 3.3 and Figure 3.2 respectively. The target thickness (areal density) was chosen such that no more than 1% of the beam energy was lost in the target. The targets were mounted on frames made of flat shim stock (0.2 mm thick). Each target frame was attached to an insertion rod, which was mounted on a tray that can be moved parallel to the beam axis. An electromagnetic clutch provided the coupling between the insertion and retraction drives, and a third drive allowed rotation of an inserted target about the axis of the insertion rod. The remote computer control of this target mechanism allowed the targets to be changed quickly without opening the scattering chamber.

Table 3.3 : Thickness of Targets.

Target	Z	A	mg/cm^2
Cu	29	64	2.0
Y	39	89	1.0
Ho	67	165	2.0
Au	79	197	1.3

3.1.2 MSU Miniball Phoswich Array

An artist's perspective of the three–dimensional geometrical assembly of the Miniball Array and a half–plane section in the vertical plane which contains the beam axis are shown in Figures 3.3 and 3.4. The array consists of 11 independent rings coaxial about the beam axis, and individual rings are labelled by the ring numbers $1-11$ which increase from forward to backward angles. The detectors of a given ring are identical in shape and have the same polar angle coordinates. In this experiment, ring 1 and four detectors of ring 2 were removed from the Miniball Array to provide space for the LBL Array, and one detector of ring 8 was also removed to make room

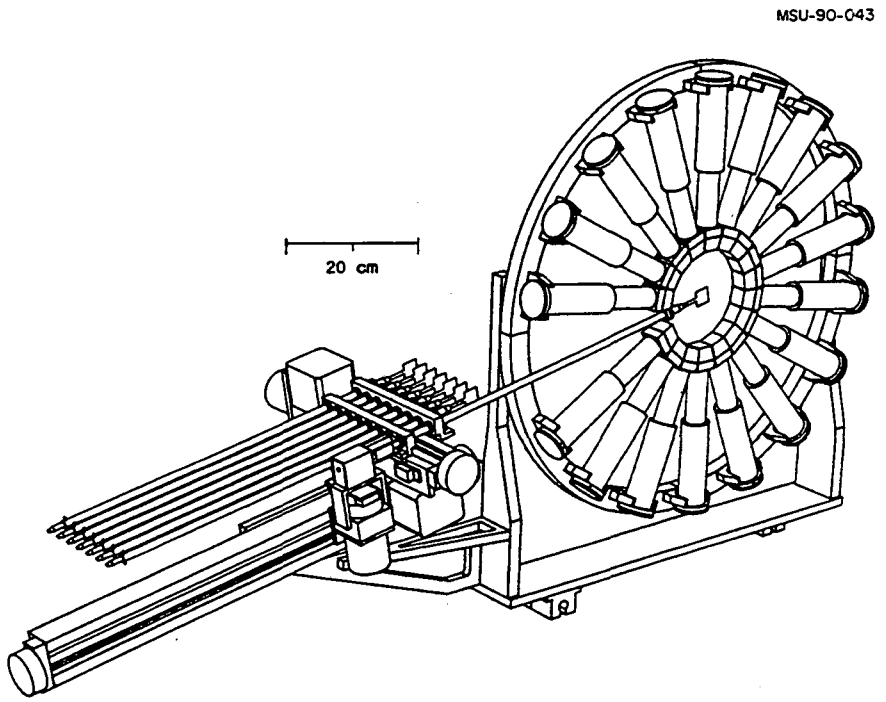

Figure 3.2 : Isometric view of the Miniball target insertion mechanism.

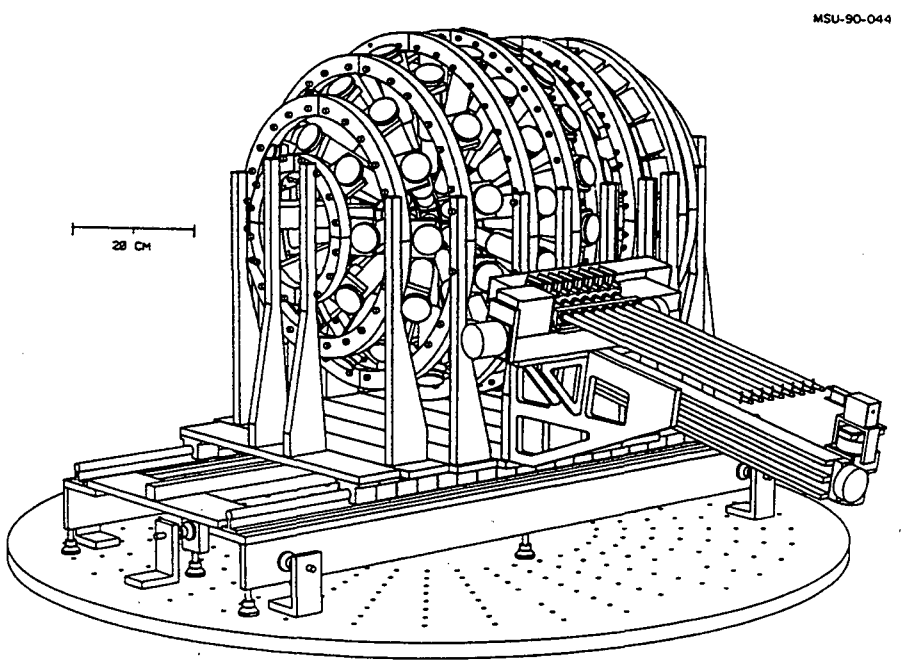

Figure 3.3 : Artist's perspective of the assembly structure of the Miniball 4π fragment detection array. For clarity, electrical connections, the light pulsing system, and the cooling system have been omitted.

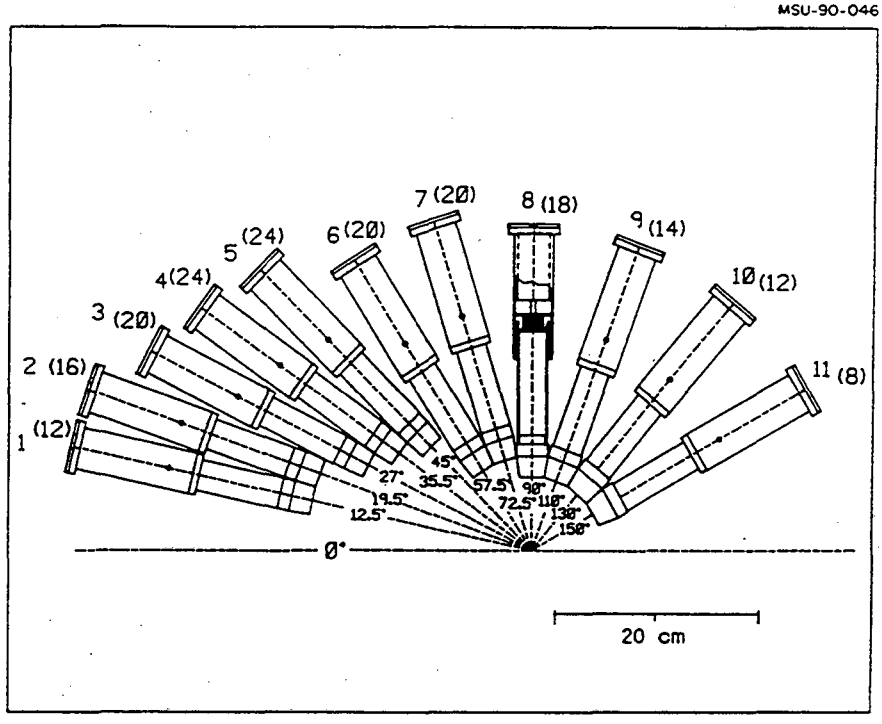

Figure 3.4 : Half–plane section of the Miniball Array. Individual detector rings are labelled 1 through 11. Numbers of detectors per ring are given in parentheses. The polar angles for the centers of the rings are indicated. The dashed horizontal line indicates the beam axis.

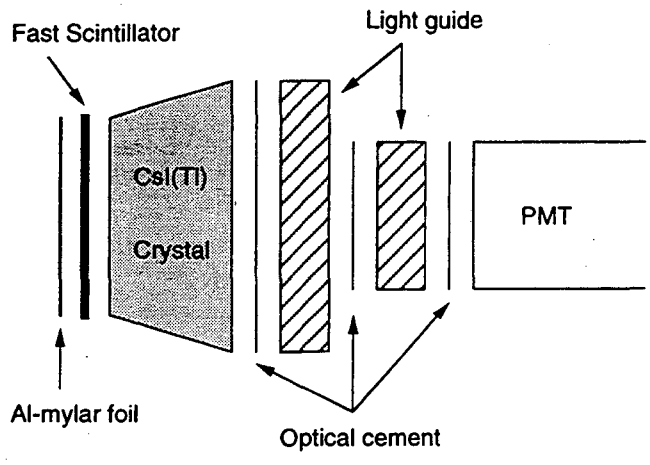

Figure 3.5 : Schematic of phoswich assembly of a Miniball detector.

for the target insertion mechanism. In this configuration, 171 phoswich detectors of the Miniball Array with a total solid angle coverage of approximately 87% of 4π were used to identify charged particles ($Z = 1 - 20$) emitted between 16° and 160° with respect to the beam axis. Identification thresholds for $Z = 3$, 10, and 18 fragments were approximately 2, 3, and 4 MeV/nucleon respectively.

Each Miniball phoswich detector consisted of a 40 μm (4 mg/cm^2) thick plastic scintillator foil backed by a 2 cm thick CsI(Tl) crystal. The scintillator foils were spun from Bicron BC-498X scintillator solution, and they were selected to have a uniformed thickness of 4.0 ± 0.12 mg/cm^2. Previous experience with CsI(Tl) crystals had revealed difficulties in the production of scintillators with uniform scintillation response [Gong 88, Gong 90]. This nonuniformity of the scintillation efficiency can be detected very sensitively by scanning the CsI(Tl) crystals with a collimated α-source in vacuum. Good quality CsI(Tl) crystals with a uniformity of scintillation response better than 2.5% were selected by scanning the surface of crystals along two perpendicular axes.

A schematic of the detector design is given in Figure 3.5. Each detector had an aluminized mylar foil (0.15 mg/cm^2 mylar and 0.02 mg/cm^2 aluminum) placed in front of the plastic scintillator foil. In order to retain flexibility in the choice of scintillator foil thickness, the scintillator foil was placed on the front face of the CsI(Tl) crystal without bonding material. The back face of the CsI(Tl) crystal was glued to a flat light guide made of UVT Plexiglas which, in turn, was glued to a second cylindrical piece of UVT Plexiglas. UVT Plexiglas rather than standard Plexiglas was used in order to minimize additional absorption in these light guides. The 10–stage photomultiplier tube manufactured by Burle Industries (Model C83062E) was chosen because of its good timing characteristics ($\tau_R \approx 2.3$ ns), its large nominal gain ($\approx 10^7$) and its good linearity for fast signals.

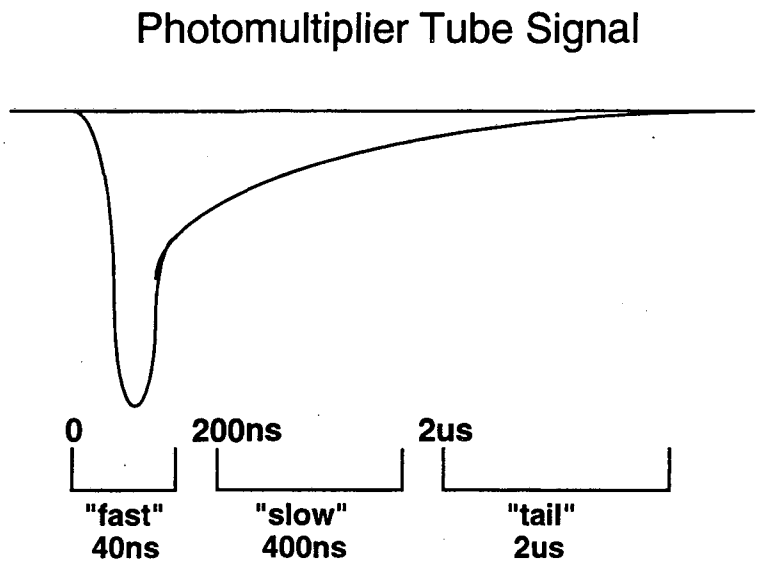

Figure 3.6 : Timing and widths of the fast, slow and tail gates of the Miniball phoswich detector signal.

For each Miniball phoswich detector, light from both the scintillator foil and the CsI(Tl) crystal was collected by the same photomultiplier tube. The light emission of the scintillator foil was much faster than that of the CsI(Tl) crystal, so that most of the plastic signal was collected before the slower CsI(Tl) signal became dominant [Gutb 89]. This large difference between the time characteristics of the two scintillators suggested that the plastic and the CsI(Tl) signals associated with an incident particle could be obtained by using different time gates as shown in Figure 3.6. The "Fast" component (0 – 40 ns) was mainly contributed by the thin scintillator foil. The "Slow" and "Tail" components due to the CsI(Tl) crystal had typical ranges of 400 ns and 2 μs respectively. Two components were obtained for CsI(Tl) since the resulting signal could be approximated as the sum of two exponential decays [Helt 87].

The relative intensities of the two parts were dependent upon the rate of energy loss of the incident particle. As a result, the "Fast–Slow" combination provided ΔE and E signals for intermediate mass fragments ($3 \leq Z \leq 20$), while the "Slow–Tail" combination gave ΔE and E signals for light charged particles ($Z \leq 2$) as long as their energies did not go above the "punch through" energy at $E/A = 75$ MeV.

In this experiment, a simple and compact light pulser system was installed at each ring to monitor gain drifts of the photomultiplier tubes. This light pulser system operated in vacuum was triggered by an external NIM logic signal at a rate of about 1 Hz. The gain variations were corrected in the off–line analysis according to information obtained by the light pulser system. Gain stability to better than 1% was achieved when the temperature of the CsI(Tl) crystals was kept constant.

3.1.3 LBL Si–Si–Pl Array

The LBL Array, consisted of 16 Si–Si(Li)–Plastic telescopes with a total geometrical efficiency of 64%, was used to detect charged particles at very forward angles, from 2° to 16°. In this configuration, two 3×3 arrays were placed one behind the other, and the array (downstream) farthest from the target subtended the central opening in the closer array (upstream). To be more precise, the distance from the target to the upstream and downstream arrays were 35.0 cm and 97.1 cm, and their angular coverage with respect to the beam axis were $5° - 16°$ and $2° - 5°$, respectively. This forward angular coverage thus allowed the detection of very heavy reaction products that were emitted at small angles with near beam velocities. The array with good segmentation was also efficient to detect several complex fragments in coincidence.

The individual components of a telescope are shown in an exploded view in Figure 3.7. A square geometry was chosen for the detectors to facilitate close

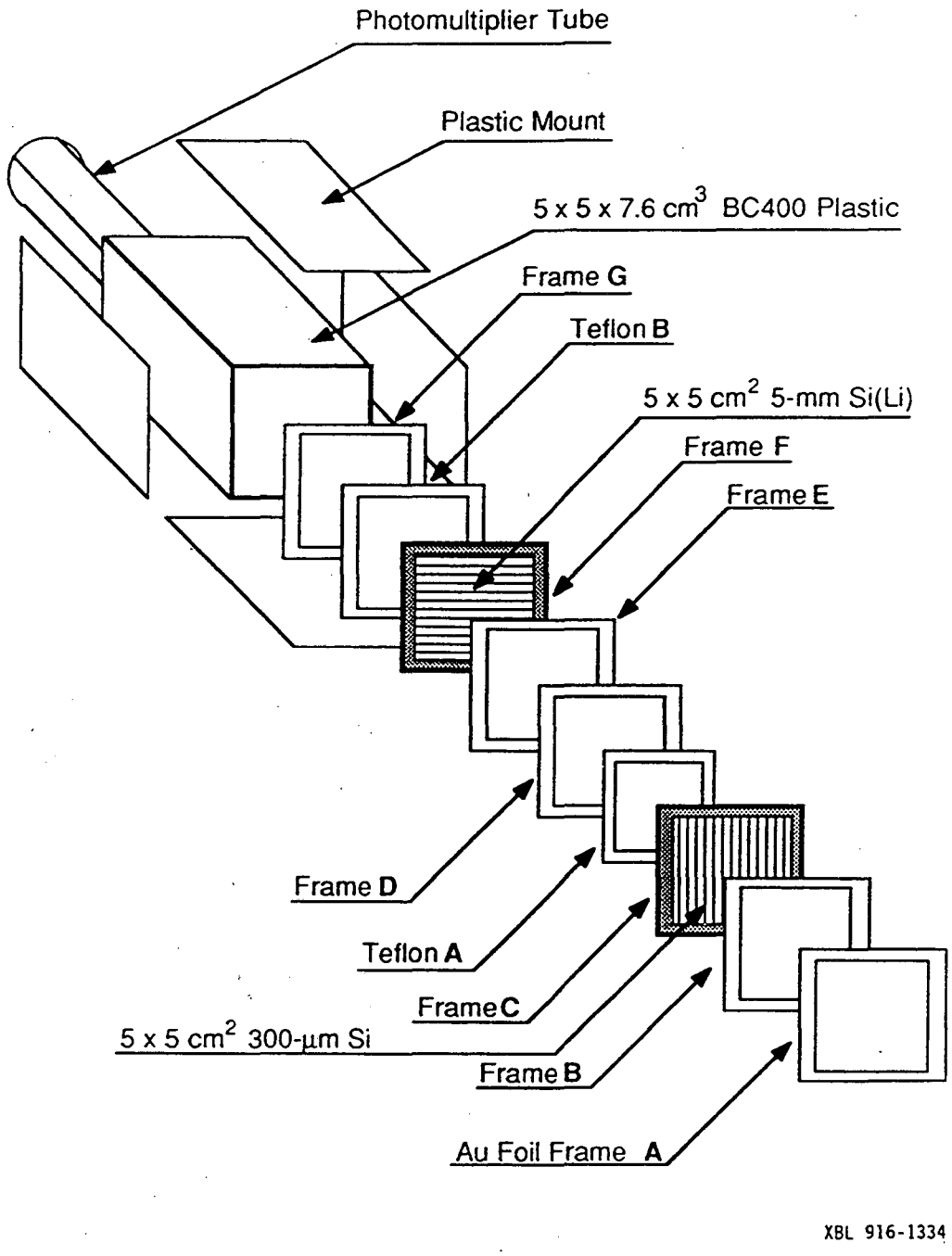

Figure 3.7 : Exploded view of the Si–Si(Li)–Pl Array telescope showing the components of the detector packages.

packaging of adjacent telescopes. Each telescope consisted of a 300 μm and a 5 mm thick silicon detector followed by a 7.6 cm thick plastic scintillator. Such a three element telescope has a large dynamic range to measure the energy, position and charge of reaction products from protons up to the projectile charge. In particular, the three detectors were employed in two successive $\Delta E - E$ telescopes with the 5 mm silicon detector common to both telescopes. The first and second detectors were used to identify fragments with $Z \geq 4$, and the second and third detectors to identify fragments with $Z < 4$. Representative detection thresholds for fragments of $Z = 2$, 8, 20, and 54 were approximately 6, 13, 21, and 27 MeV/nucleon respectively.

The 300 μm detector is an oxide passivated diffused junction n^+p diode fabricated from 5000 Ω-cm p-type silicon. The 5 mm detector is a lithium–drifted silicon diode, Si(Li), fabricated from 1000 Ω-cm p-type silicon. The front faces of the silicon detectors are 50.8 $\times$ 50.8 mm^2 squares, and have active areas of 44.8 $\times$ 44.8 mm^2. Both of these detectors were fabricated by the Silicon Detector Laboratory at Lawrence Berkeley Laboratory. The 300 μm detectors were reversed biased with voltages ranging from +70 to +150 V, and the 5 mm detectors were biased with +600 V. The 7.6 cm plastic scintillator purchased from Bicron (Model BC-400) has a high light output and good light transmission properties. The entrance window (52.1 $\times$ 52.1 mm^2) was made light tight by evaporating a very thin layer of aluminum on it. An RCA model 2060 photomultiplier tube (PMT) with a ten stage dynode was coupled to each plastic scintillator, and was operated with +600 to +800 V.

3.1.4 Data Acquisition Electronics

Figure 3.8 shows a simplified electronic scheme for the multidetector system coupling the MSU Miniball Array and the LBL Si–Si(Li)–Pl Array. In this experiment, the two arrays ran as independent devices, and an event was taken when there

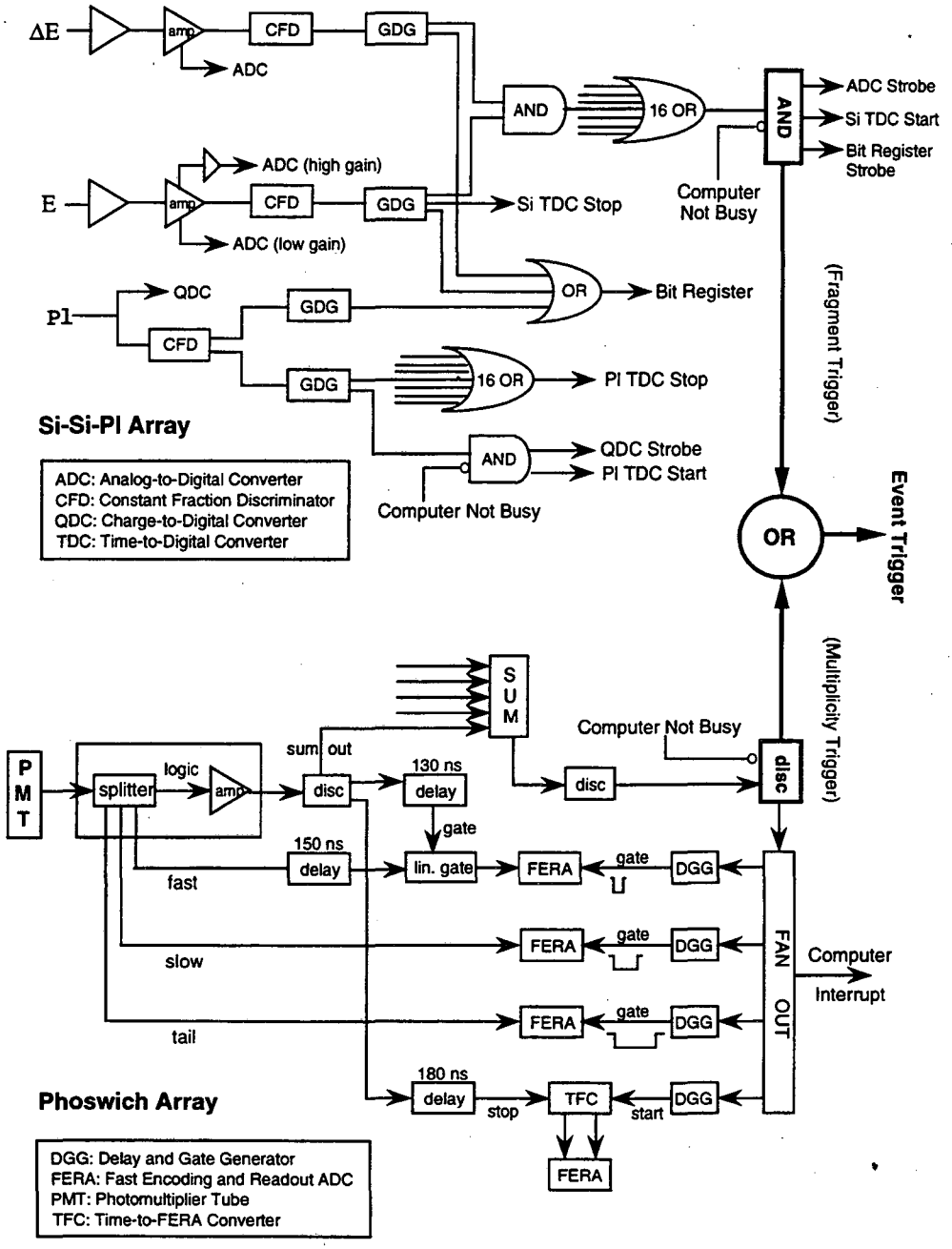

Figure 3.8 : Schematic electronic diagram for the multidetector system coupling the LBL Si–Si(Li)–Pl Array and the MSU Miniball Array.

was either a LBL event trigger or a MSU event trigger. The LBL trigger required at least one fragment ($Z > 2$) being detected, while a multiplicity of charged particles ($Z \geq 1$) above a set threshold was required for the MSU trigger. When a valid event trigger was received, the ADCs, TDCs and FERAs corresponding to the channels with set bits were read out. The event trigger was vetoed by the computer deadtime. The signals from both the MSU Miniball and LBL Array were written event–by–event on magnetic tapes for off–line analysis and to disk for on–line monitoring by a dedicated computer.

3.1.4.1 MSU Miniball Array

The anode current from a photomultiplier is split via passive splitters into the "fast", "slow", "tail", and "logic" branches. The slow and tail signals are connected directly from the splitter to their respective fast encoding readout analog–to–digital converters (FERAs). The gates shown in Figure 3.6 for the "slow" and "tail" FERAs are 400 ns and 2 μs wide and open 200 ns and 2 μs after the leading edge of the linear signal, respectively. In order to gate individual "fast" channel, a linear gate is inserted between the passive splitter and the "fast" FERA. This linear gate is opened 5 ns prior to the leading edge of the linear signal and for a duration of 35 ns. The "fast" FERA is gated by a common gate of 100 ns width which begins approximately 35 ns prior to the leading edge of the linear input signal.

The "logic" signal is reamplified by a fast amplifier and fed into a leading edge discriminator module. One output is then used to provide the stop signal for the time–to–FERA converter and another opens the linear gate for the "fast" channel. The sum output for the 16 channels of each discriminator module is proportional to the number of channels that have been triggered. By setting a discriminator level on the linear addition of all discriminator sum outputs, a simple multiplicity trigger is

obtained.

3.1.4.2 LBL Si–Si–Pl Array

Each fired detector sets a bit in a bit register and stops a time–to–digital converter (TDC). The timing of the telescopes is limited by the 5 mm Si(Li) detector signal which has a slow risetime. In addition, the signal risetime has a strong position dependence due to the substantial resisitive layer on the detector. Energy signals from the two silicon detectors of each telescope are sent to peak–sensitive analog–to–digital converters (ADCs). To improve the energy measurement and particle identification of relatively light fragments, a high–gain signal from each silicon detector is also sent to a peak–sensitive ADC. The high–gain signals are obtained by post amplifying the linear output of the shaping amplifier by an additional factor of 10 to 40. The plastic signal which is essential for the identification of energetic light charged particles is sent to a charge–to–digital converter (QDC).

To trigger the LBL Array, a coincidence between the 300 μm Si and the 5 mm Si(Li) detector signals of any of the array telescopes is required. Constant fraction discriminators on the 300 μm detectors are set to exclude particles with $Z < 3$. Therefore, these light charged particles with sizable signals on the 5 mm Si(Li) and the plastic detectors are not taken unless accompanied by a heavier fragment. In fact, a fast clear is employed to reject these uninterested events that only trigger a plastic detector.

3.2 Calibrations

The raw energy and position signals collected during the experiment must be converted to physical units such as MeV, θ and ϕ in the laboratory frame. This

conversion must be calibrated with reference points of known energy and position. In practice, this was done by measuring the position of each detector with respect to the center of the target and by exposing the detectors to calibration beams of known energy and charge. The calibration techniques used to extract positions, energies and particle identifications are described in the following section.

3.2.1 Position Calibration and Resolution

For the MSU Miniball Array, the position of a detected particle was given by the coordinate corresponding to the center of the fired detector. Hence the laboratory angles θ and ϕ of an incident particle were extracted readily from the geometry of the Array and the configuration of the detectors. On the other hand, the position information of a particle that hit a LBL telescope was obtained from the position sensitive (one dimension) silicon detectors by the method of resistive charge division. The front side of each silicon detector was divided into 15 high conductivity Au strips of 2.42 mm and 14 high resistivity gaps of 0.607 mm. Electrons created by the passage of a charged particle through the detector were then collected at a Au ohmic contact (n^+ contact) on the back face of the detector. This signal essentially measured the deposited energy (E) of the incident particle. The holes collected on the front through the resistor–divider p contact gave a signal XE proportional to the position. In particular, the side of the front face that was closer to the beam was terminated to ground through a 50 Ω resistor, and the position X of the incident particle was simply proportional to the hole signal divided by the electron signal (i.e. $X \propto XE/E$). In this experiment, the strips of the 300 μm detector were arranged orthogonally to the strips of the 5 mm detector within each telescope so that both X and Y position signals were obtained for each detected particle.

Density plots of the raw position signals ($X\Delta E$, YE) versus the correspond-

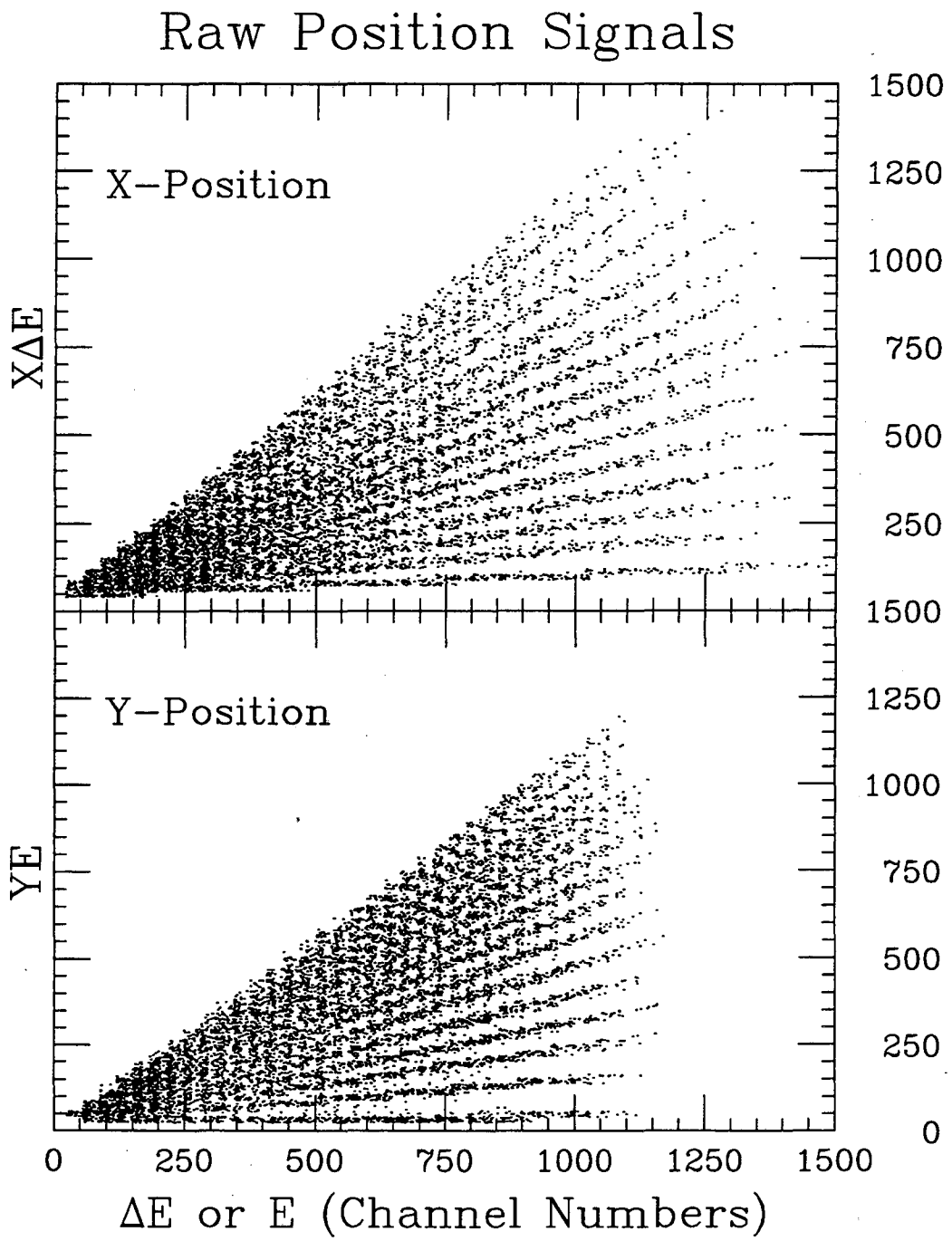

Figure 3.9 : Raw position spectra for a 300 μm Si detector (top) and a 5 mm Si(Li) detector (bottom) in the ^{129}Xe + ^{nat}Cu reaction at $E/A = 60$ MeV. The $X\Delta E$ and YE position signals (holes) are plotted versus the ΔE and E energy signals (electrons). The 15 diagonal lines that are well separated correspond to the 15 discrete position elements of the devices.

ing energy signals (ΔE, E) are shown in Figure 3.9 for a 300 μm ΔE detector and a 5 mm E detector. Lines associated with the 15 discrete Au strips are clearly visible. Following the method outlined by Kaufman et al. [Kauf 70], X and Y positions can be determined from the ratios:

$$X = \frac{X\Delta E - P_o}{\Delta E - \Delta E_o} \qquad Y = \frac{YE - P_o}{E - E_o},$$

with

X, Y	=	horizontal and vertical distances from the grounded end of detectors
$X\Delta E, YE$	=	raw position signals for the 300 μm and 5 mm detectors
$\Delta E, E$	=	raw energy signals for the 300 μm and 5 mm detectors
$\Delta E_o, E_o, P_o$	=	electronic base-line offsets (pedestals).

Therefore, the lowest line in both panels of Figure 3.9 corresponds to the strip farthest away from the signal contact and vice versa. The resulting spectra of X and Y positions are shown in Figure 3.10. The position of each peak is given by the center position of the associated Au strip. In other words, these silicon detectors are self-calibrating in position, and no special runs are required for the position calibration. Since the total width of a strip and a gap is (2.42 + 0.607)mm, the theoretical position resolution of these silicon detectors is $\pm$ 1.5 mm or 0.1°.

3.2.2 Energy Calibration and Resolution

The MSU Miniball Array had been extensively calibrated in an earlier experiment [Kim 92]. In this previous run, the energy calibration of the Miniball detectors was obtained by measuring the elastic scattering of several light ion beams ($2 \leq Z \leq 18$) from a ^{197}Au target at relatively low incident energies ($E/A \leq 20$ MeV). In these calibrations, the following functional form was assumed for the energy (E_{CsI})

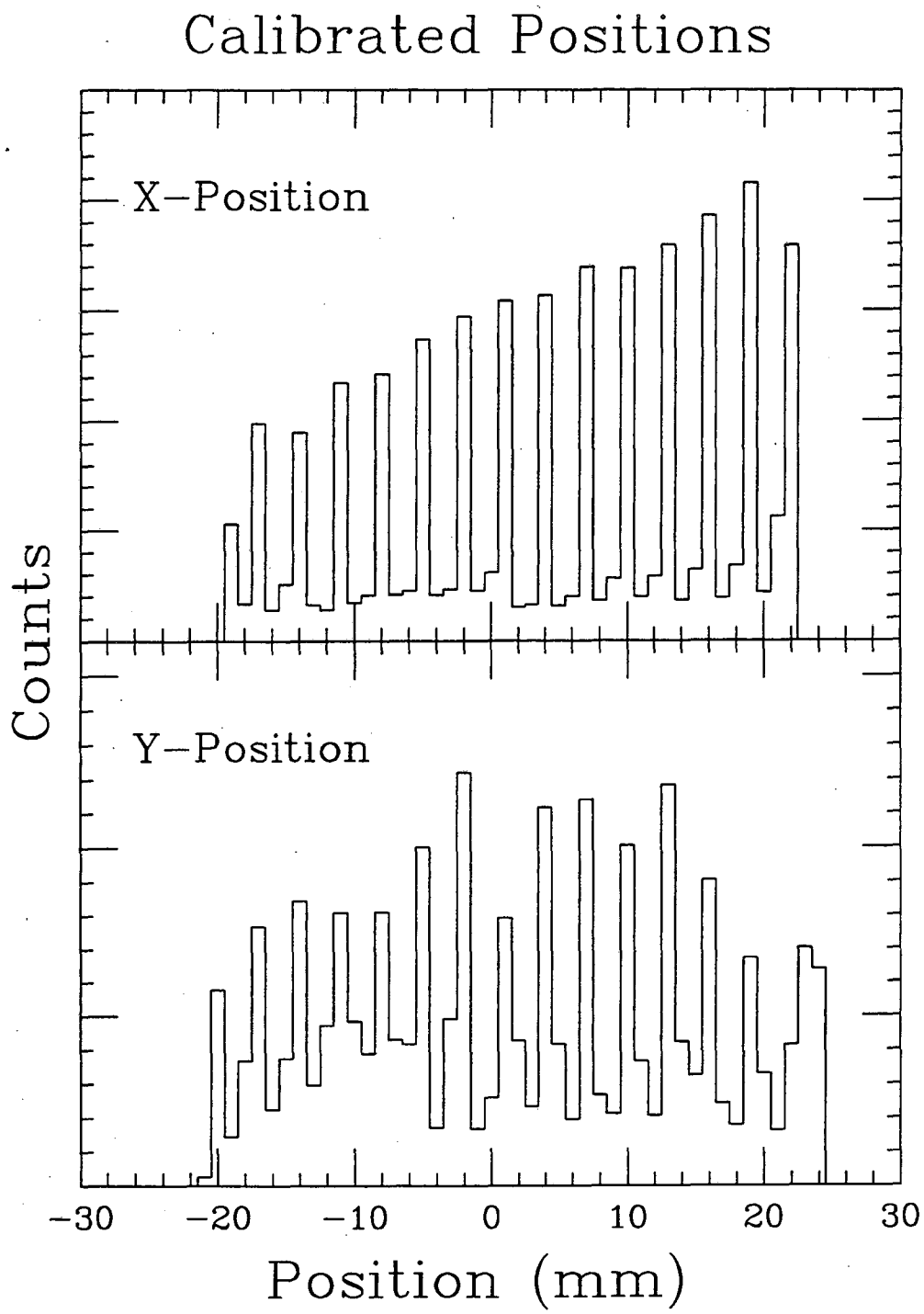

Figure 3.10 : The calibrated X (top) and Y (bottom) positions are shown for one of the LBL Si–Si(Li)–Pl telescopes in the ^{129}Xe + ^{nat}Cu reaction at E/A = 60 MeV. Each peak corresponds to a different strip on the detector. The position is expressed as the distance, in mm, from the center of the detector.

dependence of the light output (L) measured in QDC channel numbers (C_{QDC}):

$$L = C_{QDC} = \gamma E_{CsI} + \beta \left(e^{-\alpha E_{CsI}} - 1 \right).$$

The values of α, β and γ were extracted as a function of Z, and the energy calibration was estimated to be accurate within 5%. In this experiment, the energy calibration was obtained by scaling the previous calibration [Kim 92] for every phoswich detector. The scaling constant was simply the ratio between the corresponding hydrogen punch–through points of a given detector in the two experiments:

$$C^o_{QDC} = C_{QDC} \cdot \frac{C^o_{HPT}}{C_{HPT}}. \tag{3.1}$$

Here C^o_{HPT} and C_{HPT} are the hydrogen punch–through points of a given detector in the previous calibration run and in this experiment, respectively. The light output measured in this experiment (C_{QDC}) was first converted to C^o_{QDC} using Equation 3.1. Then the parameters α, β and γ determined in the previous calibration were used to give the desired relationship between the light output (C^o_{QDC}) and the energy (E_{CsI}):

$$C^o_{QDC} \;=\; \gamma E_{CsI} + \beta \left(e^{-\alpha E_{CsI}} - 1 \right).$$

This procedure was checked for a subset of 8 Miniball detectors that were calibrated by sweeping the $q/m = 1/6$ light ion beams ($^{18}O^{+3}$, $^{12}C^{+2}$, $^{4}HeD^{+}$, $^{6}Li^{+}$) across their surface. For this limited subset of detectors, satisfactory agreement with the existing calibration was found.

The energy calibration of the LBL silicon detectors was performed by directly exposing the silicon detectors to low intensity calibration beams of different energies and masses. The intensity of the calibration beams was kept at less than 100 particles/second in order to minimize radiation damage to the silicon detectors. As mentioned in section 3.1.1, multiple beams with ions of the same charge–to–mass ratio

(q/m) were used to reduce the calibration time. An example of a triplet beam that was used in the calibration consisted of $^{129}Xe^{+30}$, $^{86}Kr^{+20}$ and $^{43}Ca^{+10}$ ions ($q/m = 0.233$). These ions were stopped directly in a 5 mm Si(Li) detector without the 300 μm Si detector in front. Figure 3.11a shows the corresponding energy spectrum, in which the energy is expressed in units of ADC channel numbers ($E_{channel}$).

Since a 5 mm Si(Li) detector is sufficiently thick to stop the incident ions of the calibration beams, the channel numbers of the three peaks in Figure 3.11a correspond to the measured energies of ^{129}Xe, ^{86}Kr and ^{43}Ca ions. The measured energy E_m in MeV is less than the true beam energy E_{true} due to the pulse–height–defect E_{phd} (i.e. $E_m = E_{true} - E_{phd}$). Correction was made for this pulse–height–defect in the 5 mm Si(Li) detectors based on the systematics of Moulton et al. [Moul 78]. A simple power–law formula given in reference [Moul 78] was used to calculate the energy loss due to the pulse–height–defect as a function of E_m and Z of the ion. The contributed uncertainity in the energy due to this procedure was estimated to be less than 1% of the total energy. The measured energy E_m was then plotted as a function of the averaged $E_{channel}$ for the corresponding ions. The best linear fit through the points gave the desired relation between the deposited energy in MeV and the ADC channel number:

$$E_m(MeV) = a + b \cdot E_{channel}. \tag{3.2}$$

An example of a raw ADC energy spectrum for the above triplet calibration beam in a 300 μm Si detector is shown in Figure 3.11b. Again the channel numbers of the three peaks correspond to the measured energies deposited by $^{129}Xe^{+30}$, $^{86}Kr^{+20}$ and $^{43}Ca^{+10}$ ions in a 300 μm Si detector. This deposited energy ΔE_m in MeV was determined from the measured energy difference in a 5 mm Si(Li) detector with and without a 300 μm detector in front. Similarly, the energy ΔE_m (MeV) for each ion

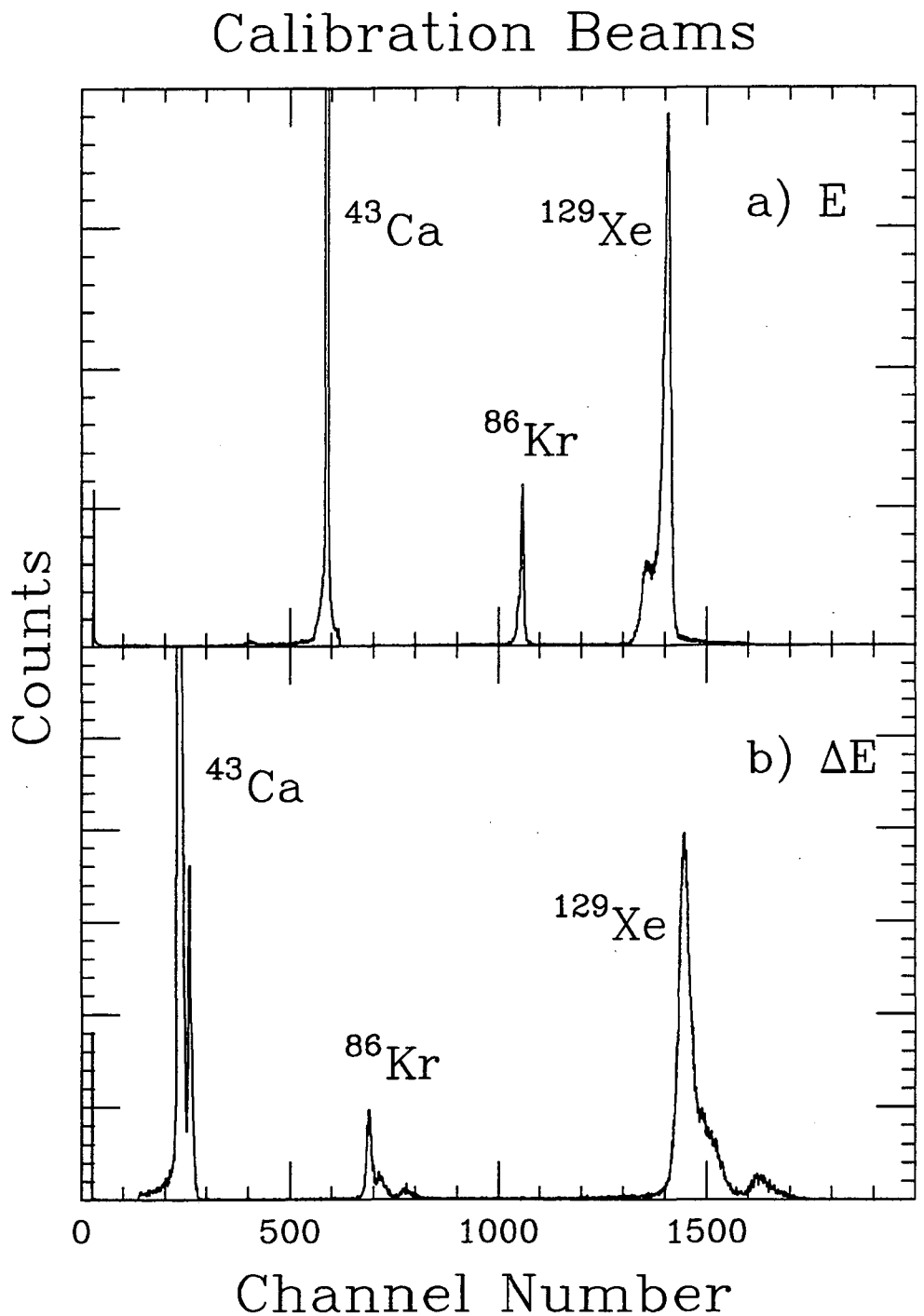

Figure 3.11 : Energy spectrum of a) 5 mm and b) 300 μm silicon detector exposed to a triplet beam of ^{129}Xe, ^{86}Kr and ^{43}Ca ions. These three ions with the same charge–to–mass ratio (q/m = 0.233) were simultaneously accelerated to E/A = 60 MeV.

was plotted versus the mean value $\Delta E_{channel}$ of the corresponding peak, and the best linear fit through the points gave the desired relation between ΔE_m (MeV) and $\Delta E_{channel}$. Since the pulse–height–defect was thought to be primarily an end–of–range effect, no correction was applied to the 300 μm detectors in which the incident fragments were not stopped. However, the peaks in some of the energy (ADC) spectra for the 300 μm Si detectors were not sharp due to the thickness nonuniformity of these detectors. The variations in thickness were $2-10\%$ and $\leq 2\%$ for the 300 μm and 5 mm silicon detectors respectively. A correction for the nonuniformity was performed by scanning the surface of each silicon detector with the calibration beams along two perpendicular axes.

After the energy calibration for the silicon detectors was finished, scattering of molecular beams ($^4HeH^+$ and H_2D^+) from a ^{197}Au target at relatively high incident energies ($E/A = 40$ and 60 MeV) was used to provide some calibration points for the plastic detectors behind the silicon detectors. Since the 300 μm silicon detectors had been removed, the energy deposited in a plastic scintillator was simply the difference between the incident energy and the energy loss in the 5 mm Si(Li) detector. The 5 mm Si(Li) detectors had been calibrated and thus the corresponding energy loss could be calculated readily. In order to produce calibration points at lower energies, degraded beams were generated by placing aluminum foils of thickness ranged from 0.015 to 0.15 inch at the target positions.

Finally, the 5 mm Si(Li) detectors were removed and the plastic detectors were calibrated with the light ion beams of $^{18}O^{+3}$, $^{12}C^{+2}$, $^4HeD^+$, and $^6Li^+$ at low intensities. These calibration beams at $E/A = 22$ MeV had also been used to calibrate the Miniball detectors. Similarly, the measurement of the light output was extended to lower energies by means of aluminum degraders. In practice, the degraded beams were first stopped by a well calibrated 5 mm Si(Li) detector in order to determine

their energies accurately.

Like other scintillators, the light output from the plastic detectors exhibits a strong dependence on the atomic number and energy of the detected ion. Therefore, the functional form that was used to fit the response function of the Miniball CsI(Tl) crystals was assumed for the light output of the plastic scintillators:

$$L = C_{QDC} = \gamma E_{Pl} + \beta \left(e^{-\alpha E_{Pl}} - 1 \right). \tag{3.3}$$

Figure 3.12a shows the measured light output, in QDC channel numbers, as a function of energy (E_{Pl}) for a set of representative ions from ^{2}D to ^{12}C. The symbols that represent the experimental data agree very well with the curves obtained from the least square fits with the above functional form for the light output. The parameters α, β and γ extracted from these fits were found to be functions of mass and charge of an incident ion. In fact, empirical expressions were given for the parameters α, β and γ in terms of Z and A:

$$\begin{aligned} \alpha &= \frac{P_5}{A \cdot Z} \\ \beta &= (P_3 \cdot A \cdot Z) + P_4 \\ \gamma &= \frac{P_1}{A \cdot Z} + P_2. \end{aligned}$$

Here P_1 to P_5 are the fitting parameters that reflect the different properties of individual scintillators. This charge and mass dependence of the response function essentially says that the deposited energy cannot be determined unless the incident particle is identified. This coupling between Z and E_{Pl} in the light output is a major drawback for the scintillator detectors.

For each fragment detected by the LBL telescopes, small corrections were further applied using range energy tables for the energy losses in the target and in the 1.5 mg/cm^2 Au foils that were used for electron suppression. The overall energy

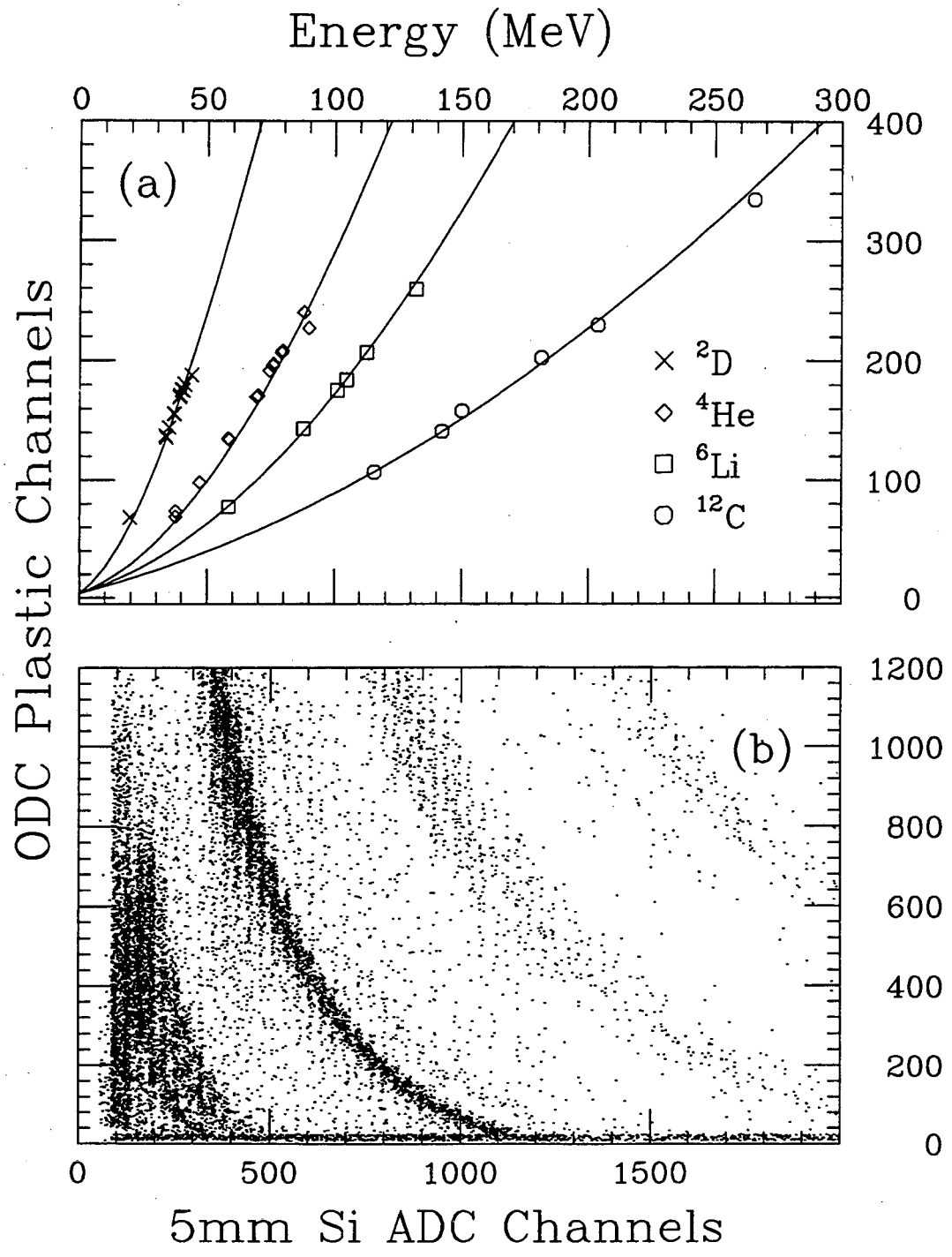

Figure 3.12 : (a) Light output of a Plastic Scintillator as a function of energy for some representative ions. The solid curves are the results of fits with Equation 3.3. (b) Particle identification obtained from two–dimensional density plot of E (Plastic) vs ΔE (5 mm Si) signals for one of the LBL Si–Si(Li)–Pl telescopes in the ^{129}Xe + ^{nat}Cu reaction at $E/A = 60$ MeV.

calibration was estimated to be accurate to approximately 1%.

3.2.3 Particle Identification and Resolution

The Z identification of a fragment detected by a $\Delta E - E$ telescope is often achieved based on the expression of the classical Bohr equation [Bohr 48] for the energy loss of a charged particle in a medium. The Bohr equation predicts that the amount of energy lost (dE) by a particle after travelling a small distance (dX) in some medium depends on the charge (Z) and the velocity (v) of the particle:

$$-\frac{dE}{dX} \propto \frac{Z^2}{v^2} \propto \frac{MZ^2}{E} \propto \frac{Z^3}{E}. \tag{3.4}$$

Under the assumption that mass (M) is proportional to Z, this energy loss is shown to be inversely proportional to the total energy of the particle (E). For a thin ΔE transmission detector, the deposited energy ΔE can be equated to $\frac{dE}{dX}$. Consequently, the product $\Delta E \cdot E \propto Z^3$ becomes a hyperbola with a Z dependence.

For the LBL Array, the 300 μm and 5 mm silicon detectors were used as ΔE transmission and E stopping detectors respectively. The raw ΔE and E signals were first converted to energy units in MeV with the procedures described above, and the total energy E was then calculated from their sum. The correlation between the total energy E and the energy lost in the transmission detector ΔE is shown as a density plot in Figure 3.13. Clearly, an intensity pattern of alternating valleys and ridges is observed. According to Equation 3.4, each ridge corresponds to an element that essentially defines a "Z" line, and thus can be used to extract the atomic charge of the detected fragments.

In practice, the curved ridges in the $\Delta E - E$ plots were transformed to straight "Z" lines by constructing a Particle Identification function defined as :

$$PID \equiv [(\Delta E + a) \cdot (E + b)]^{1/3}, \tag{3.5}$$

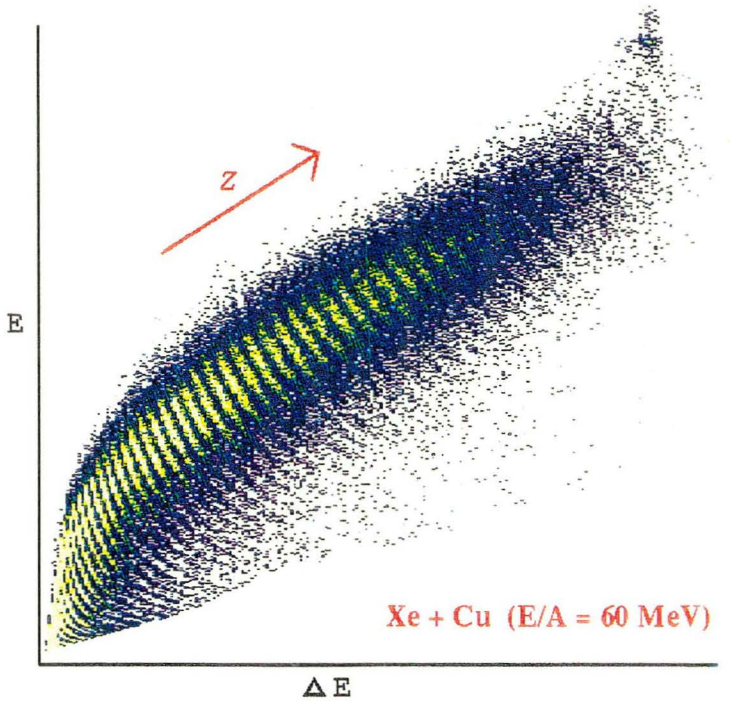

Figure 3.13 : Density plot of E (total energy) versus ΔE (energy loss in the 300 μm Si) for one of the LBL Si–Si(Li)–Pl telescopes in the ^{129}Xe + ^{nat}Cu reaction at E/A = 60 MeV. The individual ridge lines correspond to different elements.

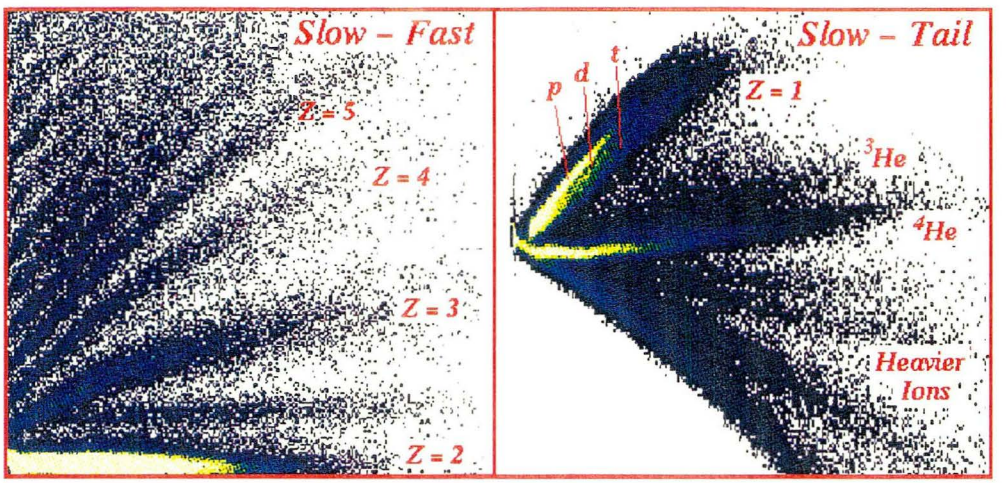

Figure 3.14 : Particle identification obtained from two–dimensional "tail vs slow" and "fast vs slow" plots for one of the MSU Miniball detector in the ^{129}Xe + ^{nat}Cu reaction at E/A = 60 MeV

where a and b were parameters chosen by trial and error in order to minimize the curvature of the "Z" lines. The "Z" lines for the above calibration beams were also constructed and used as reference points to check the atomic numbers assigned for individual "Z" lines. Finally, the mean PID value of each "Z" line was fit as a function of Z in order to extract the desired relation between PID and Z. Figure 3.15a shows the extracted atomic numbers for one of the most forward LBL detector near the beam. Individual peaks corresponding to atomic number up to the projectile charge ($Z = 54$) are visible.

For light fragments that punched through the 5 mm silicon detectors and stopped in the plastic scintillators, their energy losses in the 300 μm silicon detectors were negligible. In this case, the 5 mm detector was used as the transmission detector and the plastic detector was the stopping detector. To identify the atomic number of these energetic light fragments, $\Delta E - E$ plots were constructed by utilizing the high–gain signal from the 5 mm detector and the plastic signal as shown in Figure 3.12b for a LBL telescope. However PID functions were not constructed since the energy E deposited in a plastic scintillator could not be extracted from the light output unless the particle was identified. Alternatively, free form gates around each of the "Z" lines in the $\Delta E - E$ maps were drawn to improve the Z resolution of light fragments.

Like the plastic scintillators, the MSU CsI crystals are also limited by the Z dependence of their light outputs. Therefore, the standard method to draw free form gates around each of the "Z" lines in the $\Delta E - E$ plots was used. Figure 3.14 shows a typical two–dimensional slow–fast and slow–tail density plots for the Miniball detector. The slow–fast signals were used to identify fragments with $Z \geq 2$, while the slow–tail signals were used to identify light charged particles and their isotopes. Clearly, good isotope resolution is achieved for Hydrogen and Helium. However, the

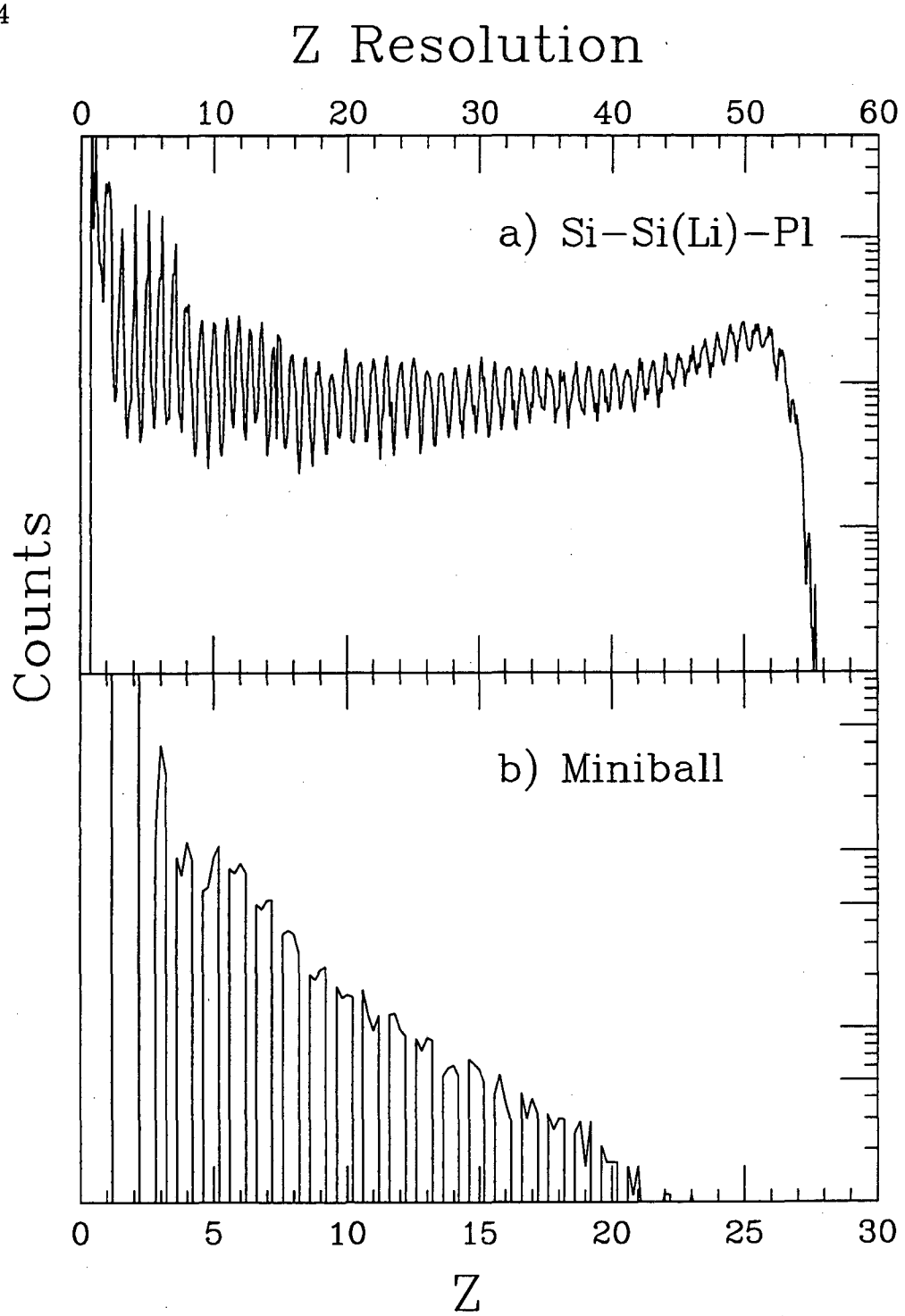

Figure 3.15 : Particle identification spectra for a LBL Si–Si(Li)–Pl telescope (a) and a MSU Miniball detector (b) in the ^{129}Xe + ^{nat}Cu reaction at E/A = 60 MeV. Individual atomic numbers are resolved up to the projectile (Z = 54) for a LBL detector near the beam.

extrapolation of particle identification beyond the region in which the lines are visible is not very accurate. Figure 3.15b shows the charge resolution for Z up to 20 for a typical Miniball detector.

Naturally, masses for light charged particles were obtained from their isotope resolutions. However, an average mass associated with each Z must be determined for heavier fragments. The evaporation code PACE had been used to estimate the secondary masses following sequential evaporation of light particles from the excited primary fragments [Char 88a]. The average mass for each Z determined from the PACE simulations ($A = 2.08Z + 0.0029Z^2$) was used in this analysis. This mass parameterization was found to agree with average masses determined experimentally [Auge 87].

Chapter 4

Excitation Functions

In this chapter, the excitation functions for multiple emission of fragments are presented for the ^{129}Xe–induced reactions on ^{nat}Cu, ^{89}Y, ^{165}Ho and ^{197}Au targets at bombarding energies of E/A = 40 and 60 MeV. The excitation energy of the system is measured by the transverse energy introduced in section 4.1. In section 4.2, the multifragment emission probabilities as a function of transverse energy for the reaction ^{129}Xe + ^{197}Au at both bombarding energies are shown to be binomial and reducible to an elementary binary decay probability that has a thermal dependence. The physical interpretation and significance of this thermal reducibility is explored in sections 4.3 and 4.4. The technical issue concerning the auto–correlation between the measured transverse energy and the observed fragment multiplicity is addressed in section 4.5, and the effects of the finite detection efficiency on the extraction of various binomial parameters are studied in section 4.6. Finally, the results for the ^{129}Xe–induced reactions on other targets are compared and presented in section 4.7.

4.1 Transverse Energy

In the last several years, experimental studies have succeeded in isolating and characterizing what appear to be true multifragmentation sources formed in reverse kinematics intermediate energy heavy–ion reactions [Blum 91, More 93a, Rous 93]. In these experiments, the probability of emitting n fragments was studied as a function of excitation energy, which was determined kinematically from the parallel source velocity assuming an incomplete fusion picture [More 86, Bowm 89, Guer 89]. In these reverse kinematics reactions, the large velocity of the source dramatically increases the laboratory velocity of all fragments emitted in the source frame. This gives rise to a strong forward focusing of the reaction products, thus eliminating the need of a 4π detection system. However, such a 4π detector becomes essential for the ^{129}Xe–induced reactions on various targets ranging from reverse to normal kinematics. In normal kinematics, the forward focusing effect is relatively weak because of the small source velocity. A complete angular coverage is then necessary in order to detect all emitted fragments. In this study of ^{129}Xe–induced reactions, the MSU Miniball [deSo 90] was coupled with the LBL Array [Keho 92] to provide a large phase space coverage for fragments as well as light charged particles.

In order to measure the excitation energy, the transverse energy is calculated for each event. The transverse energy E_t is defined as the sum of the kinetic energies E, weighted by the sine squared of the detected polar angle θ for all charged particles in an event:

$$E_t \equiv \sum_{i}^{N_c} E_i sin^2\theta_i. \tag{4.1}$$

The kinetic energy E_i of a detected particle can be expressed in terms of its mass and

velocity, $E_i = \frac{1}{2}M_iV_i^2$, and the above equation for E_t becomes

$$E_t = \sum_i^{N_c} \frac{1}{2}M_iV_i^2 sin^2\theta_i = \sum_i^{N_c} \frac{1}{2}M_i(V_i^y)^2, \tag{4.2}$$

where V_i is the velocity of the ith particle and V_i^y is the corresponding y–component of the velocity. This expression for E_t shows no dependence on the x–component of the velocity (V_i^x) indicating that the transverse energy is invariant with respect to the Galilean transformation from the laboratory to the center–of–mass frame. In other words, the transverse energy measured in the laboratory frame is essentially equal to the transverse energy in the center–of–mass frame.

A question naturally arises whether the transverse energy E_t is proportional to the excitation energy E^*. For the sake of illustration, consider a simple thermal model where the excitation energy is evenly distributed among the charged particles (i.e. $E_i = E^*/N_c$), and the angular distribution of the particles is isotropic. Under these conditions, the average transverse energy for events of a fixed excitation energy can be shown to be proportional to the excitation energy,

$$\langle E_t \rangle = \left\langle \sum_i^{N_c} \frac{E^*}{N_c} sin^2\theta_i \right\rangle = \sum_i^{N_c} \frac{E^*}{N_c} \left\langle sin^2\theta_i \right\rangle = E^* \frac{\int sin^2\theta_i dcos\theta_i}{\int dcos\theta_i} = \frac{2}{3}E^*. \tag{4.3}$$

An example of the E_t spectra for the ^{129}Xe–induced reactions on four targets at a bombarding energy of $E/A = 40$ MeV is shown in Figure 4.1. The dramatic decrease in the number of events with increasing E_t is consistent with the decrease of the geometric reaction cross section from the most peripheral collisions (low excitation energy) to the most central collisions (high excitation energy). For the sake of comparison, an upper limit of the measured E_t is chosen to exclude 0.1% of the total integrated yield at the tail of the E_t distribution. The observed target dependence in the end points of these E_t distributions suggests a correlation between this upper limit of the measured E_t and the available energy in the center–of–mass frame E_{cm}. A

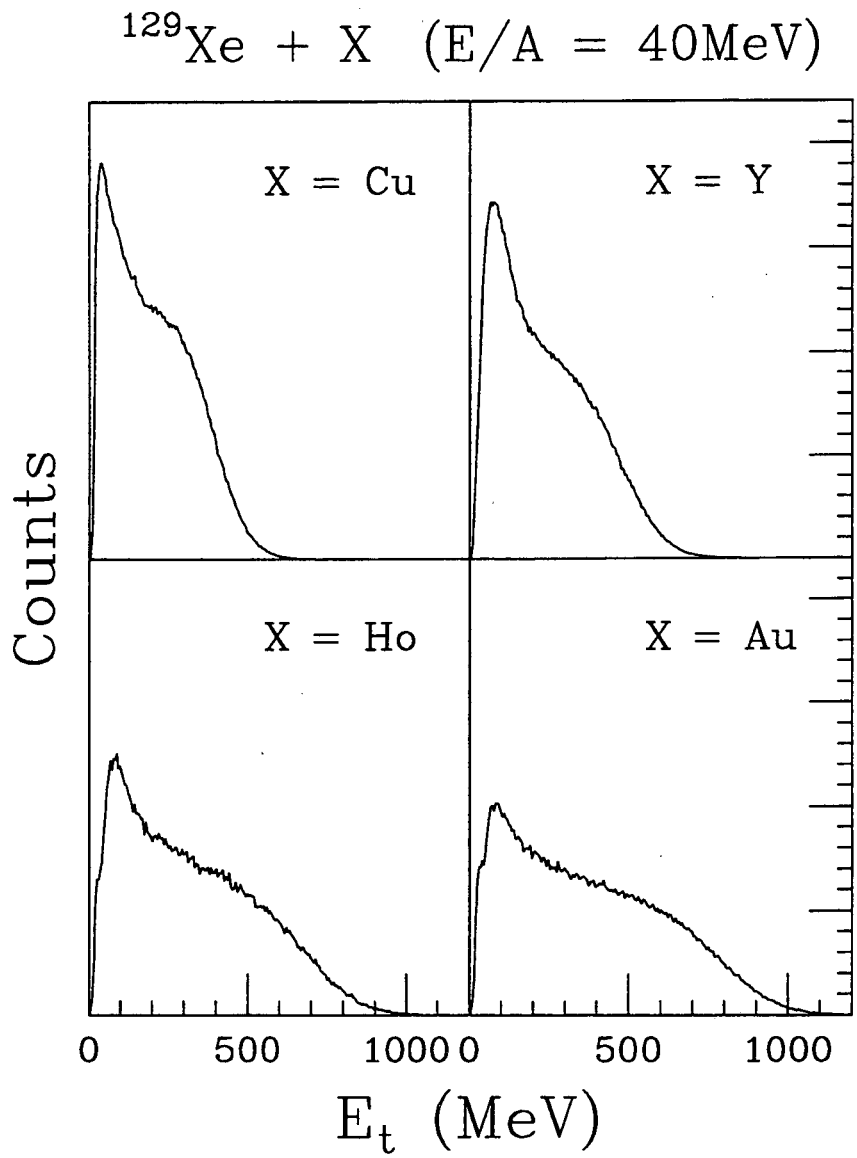

Figure 4.1 : Transverse energy E_t distributions observed for the ^{129}Xe–induced reactions on ^{nat}Cu, ^{89}Y, ^{165}Ho and ^{197}Au targets at a bombarding energy of E/A = 40 MeV.

linear correlation between E_{cm} and E_t is indeed observed in Figure 4.2 for the ^{129}Xe–induced reactions on four different targets and at two bombarding energies. This is consistent with the assumption that the transverse energy is proportional to the excitation energy [Boug 94] . A similar correlation between the transverse energy and the excitation energy E^* is assumed in the following analysis: $E_t = K(E_{beam}, A_P, A_T)E^*$. Here K is the proportionality constant that depends on the bombarding energy E_{beam}, the mass of the projectile A_P and the mass of the target A_T.

As mentioned earlier, the excitation energy can be determined kinematically from the source velocity in an incomplete fusion picture [More 86, Bowm 89, Guer 89]. In reverse kinematics reactions, the excitation energy E^* is related to the parallel source velocity V_s by

$$E^* = E_{beam}\left(1 - \frac{V_s}{V_{beam}}\right), \tag{4.4}$$

where V_{beam} is the beam velocity. Figure 4.3 shows the correlation between this calculated excitation energy and the measured transverse energy for the reaction ^{129}Xe + ^{nat}Cu at bombarding energies of E/A = 40 and 60 MeV. The observed linear correlation further justifies the assumption that the transverse energy is linearly related to the excitation energy.

There are some advantages to use the transverse energy instead of the source velocity as a measure of the excitation energy. One advantage is the additional zero–fold and one–fold probabilities in the excitation functions. Since at least two IMFs must be detected in a given event for the construction of the source velocity, zero–fold and one–fold events must be discarded if the excitation energy is inferred from the parallel source velocity. Moreover, the distribution of the constructed source velocities might be broadened considerably by contaminations from the pre–equilibrium emission of light charged particles. Even if this contamination can be minimized by

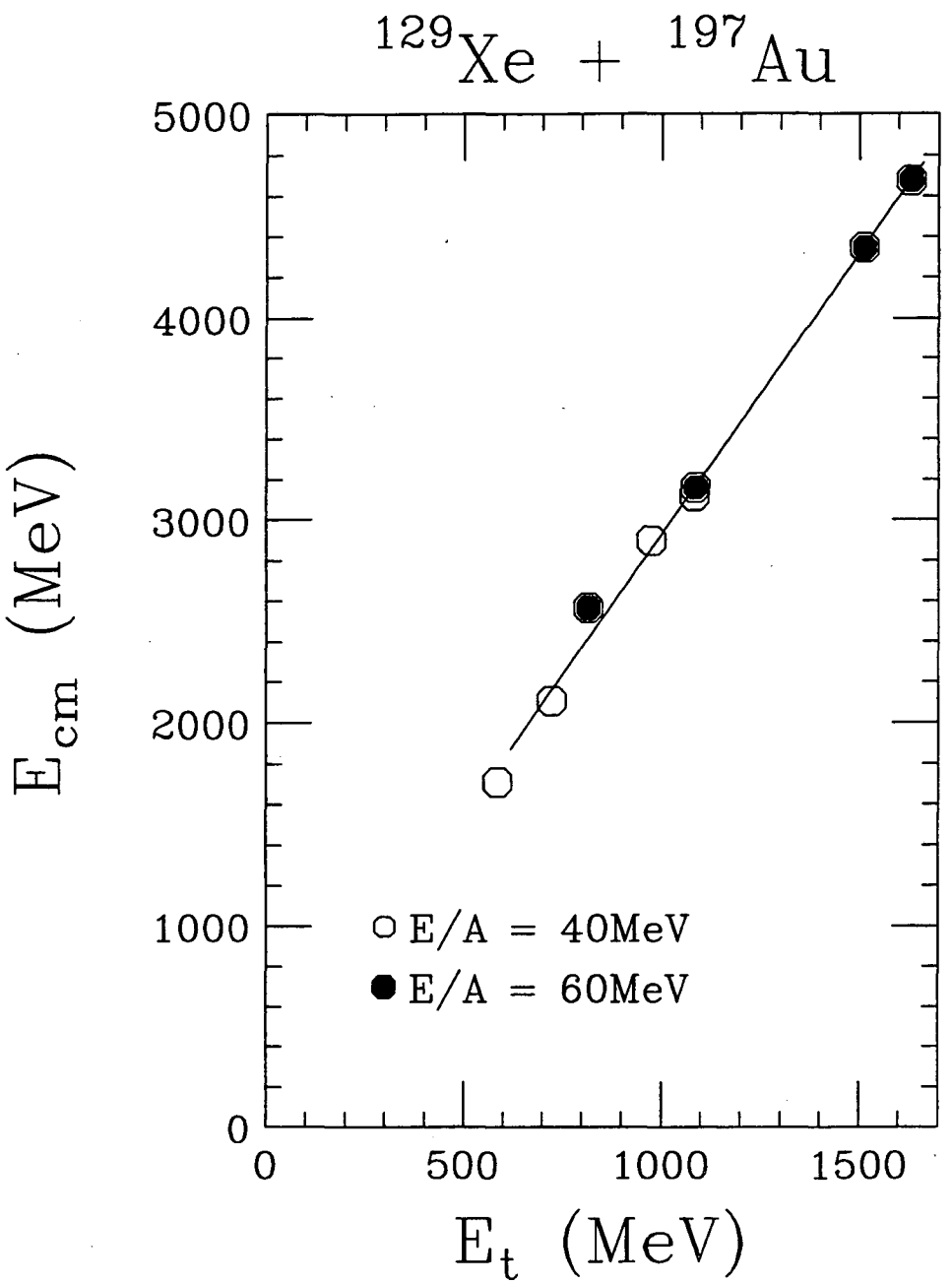

Figure 4.2 : The available energy in the center–of–mass frame E_{cm} as a function of the upper limit of E_t for the ^{129}Xe–induced reactions on four different targets (^{nat}Cu, ^{89}Y, ^{165}Ho, ^{197}Au) at bombarding energies of $E/A = 40$ MeV (open symbols) and 60 MeV (solid symbols). The line is a linear fit to the data.

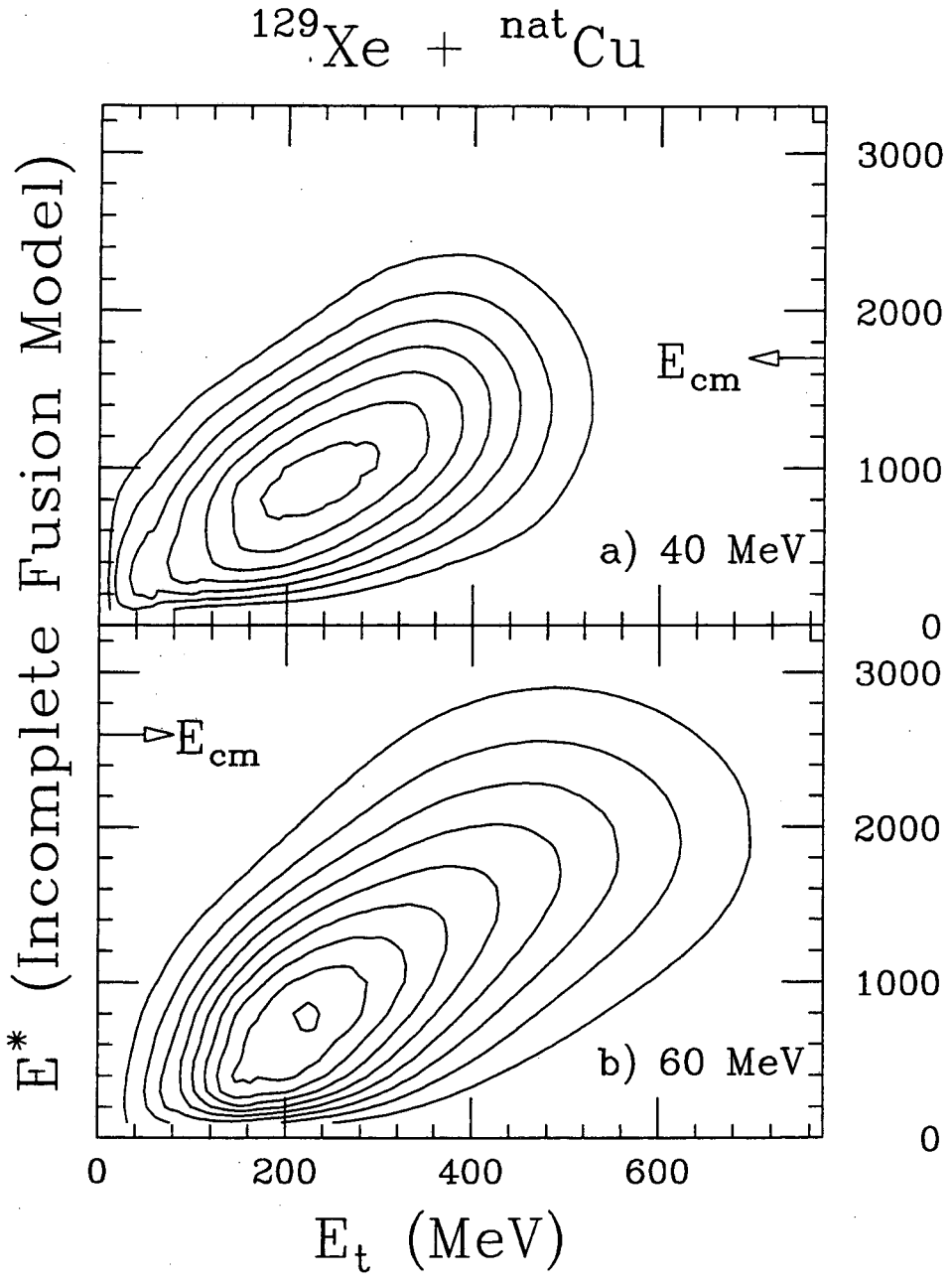

Figure 4.3 : Linear contour plot of the correlation between the transverse energy E_t and E^*, the approximate excitation energy from the incomplete fusion picture. The excitation energy for the reaction ^{129}Xe + ^{nat}Cu at E/A = 40 and 60 MeV is calculated from the parallel source velocity according to Equation 4.4.

excluding light charged particles in the source construction, contamination associated with the spectator nuclei may not be neglected. The target remnant nucleus is often a minor problem because it is usually not detected due to its slow speed. On the other hand, the fast massive projectile spectator is easily detected and severely contaminates the resulting source velocity. Since these contaminations are dominant at forward angles, their contributions to the transverse energy are significantly suppressed by the factor $sin^2\theta$.

4.2 Binomial Reducibility and Thermal Scaling of multi-fragment Emission Probability

The probability P_n of emitting n intermediate mass fragments (IMF: $3 \leq Z \leq 20$) was measured as a function of transverse energy E_t for the reaction ^{129}Xe + ^{197}Au at bombarding energies of $E/A = 40$ and 60 MeV. P_n is defined as:

$$P_n \equiv \frac{N(n)}{\sum N(n)}, \tag{4.5}$$

where $N(n)$ is the number of events with n IMFs. The excitation functions (P_n versus E_t) for both energies are plotted in Figure 4.4 from $n = 0 - 10$. At both bombarding energies, the value of n that corresponds to the most probable n–fold event at a given E_t increases with E_t. This suggests that the average fragment multiplicity increases smoothly and substantially with E_t.

An interesting result is obtained when the natural logarithm of the probability for n–fragment emission is plotted as a function of $1/\sqrt{E_t}$ in Figure 4.5. A linear dependence on $1/\sqrt{E_t}$ is observed for the 3-, 4-, 5- and 6–fold normalized probabilities. Since nuclear temperature T is proportional to $\sqrt{E^*}$ in the Fermi gas model, this observed linearity indicates a statistical energy dependence of the n–fragment

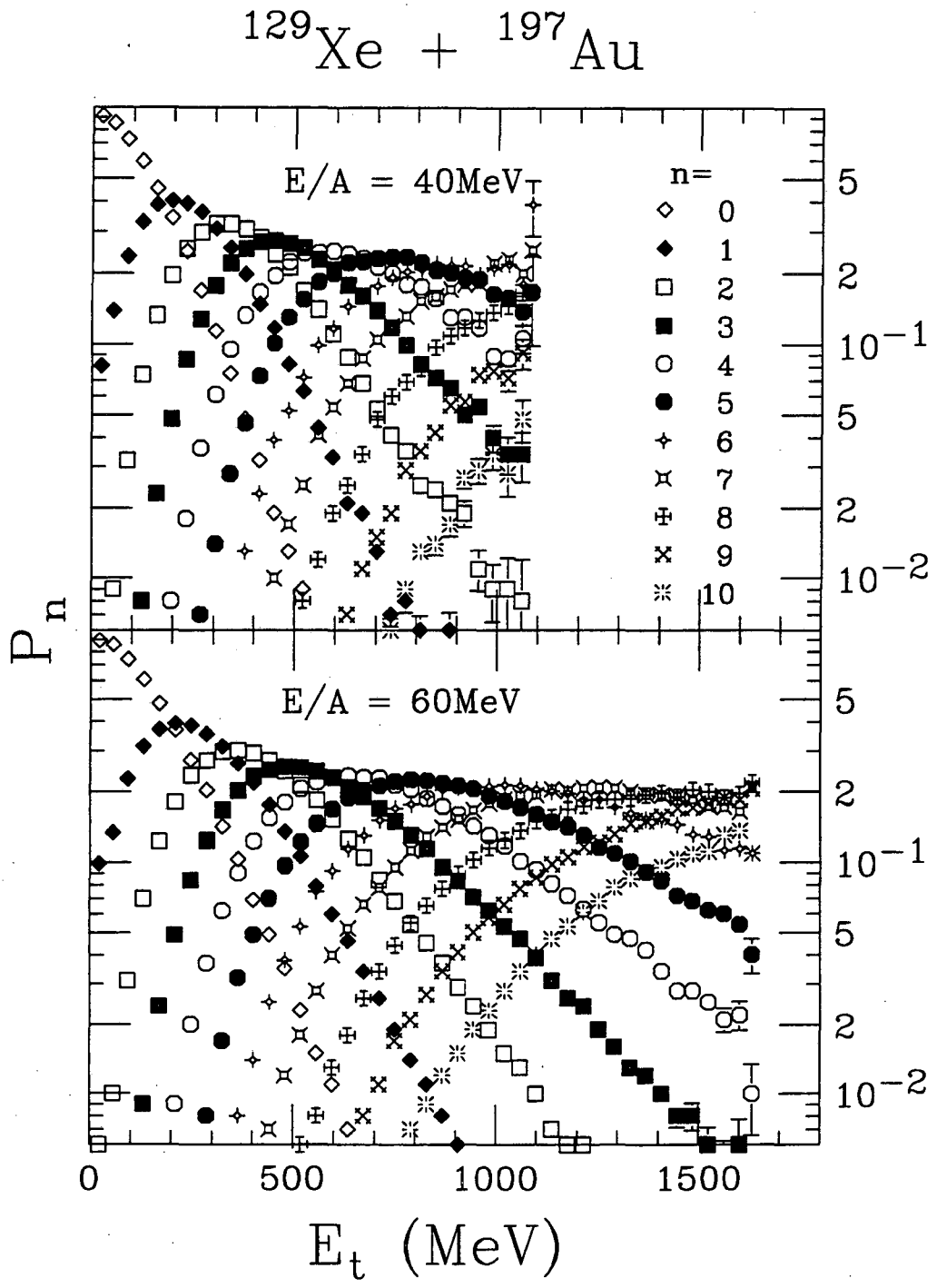

Figure 4.4 : The probability P_n to emit n intermediate mass fragments (IMF : $3 \leq Z \leq 20$) as a function of E_t for the reaction ^{129}Xe + ^{197}Au at bombarding energies of $E/A = 40$ MeV (top panel) and 60 MeV (bottom panel).

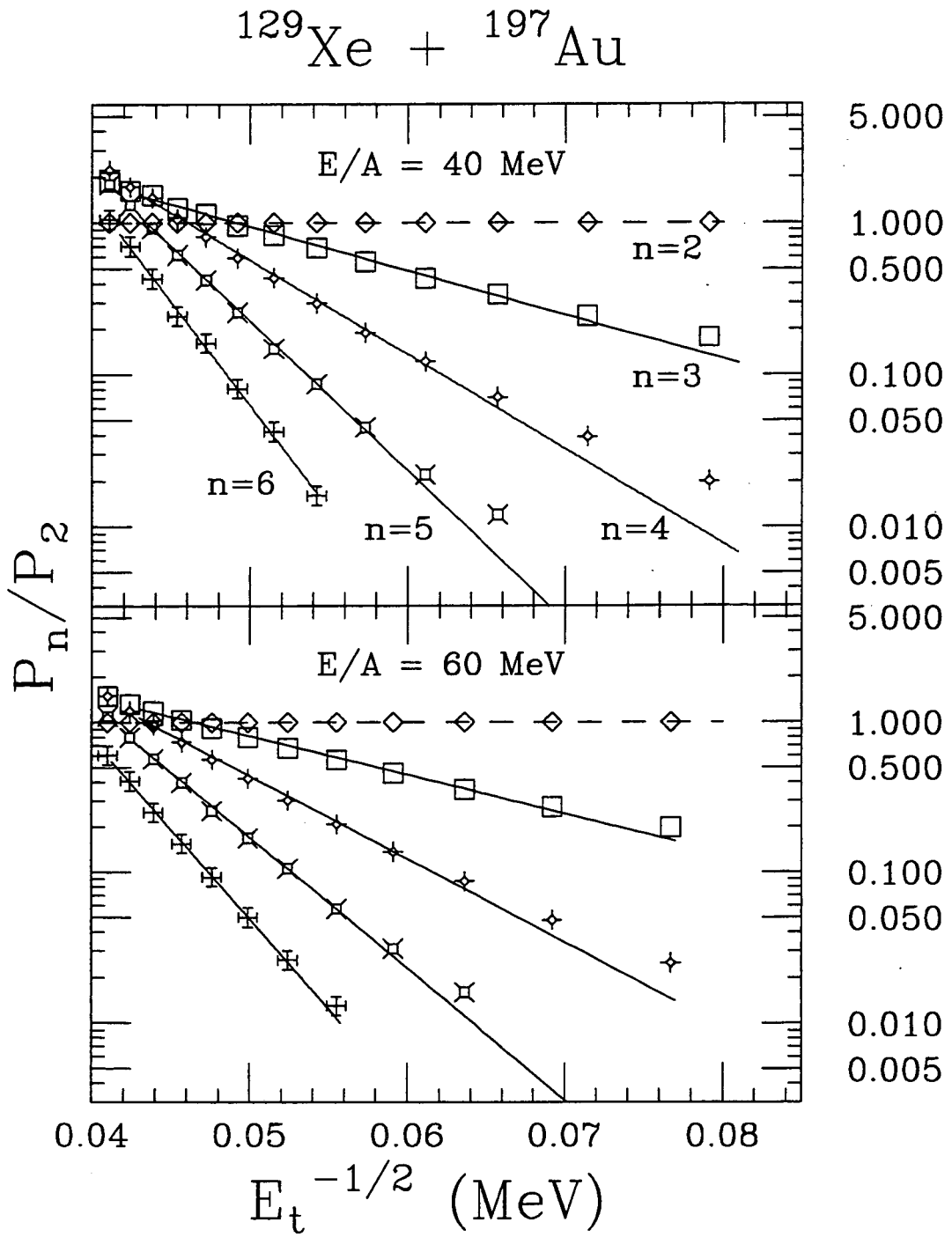

Figure 4.5 : The natural logarithm of the ratio of the 2, 3, 4, 5 and 6–fold to the 2–fold probability (symbols) as a function of $E_t^{-1/2}$ for the reaction ^{129}Xe + ^{197}Au at bombarding energies of E/A = 40 MeV (top panel) and 60 MeV (bottom panel). The lines are linear fits to the data.

emission probabilities under the assumption that $E_t \propto E^*$:

$$P_n(E_t) \propto e^{-\frac{B_n}{\sqrt{E_t}}} \propto e^{-\frac{B_n}{T}}. \tag{4.6}$$

Accordingly, the slopes in Figure 4.5 are proportional to the average n–fragment decay barriers B_n. Although the extracted slopes are not comparable with barriers since an absolute scale for the excitation energy is not yet available, the fact that they become steeper with increasing values of n further reinforces the above statistical interpretation. The barrier B_n can be considered as the "potential energy" of the n-fragment configuration in a prompt multifragmentation picture. The same energy dependence can also be derived for a sequential decay, in which the system undergoes successive binary decays with barriers $b_1, b_2, b_3, ..., b_n$. In this case, B_n is simply the sum of the one–fragment emission barriers, $B_n = b_1 + b_2 + b_3 + ... + b_n$ under the assumption that the temperature is nearly constant at all stages of emission. Therefore, this approach cannot conclude whether the statistical multifragment emission is sequential or simultaneous.

Another relevant question that remains unanswered is the fundamental issue of reducibility: can multifragmentation be reduced to a combination of independent emissions of fragments? More specifically, can the probability for the emission of n fragments be reduced to the emission probability of just one fragment? A system which emits "inert" fragments independently with constant probability p is a simple scenario that is consistent with this reducibility. The probability P_n^m of emitting n fragments in m independent tries is given by the binomial distribution:

$$P_n^m = \frac{m!}{n!(m-n)!} p^n (1-p)^{m-n}. \tag{4.7}$$

The average multiplicity is then

$$\langle n \rangle = mp, \tag{4.8}$$

and the corresponding variance is

$$\sigma^2 = \langle n \rangle (1 - p). \tag{4.9}$$

To verify whether the excitation functions (Figure 4.4) follow the above binomial distribution, the values of p and m have been extracted from the experimental values of the mean and variance:

$$m = \frac{\langle n \rangle}{1 - \frac{\sigma^2}{\langle n \rangle}} \tag{4.10}$$

and

$$p = 1 - \frac{\sigma^2}{\langle n \rangle}. \tag{4.11}$$

The extracted values of m and p are plotted as a function of transverse energy in Figure 4.6 for the reaction ^{129}Xe + ^{197}Au at both bombarding energies. These values of p and m are then used in the binomial distribution (Equation 4.7) to calculate the corresponding excitation functions. Figure 4.7 shows an excellent agreement between the experimental n–fragment emission probabilities (symbols) and the binomial calculations (curves) for values of n up to 10 at both bombarding energies. This extraordinary quantitative agreement between the calculations and the experimental data over the entire range of measured E_t confirms the binomiality of the probability P_n and its reducibility to an elementary binary decay probability p.

In a statistical decay, the probability p for the emission of a single fragment is connected with the corresponding partial decay width. The partial decay width associated with a given channel is approximated by

$$\Gamma = \hbar\omega_o e^{-B/T}, \tag{4.12}$$

where ω_o is a frequency characteristic of the channel under consideration, B is the barrier associated with the channel, and T is the temperature. For instance, in fission ω_o is the collective frequency of assault on the barrier ($\sim$ beta vibration frequency)

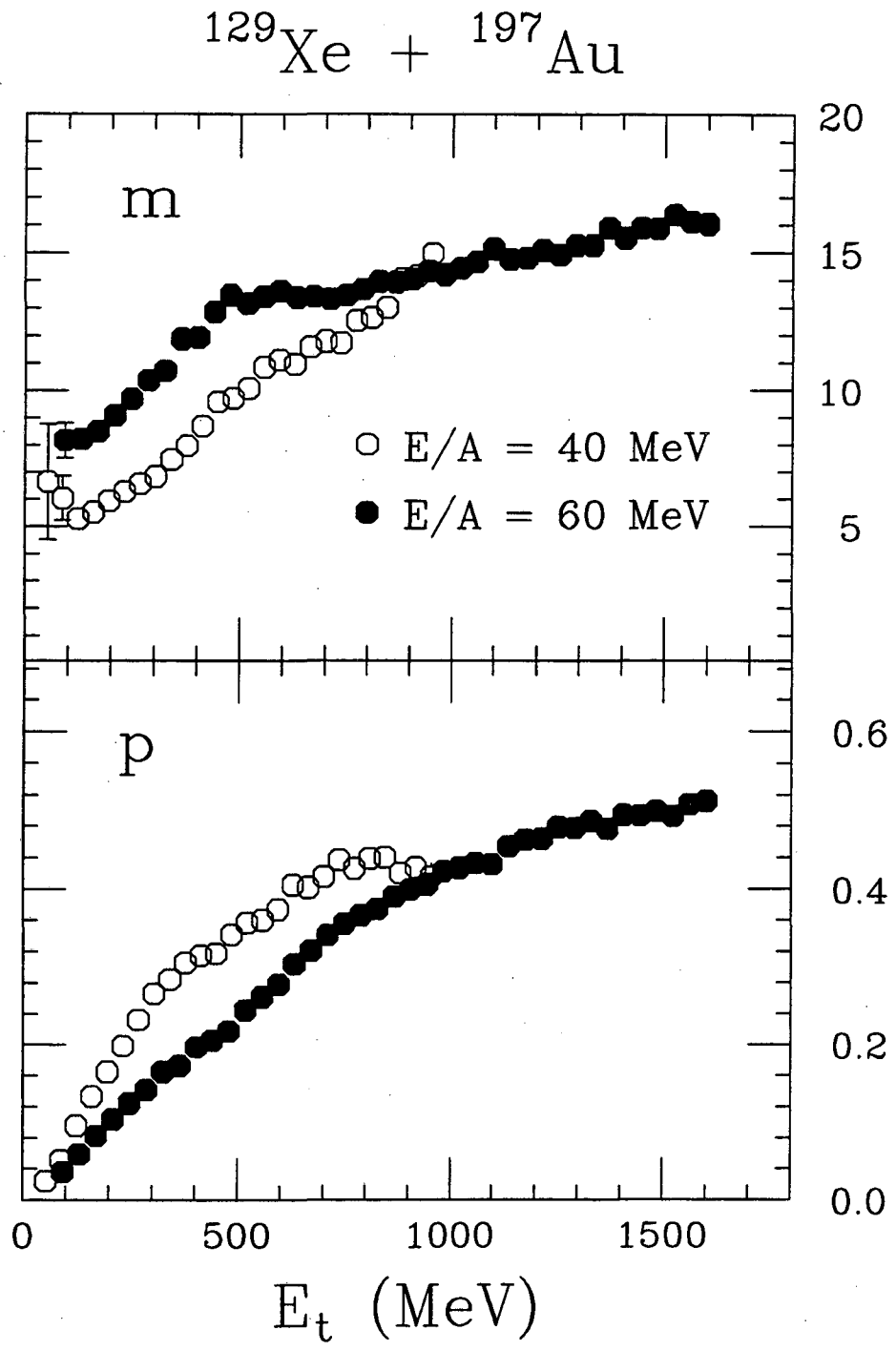

Figure 4.6 : The extracted values of $m = \frac{\langle n \rangle^2}{\langle n \rangle - \sigma^2}$ and $p = 1 - \frac{\sigma^2}{\langle n \rangle}$ as a function of E_t for the reaction ^{129}Xe + ^{197}Au at bombarding energies of $E/A = 40$ MeV (open symbols) and 60 MeV (solid symbols).

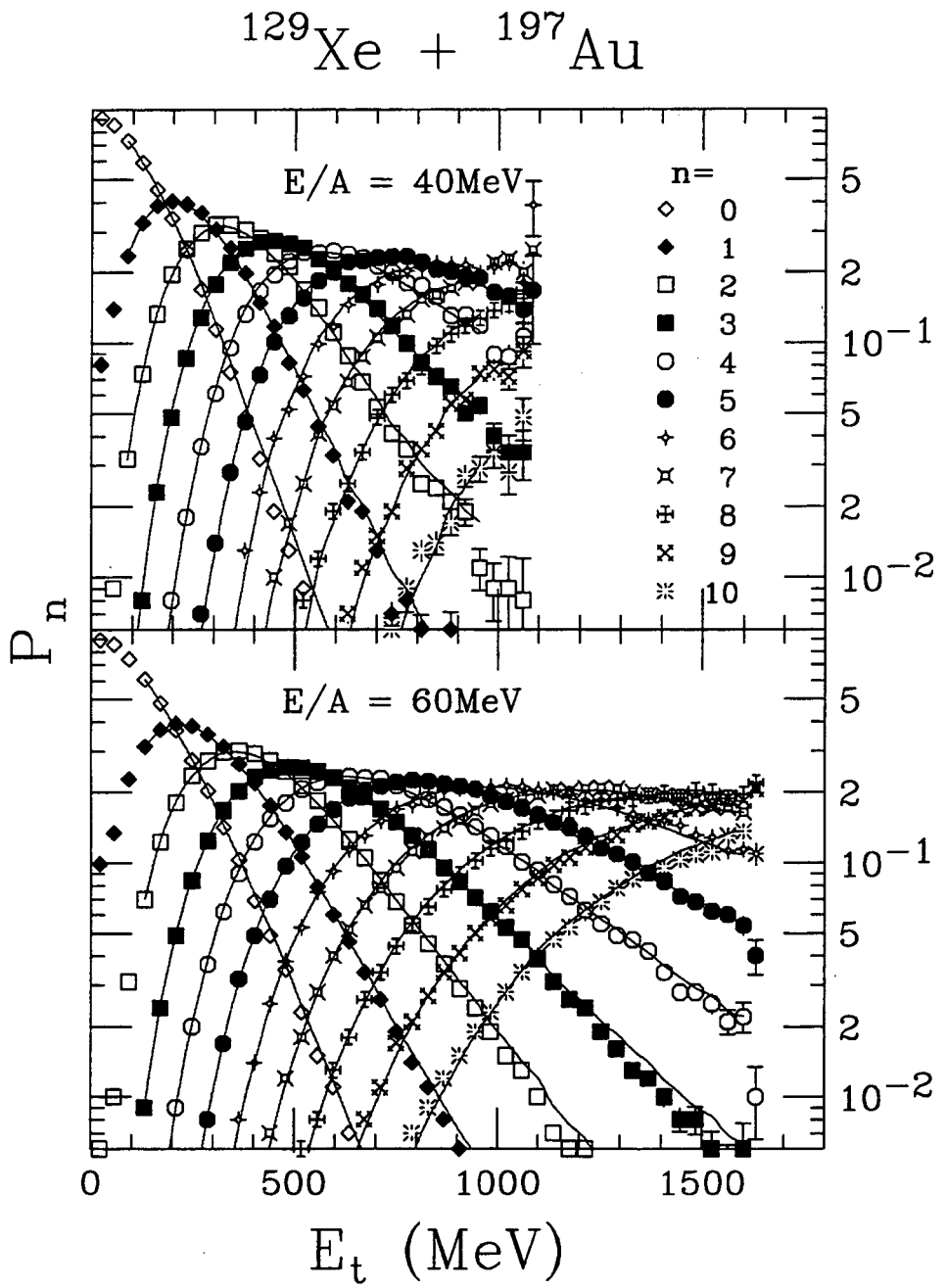

Figure 4.7 : A comparison between the experimental probability (symbols) and the calculated probability (solid lines) to emit n intermediate mass fragments as a function of E_t for the reaction ^{129}Xe + ^{197}Au at bombarding energies of $E/A = 40$ MeV (upper panel) and 60 MeV (bottom panel). For number of fragments $n = 0$–10, P_n is calculated assuming a binomial distribution (see Equation 4.7) with the values of p and m shown in Figure 4.6.

and B is the fission barrier. The elementary probability p for a binary decay to occur at any given "try" defined by the channel period $\tau_o = 1/\omega_o$ is:

$$p = \frac{\Gamma}{\hbar\omega_o} = e^{-B/T}. \tag{4.13}$$

This expected thermal nature is shown in Figure 4.6 where the extracted values of p increase rapidly as a function of E_t until they gradually saturate at values of 0.43 and 0.51 for $E/A = 40$ and 60 MeV respectively. To make the temperature dependence of this elementary binary decay probability more apparent, the natural logarithm of $1/p$ is plotted as a function of $1/\sqrt{E_t}$ in Figure 4.8 (Arrhenius plot). At both bombarding energies, the values of $1/p$ (symbols) collapse remarkably well onto the solid lines that are linear fits to the data. The linearity of this plot strongly indicates a "thermal" nature of p of the form $e^{-B/T}$ over the entire range of measured E_t. In addition, the difference in the extracted slopes for the two bombarding energies suggests an energy dependent proportionality constant between E_t and E^*.

Concerning the linearity of the above Arrhenius plots, our eyes may be mostly impressed by the tail of the data points at low transverse energy, but the data points at high transverse energy agree with the fit very well as shown in Figure 4.9. In fact, the fitting procedure unlike our eyes is dominated by the large amount of data available at high transverse energy. The good agreement between the fits and the data shown in the above Arrhenius plots clearly demonstrates the linearity over the entire measured E_t range.

The value of p can also be extracted "differentially" from any two consecutive excitation functions P_n, P_{n+1} as given below:

$$\frac{1}{p} = \frac{P_n^m}{P_{n+1}^m}\frac{m-n}{n+1} + 1. \tag{4.14}$$

The values of p obtained "differentially" using Equation 4.14 are compared with those calculated "integrally" from $\langle n \rangle$ and σ^2 of the IMF multiplicity distributions. Figure

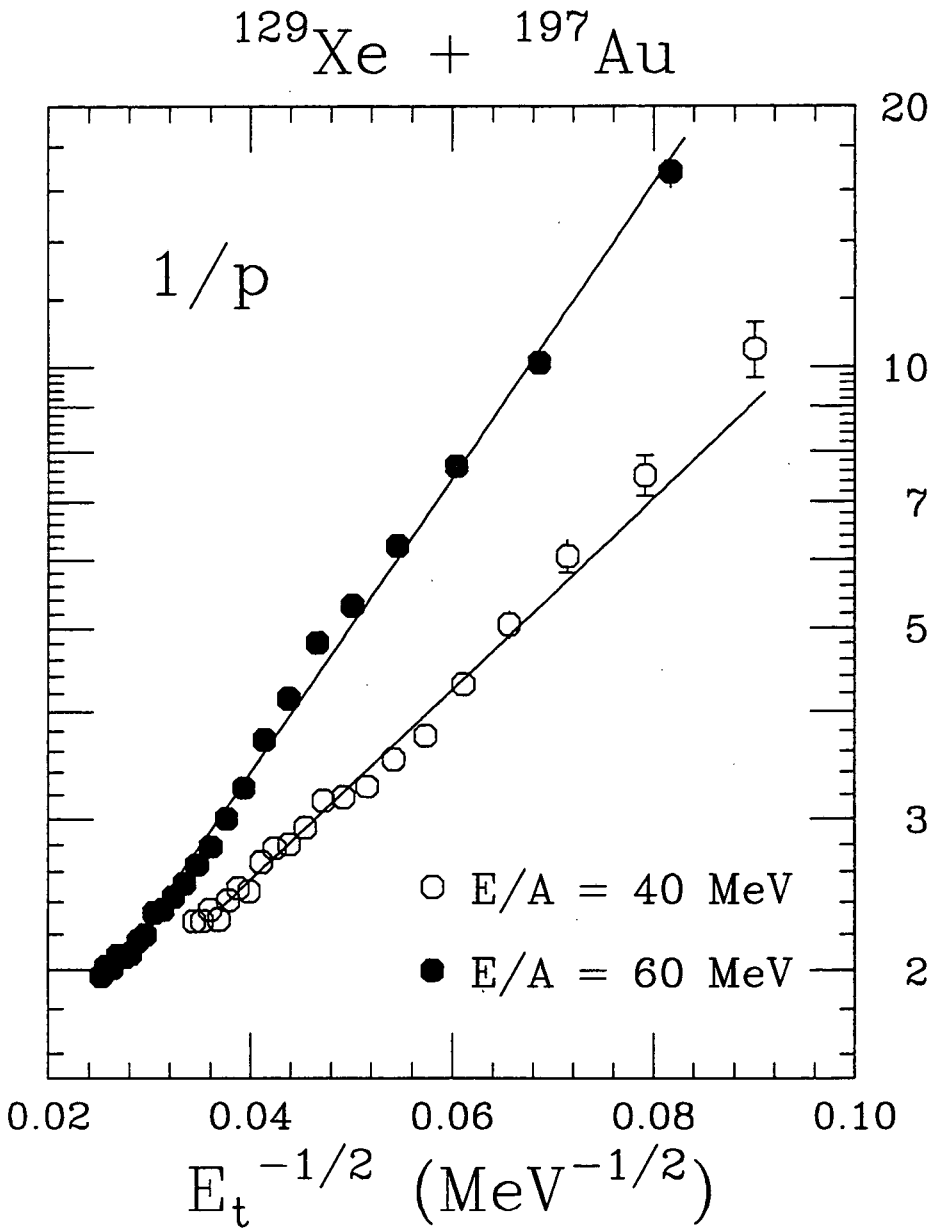

Figure 4.8 : The reciprocal of the binary decay probability $1/p$ as a function of $E_t^{-1/2}$ (Arrhenius plot) for the reaction ^{129}Xe + ^{197}Au at bombarding energies of E/A = 40 MeV (open symbols) and 60 MeV (solid symbols). The solid lines are linear fits to the data.

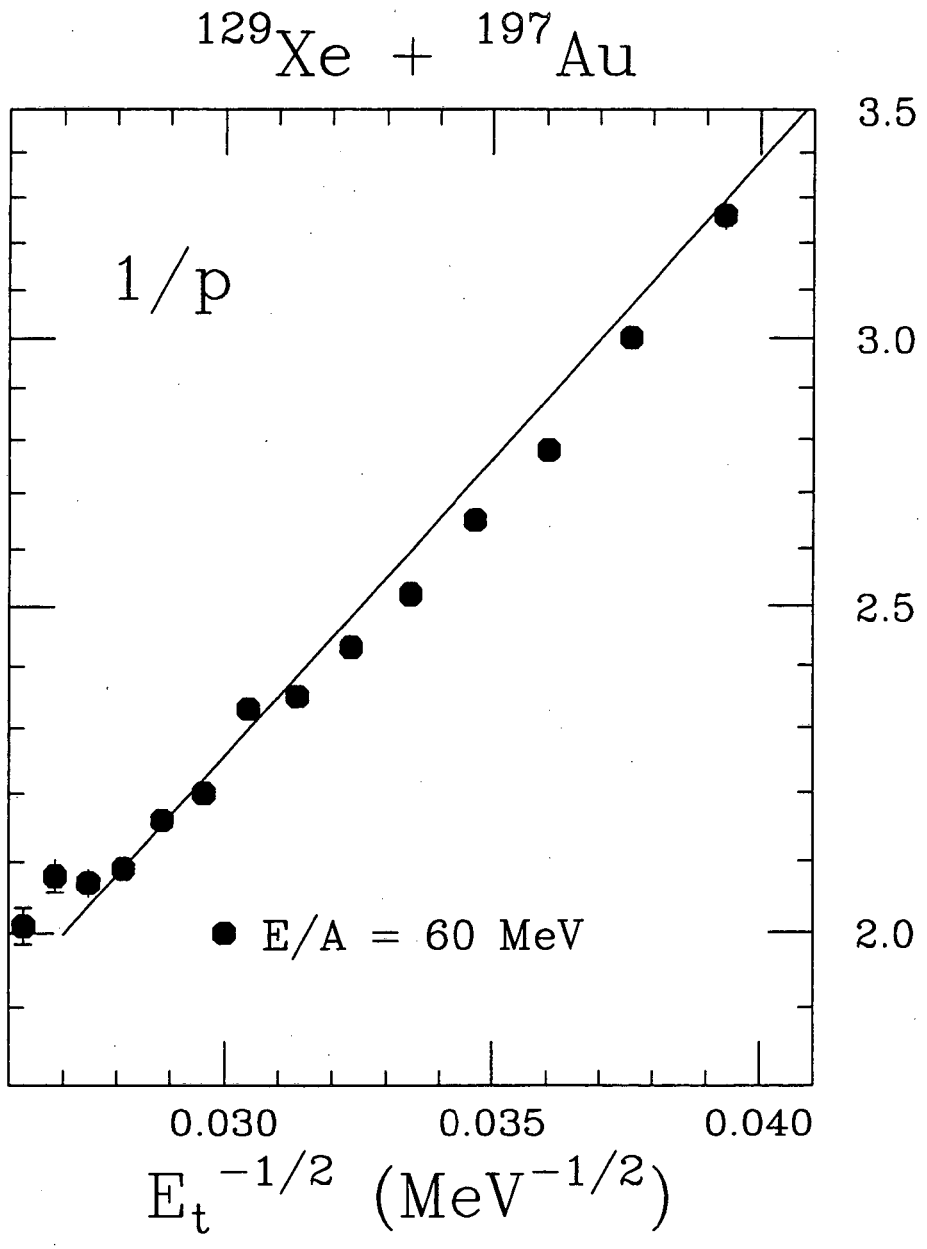

Figure 4.9 : The extracted values of $1/p$ as a function of $E_t^{-1/2}$ for the reaction ^{129}Xe + ^{197}Au at bombarding energy of $E/A = 40$ MeV. The data with E_t less than 700 MeV are not shown. The solid line is a linear fit to the data shown in Figure 4.8.

4.10 shows the differentially determined values of p up to $n = 4$ collapse onto the fits (lines) of Figure 4.8 for bombarding energies at $E/A = 40$ and 60 MeV. For $n > 4$ (data not shown), good agreement is observed at high transverse energy ($E_t > 400$ MeV) although scattering about the fitted line occurs at low transverse energy due to poor statistics.

These two methods are not independent since the value of m needed for the "differential" derivation (Equation 4.14) must first be calculated from $\langle n \rangle$ and σ^2 using Equation 4.10. However, there is an independent method (neither $\langle n \rangle$ nor σ^2 is used) for the extraction of p and m from any three consecutive excitation functions P_n, P_{n+1}, and P_{n+2}. In this approach, an equation similar to (4.14) can be constructed from the excitation functions P_{n+1} and P_{n+2}:

$$\frac{1}{p} = \frac{P_{n+1}^m}{P_{n+2}^m} \frac{m-n-1}{n+2} + 1. \tag{4.15}$$

By solving the two simultaneous equations (4.14 and 4.15), solutions for the two variables m and p are obtained:

$$m = n - \frac{(n+1)(P_{n+1})^2}{(n+2)P_n P_{n+2} - (n+1)(P_{n+1})^2} \tag{4.16}$$

and

$$\frac{1}{p} = \frac{P_n P_{n+1}}{(n+1)(P_{n+1})^2 - (n+2)P_n P_{n+2}}. \tag{4.17}$$

To minimize the statistical uncertainty associated with this approach, the value of n is taken to be the most probable n–fold event at a given transverse energy. Figure 4.11 shows that the extracted values of p (symbols) for both bombarding energies at $E/A = 40$ and 60 MeV agree reasonably well with those obtained integrally (line) over the entire range of the measured E_t.

The observed agreement between three different methods for the extraction of p confirms: 1) The probability P_n of producing n fragments in a multifragmentation

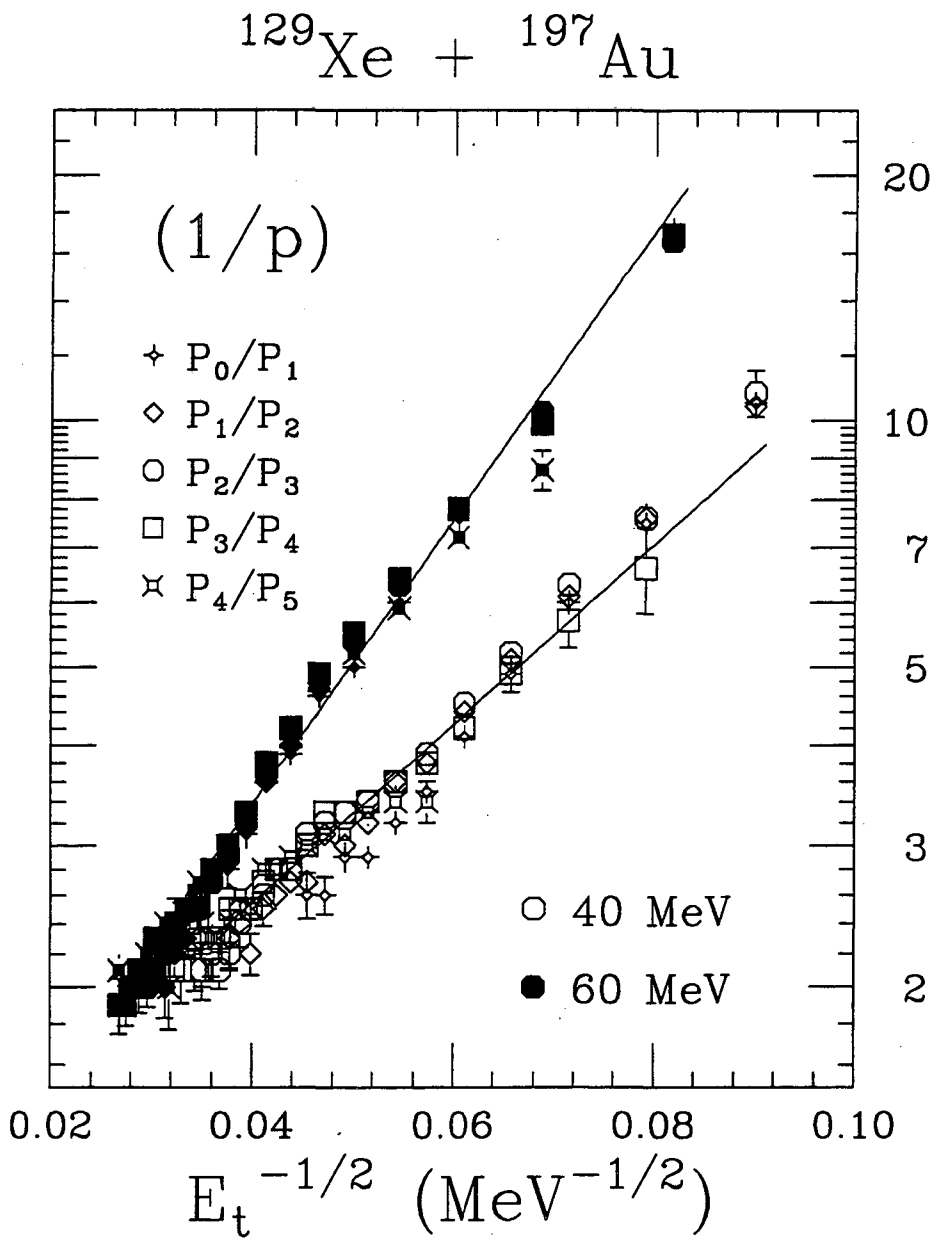

Figure 4.10 : The values of $1/p$ extracted "differentially" using Equation 4.14 as a function of $E_t^{-1/2}$ for the reaction ^{129}Xe + ^{197}Au at bombarding energies of E/A = 40 MeV (open symbols) and 60 MeV (solid symbols). The different symbols represent the probabilities p extracted from the indicated values of P_n, and the solid lines are linear fits to the data shown in Figure 4.8.

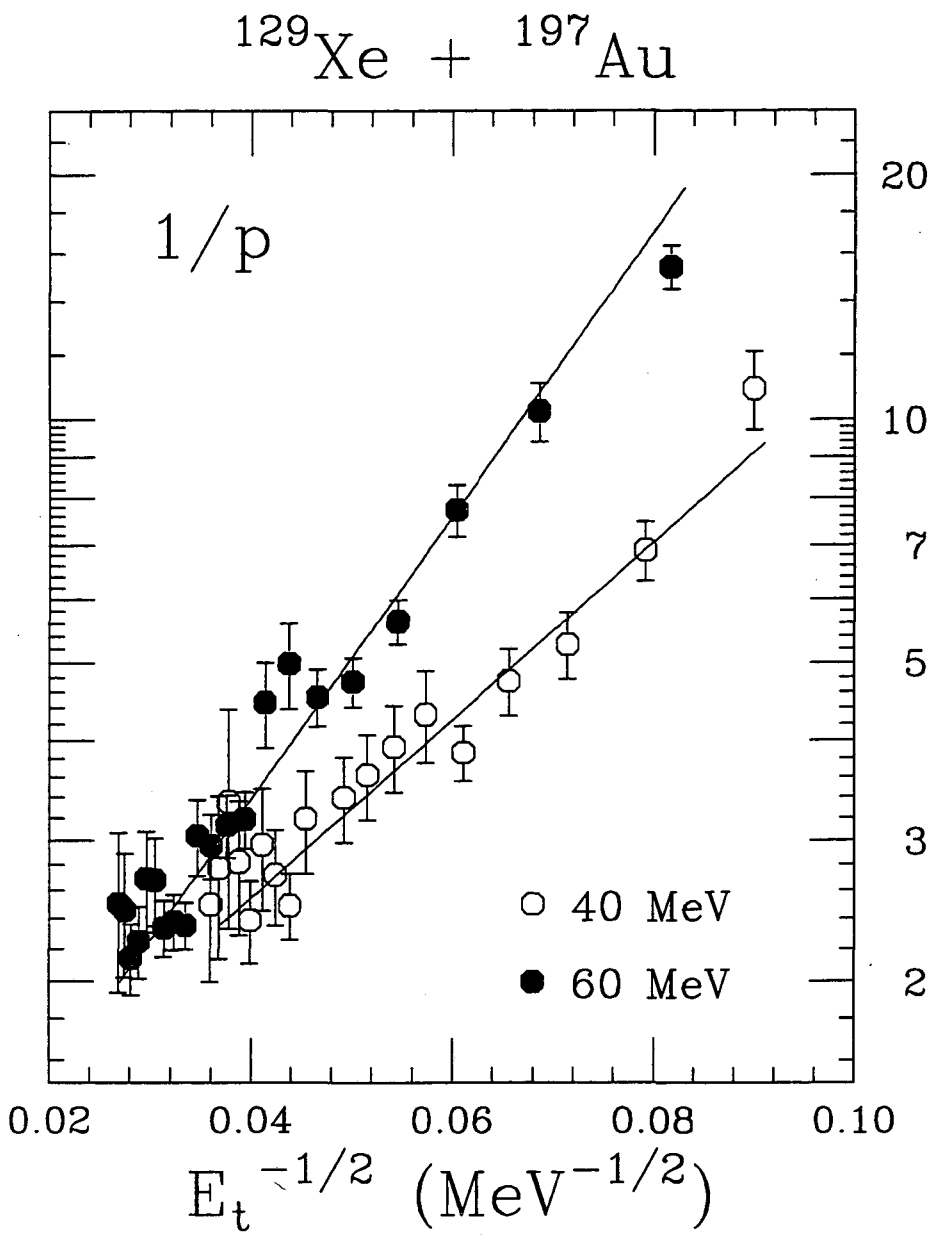

Figure 4.11 : The values of $1/p$ extracted "independently" using Equation 4.17 as a function of $E_t^{-1/2}$ for the reaction ^{129}Xe + ^{197}Au at bombarding energies of $E/A =$ 40 MeV (open symbols) and 60 MeV (solid symbols). The solid lines are linear fits to the data shown in Figure 4.8.

event can be experimentally reduced to the probability p of emitting one fragment according to the binomial distribution. 2) The probability p so obtained has a "thermal" energy dependence with the assumption that the excitation energy is proportional to the transverse energy.

A natural interpretation of the binomiality and thus the reducibility is a sequential decay with constant probability at all stages. However, the binomiality may not necessarily be consistent with more general sequential descriptions of multifragmentation. For example, if each emitted fragment is no longer assumed to be inert, it may in turn decay into two fragments and the subsequent decay chain can be very complicated. The resulting fragment multiplicity distribution from such a sequential model, associated with different decay branching, may be drastically nonbinomial. On the other hand, a non–sequential description may possibly be consistent with the binomiality. A simple example is a chain consists of $m+1$ pre–fragments linked by m bonds. If p is interpreted as the bond–breaking probability, one obtains a binomial distribution for the probability that n links are broken (Equation 4.7). Obviously, this chain model has no time aspect to it, and its relevance to multifragmentation is rather unclear. Nevertheless, it stresses again that the essence of the observed binomiality is the fundamental reducibility of the multifragmentation probability to a binary break–up probability.

4.3 General Interpretation of Reducibility

The observed reducibility implies that multifragmentation itself is empirically reducible to a combination of nearly independent fragment emissions. In other words, all the physics contained in P_n is reducible to the physical content of p. The thermal nature of this elementary binary decay probability ($p = e^{-B/T}$) has already

been demonstrated by the observed linear dependence in the Arrhenius plots. The more directly interpretable physical parameter contained in this analysis is the binary decay barrier B which is proportional to the slope of the Arrhenius plot. One may wonder why a single barrier suffices, since mass asymmetries with many different barriers may be present. Let us consider a barrier distribution as a function of mass asymmetry x of the form $B = B_o + ax^n$, where B_o is the lowest barrier in the range considered. Then,

$$p = \frac{\Gamma}{\hbar\omega_o} = \int e^{-B_o/T} e^{-ax^n/T} dx \approx \left(\frac{T}{a}\right)^{1/n} e^{-B_o/T}. \tag{4.18}$$

The simple form of Equation 4.13 is retained with a small and renormalizable pre–exponential modification. The average value of p essentially corresponds to the emission of the lightest fragment ($Z_{threshold}$) with the lowest barrier in the range considered. Accordingly, the slopes of the above Arrhenius plots (Figure 4.8) are proportional to the barrier for Li emission, the lowest barrier in the range of fragments considered.

In order to explore the dependence of the barrier upon $Z_{threshold}$, the same analysis was performed by progressively increasing the values of $Z_{threshold}$. The excitation functions and their corresponding Arrhenius plots with different values of $Z_{threshold}$ (3 to 7) are shown in Figure 4.12 and 4.13 for the reaction ^{129}Xe + ^{197}Au at bombarding energies of $E/A = 40$ MeV and 60 MeV respectively. A remarkable result is that these excitation functions though dramatically changed, retain their binomial reducibility. More specifically, the solid curves, which are binomial calculations of P_n using the values of p and m extracted from the mean and variance of the fragment multiplicity distributions, fit the corresponding data (symbols) very well for all three values of $Z_{threshold}$ at both bombarding energies.

The resulting Arrhenius plots associated with different values of $Z_{threshold}$ are also shown to be linear in Figure 4.12 and 4.13. The slope, which is proportional

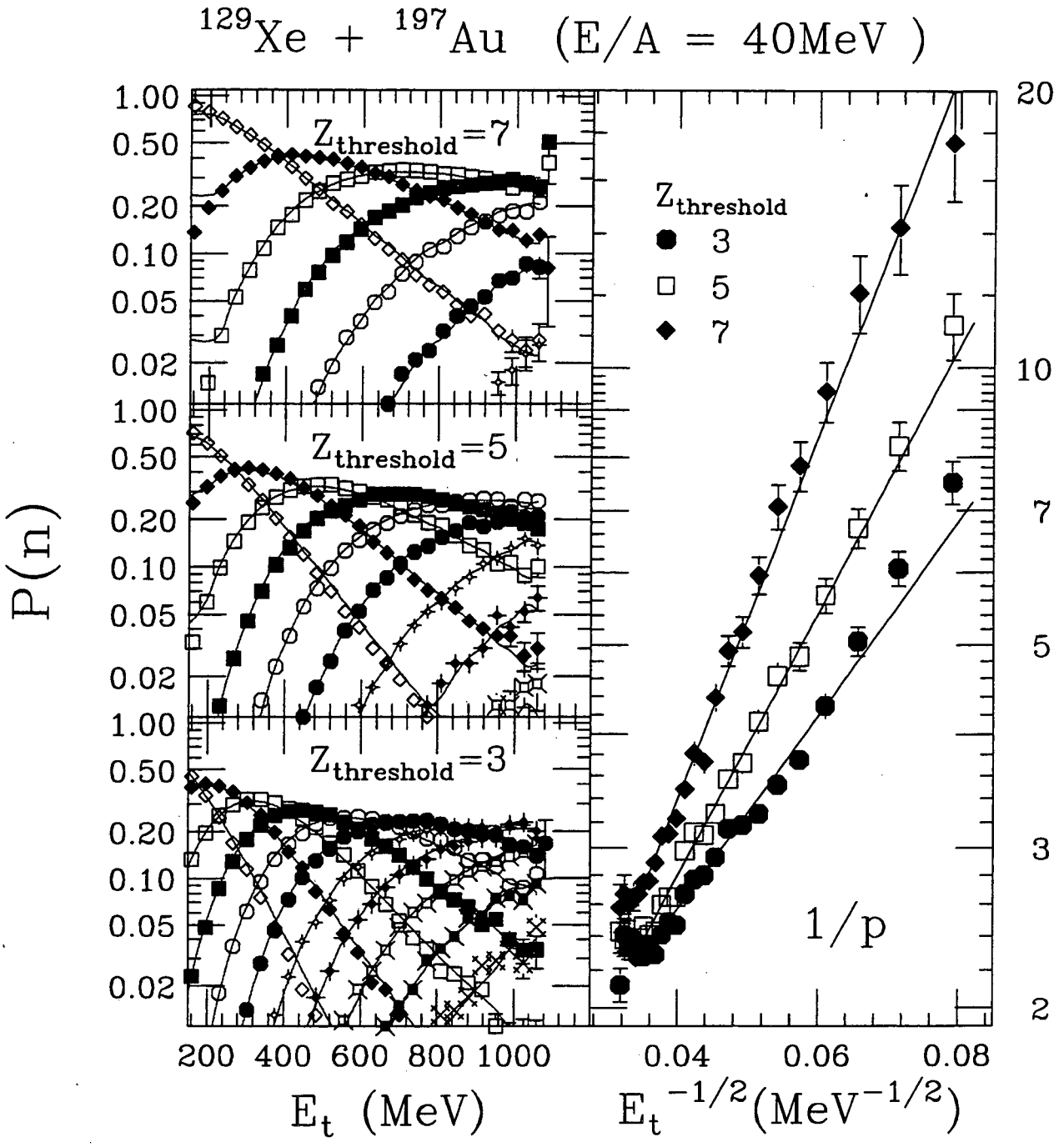

Figure 4.12 : (left column) The probability P_n for emitting n IMFs as a function of E_t for the reaction ^{129}Xe + ^{197}Au at E/A = 40 MeV with different values of the lower threshold in the definition of IMF: $Z_{threshold}$ = 3 (bottom panel), $Z_{threshold}$ = 5 (middle panel) and $Z_{threshold}$ = 7 (top panel). (right column) The corresponding values of $1/p$ as a function of $E_t^{-1/2}$. The solid lines are linear fits to the data.

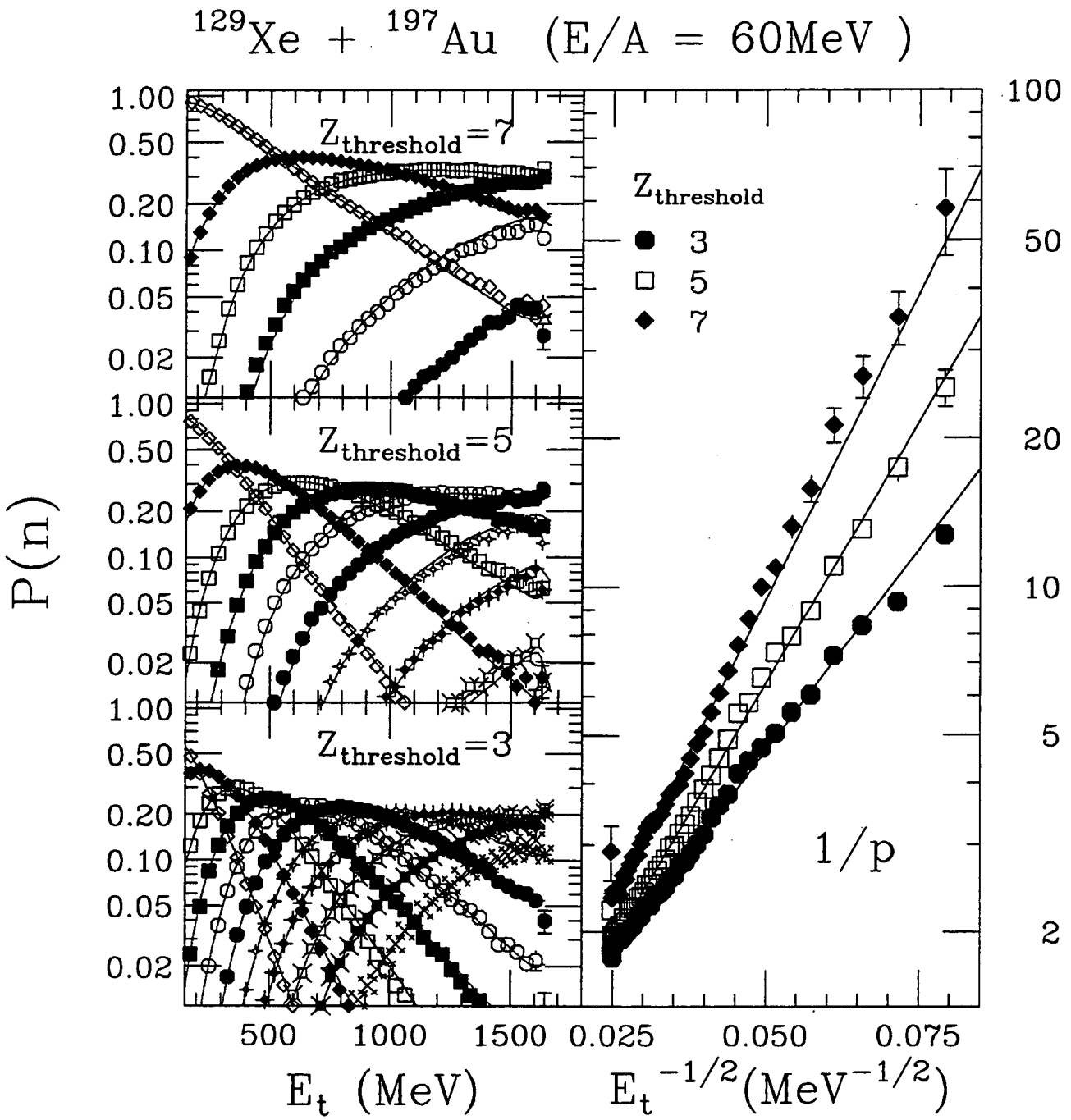

Figure 4.13 : (left column) The probability P_n for emitting n IMFs as a function of E_t for the reaction ^{129}Xe + ^{197}Au at E/A = 60 MeV with different values of the lower threshold in the definition of IMF: $Z_{threshold}$ = 3 (bottom panel), $Z_{threshold}$ = 5 (middle panel) and $Z_{threshold}$ = 7 (top panel). (right column) The corresponding values of $1/p$ as a function of $E_t^{-1/2}$. The solid lines are linear fits to the data.

to the barrier for emitting a fragment $Z_{threshold}$, becomes progressively steeper with increasing values of $Z_{threshold}$. Since the decay barrier, dominated by the Coulomb interaction, is proportional to the atomic number of the emitted fragment, the observed $Z_{threshold}$ dependence suggests that the decay is truly dominated by the lightest fragment. However, the units in which these slopes or barriers are measured are not clear since a quantitative relationship between the excitation energy and the measured transverse energy is not yet available. Nonetheless, the sensitivity of these slopes to $Z_{threshold}$ is consistent with the Z dependence of the emission barriers $B(Z)$, and this is a powerful signal for the physical meaning of p.

The reducibility of the n–fragment emission probability to an elementary binary decay probability implies that one can derive the probability of emitting n fragments solely from the probability of emitting one. Hence multifragmentation does not exist as an independent process. The thermal behavior of p further shows the statistical nature of the emission, and the slope of the Arrhenius plot provides information for the decay barrier of relevant channels. These experimental observations are very important because they are direct findings that do not rely on any theory or assumption for the interpretation, but rely only on plotting the experimental data in a particularly revealing way.

4.4 Sequential Interpretation of p and m

In section 4.2, sequential decay with constant probability p has been shown as a possible interpretation for the binomial nature and thus the reducibility of the multifragment emission probability. This specific sequential decay is a rather simplified description of multifragmentation, since the emission probability is assumed to remain unchanged at all stages, and the emitted fragments are assumed to be inert

(they do not generate additional fragments or disappear). It will be shown in this section that the emission probability p can be translated into the mean time separation between fragments in this framework of sequential decay. The physical significance of the other binomial parameter m is also explored.

In a statistical decay, the lifetime τ is related to the total decay width Γ_{tot} by the uncertainty principle $\tau = \hbar/\Gamma_{tot}$. In the case of a compound nucleus, the total decay width is the sum of the widths of all channels, and the lifetime is calculated accordingly. This lifetime defines the survival of the initial unmodified compound nucleus. For sequential multifragmentation, only the decay width and lifetime for binary fragment formation need be considered, while the abundant light particle decay can be treated as a background that progressively decreases the temperature and possibly the barrier.

The corresponding time associated with binary fragment decay derived from the uncertainty principle is

$$\tau = \frac{\hbar}{\Gamma} = \frac{\hbar}{\hbar w_o e^{-B/T}} = \frac{1}{w_o} e^{B/T} = \tau_o e^{B/T}. \tag{4.19}$$

This exponential dependence shows that the decay lifetime can be calculated from the elementary binary probability,

$$\frac{\tau}{\tau_o} = e^{B/T} = \frac{1}{p}. \tag{4.20}$$

The above equation shows that the decay lifetime is dramatically affected even by moderate changes in temperature. For a binary fission–like decay with a barrier of approximately 20 MeV, a change in temperature from 2 to 5 MeV decreases the lifetime by a factor of 400 and increases the binary decay probability accordingly. Furthermore, as the temperature becomes much larger than the barrier, the binary decay probability approaches unity and the lifetime approaches the channel period τ_o.

In a sequential description of multifragmentation, the decay lifetime τ also reflects the time scale associated with subsequent fragment emission. Consequently, one can infer the mean time separation between fragments from the n–fragment emission probability through its reducibility to the binary decay probability. The observed linearity of the Arrhenius plot thus says that the emission time scale decreases exponentially with $1/\sqrt{E_t}$ even though the channel period τ_o can not be determined. In the framework of sequential decay, this contraction of emission time with increasing excitation energy is a natural consequence of the thermal dependence of $1/p$ (Equation 4.20). In other words, short emission time scales result from large thermal probabilities and vice versa. Hence, a drastic decrease of the emission time with increasing excitation energy may not necessarily imply a transition from sequential to "prompt" multifragmentation. If this is indeed the case, a separate multifragmentation theory may not be necessary, since this process is reducible to a sequence of binary decays that can be described in a standard way. In particular, the structure of the n–fragment probability remains "sequential" and the corresponding emission time follows directly from the thermal dependence of the binary decay probability p.

The other parameter associated with a binomial distribution is m, the number of "tries" successful plus unsuccessful that a system has available in order to emit a fragment with fixed probability p in a sequential description. In this context, the product $m\tau_o$ is the overall time available for fragment emission, and the parameter m can be interpreted as the total emission time measured in units of the channel period τ_o.

In section 4.3, the binomial reducibility and the $Z_{threshold}$ dependence of the decay barriers have been demonstrated for various values of $Z_{threshold}$. The effect of raising $Z_{threshold}$ on the extraction of m is studied in this section. In Figure 4.14, the extracted values of m are plotted as a function of E_t for various values of $Z_{threshold}$

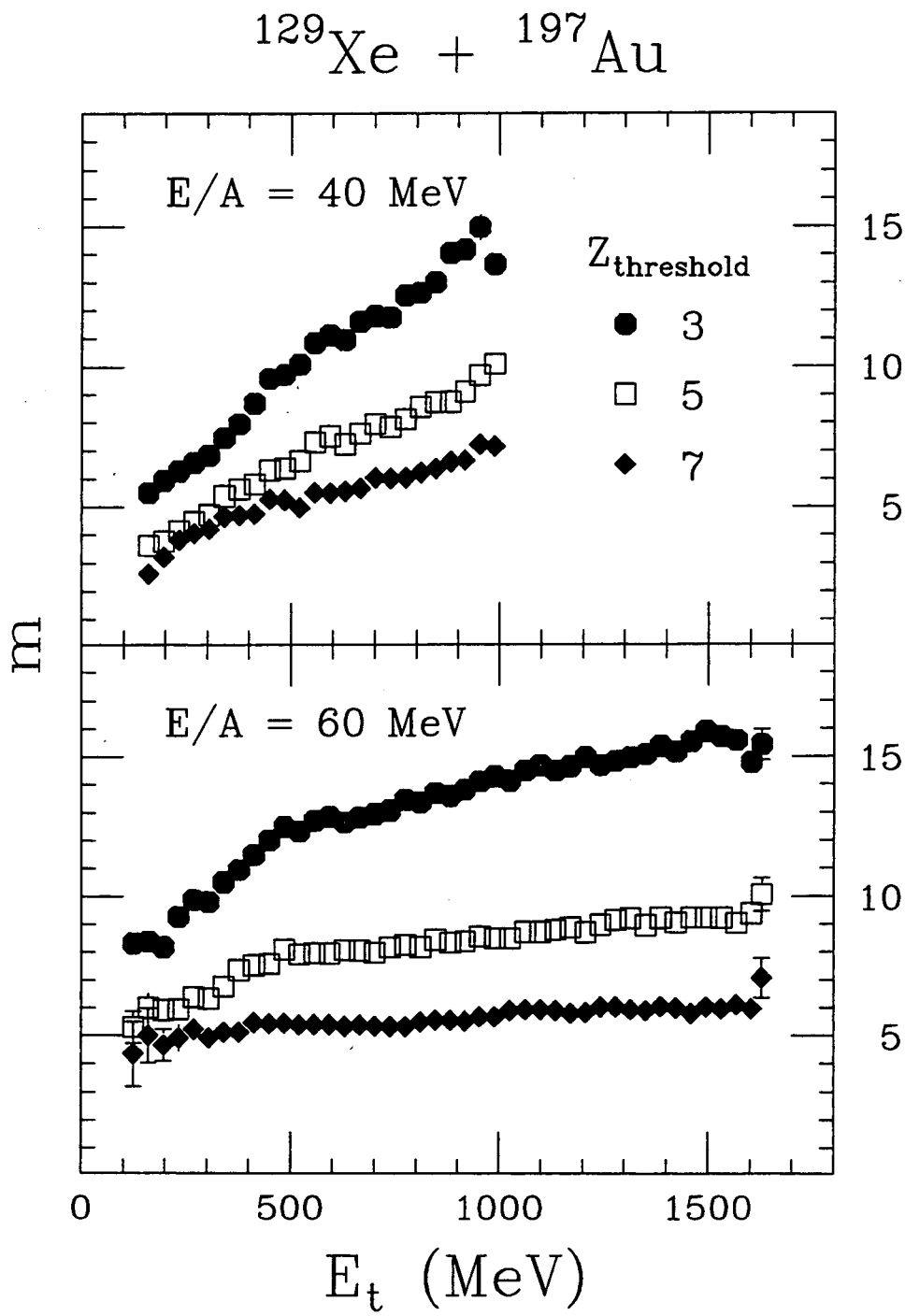

Figure 4.14 : The extracted values of m as a function of E_t for the reaction ^{129}Xe + ^{197}Au at bombarding energies of $E/A = 40$ MeV (top panel) and 60 MeV (bottom panel). The different symbols represent values of m extracted with different values of $Z_{threshold}$ (3, 5 and 7).

for the reaction ^{129}Xe + ^{197}Au at bombarding energies of E/A = 40 & 60 MeV. A strong dependence of m on this lower threshold is observed, with m decreasing dramatically with increasing $Z_{threshold}$. Let us consider the following two explanations that are consistent with this observed $Z_{threshold}$ dependence. The first is that the channel period τ_o is constant and the overall emission time $m\tau_o \propto m$ decreases with increasing $Z_{threshold}$. The second is that the overall time $m\tau_o$ for multifragmentation is constant but the channel period τ_o increases and thus m decreases accordingly with the mass of the emitted fragment. The second explanation is more reasonable since the dynamical frequency of the channel w_o is expected to have a mass dependence through the restoring force. If the simple model of the particle in a box is assumed, the period τ_o is proportional to the mass, and the overall emission time $m\tau_o$ should be proportional to the value of $mZ_{threshold}$. When the quantity $mZ_{threshold}$ is plotted in Figure 4.15, the three different curves from Figure 4.14 collapse onto a nearly universal curve, consistent with the interpretation that the overall emission time is constant. This observed $Z_{threshold}$ dependence on the extraction of m offers a glimpse of a possible functional form for the dynamical period τ_o even though the absolute scale is still not determined.

4.5 Auto–Correlation Effects

In the above excitation function analysis, the transverse energy ($E_t = \sum E_i$ $sin^2\theta_i$, where E_i and θ_i are the kinetic energy and the laboratory angle of each fragment respectively) is used as a measure of the excitation energy E^*. However, there may not be a one–to–one correspondence between E^* and E_t. Indeed, a distribution of E^* can be constructed from events of a fixed value of E_t and vice versa. Consequently, event–to–event fluctuations become inevitable when events are sorted by E_t,

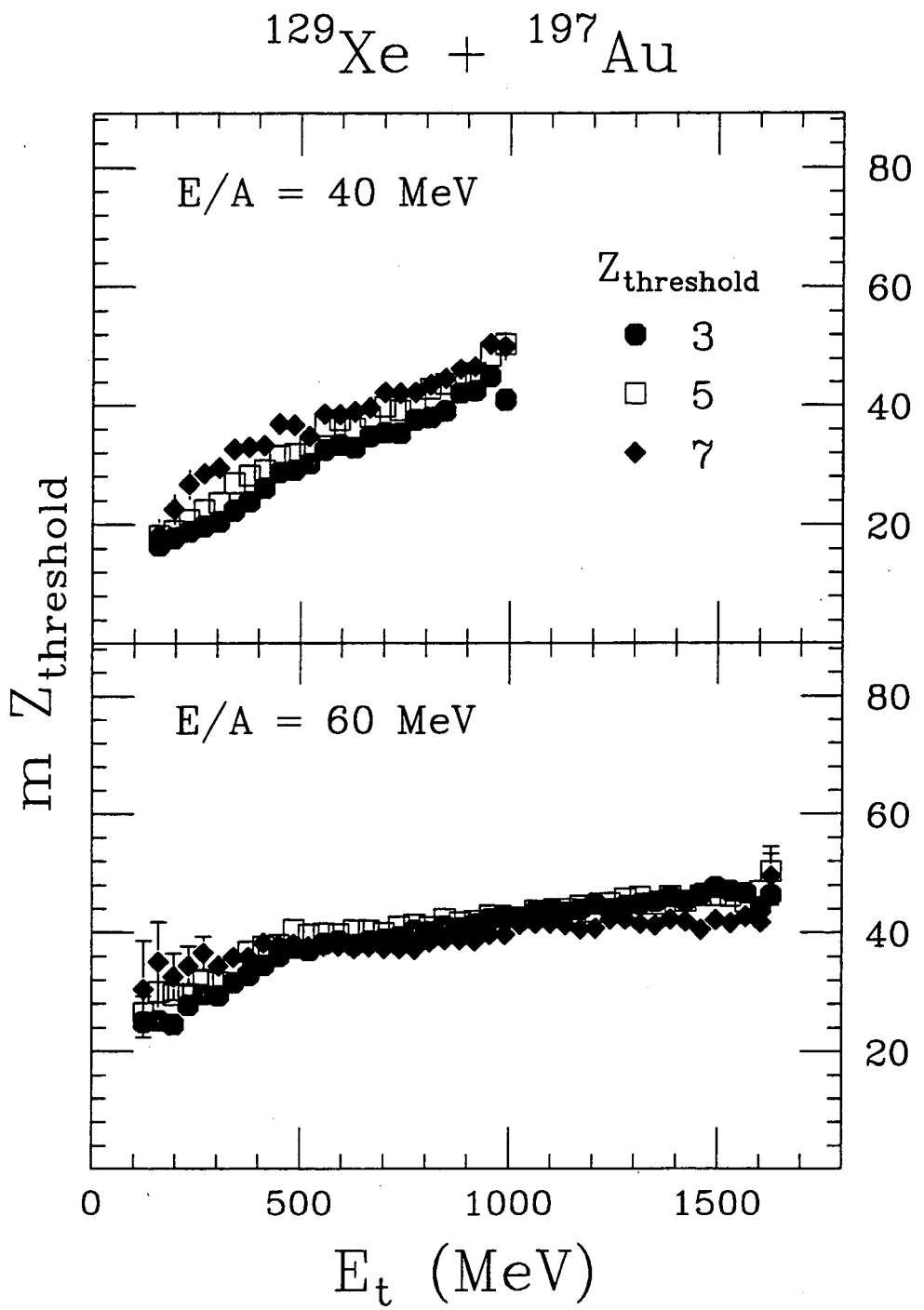

Figure 4.15 : The products of m and $Z_{threshold}$ as a function of E_t for the reaction ^{129}Xe + ^{197}Au at bombarding energies of E/A = 40 MeV (top panel) and 60 MeV (bottom panel). Results for different values of $Z_{threshold}$ (3, 5 and 7) are plotted with different symbols.

and this may place a limitation on the analysis.

Recently, Del Zoppo et al. claimed that the use of global observables (e.g. E_t), which exhibit event–to–event fluctuations, might introduce auto–correlations between pairs of observables that "may simulate specific signatures of particular physical regimes" [DelZ 95]. In their analysis of detected light charged particles ($Z \leq 2$) emitted from the reaction ^{132}Xe + ^{158}Gd at a bombarding energy of $E/A = 44$ MeV, they observed empirically that the light charged particle multiplicities (N_{LCP}) are binomially distributed as a function of the measured transverse energy. A Poisson origin for these distributions was assumed, and the observed binomial nature was shown to arise from the auto–correlation (whose origin will be explained later) between the measured transverse energy and the light charged particle multiplicity.

In such an analysis, the very particles whose multiplicities are studied contribute extensively to the measurement of the transverse energy. The measured value of the transverse energy becomes dependent upon the number of particles detected. This auto–correlation leads to narrow distributions of N_{LCP} over the entire range of measured transverse energy. Consequently, the variance σ^2 becomes smaller than the mean $\langle N_{LCP} \rangle$ and this deviation from the Poisson distribution grows with increasing auto–correlation. Eventually, the binomial approach becomes more appropriate for describing the N_{LCP} multiplicity distribution. This result has lead to Del Zoppo's conclusion that "the binomial–like multiplicity distributions do not necessarily imply evidence of reducibility to an elementary binary emission probability" [DelZ 95]. An immediate question was raised concerning the implications of the empirically observed binomial fragment multiplicity distributions, namely, would this observed binomial distribution also be Poisson in orgin?

4.5.1 Poisson Simulations

In this section, the event fluctuations associated with the use of the transverse energy are studied in order to investigate the conditions under which these fluctuations are sufficiently large to distort a Poisson distribution into a binomial distribution. In particular, simple Poisson simulations were performed for intermediate mass fragment (IMF), light charged particle (LCP), and neutron (NEUT) multiplicities as a function of excitation energy. The resulting multiplicity distributions were studied as a function of transverse energy to assess the possible bias to the results which might arise from using E_t as a measure of the excitation energy.

Poisson distributions of IMF, LCP, and NEUT multiplicities were generated as a function of E^* from input values of $\langle N_{IMF} \rangle$, $\langle N_{LCP} \rangle$ and $\langle N_{NEUT} \rangle$ respectively. In Figure 4.16a, these quantities are shown as a function of E^*. The inputs for $\langle N_{IMF} \rangle$ and $\langle N_{LCP} \rangle$ were taken from the experimental data of the ^{129}Xe + ^{197}Au reaction at a bombarding energy of $E/A = 60$ MeV, assuming E^* equals to $3E_t^{\rm exp}$, where $E_t^{\rm exp}$ is the experimentally measured transverse energy. For simplicity, the input for $\langle N_{NEUT} \rangle$ was taken to be equal to $\langle N_{LCP} \rangle$ with the same excitation energy dependence. The resulting distributions in N_{IMF}, N_{LCP}, and N_{NEUT} were completely independent, since no charge or mass conservation was applied. In fact, no charge or mass information was used, and the distributions were identical except that they were generated from different mean values and labeled as IMF, LCP, and NEUT respectively. The polar (θ) and the azimuthal angles (ϕ) of these emitted particles were distributed isotropically. The excitation energy was assumed to be thermal, and the kinetic energy of each particle was set equal to $E = E^*/N$ with $N = N_{IMF} + N_{LCP} + N_{NEUT}$. For simplicity, no Coulomb trajectory calculation was implemented, and the transverse energy of each particle was calculated according to its definition,

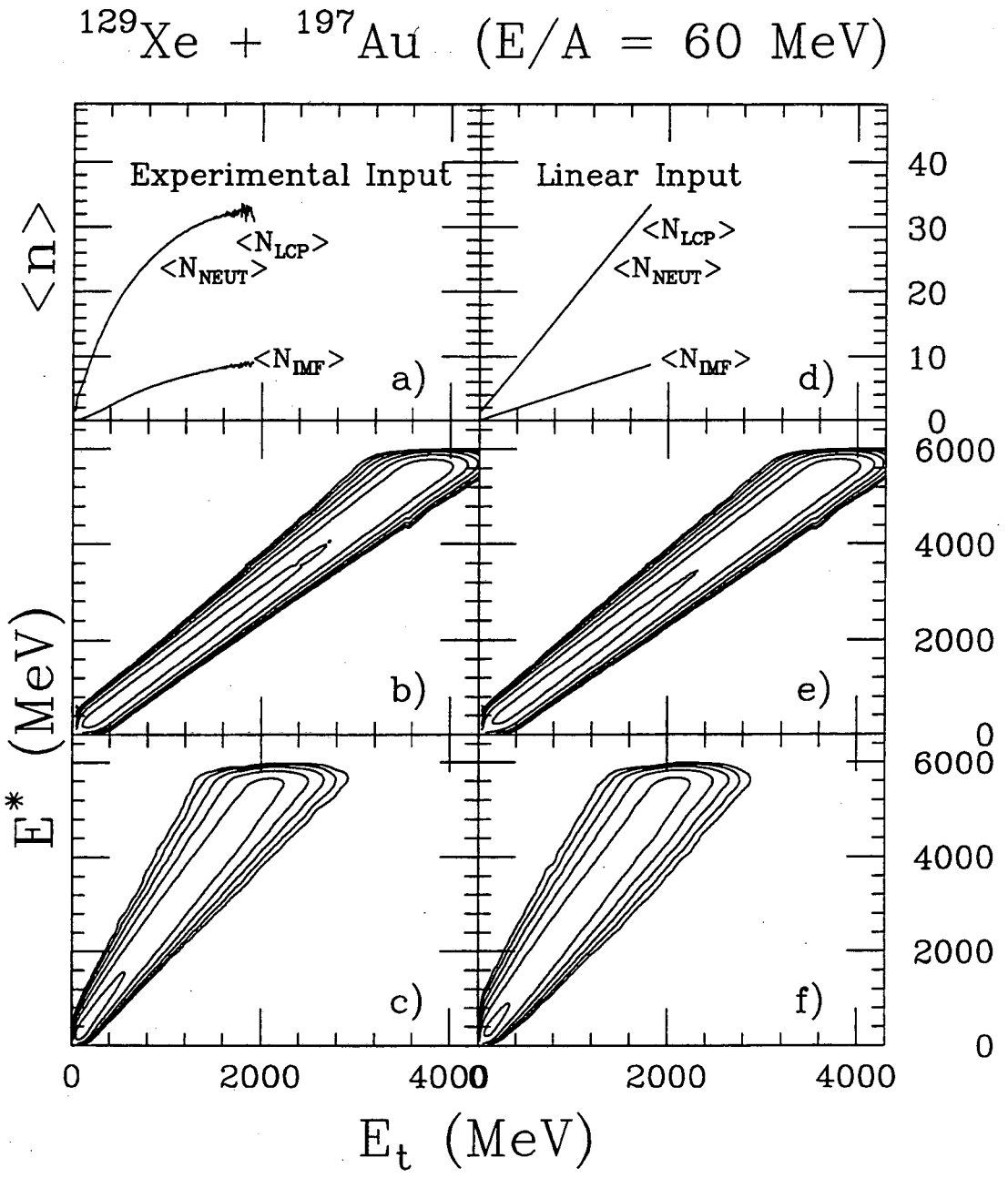

Figure 4.16 : a) The experimental input values of $\langle N_{NEUT}\rangle$, $\langle N_{LCP}\rangle$, $\langle N_{IMF}\rangle$ as a function of E_t^{exp} taken from the data of the reaction ^{129}Xe + ^{197}Au at $E/A = 60$ MeV. b) The logarithm contour plot shows the correlations between E^* and E_t (including neutron contribution) observed for the Poisson simulations of particle emissions. c) The correlations between E^* and E_t^m (excluding neutron contribution). d) The linear input values of $\langle N_{NEUT}\rangle$, $\langle N_{LCP}\rangle$, $\langle N_{IMF}\rangle$ as a function of E_t^{exp}. e) The correlations between E^* and E_t. f) The correlations between E^* and E_t^m.

$E_t^i = E sin^2\theta_i$.

4.5.2 Event–to–Event Fluctuations

The average transverse energy for events of a fixed excitation energy can be calculated according to Equation 4.3,

$$\begin{aligned} \langle E_t \rangle &= \left\langle \sum_i^N \frac{E^*}{N} sin^2\theta_i \right\rangle = \sum_i^N \frac{E^*}{N} \left\langle sin^2\theta_i \right\rangle \\ \langle E_t \rangle &= E^* \frac{\int sin^2\theta_i dcos\theta_i}{\int dcos\theta_i} = \frac{2}{3} E^*. \end{aligned}$$

The above equation clearly shows that the average transverse energy of a class of events depends solely on the excitation energy, and is independent of the number of particles emitted. This implies that there is no correlation between the particle multiplicity n and the transverse energy of an event other than their individual dependence on the excitation energy. In this context, n can be N_{IMF}, N_{LCP} or N_{NEUT} for fragment, light charged particle and neutron multiplicities respectively.

The simulated correlation between E_t and E^* is plotted in Figure 4.16b. A linear correlation is observed and the value of $\langle E_t \rangle$ is 2/3 E^*, consistent with the prediction of Equation 4.3. This shows that the events of a given E_t come from a rather narrow distribution of E^* with centroid = 3/2 E_t. Therefore, the resulting multiplicity distribution at a given transverse energy $P_{E_t}(n)$ is an average of multiplicity distributions $P_{E^*}(n)$ weighted by the excitation energy distribution at that transverse energy $P_{E_t}(E^*)$,

$$P_{E_t}(n) = \int P_{E_t}(E^*) \cdot P_{E^*}(n) dE^*. \tag{4.21}$$

The question naturally arises whether this folding procedure introduces large event fluctuations. In particular, under what circumstances will the mean and variance information of $P_{E^*}(n)$ be preserved in the resulting multiplicity distribution $P_{E_t}(n)$?

A trivial case is considered by assuming the multiplicity distribution $P_{E^*}(n)$ to be energy independent. The resulting multiplicity distribution from the above folding procedure (Equation 4.21) simply preserves the mean and variance information as shown below,

$$P_{E_t}(n) = \int P_{E_t}(E^*) \cdot P_{E^*}(n) dE^* = P(n) \int P_{E_t}(E^*) dE^* = P(n). \tag{4.22}$$

For more realistic situations, the particle emission probability (in statistical decays) increases with nuclear temperature, and thus introduces an energy dependence to the multiplicity distribution $P_{E^*}(n)$. In these cases, the fluctuations due to the spread in the excitation energy associated with events of a given transverse energy can no longer be neglected. In fact, the resulting variance $\sigma^2_{E_t}$ of $P_{E_t}(n)$ strongly depends on the variance $\sigma^2_{E^*E_t}$ of the excitation energy distribution $P_{E_t}(E^*)$.

When the correlation between E_t and E^* is strong, the distribution $P_{E_t}(E^*)$ becomes a δ function and its corresponding variance $\sigma^2_{E^*E_t}$ approaches zero,

$$\begin{aligned} P_{E_t}(E^*) &= 1 \quad for \quad E^* = (3/2)E_t \\ P_{E_t}(E^*) &= 0 \quad for \quad E^* \neq (3/2)E_t. \end{aligned} \tag{4.23}$$

In this limit, the resulting multiplicity distribution preserves the mean and variance information, namely,

$$\begin{aligned} P_{E_t}(n) &= P_{E^*}(n) \\ \langle n \rangle_{E_t} &= \langle n \rangle_{E^*} \qquad for \quad E^* = \frac{3}{2}E_t. \\ \sigma^2_{E_t} &= \sigma^2_{E^*} \end{aligned} \tag{4.24}$$

However, when the correlation between E_t and E^* is weakened, the spread in the excitation energy at a given value of E_t becomes broader (i.e. $\sigma^2_{E^*E_t} > 0$). The multiplicity distribution $P_{E_t}(n)$ is now an average over events with a range of E^*,

and this introduces event fluctuations. When the excitation energy distribution is symmetric with respect to $E^* = \frac{2}{3}E_t$, the information for the average multiplicity $\langle n \rangle$ is still preserved according to the above equation, but the corresponding variance is broadened by this folding procedure, namely,

$$\sigma^2_{E_t} > \sigma^2_{E^*=\frac{2}{3}E_t}. \tag{4.25}$$

As a result, the ratio $\frac{\sigma^2_{E_t}}{\langle n \rangle_{E_t}}$ becomes larger than the Poisson value of 1. Hence, this distortion of a Poisson distribution due to event fluctuations arising from the use of E_t does not lead to a binomial distribution which is characterized by a ratio of $\sigma^2 / \langle n \rangle$ less than 1.

To verify whether a Poisson distribution is distorted, several quantities that bear unique properties in the Poisson limit are examined. First of all, the ratio $\sigma^2 / \langle n \rangle$ and its deviation from the Poisson value of 1 is examined. Then the quantity of $g(n)$ defined as follows is studied:

$$g(n) \equiv \frac{(n+1)P(n+1)}{P(n)} = \frac{(n+1)\frac{<n>^{n+1}e^{-<n>}}{(n+1)!}}{\frac{<n>^n e^{-<n>}}{n!}} = \langle n \rangle \,, \tag{4.26}$$

where $P(n)$ is the corresponding Poisson probability to observe an event of particle multiplicity n. The above equation shows that the quantity $g(n)$ is independent of n in the Poisson limit. Therefore, the slope of $g(n)$ vs. n is 0, and the corresponding y–intercept is equal to the average particle multiplicity $\langle n \rangle$.

Transverse Energy Measured From All Particles The effect of event–to–event fluctuations on the N_{IMF} and N_{LCP} distributions is studied in the following. In Figure 4.17, the ratio $\sigma^2 / \langle n \rangle$ along with the slope and y–intercept of $g(n)$ vs. n are plotted as a function of transverse energy for both the N_{IMF} and N_{LCP} distributions obtained from the above Poisson simulations. In both cases, the ratios $\sigma^2 / \langle n \rangle$ are scattering

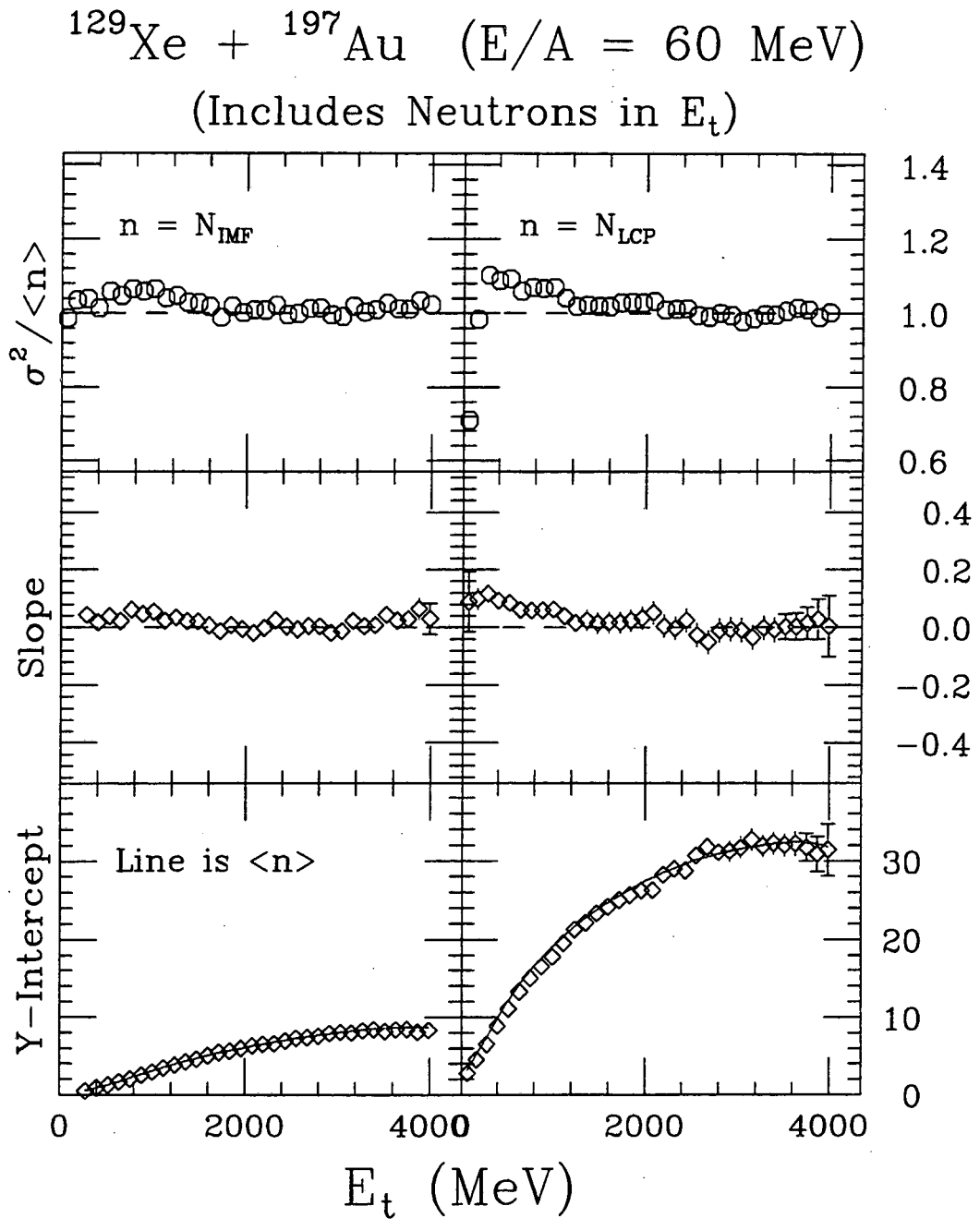

Figure 4.17 : For the N_{IMF} (left column) and N_{LCP} distributions (right column) generated from the Poisson simulations using the experimental inputs: the ratio of $\frac{\sigma^2}{\langle n\rangle}$ (top panel), the slope (middle panel) and the y–intercept (bottom panel) of $g(n)$ vs n are shown as a function of E_t. The solid curves on the bottom panels indicate the values of $\langle N_{IMF}\rangle$ and $\langle N_{LCP}\rangle$ as a function of E_t.

around the value of 1. The plots of the slopes of $g(n)$ vs. n are found to be flat and their y–intercepts agree reasonably well with the solid curves corresponding to the average particle multiplicities $\langle n \rangle$. These observations indicate that the Poisson nature of the N_{IMF} and N_{LCP} distributions is preserved when one uses E_t as a measure of E^*. This is indeed consistent with the above discussion that E_t is not auto–correlated with N_{IMF} or N_{LCP}. However, if Figure 4.17 is examined more carefully, a small systematic discrepancy is observed between the slopes (symbols) of $g(n)$ vs. n and the dashed lines at low E_t. The fact that the ratios $\sigma^2/\langle n \rangle$ are slightly larger than 1 in the same region suggests that this small deviation from the Poisson limit is not caused by auto–correlation, but rather by the random event fluctuations as a result of the folding procedure described by Equation 4.21. In this case, the distorted distribution might be well fitted by a negative binomial distribution characterized by a negative binomial probability (i.e. $\sigma^2/\langle n \rangle > 1$).

The results of these Poisson simulations show that there is no auto–correlation between E_t and N_{IMF} or N_{LCP} under the assumption that the excitation energy is thermal and evenly distributed among the emitted particles. The event fluctuations associated with E_t will at most increase the ratio $\sigma^2/\langle n \rangle$ of the resulting multiplicity distribution $P_{E_t}(n)$. Hence, this distortion of a Poisson distribution does not lead to a binomial distribution.

Transverse Energy Measured From Charged Particles Only In the above analysis, an 100% efficiency in the measurement of E_t is assumed. In actual experiments the detection system is not perfect, and the measured transverse energy E_t^m may be different from the true E_t. For instance, neutrons have not been detected in many experiments even though they carry kinetic energy and contribute significantly to the transverse energy of a given event. In this case, the transverse energy of a

given event is substantially underestimated (i.e. $E_t^m << E_t$).

In an attempt to study the effect of the missing neutrons on the measurement of the transverse energy, the above analysis was repeated with E_t^m calculated from charged particles only. The simulated correlation between E_t^m and E^* is plotted in Figure 4.16c, and is compared with the correlation between E_t and E^* plotted in Figure 4.16b. A linear correlation between $\langle E_t^m \rangle$ and E^* still exists, but the E^* distribution at a given E_t^m becomes broader.

In Figure 4.18, the ratio $\sigma^2/\langle n \rangle$ along with the slope and y–intercept of $g(n)$ vs. n are plotted as a function of E_t^m for both the N_{IMF} and N_{LCP} distributions obtained from the above Poisson simulations. For the N_{LCP} distribution, the ratio $\sigma^2/\langle N_{LCP} \rangle$ is scattering around a value of 0.8. The slope of $g(N_{LCP})$ vs. N_{LCP} is found to be negative, and the y–intercept is larger than the mean multiplicity $\langle N_{LCP} \rangle$ at all values of E_t^m. In other words, the Poisson nature of N_{LCP} is not preserved at all values of E_t^m. Since the value of N_C and thus of E_t^m arise mainly from LCP, a strong auto–correlation between N_{LCP} and E_t^m is not unexpected. In this case, events of a given E_t^m arise from a very narrow distribution of N_{LCP}. Consequently, the variance becomes less than the mean, and the extraction of the binomial parameters p and m becomes feasible. These extracted quantities are plotted as a function of E_t^m in Figure 4.19. The probabilities of emitting n light charged particles for $N_{LCP} = 3 - 30$ are also plotted as a function of E_t^m using different symbols, together with the solid curves generated from the binomial calculations using the above extracted values of p and m. Excellent agreement between the data (symbols) and the calculations (curves) for the entire range of E_t^m confirms the binomial nature of the distorted distribution.

On the other hand, IMFs contribute very little to N_C and thus to E_t^m, so the auto–correlation between E_t^m and N_{IMF} should be relatively weak. The y–intercept of the $g(N_{IMF})$ vs. N_{IMF} plot collapses onto the line corresponding to the mean

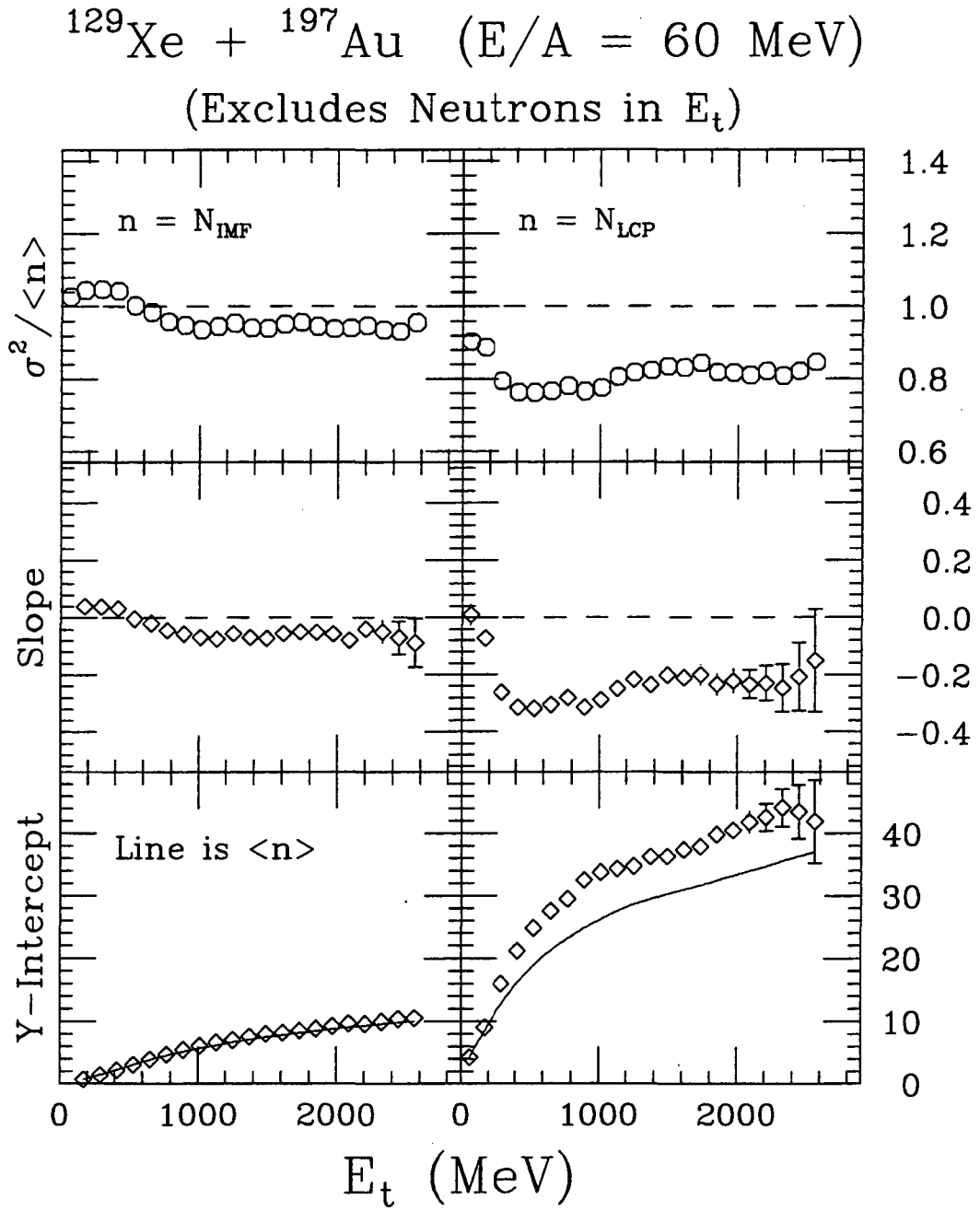

Figure 4.18 : For the N_{IMF} (left column) and N_{LCP} distributions (right column) generated from the Poisson simulations using the experimental inputs: the ratio of $\frac{\sigma^2}{\langle n\rangle}$ (top panel), the slope (middle panel) and the y–intercept (bottom panel) of $g(n)$ vs n are shown as a function of E_t^m. The solid curves on the bottom panels indicate the values of $\langle N_{IMF}\rangle$ and $\langle N_{LCP}\rangle$ as a function of E_t^m.

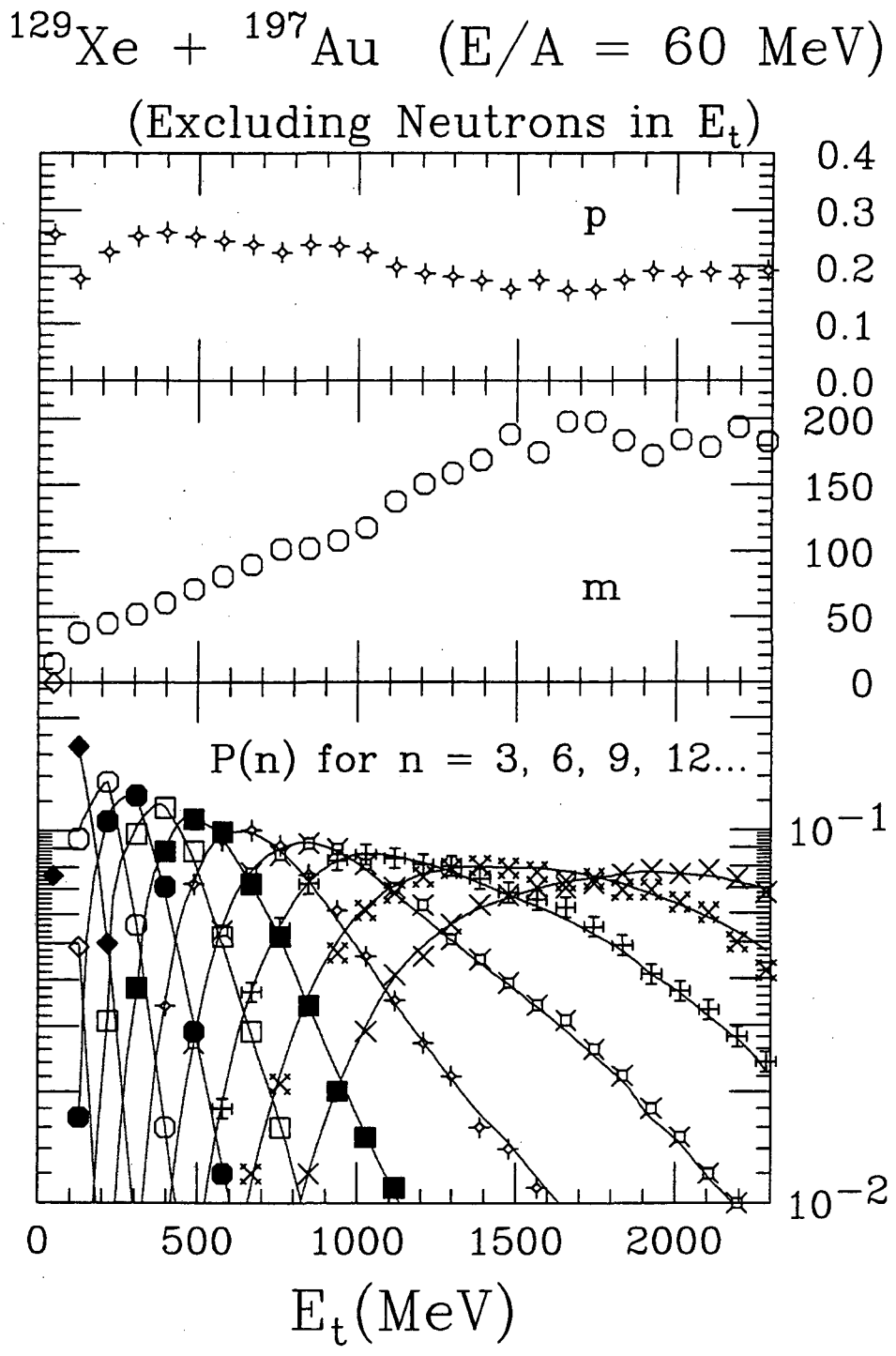

Figure 4.19 : For the N_{LCP} distribution generated from the Poisson simulation: the values of p (top panel) and m (middle panel) are extracted from the mean and variance as a function of E_t^m. (bottom panel) The probability to emit n light charged particles as a function of E_t^m. The curves are binomial calculations.

fragment multiplicity $\langle N_{IMF} \rangle$ at all values of E_t^m. However, a small negative slope is observed, and the ratio $\sigma^2 / \langle N_{IMF} \rangle$ is found to be slightly less than unity except at the region of low E_t^m, where the slope and the ratio $\sigma^2 / \langle N_{IMF} \rangle$ are just above zero and unity respectively. This suggests that at low E_t^m, the auto–correlation between N_{IMF} and E_t^m is negligible, and the residual event fluctuations slightly increase the variance of the N_{IMF} distribution. At higher E_t^m, the auto–correlation becomes observable, but the distortion of the Poisson nature is still very weak since the IMF contribution to E_t^m is at most 20%.

Thus far, these results are obtained based on the Poisson distributions generated from a specific set of inputs. In order to study the sensitivity of the multiplicity distributions to different inputs, and for the sake of comparison, Poisson simulations were performed with a new set of inputs that are linear functions of E^*. More specifically, in Figure 4.16d, the end points of the experimental inputs (Figure 4.16a) are joined with straight lines to be used as linear inputs. The simulated correlations between the transverse energies (E_t & E_t^m) and the excitation energy (E^*) are shown in Figure 4.16e and Figure 4.16f respectively. In both cases, the correlations are linear and consistent with the prediction of Equation 4.3. The effects of fluctuations associated with E_t and E_t^m on the resulting N_{LCP} distributions were also studied. The results shown in Figure 4.20 are similar to those obtained earlier for the experimental inputs. The event fluctuations associated with E_t clearly broaden the N_{LCP} distribution and thus increase the ratio $\sigma^2 / \langle N_{LCP} \rangle$. On the other hand, the strong auto–correlation between E_t^m and N_{LCP} distorts the Poisson distribution in the opposite direction by decreasing the ratio $\sigma^2 / \langle N_{LCP} \rangle$. Consequently, the relative magnitude of $\sigma^2 / \langle N_{LCP} \rangle$ can be used to distinguish the effect of random event fluctuations from that of auto–correlation.

The above study suggests that the transverse energy serves as a good ob-

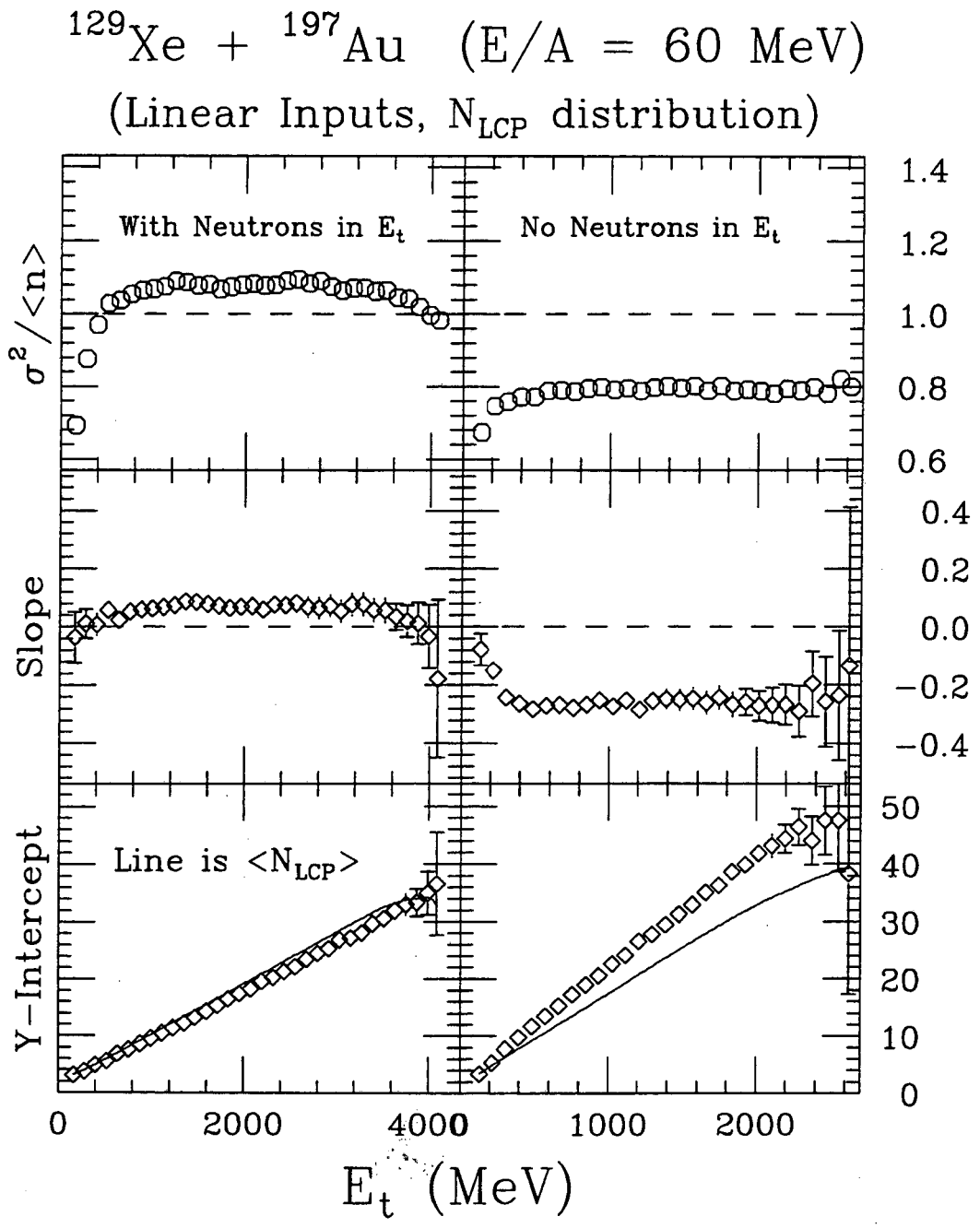

Figure 4.20 : For the N_{LCP} distribution generated from Poisson simulation using the linear input: the ratio of $\frac{\sigma^2}{\langle n \rangle}$ (top panel), the slope (middle panel) and the y-intercept (bottom panel) of $g(n)$ vs n are shown as a function of E_t (left column) and E_t^m (right column). The solid curves on the bottom panels indicate the values of $\langle N_{LCP} \rangle$ as a function of E_t and E_t^m.

servable for the measurement of the excitation energy. It has a sharp correlation with the excitation energy and has no auto–correlation with the fragment and the light charged particle multiplicities being studied. On the other hand, if the measurement of the transverse energy is not perfect (possibly due to finite detection efficiency), an auto–correlation between N_{LCP} and the measured transverse energy E_t^m may be introduced. The experimental setup of Del Zoppo et al. [DelZ 95] does not measure neutrons, and the geometric acceptance for charged particles is rather limited due to the lack of forward angular coverage. As a result, the auto–correlation effect in their analysis could be strong, and this might be the reason for their observation of binomial distributions characterized by flat Arrhenius plots for the light charged particle multiplicities. On the other hand, IMF yields contribute at most 20% to the measured transverse energy E_t^m in the multifragmentation studies at intermediate energies. Therefore, the auto–correlation between N_{IMF} and E_t^m is not sufficient to distort a Poisson distribution into a binomial distribution.

4.6 Efficiency Effect on Binomial Parameters

The above discussion demonstrates that the transverse energy serves as a good observable for the measurement of the excitation energy in multifragmentation studies. In particular, the mean and variance of the N_{IMF} distribution are reasonably well preserved even when the measurement of E_t is limited by the detection efficiency. This leads one to believe that the experimentally observed binomial fragment multiplicity distributions as a function of E_t have indeed their origin from binomial parent distributions. However, it is still important to explore the effects of the finite detection efficiency on the mean multiplicity, the variance, and the extraction of the binomial parameters p and m.

At intermediate energy heavy–ion reactions, the large source velocity considerably increases the laboratory velocity of all fragments emitted in the center–of–mass. The constraint imposed by the detector's energy threshold becomes a minor problem compared to the limitation due to the incomplete geometric acceptance. In this particular experimental setup for the ^{129}Xe–induced reactions, the combined detector system (MSU Miniball + LBL Array) covers a large fraction of the available solid angle as shown in Figure 4.21. The forward angular acceptance is especially crucial when the effect of forward focusing is very strong in case of a large center–of–mass velocity. However, the geometric efficiency of the forward LBL Array is only 64% since these detectors have relatively large dead area in comparison to the more efficient Miniball (89%) detectors at the back. This limited forward geometric acceptance causes an underestimate on the fragment multiplicity, but the effect of these undetected forward particles on the transverse energy measurement is reduced significantly by the factor $sin^2\theta$.

In the following, the efficiency effect on the E_t measurement is assumed to be minimal; details associated with anisotropies and multiple hits are also disregarded. While the number of tries m should be independent of the geometric efficiency ϵ, the observed probability p_{obs} should be related to the true probability p by the relationship

$$p_{obs} = \epsilon p. \tag{4.27}$$

This observed probability p_{obs} combines exactly like p in the binomial distribution (Equation 4.7), and the finite efficiency effect on the Arrhenius plot is straight forward since

$$\log \frac{1}{p_{obs}} = \log \frac{1}{\epsilon p} = \log \frac{1}{\epsilon} + \log \frac{1}{p} = \log \frac{1}{\epsilon} + B/T. \tag{4.28}$$

The above equation shows that the linearity and the corresponding slope of the Arrhenius plot are preserved, but the y–intercept is shifted upwards by an efficiency

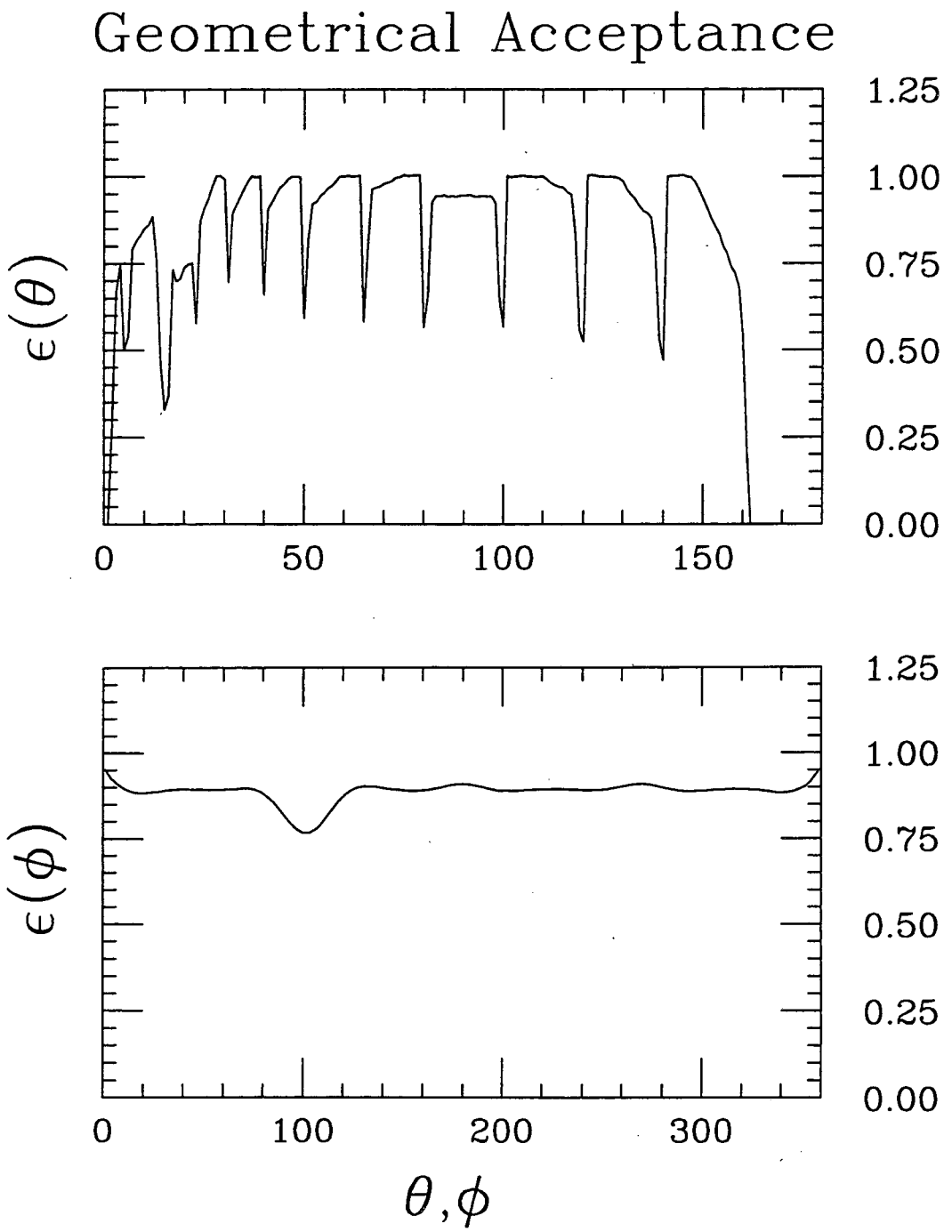

Figure 4.21 : Geometrical acceptance of the device (Miniball + Array) as a function of the polar angle θ (top panel) and the azimuthal angle ϕ (bottom panel).

dependent quantity $\log(1/\epsilon)$. In other words, the extraction of the barrier for single fragment emission is independent of the geometric efficiency, while the absolute value of the observed elementary probability p_{obs} is modified.

To verify these ideas about the effect of instrumental efficiency on the experimental observables, selected Miniball detectors were deactivated (in software) in the measurement of fragment multiplicity. The results obtained by activating only one–third, one–half and all of the Miniball detectors were studied and compared. Only the Miniball detectors were used in this efficiency study because of their simple symmetries with respect to the beam axis. Since the above blocking was not applied to the measurement of the transverse energy, the results shown as a function of E_t or $1/\sqrt{E_t}$ can be compared readily.

The resulting excitation functions P_n, the extracted binomial parameters m and p are shown as a function of E_t in Figure 4.22 and 4.23 respectively for the reaction ^{129}Xe + ^{197}Au at a bombarding energy of $E/A = 60$ MeV. Excellent agreement between the experimental n–fragment emission probabilities (symbols) and the binomial calculations (curves) is observed in Figure 4.22 independent of the geometric efficiency. Moreover, the values of m shown in the top panel of Figure 4.23 do not depend on the geometric efficiency at all values of E_t, while the observed probabilities p_{obs} in the bottom panel decrease with increasing amount of detector blocking. When some of the Miniball detectors are blocked, the detection efficiency ϵ is reduced correspondingly, and the gradual decrease in p_{obs} is thus consistent with Equation 4.27 qualitatively.

The Arrhenius plots associated with different geometric efficiency mentioned in the above are shown to be linear and parallel with each other in Figure 4.24. The absolute values of $\log(1/p)$ obtained by using only 1/2 and 1/3 of the Miniball detectors are found to be shifted upwards by a value of $\log(2)$ and $\log(3)$ respectively. This

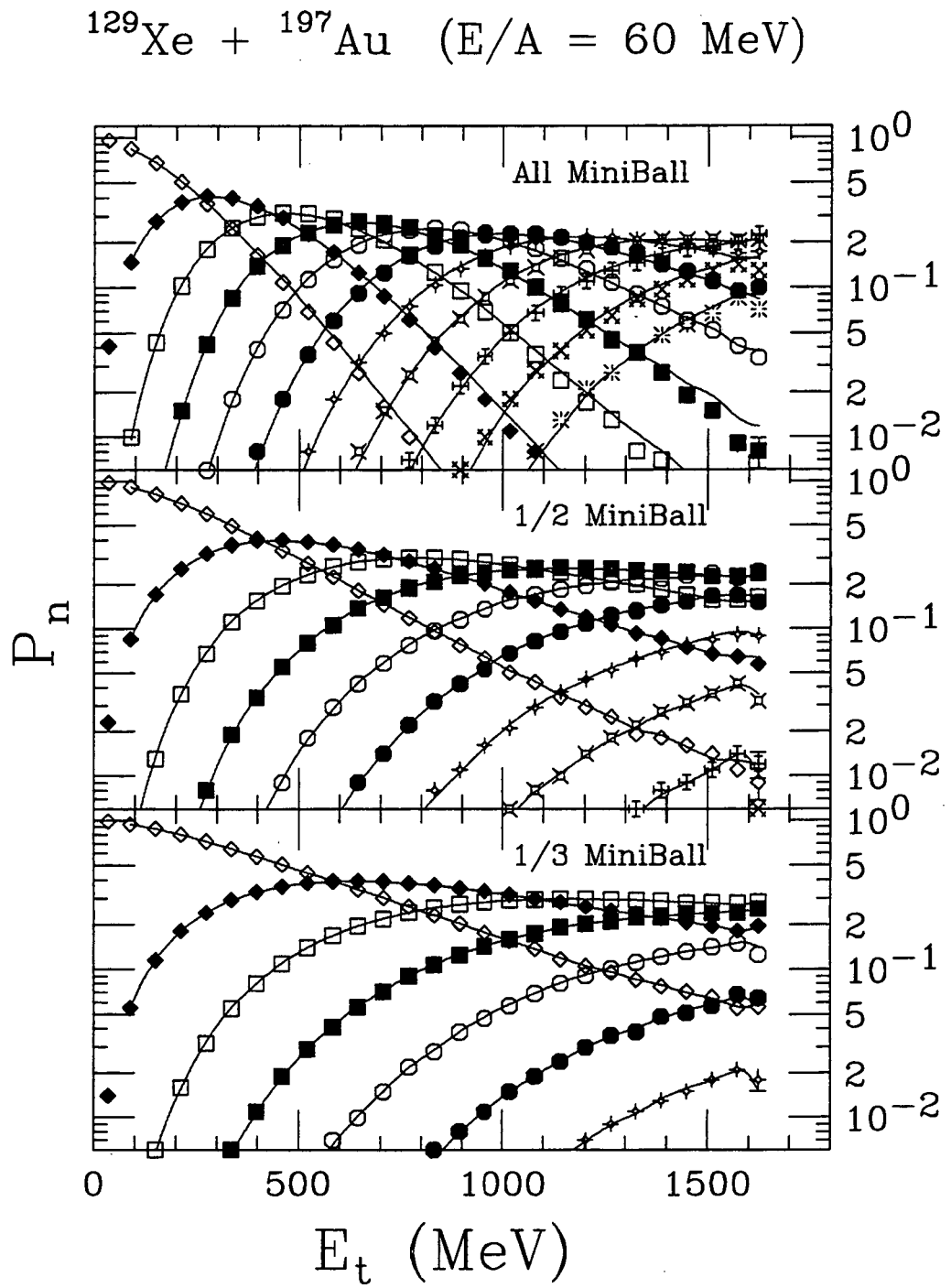

Figure 4.22 : The probability P_n of detecting n IMFs by using all (top panel), 1/2 (middle panel) and 1/3 (bottom panel) of Miniball detectors is shown as a function of E_t for the reaction ^{129}Xe + ^{197}Au at a bombarding energy of E/A = 60 MeV. The solid curves are calculated P_n assuming a binomial distribution using extracted values of p and m shown in Figure 4.23.

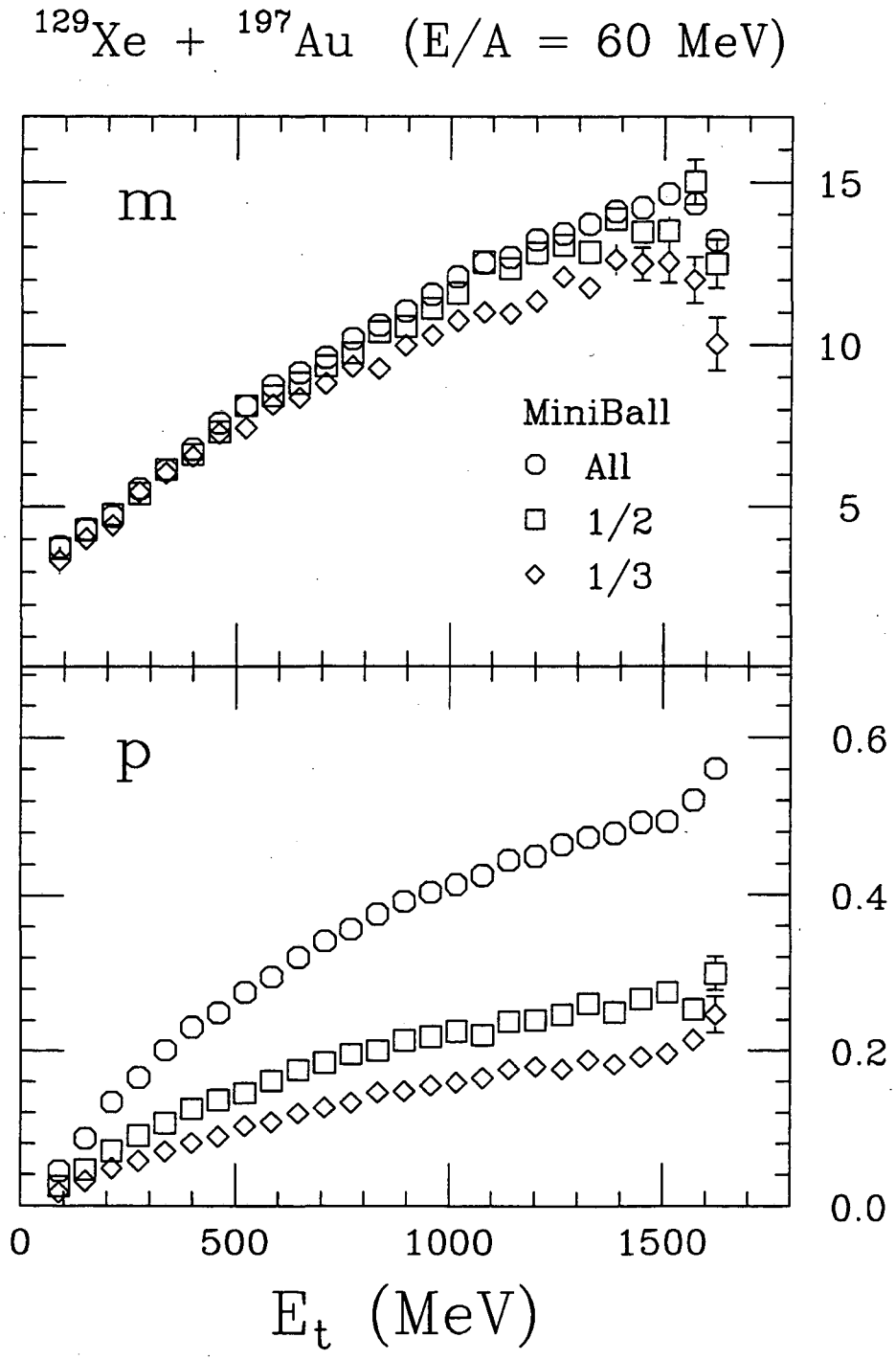

Figure 4.23 : The values of p (bottom panel) and m (top panel) extracted from the N_{IMF} distributions shown in Figure 4.22 as a function of E_t for the reaction ^{129}Xe + ^{197}Au at a bombarding energy of $E/A = 60$ MeV.

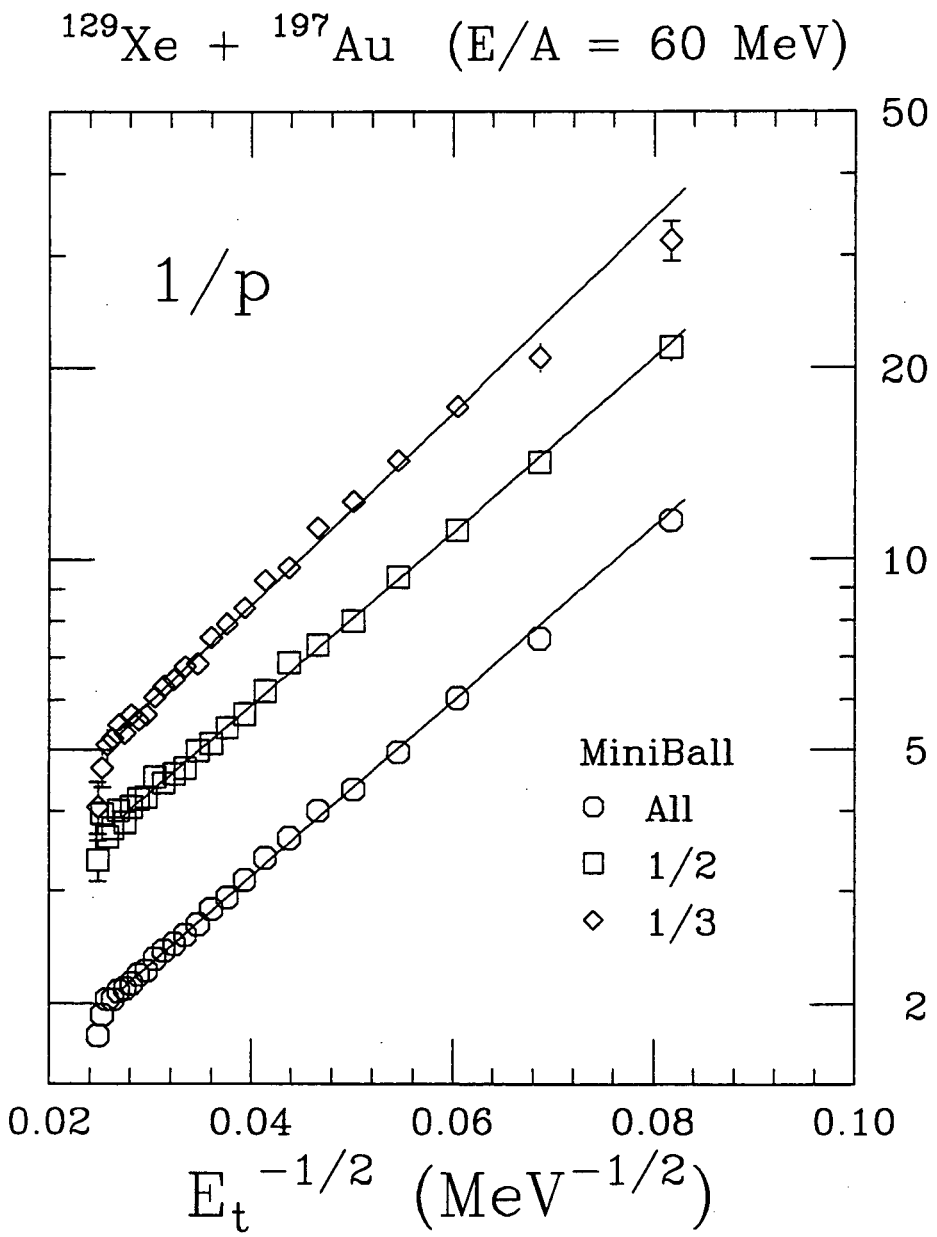

Figure 4.24 : The values of $1/p$ extracted from the N_{IMF} distributions shown in Figure 4.22 as a function of $E_t^{-1/2}$ for the reaction ^{129}Xe + ^{197}Au at a bombarding energy of $E/A = 60$ MeV.

quantitatively confirms the idea that $p_{obs} = \epsilon p$, where the efficiency ϵ can be taken as 1, 1/2 and 1/3 for the counting procedures including all, 1/2 and 1/3 of the Miniball detectors respectively. This excellent agreement with Equation 4.27 further reinforces the physical interpretation of p as the probability for single–fragment emission.

The above exercise shows that the binomial nature of the fragment multiplicity distributions is independent of the device geometric acceptance under the circumstances that the transverse energy is reasonably well measured. In fact, the slope of the Arrhenius plot, which is proportional to the binary decay barrier for single–fragment emission, is unaffected by the geometric acceptance. However, to obtain the actual value for the barrier extracted from the slope, a quantitative relationship between the excitation energy and the measured transverse energy must first be established. On the other hand, the extraction of the single–fragment emission probability depends on the geometric efficiency (Equation 4.27), but can be easily corrected if the efficiency is known.

4.7 Target Independence

The empirical observation that multifragmentation is reducible to single–fragment emission is intriguing. Thus far, the analysis has been focused on a single reaction of ^{129}Xe + ^{197}Au. It is important to map out the extent of this phenomenon and to determine whether or not it is a universal feature of the multifragmentation process. In this section, the excitation function analysis is extended to the ^{129}Xe–induced reactions on ^{nat}Cu, ^{89}Y and ^{165}Ho targets.

Figure 4.25 shows the excitation functions for the ^{129}Xe–induced reactions on ^{nat}Cu, ^{89}Y and ^{165}Ho targets at a bombarding energy of E/A = 40 MeV. The values of the corresponding mean and variance of these fragment multiplicity distri-

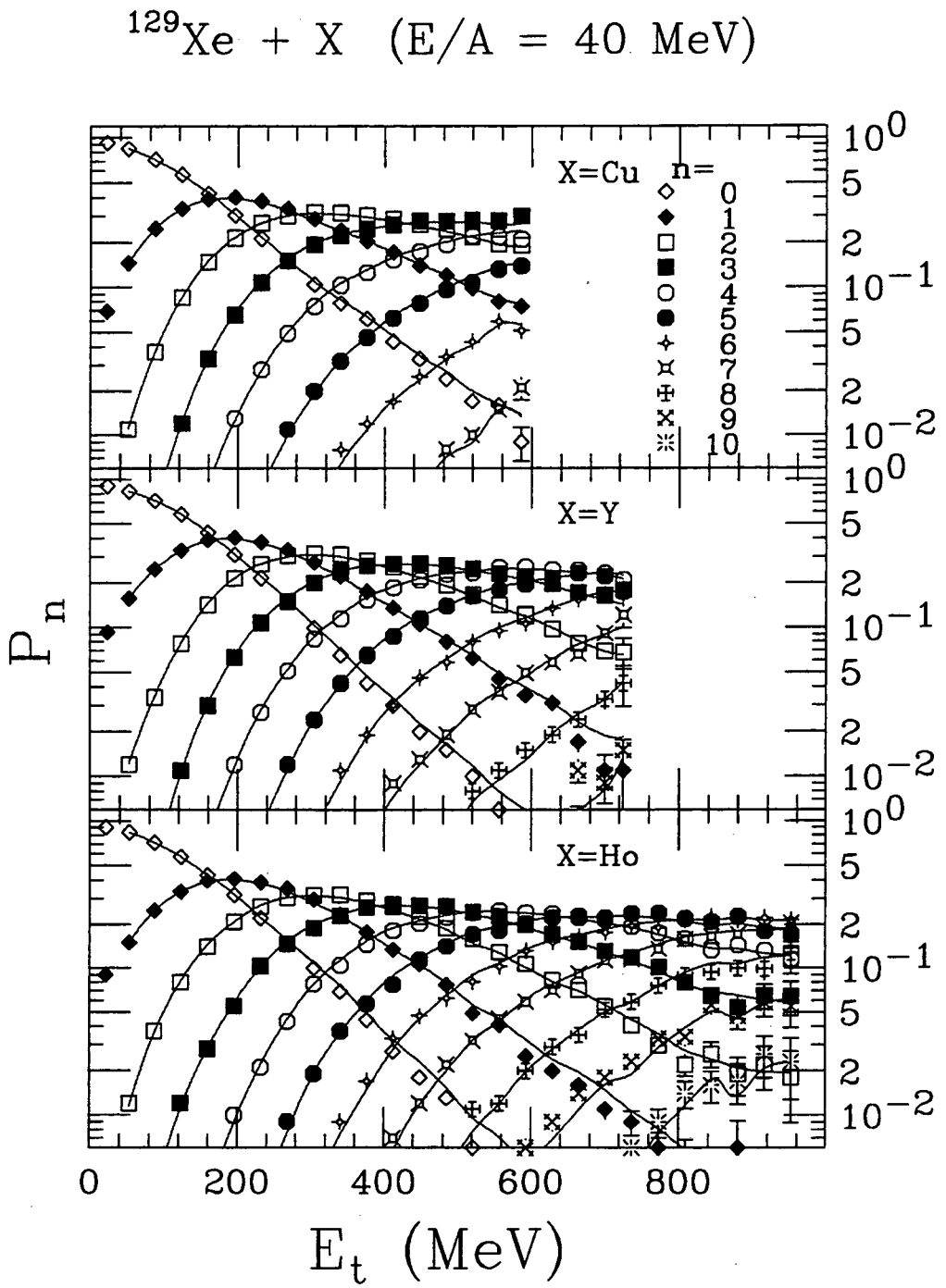

Figure 4.25 : The probability P_n for emitting n IMFs as a function of E_t for the ^{129}Xe– induced reactions at $E/A = 40$ MeV on different targets: ^{nat}Cu (top panel), ^{89}Y (middle panel) and ^{165}Ho (bottom panel). The solid curves are binomial calculations of P_n using values of p and m extracted from $\langle N_{IMF} \rangle$ and the corresponding σ^2 shown in Figure 4.26.

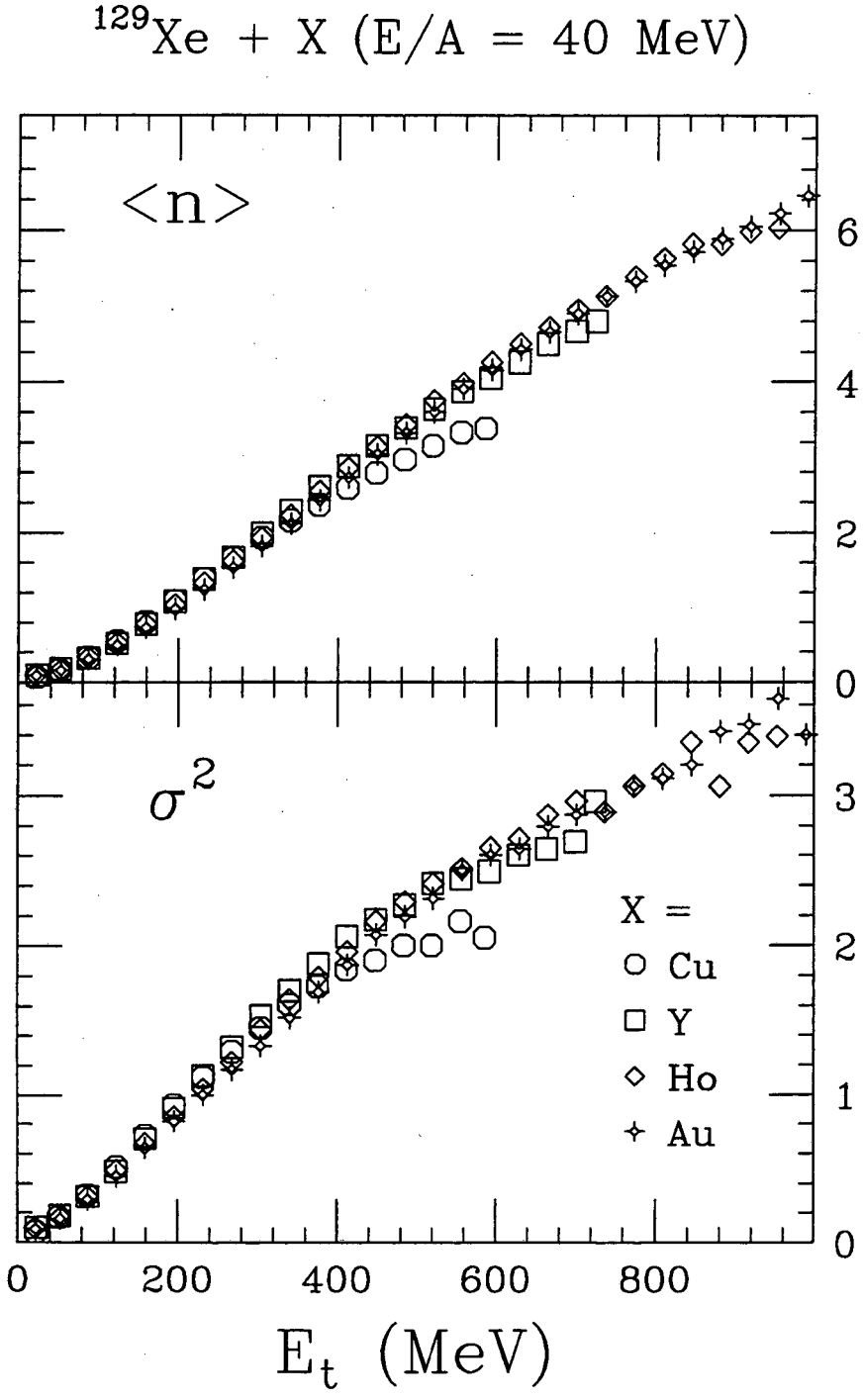

Figure 4.26 : The values of $\langle n \rangle$ (top panel) and σ^2 (bottom panel) as a function of E_t observed for the IMF multiplicity distributions of the ^{129}Xe–induced reactions at $E/A = 40$ MeV on ^{nat}Cu, ^{89}Y, ^{165}Ho and ^{197}Au targets represented by different symbols.

butions are plotted as a function of transverse energy in Figure 4.26. The binomial parameters p and m extracted from these mean and variance are used to generate the curves shown in Figure 4.25. The excellent agreement between the data (symbols) and the binomial calculations (curves) for the fragment multiplicity distributions demonstrates the binomial nature of P_n and its reducibility to p independent of the specific target.

Interestingly, the excitation functions (Figure 4.25) and thus their corresponding values of $\langle n \rangle$ and σ^2 (Figure 4.26) are almost identical for all three targets over the entire range of measured transverse energy. Target independence was also observed by others in the excitation functions for emission of n IMFs [Blum 91, Rous 93, More 93a] and in the dependence of the average IMF multiplicity on the total charged particle multiplicity [Bowm 92]. A most remarkable result shown in Figure 4.27 is that the Arrhenius plots for different targets collapse onto a nearly universal line, suggesting that the thermal properties of the emission sources are independent of the specific target. In other words, the sizes as well as the excitation energies of the emission sources are nearly identical. Similar results (not shown) are obtained for the ^{129}Xe–induced reactions at the higher bombarding energy ($E/A = 60$ MeV). This observed target independence is interesting and may be used to test and to search for entrance channel mechanisms that are consistent with this experimental feature.

The incomplete fusion model [More 86, Bowm 89] which incorporates kinematics into a standard geometrical picture of a nucleus–nucleus interaction is considered. The predictions of this model have been shown to be consistent with many experimental observations of heavy–ion collisions at intermediate energies [Char 88a, Char 88b, Bowm 89, Hano 93]. For the sake of illustration, two nuclei are assumed to collide with each other at a given impact parameter as shown in Figure 4.28. There will be a portion of each nucleus that is occluded by the other. In this simple pic-

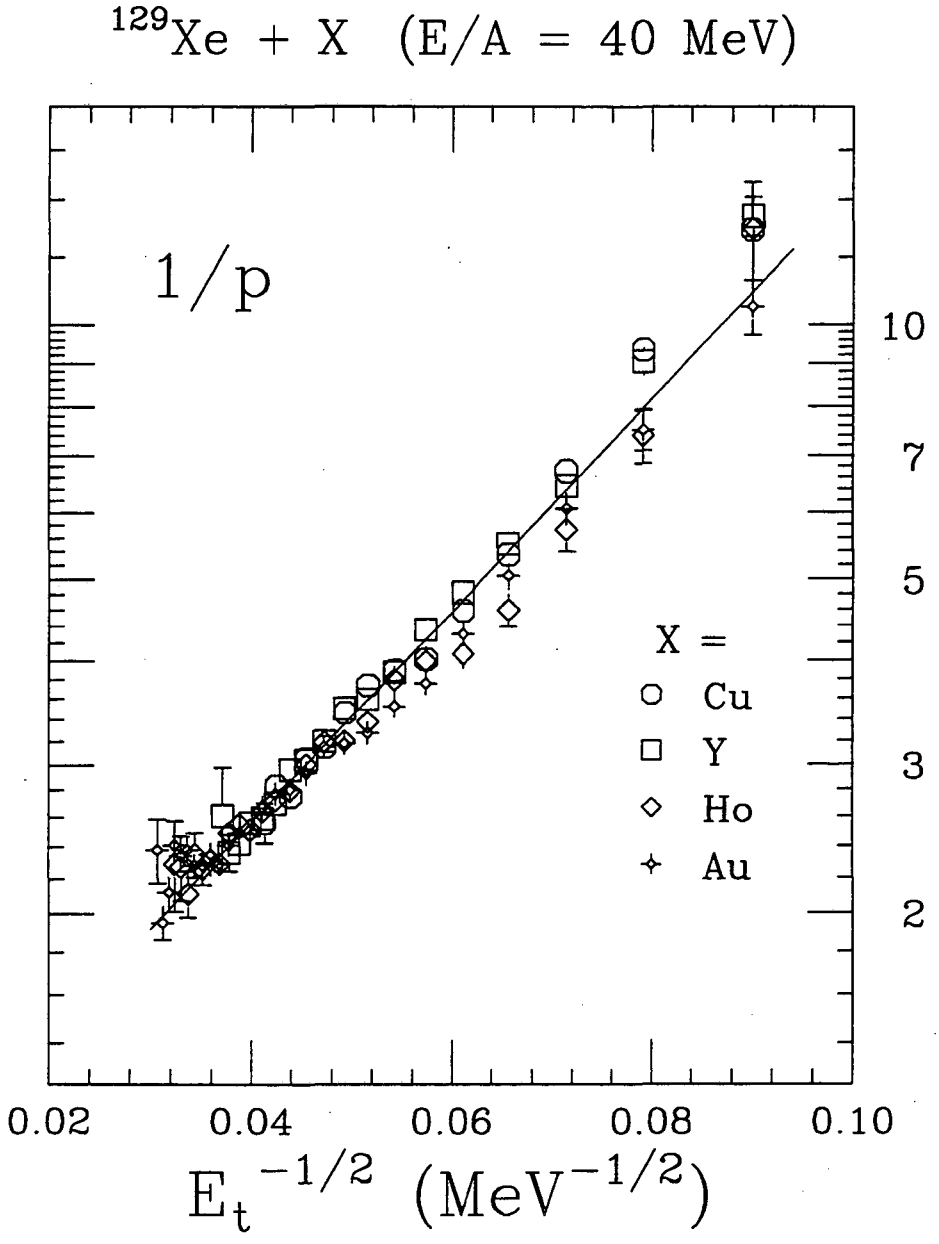

Figure 4.27 : The extracted values of $1/p$ as a function of $E_t^{-1/2}$ for the ^{129}Xe–induced reactions at E/A = 40 MeV on ^{nat}Cu, ^{89}Y, ^{165}Ho and ^{197}Au targets represented by different symbols. The line is a linear fit to the data.

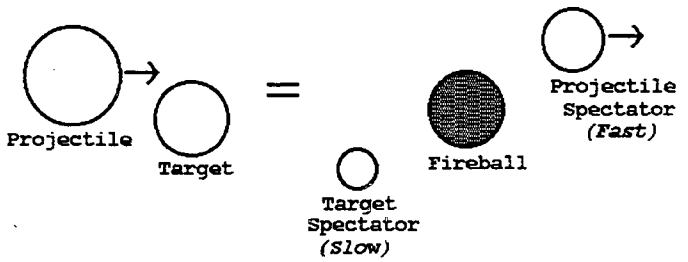

Fireball Model

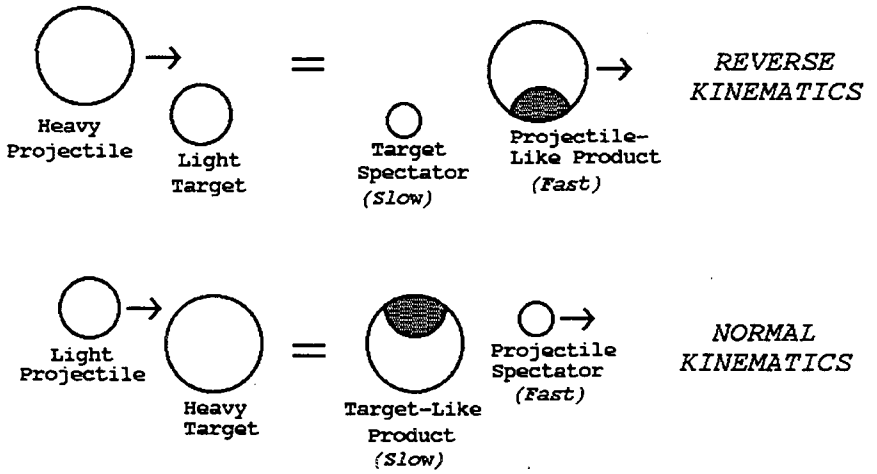

Incomplete Fusion Model

Figure 4.28 : Schematic illustrations of the incomplete fusion and fireball models.

ture, one piece of the occluded portion is sheared off and attaches itself to the other nucleus, and the separation energy is taken as the energy necessary to create new nuclear surface. In the geometrical spirit of this model, it is "cheaper" to shear off a piece from the lighter nucleus since the truncation of a heavier nucleus creates a larger amount of surface and costs more energy. Therefore, the heavier projectile picks up mass from the lighter target to form a projectile–like incomplete fusion product in reverse kinematics; whereas a target–like incomplete fusion product is formed in normal kinematics by shearing off mass from the lighter projectile (Figure 4.28). In both cases, the excitation energy of the incomplete fusion product can be calculated from the momentum transfer and the new surface created.

An example of this conventional incomplete fusion model prediction is shown in Figure 4.29 for the ^{129}Xe–induced reactions on ^{nat}Cu, ^{89}Y, ^{165}Ho and ^{197}Au targets at a bombarding energy of $E/A = 40$ MeV. In particular, the resulting velocity of the incomplete fusion product is plotted as a function of mass transfer in Figure 4.29. For ^{nat}Cu and ^{89}Y, the velocity of the projectile–like incomplete fusion product is close to the beam velocity in the most peripheral collisions (small mass transfer), and it decreases with increasing amount of mass transfer until it reaches the center–of–mass velocity in central collisions (complete fusion). On the other hand, for heavier ^{165}Ho and ^{197}Au targets, the velocity of the target–like incomplete fusion product starts at rest for the most peripheral collisions and increases gradually with increasing amount of mass transfer from the projectile. This result immediately suggests that the target independence observed in the Arrhenius plots for ^{nat}Cu and ^{89}Y finds its natural explanation within the incomplete fusion model. Neglecting Q–values and recoil effects, the ^{129}Xe–like source depends solely on the mass removed from the lighter target, and the reactions depend relatively little on the actual nature of the target. For the heavier ^{165}Ho and ^{197}Au targets, the observed target independence

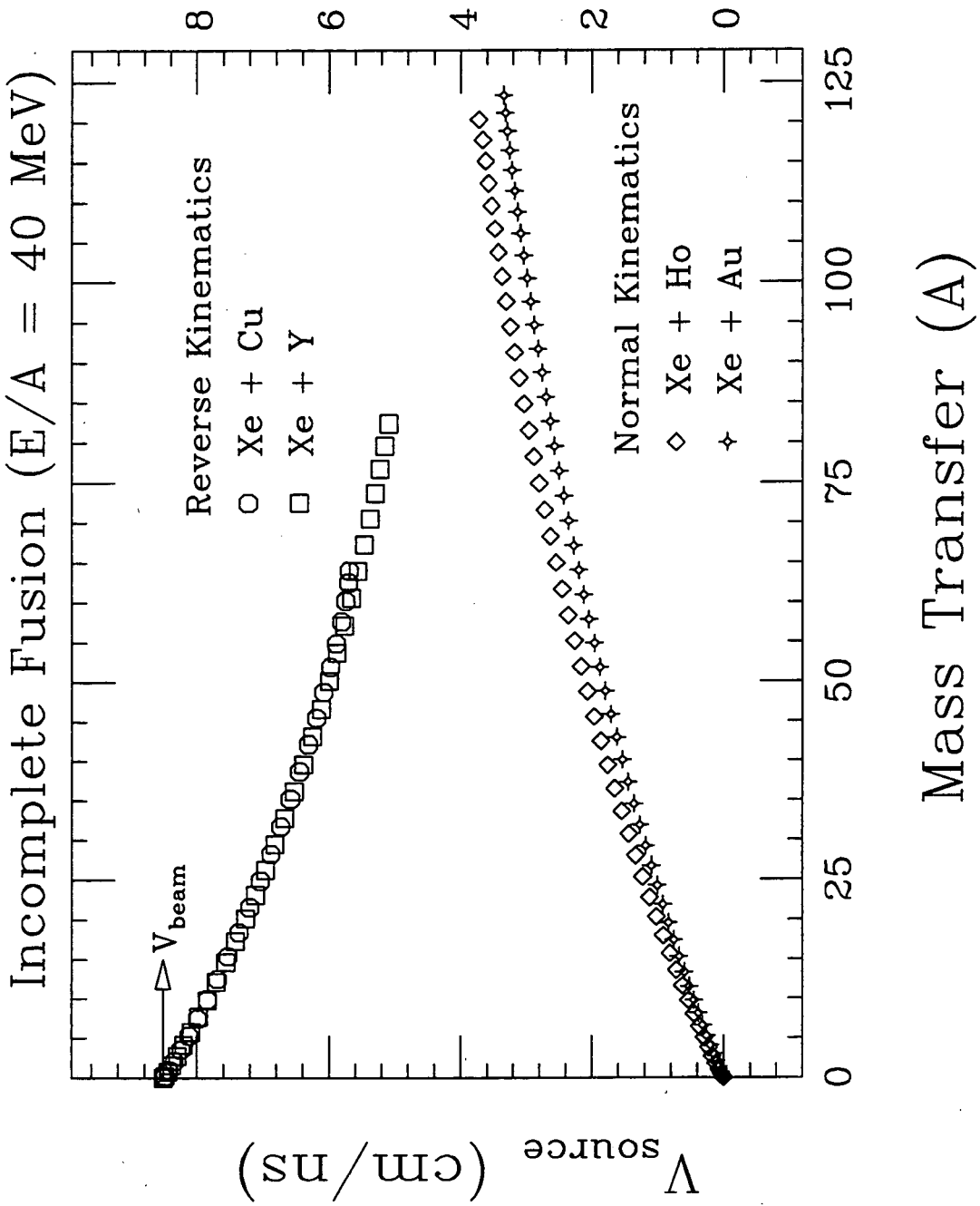

Figure 4.29 : The velocity of the projectile- and target–like sources formed in the incomplete fusion model as a function of mass transfer for the ^{129}Xe–induced reactions at E/A = 40 MeV on ^{nat}Cu, ^{89}Y, ^{165}Ho and ^{197}Au targets represented by different symbols.

seems to imply a similar mass transfer to the ^{129}Xe projectile. However, this suggested mass transfer from the heavier ^{165}Ho and ^{197}Au targets to the lighter ^{129}Xe projectile is contrary to the conventional incomplete fusion picture. In fact, a strong target dependence is expected for the target–like source formed in these normal kinematics reactions.

The above discussion demonstrates the inconsistency between the experimental observation and the conventional incomplete fusion picture, which predicts a target independence only in reverse kinematics reactions. This disagreement however, can be resolved if the thermal equilibration is achieved only in the vicinity of the overlapping region of the two nuclei (see Figure 4.28). In other words, the incomplete fusion product is only partially equilibrated and can be viewed as a composite of the relatively cold spectator matter attached to the equilibrated overlapping region. In this picture, it becomes essential to distinguish between the incomplete fusion product formed by the mass transfer in the entrance channel and the equilibrated portion that undergoes statistical emissions. For example, Figure 4.29 shows that at a given amount of mass transfer, the velocity of the projectile–like incomplete fusion product is always higher than that of the target–like incomplete fusion product. In other words, emitted fragments associated with ^{nat}Cu and ^{89}Y reactions should be more forward focused in the laboratory frame; whereas the fragment angular distributions for ^{165}Ho and ^{197}Au reactions are expected to be more isotropic. Despite the difference in their angular distributions, the thermal properties and the statistical nature of their emissions should be target independent, since they depend solely on the equilibrated overlapping portion determined by the amount of mass transfer.

This target independence can still be achieved even if the cold spectator matter is completely detached from the overlapping portion of the incomplete fusion product. This becomes essentially a picture for the fireball model, which has been

predicted for reactions at high bombarding energies ($E/A > 100$ MeV) [West 76, Goss 77]. A schematic diagram for the fireball model is also shown in Figure 4.28. In this model, the dynamical impact during the collision is sufficiently strong that the overlapping matter is sheared off both nuclei to form a hot emission source. Unlike the incomplete fusion product, the source velocity of the fireball is governed by the relative velocity of the two nuclei and their overlapping region is independent of the specific target. The laboratory angular distributions of fragments are thus similar between normal and reverse kinematics reactions.

Thus far, both the incomplete fusion (partially equilibrated) and the fireball models are shown to be consistent with the target independence observed in the Arrhenius plots. In order to rule out one of these two models, the laboratory angular distributions are studied as a function of target mass. As an example, fragments emitted at polar angles less than 24° (arbitrary) are selected and their multiplicity distributions are studied. The corresponding values of mean and variance for these multiplicity distributions are plotted as a function of the transverse energy in Figure 4.30. Since the primary interest is the target dependence, the above figures are truncated at $E_t = 600$MeV, the value of E_t beyond which no data point exists for the reaction ^{129}Xe + ^{nat}Cu. The average fragment multiplicities measured in the forward angles for ^{nat}Cu and ^{89}Y targets are nearly identical, and they account for about 40% of the average total fragment multiplicities. However, this target independence does not hold for ^{165}Ho and ^{197}Au targets, where the contribution of forward fragments accounts for only 30% of the total number of emitted fragments. Fragment yields gated at other forward polar angles have also been studied, and similar results are obtained.

This observed difference in the gated fragment yields (Figure 4.30) between normal and reverse kinematics is inconsistent with the fireball picture. On the con-

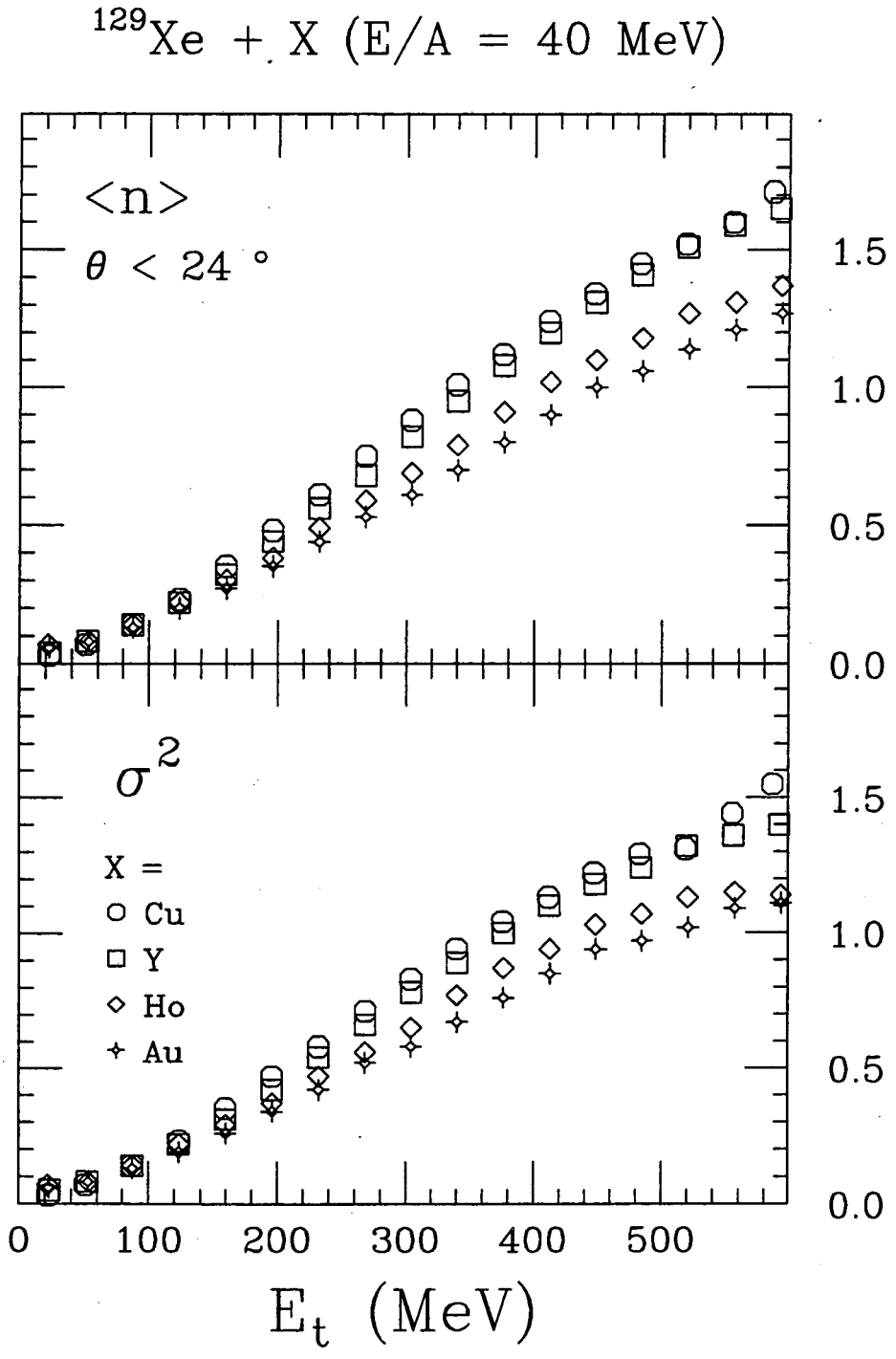

Figure 4.30 : The values of $\langle n \rangle$ (top panel) and σ^2 (bottom panel) associated with IMFs emitted at forward angles ($\theta < 24°$) as a function of E_t for the ^{129}Xe–induced reactions at $E/A = 40$ MeV on ^{nat}Cu, ^{89}Y, ^{165}Ho and ^{197}Au targets represented by different symbols.

trary, the strong forward focusing effect and the observed target independence for the reverse kinematics reactions (^{nat}Cu and ^{89}Y) suggest the formation of fast ^{129}Xe–like incomplete fusion products (Figure 4.29). Similarly, the relatively weak forward focusing effect observed in the normal kinematics reactions suggest the formation of relatively slow ^{165}Ho- or ^{197}Au–like incomplete fusion products. Furthermore, the observed target independence in the ungated fragment yields (Figure 4.26) suggests that the incomplete fusion products are only partially equilibrated. In other words, thermal equilibration is achieved only in the vicinity of the overlapping region of the two nuclei such that the subsequent statistical emissions become independent of the specific target.

In summary, the fragment multiplicity distributions as a function of the measured transverse energy observed for the ^{129}Xe–induced reactions on ^{nat}Cu, ^{89}Y, ^{165}Ho and ^{197}Au targets at bombarding energies of E/A = 40 & 60 MeV are well described by binomial distributions independent of the specific target. The thermal nature of the elementary binary decay probability and its target independence are illustrated by the nearly universal linear Arrhenius plots observed for a variety of targets. These results demonstrate that the reducibility of n–fragment emission probability to a single binary decay probability is wide–spread in intermediate energy heavy–ion reactions, and may indeed be a universal feature of multifragmentation at intermediate energies.

Chapter 5

Charge Distributions

Historically the charge (mass) distribution has played and still plays a very important role in multifragmentation. The near power–law shape of the charge and mass distributions observed experimentally in light–ion and heavy–ion collisions was often taken as an evidence of critical opalescence in hot nuclear matter [Finn 82, Lync 87]. More recent studies also attempt to extract possible signature of a phase transition from the moments of the charge distributions [Gilk 94].

In this chapter, the charge distributions of intermediate mass fragments are presented for the ^{129}Xe-induced reactions on ^{nat}Cu, ^{89}Y, ^{165}Ho and ^{197}Au targets at bombarding energies of E/A = 40 and 60 MeV. In particular, the n–fold charge distributions are shown to be reducible to the one–fold charge distributions through a simple scaling factor of the form e^{-cnZ}. The extraction and interpretation of the quantity c are discussed in section 5.1 for the reaction ^{129}Xe + ^{197}Au at both bombarding energies. The dependence of c on the transverse energy and its relevance to phase coexistence in multifragmentation are investigated in section 5.2. The residual dependence of c on $Z_{threshold}$ in the IMF definition is studied in section 5.3. Finally, the results obtained for the ^{129}Xe-induced reactions on other targets are presented in

section 5.4.

5.1 Reducibility and Thermal Scaling

In Chapter 4, the reducibility and thermal scaling of the multifragment emission probabilities were demonstrated with data integrated over a broad range of fragment atomic numbers ($3 \leq Z \leq 20$). In this approach, an average value of the elementary decay probability $p = \langle p(Z) \rangle$ was extracted and a strong dependence on $Z_{threshold}$ was observed. This suggests that the lightest member ($Z_{threshold}$) of IMFs dominates fragment emission and the resulting charge distribution $P(Z)$ should have a functional form that decreases dramatically with Z. In this section, the charge distributions of IMFs are studied as a function of E_t, and the consequence of the observed reducibility and thermal scaling on the resulting charge distributions is explored.

First, the aspect of reducibility as it applies to the charge distributions is considered. The physical implication of reducibility is that multifragmentation itself is reducible to a combination of independent fragment emissions. In its broadest form, this reducibility demands that the single fragment emission probability $p(Z)$, from which an event of n fragments is generated by m trials, is the same at every step of extraction. The consequence of this extreme reducibility is straightforward: the charge distribution for the one–fold events is the same as that for the n–fold events and equal to the singles distribution, i.e.,

$$P_{(1)}(Z) = P_{(n)}(Z) = P_{singles}(Z) = p(Z). \tag{5.1}$$

Second, the consequence of the thermal dependence of p on the charge distributions is considered. If the one–fold = n–fold = singles distribution is thermal, then

$$P(Z) \propto e^{-\frac{B(Z)}{T}}. \tag{5.2}$$

Here $B(Z)$ is the barrier for the emission of a fragment Z and T is the nuclear temperature of the emission source. This functional form of $P(Z)$ suggests that, under the usual assumption $E_t \propto E^*$, the expression

$$\sqrt{E_t} \ln P(Z) \propto -B(Z) \tag{5.3}$$

should be able to collapse the charge distributions associated with different E_t to a universal function of Z.

5.1.1 Extraction of c

Empirically the charge distributions for the reaction ^{129}Xe + ^{197}Au are found to be nearly exponential functions of Z except for events of relatively low transverse energy. The probability to emit an intermediate mass fragment of a given charge is shown in Figure 5.1 for different cuts on the transverse energy and fragment multiplicity for the reaction ^{129}Xe + ^{197}Au at bombarding energies of $E/A = 40$ and 60 MeV. The distributions are reasonably well described by the lines which are exponential fits for charges from 4 to 20 with α_n being the exponential fit parameter:

$$P_n(Z) \propto e^{-\alpha_n Z}. \tag{5.4}$$

This observed exponential fall off of $P(Z)$ with increasing Z shows that fragment emission is indeed dominated by the lightest fragment in the range considered, and this is consistent with the observed $Z_{threshold}$ dependence of the elementary decay probability p discussed in section 4.3.

If the charge distributions are thermal, then the exponential fits to the charge distributions should show a thermal behavior, and α_n would have a linear dependence on $1/\sqrt{E_t}$ (see Equation 5.2):

$$\alpha_n \propto \frac{1}{T} \propto \frac{1}{\sqrt{E_t}}. \tag{5.5}$$

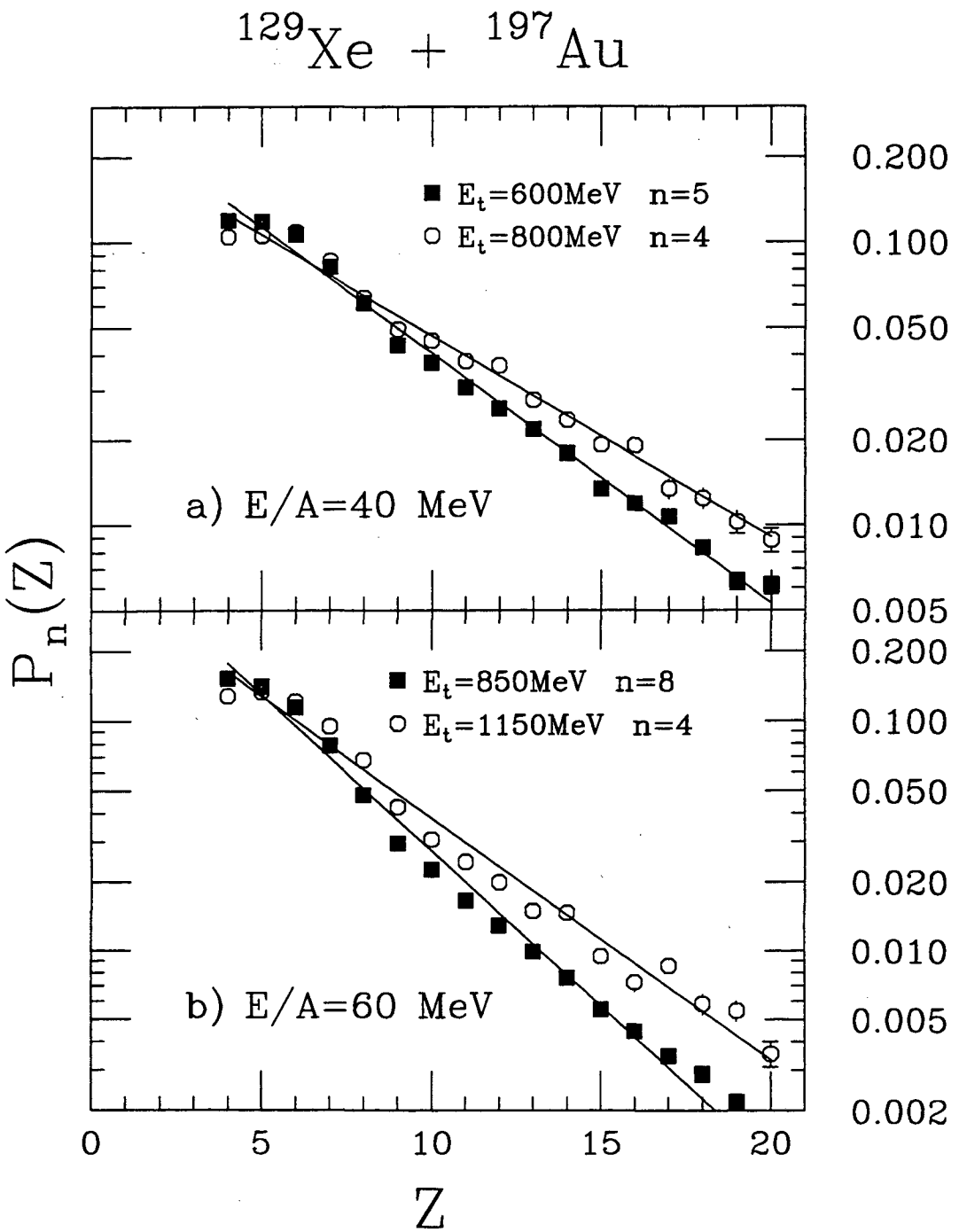

Figure 5.1 : The n–fold charge distributions $P_n(Z)$ for intermediate mass fragments (IMF: $3 \leq Z \leq 20$) are plotted for the indicated cuts on transverse energy E_t and IMF multiplicity n. The width of the cuts ΔE_t is 50 MeV. The solid lines are exponential fits over the range $Z = 4 - 20$.

Figure 5.2 plots the fitted values of α_n as a function of $1/\sqrt{E_t}$ for the charge distributions of the reaction ^{129}Xe + ^{197}Au. The expectation of the thermal scaling appears to be met quite nicely. For each value of n, the exponent α_n shows a linear dependence on $1/\sqrt{E_t}$. However, the condition of n independence (i.e. $\alpha_1 = \alpha_2 = ... = \alpha_n = \alpha$) consistent with the extreme reducibility of Equation 5.1 is not met. Rather than collapsing onto a single straight line, the values of α_n for different fragment multiplicities are offset one with respect to another by what looks like a constant quantity.

In fact, all of the data are well fitted by assuming for α_n a functional form equal to a term proportional to $1/\sqrt{E_t}$ and another term proportional to n:

$$\alpha_n = \frac{K'}{\sqrt{E_t}} + nc. \tag{5.6}$$

Here c represents the constant spacing between these fitted lines and accounts for the observed n dependence. It is noted that over 80 different charge distributions at each bombarding energy are represented in Figure 5.2. The good agreement between the data (symbols) and the fit (lines) suggests the following reducible expression for the charge distribution:

$$P_n(Z) \propto e^{-\alpha_n Z} = e^{-\frac{K'Z}{\sqrt{E_t}} - cnZ}. \tag{5.7}$$

If one takes the log of both sides and moves terms around, one arrives at an expression that should scale for all fragment multiplicities n and transverse energies E_t:

$$[\ln P_n(Z) + cnZ]\sqrt{E_t} = -K'Z. \tag{5.8}$$

This equation indicates that it should be possible to reduce the charge distributions associated with any intermediate mass fragment multiplicity and transverse energy to a universal straight line. The slope of this universal line reflects the Z dependence of the barrier for a single–fragment emission. As a demonstration of this thermal

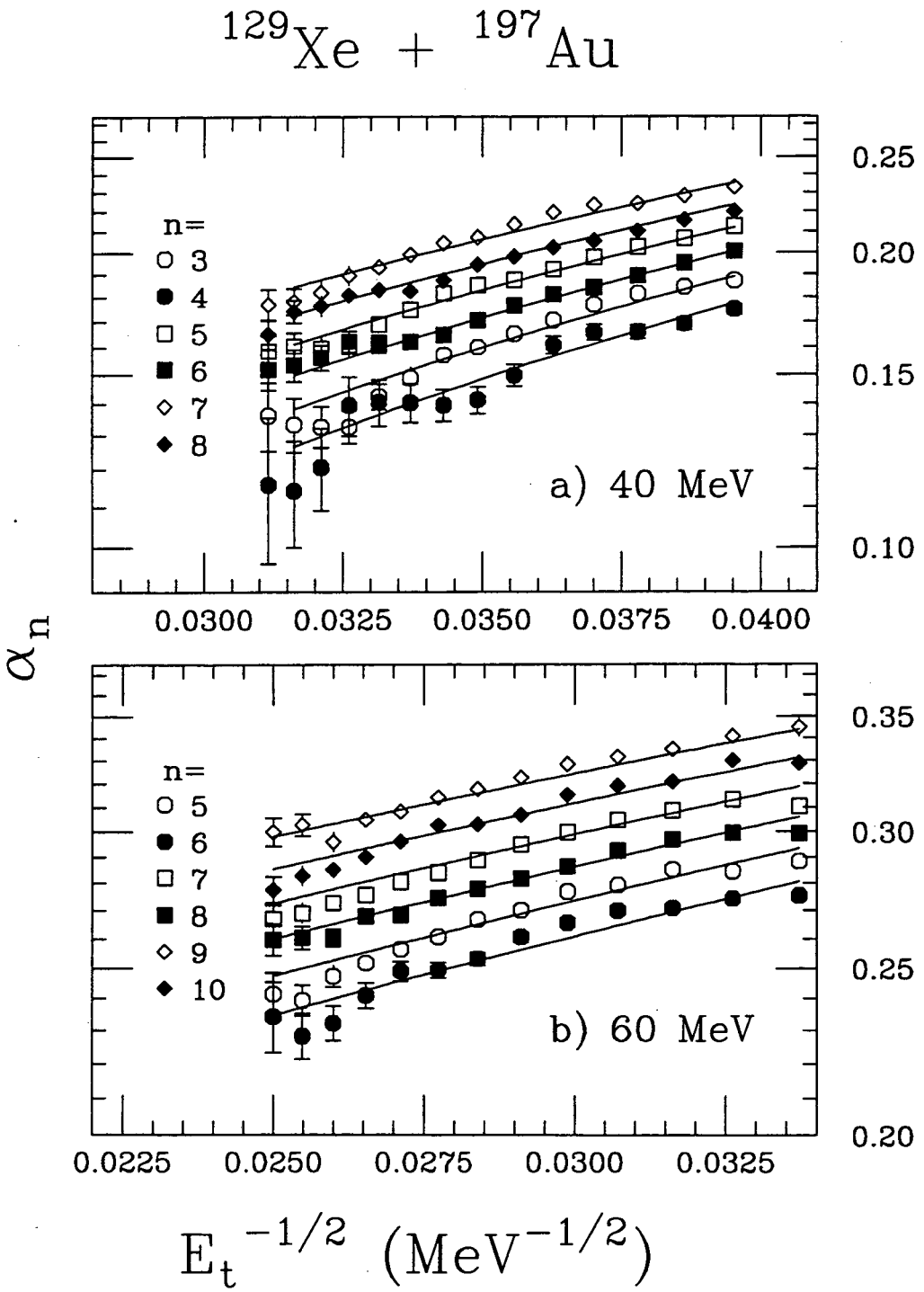

Figure 5.2 : The exponential fit parameter α_n (from fits to the charge distributions, see Equation 5.4) is plotted as a function of $1/\sqrt{E_t}$. The solid lines are fits to the values of α_n using Equation 5.6 .

reducibility, the reduced quantity $-K'Z = [\ln P_n(Z) + cnZ]\sqrt{E_t}$ for the charge distributions shown in Figure 5.1 is plotted in Figure 5.3. The charge distributions in Figure 5.1 with different cuts on E_t and n clearly have different slopes, and now they collapse onto a single curve confirming the thermal scaling and reducible nature of the charge distributions.

5.1.2 Other Methods of c Extraction

Thus far, the analysis has been focused on charge distributions of an exponential form (see Equation 5.7), in which the fragment emission barrier is linearly proportional to Z (i.e. $B(Z) = K'Z$). For small values of Z, the barriers are dominated by the Coulomb interaction, and are thus proportional to Z. However, other terms like the surface energy may start to set in for higher values of Z, causing a deviation from the linear Z dependence. Indeed, systematic deviations from the exponential fits are observed for large Z values of the charge distributions at low transverse energies.

Let us consider a charge distribution generated from fragment emissions associated with a barrier $B(Z)$ of any functional form:

$$P_n(Z) \propto e^{-\frac{B(Z)}{\sqrt{E_t}} - cnZ}. \tag{5.9}$$

To extend the previous analysis to this general expression, a similar reduced quantity $F(Z)$ is constructed,

$$[\ln P_n(Z) + cnZ]\sqrt{E_t} = -B(Z) = F(Z). \tag{5.10}$$

The reduced quantity $F(Z)$ should scale for all values of n and E_t, but this procedure is now independent of the functional form of the charge distributions.

To extract an optimum value of c to collapse the charge distributions associated with different values of n and E_t, a χ^2 is constructed in terms of the difference in

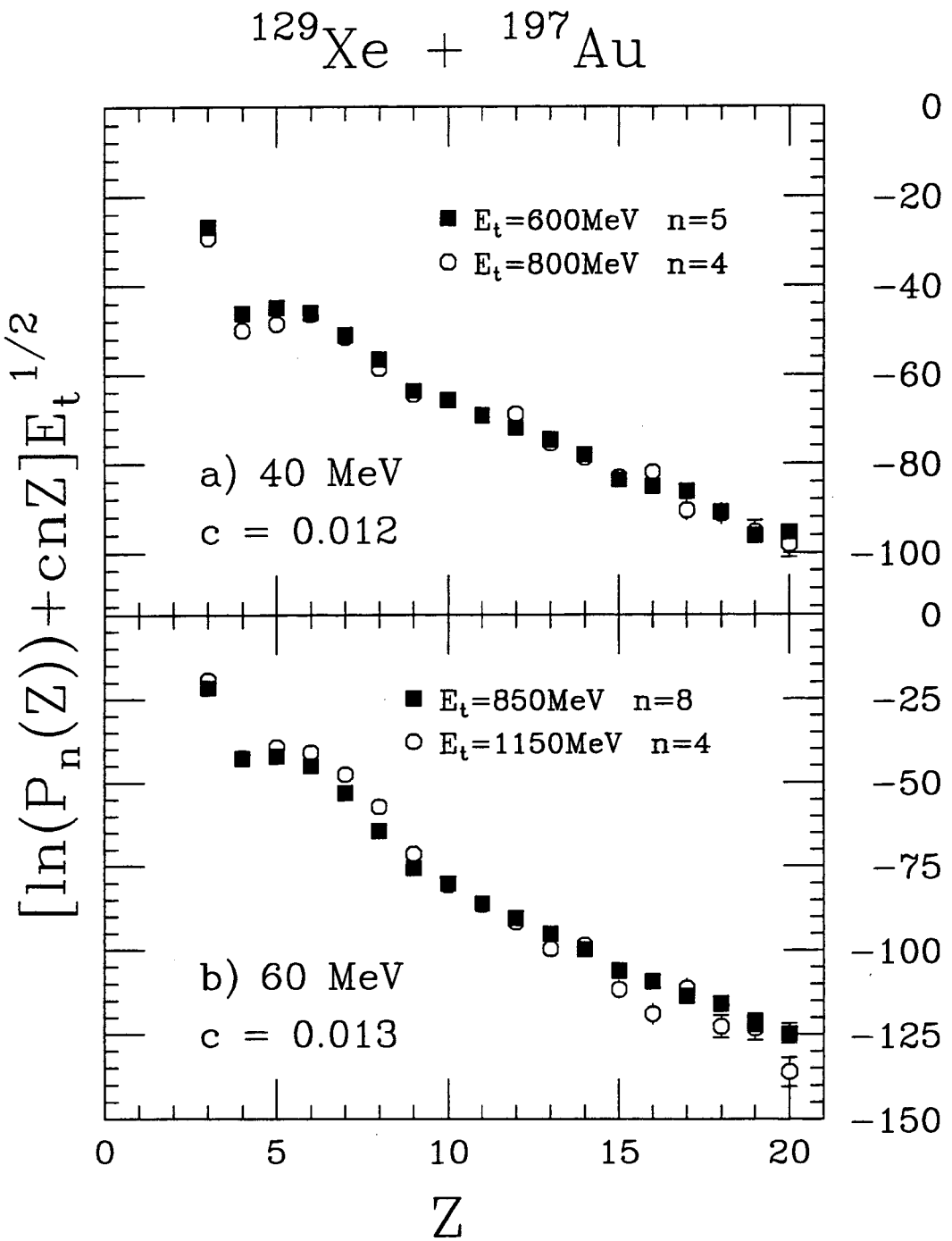

Figure 5.3 : The "reduced" charge distributions (see Equation 5.8), are plotted for the same cuts on E_t and n as Figure 5.1. The different data sets are normalized at $Z = 10$. The values of $c = 0.012$ and 0.013 are the spacings between the curves shown in Figure 5.2 for bombarding energies at $E/A = 40$ & 60 MeV respectively.

$F(Z)$ between any pair of charge distributions under investigation. More specifically, the difference in $F(Z)$ between pairs of charge distributions associated with different fragment multiplicities at a given transverse energy are accumulated and minimized as a function of c. The values of c that correspond to these minimum χ^2 are extracted and then averaged over the range of E_t. When this χ^2 approach is applied to the set of charge distributions reported in Figure 5.2, the average values of c extracted are 0.0123 ± 0.0039 and 0.0132 ± 0.0030 for the reaction ^{129}Xe + ^{197}Au at bombarding energies of $E/A = 40$ and 60 MeV respectively. These values of c agree reasonably well with those extracted from the exponential fit parameters α_n (see Table 5.1) using the approach mentioned in section 5.1.1. This consistency observed for the two different methods supports that the charge distributions shown in Figure 5.2 are indeed exponential and thus the extraction of c from α_n has not been biased by the exponential fitting procedure.

Alternatively, one can construct from a pair of charge distributions of a given E_t the ratio

$$\frac{P_n(Z)}{P_{n+1}(Z)} = e^{cZ}. \tag{5.11}$$

The natural logarithm of this ratio is plotted in Figure 5.4 as a function of Z for two of the charge distributions shown in Figure 5.1. The data (symbols) agree reasonably well with the linear fits (solid lines) except for large values of Z, where the statistics is poor. A value of c is extracted from the slope of the resulting graph for each pair of charge distributions at a given n and E_t. A weighted average of c (over all IMF multiplicities n and transverse energies E_t) can then be constructed. When this procedure is applied to the set of charge distributions ($Z = 4 - 20$) in Figure 5.2, the average values of c obtained are 0.0119 ± 0.0033 and 0.0133 ± 0.0025 for the reaction ^{129}Xe + ^{197}Au at bombarding energies of $E/A = 40$ and 60 MeV respectively (see

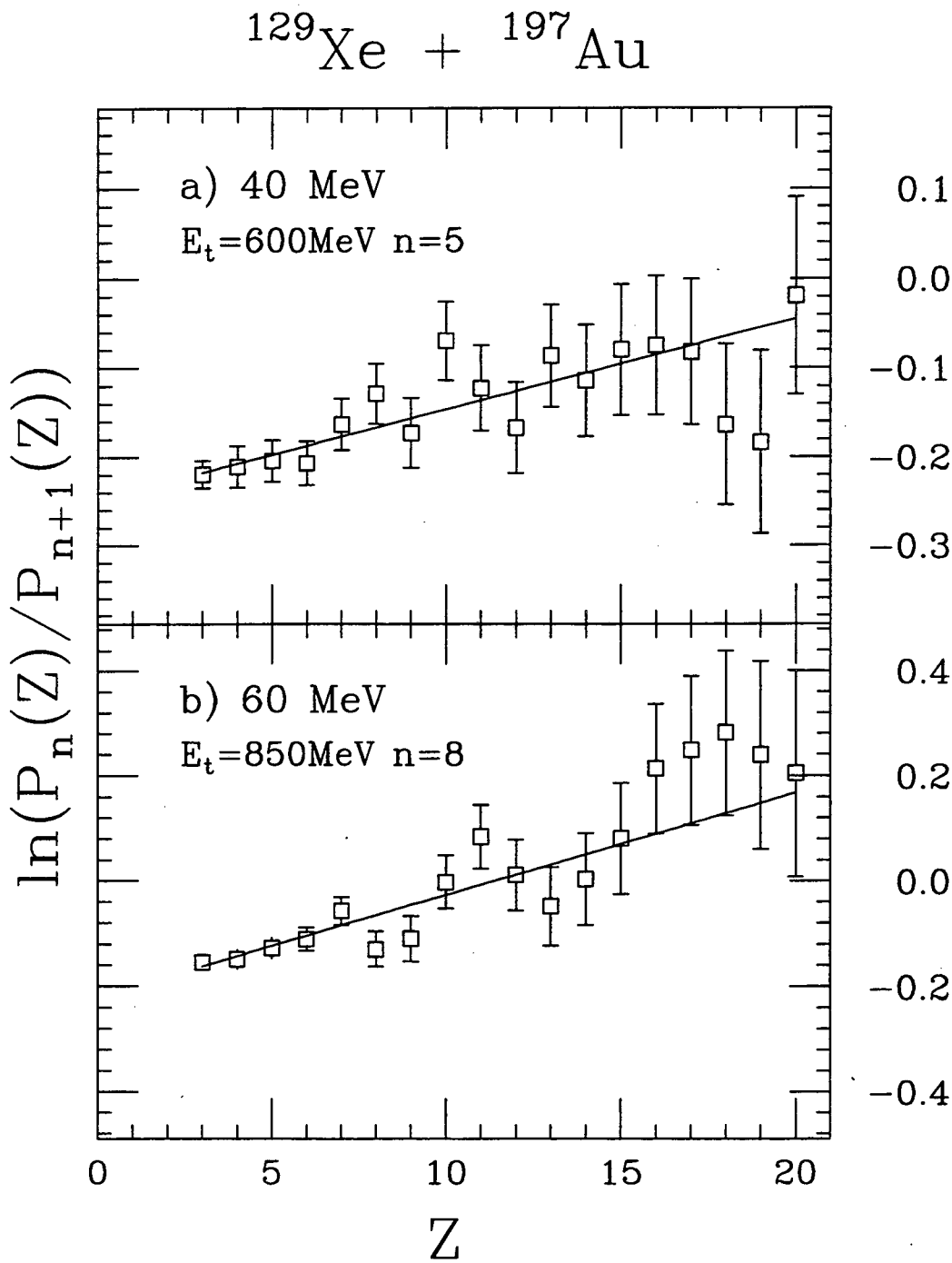

Figure 5.4 : The natural logarithm of the ratio $P_n(Z)/P_{n+1}(Z)$ is plotted as a function of Z for the indicated cuts on transverse energy E_t and IMF multiplicity n. The width of the cuts ΔE_t is 50 MeV. The solid lines are fits to the data.

Table 5.1).

The excellent agreement between the values of c extracted from three different procedures serves as a consistency test and substantiates the functional form of the scaling factor e^{-cnZ}. However, the extraction of c from α_n works for the exponential charge distributions only; whereas the ratio of $P_n(Z)/P_{n+1}(Z)$ and the χ^2 approach do not hinge on the functional form of the charge distributions.

Table 5.1 : Coefficient c extracted by three different procedures.

Method	$E/A = 40$ MeV	$E/A = 60$ MeV
α_n	0.0120	0.0130
χ^2	0.0123	0.0132
$P_n(Z)/P_{n+1}(Z)$	0.0119	0.0133

5.1.3 Origin and Interpretation of c

The physical significance of the thermal reducibility observed experimentally in the charge distributions is explored in this section. In particular, what is the origin of c or the regular offset observed in the plots of α_n vs. $1/\sqrt{E_t}$ (Figure 5.2). The general form of Equation 5.9 suggests the presence of a temperature dependent enthalpy term and an entropy term that does not depend on temperature explicitly. In thermodynamics, the general expression for the free energy

$$\Delta G = \Delta H(Z) - T\Delta S(n, Z) \tag{5.12}$$

leads to the following statistical distribution of Z:

$$P(Z) \propto e^{-\frac{\Delta H(Z)}{T} + \Delta S(n,Z)}. \tag{5.13}$$

If the transverse energy is assumed to be proportional to the excitation energy of the source, the empirically observed charge distribution of Equation 5.9 can

be rewritten in terms of temperature and its connection with Equation 5.13 becomes more apparent:

$$P(Z) \propto e^{-\frac{B(Z)}{\sqrt{E_t}}-cnZ} = e^{-\frac{B(Z)}{T}-cnZ}. \tag{5.14}$$

The first term in the exponent can be interpretated as an enthalpy term associated with the energy or barrier $B(Z)$ for the formation of a fragment. On the other hand, the connection between the second term cnZ and the entropy change ΔS needs further illustration. Typically, ΔS is of topological or combinatorial origin. In this case, it may point to an asymptotic combinatorial structure of the multifragmentation process in the limit of high temperature. In other words, when $T >> B(Z)$, the probability of emitting a fragment Z becomes nearly independent of Z, and the resulting charge distribution is constrained dominantly by charge conservation. As an example, the Euler's problem of breaking an integer into smaller integers in the least biased way is considered. Specifically, let us consider a nucleus of atomic number Z_o to be broken into n smaller pieces of integer charge. To derive the functional form for the resulting charge distribution, let n_Z be the number of fragments with charge Z. If every configuration of breaking the nucleus is equally probable, the most likely value of n_Z can be obtained by extremization of the function:

$$e^{-I} = e^{\sum[n_Z \ln n_Z - n_Z] + K\sum n_Z Z + \gamma \sum n_Z}, \tag{5.15}$$

where the Lagrange multipliers K and γ are associated with the constraints

$$\sum n_Z Z = Z_o; \qquad \sum n_Z = n. \tag{5.16}$$

From the extremization, one obtains

$$\frac{\partial I}{\partial n_Z} = \ln n_Z + KZ + \gamma = 0 \tag{5.17}$$

or

$$n_Z = e^{-KZ-\gamma}. \tag{5.18}$$

The constraints now read

$$Z_o = \sum Z e^{-KZ-\gamma} \sim \frac{e^{-\gamma}}{K^2}, \tag{5.19}$$

$$n = \sum e^{-KZ-\gamma} \sim \frac{e^{-\gamma}}{K}, \tag{5.20}$$

from which one obtains

$$n_Z = \frac{n^2}{Z_o} e^{-\frac{nZ}{Z_o}} = cn^2 e^{-cnZ}, \tag{5.21}$$

where c is defined as $1/Z_o$.

This expression has the correct asymptotic structure for $T \to \infty$ required by Equation 5.14 reinforcing the entropy interpretation. In this framework, the overall scale for the fragment charge distribution is set by the total charge Z_o. For a specific fragment multiplicity n, the scale is reduced by a factor n to the value Z_o/n. Thus the offset introduced in Equation 5.7 with increasing multiplicity n may just be due to this scale reduction. If this is so, the quantity c in Equation 5.7 takes the meaning $c = 1/Z_o$, and it reflects the size of the source. The empirical values from Figure 5.2 are $c \approx 0.012$ and $c \approx 0.013$ corresponding respectively to values of $Z_o \approx 83$ and $Z_o \approx 77$, which are quite reasonable for the source size.

The above discussion describes a scenario at high temperature, when the Z dependence of the emission barrier $B(Z)$ has a minimal effect on the resulting charge distribution (i.e. $e^{-B(Z)/T} \approx 1$). Under this condition, Euler's assumption of unbiased breaking of a source Z_o is satisfied, and a quantity c related to the source size is extracted from the multiplicity dependence of the resulting charge distributions. Simultaneous emission controlled by n–fragment transition state is a simple example. In this case, fragments are strongly aware of each other and would reflect such an awareness through the functional form e^{-cnZ} of their charge distributions. However, when temperature becomes comparable to the emission barrier $B(Z)$, competition between fragment emissions of different Z can no longer be neglected. In this

regime, the resulting charge distributions reflect the functional form of $B(Z)$ under the constraint of charge conservation according to Equation 5.14.

At very low temperature, emissions of IMFs are substantially suppressed by their large barriers and sizable residues are often found among the reaction products. In other words, Euler's assumption of unbiased partitioning of a source becomes inappropriate. The charge distributions are dominated by the term $e^{-B(Z)/T}$, and the quantity c becomes essentially 0. In this case, the sizable remnant serves as a charge conserving residue, and the resulting charge distributions are nearly independent of the fragment multiplicity. A nuclear system that undergoes sequential thermal emission is a simple illustration. Since fragment emissions are independent of one another, any fragment does not know how many other fragments will follow its emission. At each stage of the emission, charge conservation affects the charge of the emitted fragment minimally since the remaining sizable system serves as a charge conserving source. Consequently, the resulting charge distribution cannot reflect the requirement of an unbiased partition of the total charge among n fragments. This possibility of $c = 0$ suggests that while the form e^{-cnZ} implies charge conservation, it is not necessary that charge conservation be implemented in this unique way.

This predicted temperature dependence of c raises a question concerning the E_t dependence of c extracted experimentally. In particular, can one identify experimentally a transition from a regime for which $c = 0$ to a new regime for which $c > 0$? In the previous sections, an average value of c over a range of E_t has been extracted empirically and shown to be able to collapse the charge distributions of different n and E_t onto a nearly universal curve. However, the charge distributions associated with events of relatively low E_t have not been included in the previous extractions of c because they are not always exponential. Since methods have been developed to extract c from the charge distributions of non–exponential form (see

section 5.1.2), determination of c for events of low E_t becomes feasible. In fact, the E_t dependence on the shape or functional form of the charge distributions may be caused by an E_t dependence of c.

5.2 Transverse Energy Dependence of c

In this section, the energy dependence of c is studied, and an weighted average of c over all fragment multiplicities is extracted as a function of E_t over the entired measured range. For example, the extraction of c from the ratio of $P_n(Z)/P_{n+1}(Z)$ is demonstrated in Figure 5.5 for an arbitrarily chosen value of E_t. The charge distributions at $E_t = 1000$ MeV are shown in the top panel for the reaction ^{129}Xe + ^{197}Au at a bombarding energy of $E/A = 60$ MeV. The log of the ratio $P_n(Z)/P_{n+1}(Z)$ is evaluated from each pair of the charge distributions, and as an example, the result for $n = 6$ is plotted as a function of Z in the lower panel. The expected linear dependence (Equation 5.11) is demonstrated by the good agreement between the data (symbols) and the fit (solid line). A value of c is extracted from the slope and an average over different values of n is found to be 0.015 at this E_t. When this value of c is used in Equation 5.10 to calculate the reduced quantity $F(Z)$, the different charge distributions in the top panel are shown to collapse onto a universal curve in the middle panel. This confirms the reducible nature of the charge distributions. The value of c (0.015) extracted at this E_t is slightly higher than the average value reported in Table 5.1, and this reflects local deviations in the charge distributions.

The values of c extracted from the ratio of $P_n(Z)/P_{n+1}(Z)$ and by the χ^2 method are reported in Figure 5.6 as a function of E_t for the reaction ^{129}Xe + ^{197}Au at bombarding energies of $E/A = 40$ & 60 MeV. It is interesting to notice that the two procedures yield essentially the same results at both bombarding energies, namely,

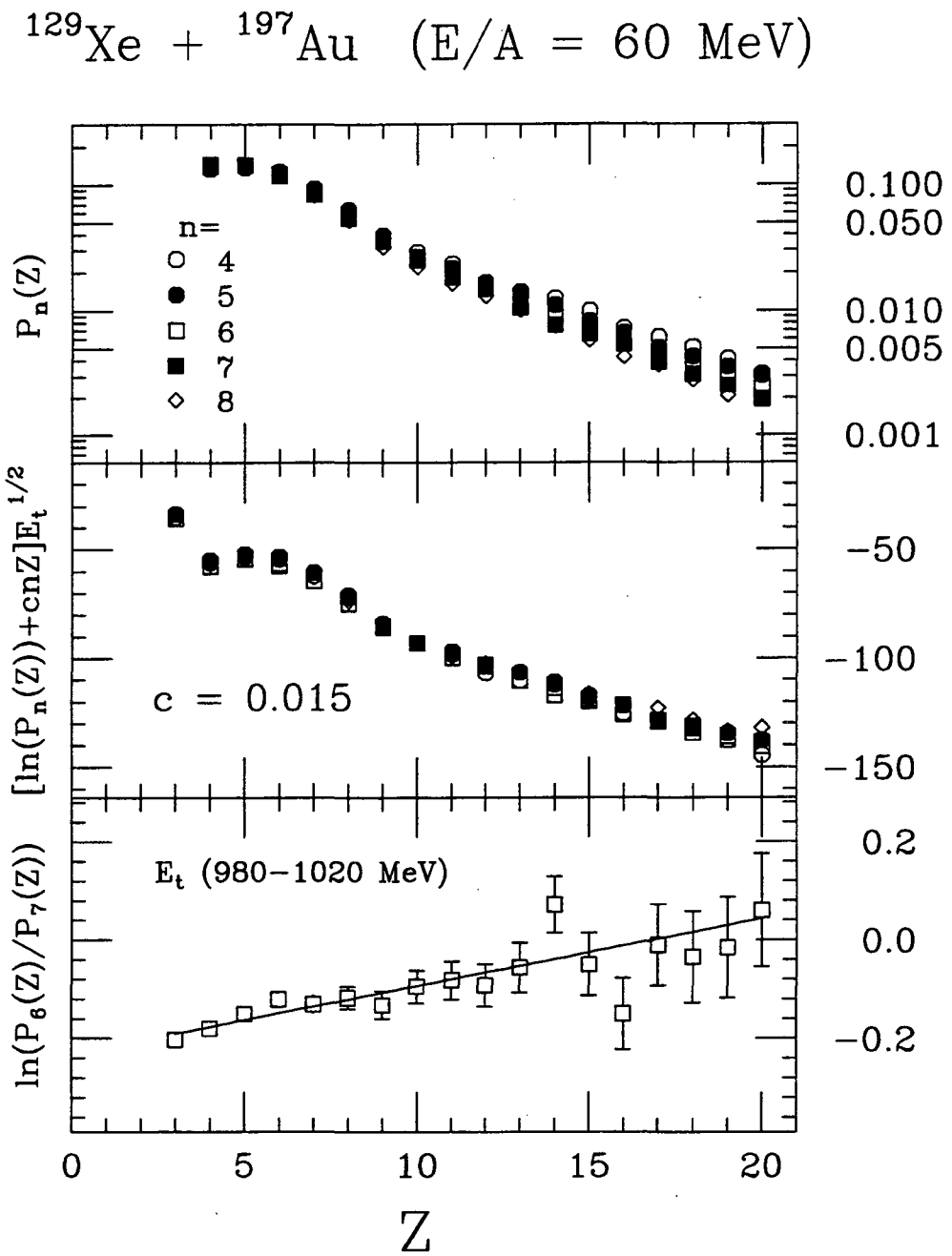

Figure 5.5 : Top panel: the charge distributions $P_n(Z)$ gated on n for the reaction ^{127}Xe+^{197}Au at $E/A = 60$ MeV. The charge distributions were constructed from events with $E_t = 1000 \pm 20$ MeV and $n = 4 - 8$. Middle panel: the "reduced" charge distributions for the same data using the indicated value of c. (The data here are normalized at $Z = 10$). Bottom panel: the log of the ratio $P_6(Z)/P_7(Z)$. The slope corresponds to c for $n = 6$ (see Equation 5.11).

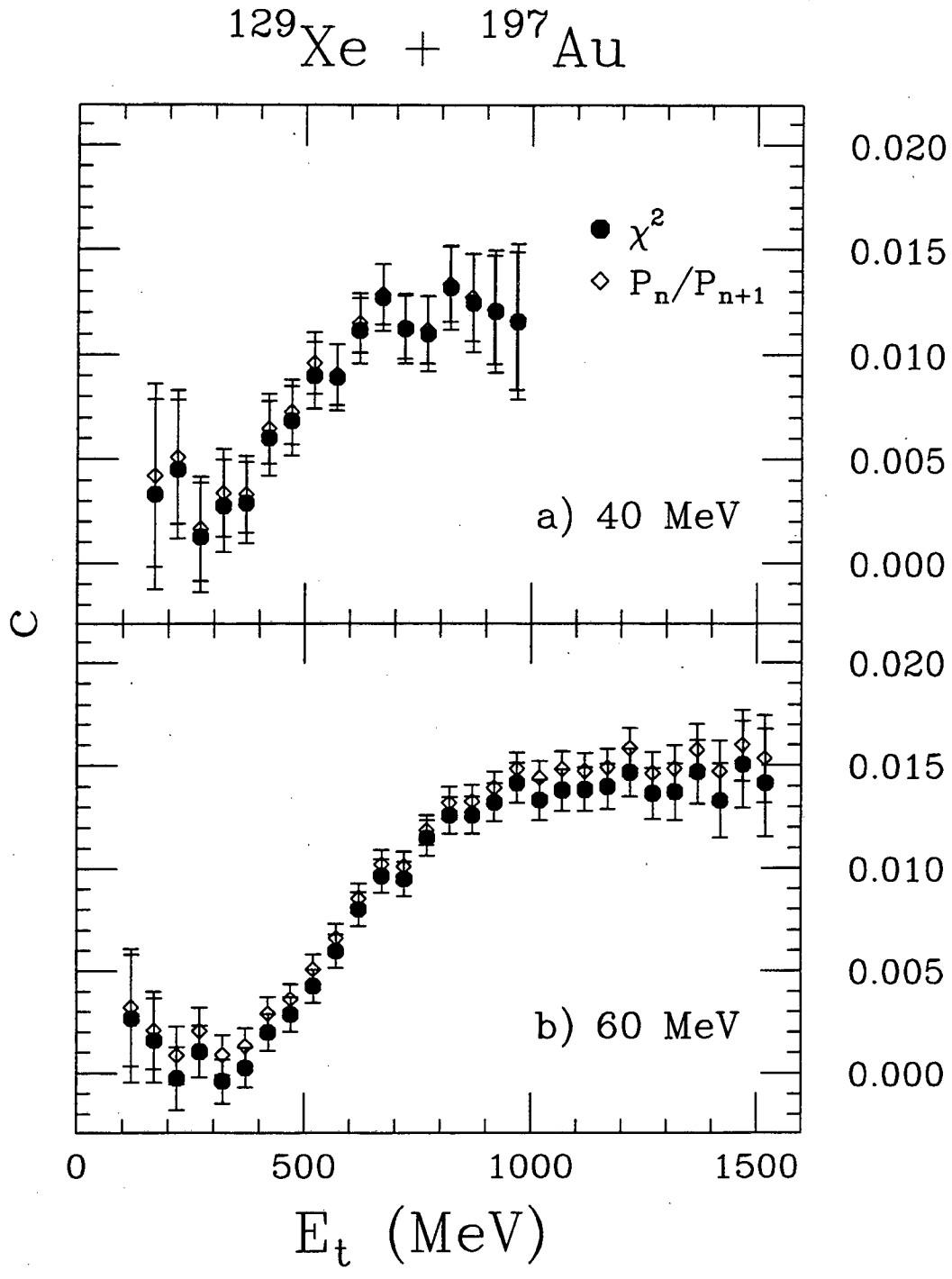

Figure 5.6 : The coefficient c extracted by the χ^2 method (solid symbols) and from the ratio of $P_n(Z)/P_{n+1}(Z)$ (open symbols) as a function of E_t for the reaction ^{129}Xe+^{197}Au at $E/A = 40$ (top panel) and 60 MeV (bottom panel).

the quantity c starts at or near zero, and it rises rapidly with increasing E_t until it reaches a saturation value at high E_t. Under the assumption that the transverse energy is proportional to the excitation energy, this observation is indeed consistent with the predicted temperature dependence of c in section 5.1.3. In other words, the $c = 0$ regime may signify an evaporative–like emission from a source which survives as a charge conserving residue, while the $c > 0$ regime may signify the complete vaporization of the source.

To test these interpretations of c, a finite percolating system has been studied. To be more precise, percolation calculations [Baue 88] were performed for systems of $Z_o = 97$, 160 and 400 as a function of the percentage of bonds broken (p_b). This quantity p_b is related to the excitation energy or temperature of the nucleus. When the nucleus is cold, the percentage of bonds broken (p_b) is small and a large cluster extending throughout the lattice exists (percolating cluster). However, when the excitation energy of the system increases, the percentage of bonds broken (p_b) increases accordingly until it reaches a critical value (p_b^{crit}) beyond which no percolating cluster exists and the nucleus breaks into many smaller clusters.

The resulting fragment charge distributions of percolation calculations have the same n dependence of the form e^{-cnZ}. Values of c are extracted as a function of p_b by the χ^2 method, and a similar dependence on p_b is observed for all three systems as shown in Figure 5.7a. For values of p_b smaller than the critical value ($p_b^{crit} \approx 0.75$), a large cluster exists and c is found to be 0. As p_b goes above its critical value, c is found to increase and eventually saturate in a way very similar to that observed experimentally. In fact, the extracted values of c decreases with increasing Z_o as expected from the Euler's solution. However their saturation values are much larger than the corresponding values of $1/Z_o$. This quantitative discrepancy possibly points out the sensitivity of c towards the dimensionality of the system. The Euler's

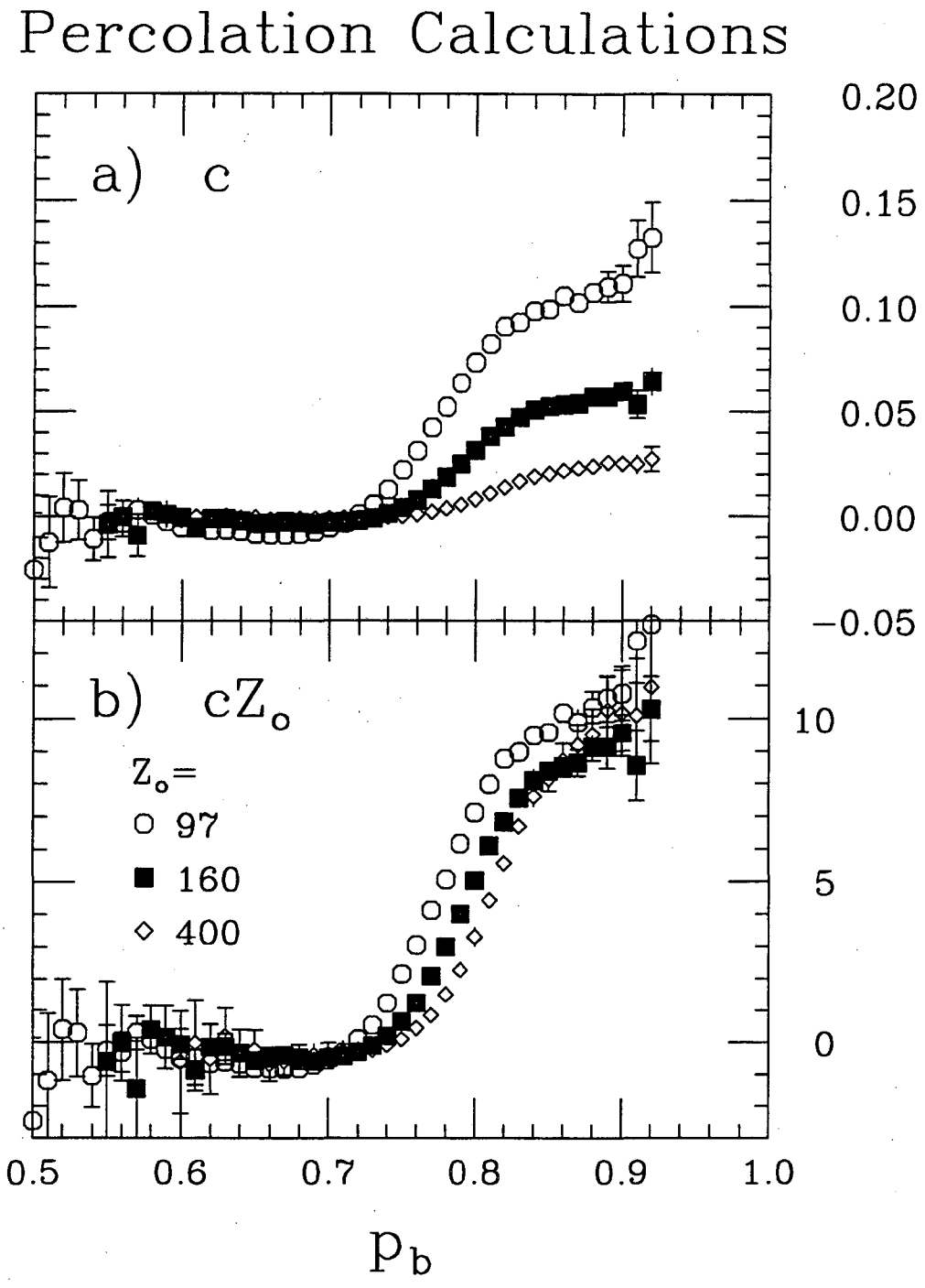

Figure 5.7 : The extracted values of c (top panel) and cZ_o (bottom panel) as a function of the percentage of bonds broken (p_b) for three different systems of indicated size Z_o.

solution (Equation 5.21) and the associated dependence of c upon Z_o have been derived for a one–dimensional percolation model. Therefore, it is possible that c is proportional, but not equal, to $1/Z_o$ for the three–dimensional percolation calculation reported in Figure 5.7a. Furthermore, the analysis is not directly comparable to the Euler's solution, since the study of how the source is partitioned into different IMF multiplicities is restricted to a limited region ($3 < Z < 20$) of the total charge distribution. The effect of this restricted partition will be discussed in section 5.3.

The observed dependence of c upon Z_o points out a possible misinterpretation of c when its value is very close to 0. There is no doubt that $c = 0$ in the presence of a charge conserving residue. However, when the size of an emission source is big, the extracted value of c also approaches 0 even if no sizable residue exists. These considerations suggest that cZ_o may be a better intensive quantity to probe the transition from the regime of $c = 0$ to $c > 0$. The idea is to scale the extracted values of c by the source size Z_o in order to remove this leading dependence, and to evidentiate the true transition from the regime of $c = 0$ to $c > 0$. The resulting product cZ_o is plotted as a function of p_b in Figure 5.7b for the above three systems of different source size. The region in which p_b is small and $c = 0$ remains unaffected by this procedure, but the different saturation values of c at high p_b are converged to a nearly universal curve confirming that c is indeed proportional to $1/Z_o$. This observed universality also stresses that the observed non–zero value of c is not just a finite–size effect. It is certainly true that c approaches 0 as the source size Z_o goes to infinity, it is also true that the product cZ_o tends to a finite limit nearly independent of Z_o.

An evaporation calculation has also been carried out for the nuclei ^{64}Cu and ^{129}Xe according to the thermal binomial scheme [Ghet 95, More 95]. The only constraint introduced is to prevent at every step the emission of fragments larger than the available source. The resulting charge distributions are very well reproduced by

Equation 5.9. The extracted quantities c and cZ_0 are plotted in Figure 5.8 as a function of excitation energy per nucleon. In both cases c goes from 0 to a positive finite value as the excitaiton energy increases. Similarly, the extracted values of c can be scaled by Z_0. The region where $c = 0$ is readily identified with the region where a large residue survives. On the other hand when $c > 0$ there is no surviving residue.

The results of these percolation and evaporation calculations demonstrate the sensitivity of c to the presence or absence of a charge conserving residue and reinforce the interpretations of c in two different regimes. Along this line, the evolution of c from zero to non–zero quantity can be compared to 1st order phase transition of a fluid moves from the region of liquid–vapor coexistence to the region of unsaturated vapor. As an illustration, Figure 5.9 shows a liquid–gas phase diagram of an ordinary fluid. The area below the dashed line is the region where mixtures of the liquid and gas phases coexist. In this coexistence region, the presence of the liquid phase guarantees mass conservation at all average densities for any given temperature. The saturated vapor pressure is solely a function of temperature, and thus for a given isotherm, a plateau is present in the coexistence region of the phase diagram indicating a constant saturated vapor pressure independent of the volume. In other words, a change in mean density (volume) merely changes the relative amount of the liquid and vapor, without altering the saturated vapor properties. Hence the vapor properties and in particular the cluster size distributions cannot reflect the total mass or even the mean density of the system. This is the region for $c = 0$. On the other hand, in the region of unsaturated vapor, there is no liquid to insure mass conservation. Thus the vapor itself must take care of this conservation, at least grand canonically. Consequently, in this state when there is only one phase of vapor, the pressure becomes a function of temperature and volume. The properties of the unsaturated vapor then depend on the total mass of fluid, and thus $c > 0$.

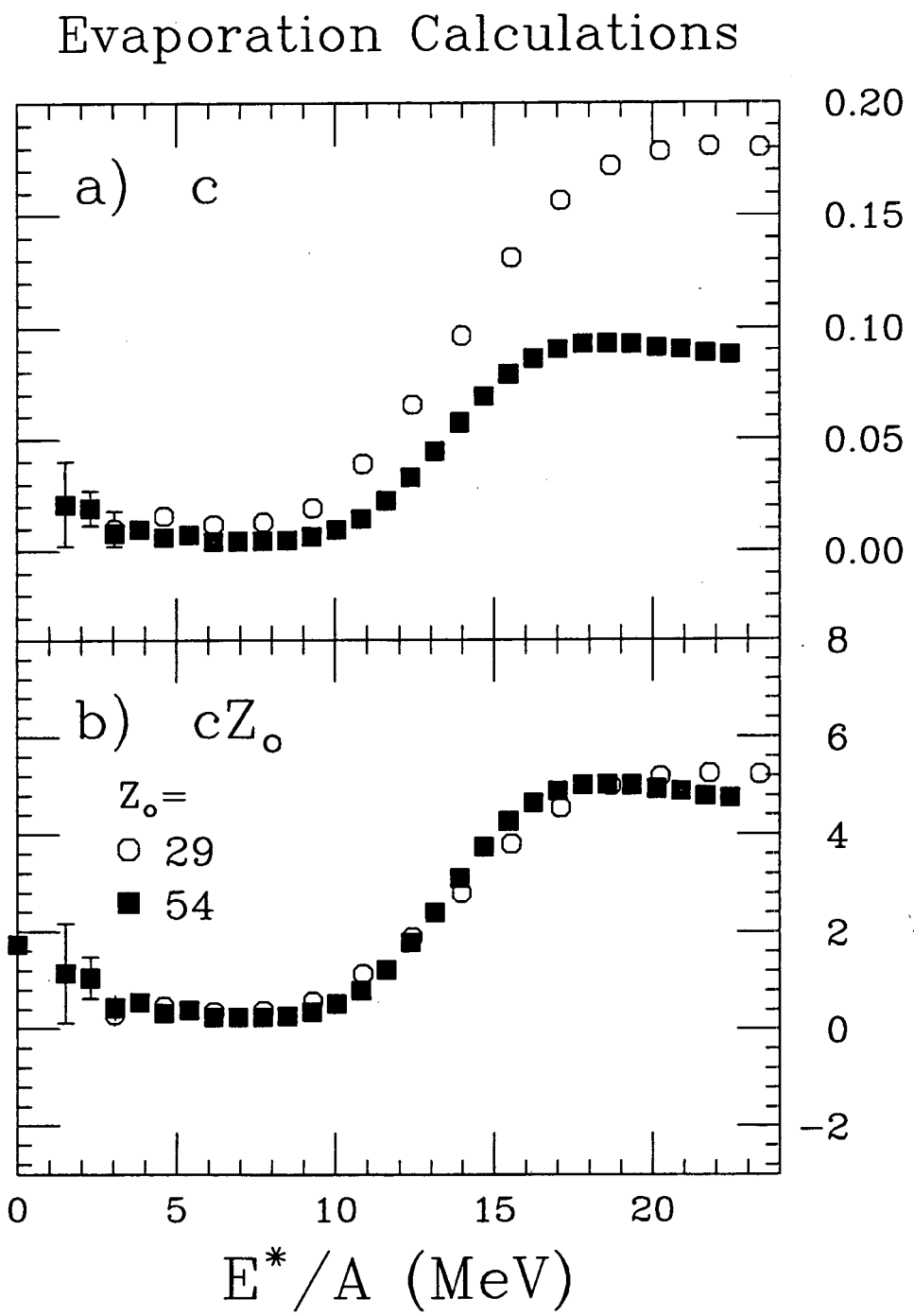

Figure 5.8 : The extracted values of c (top panel) and cZ_o (bottom panel) as a function of the excitation energy per nucleon for ^{64}Cu and ^{129}Xe nuclei from a binomial evaporation calculation.

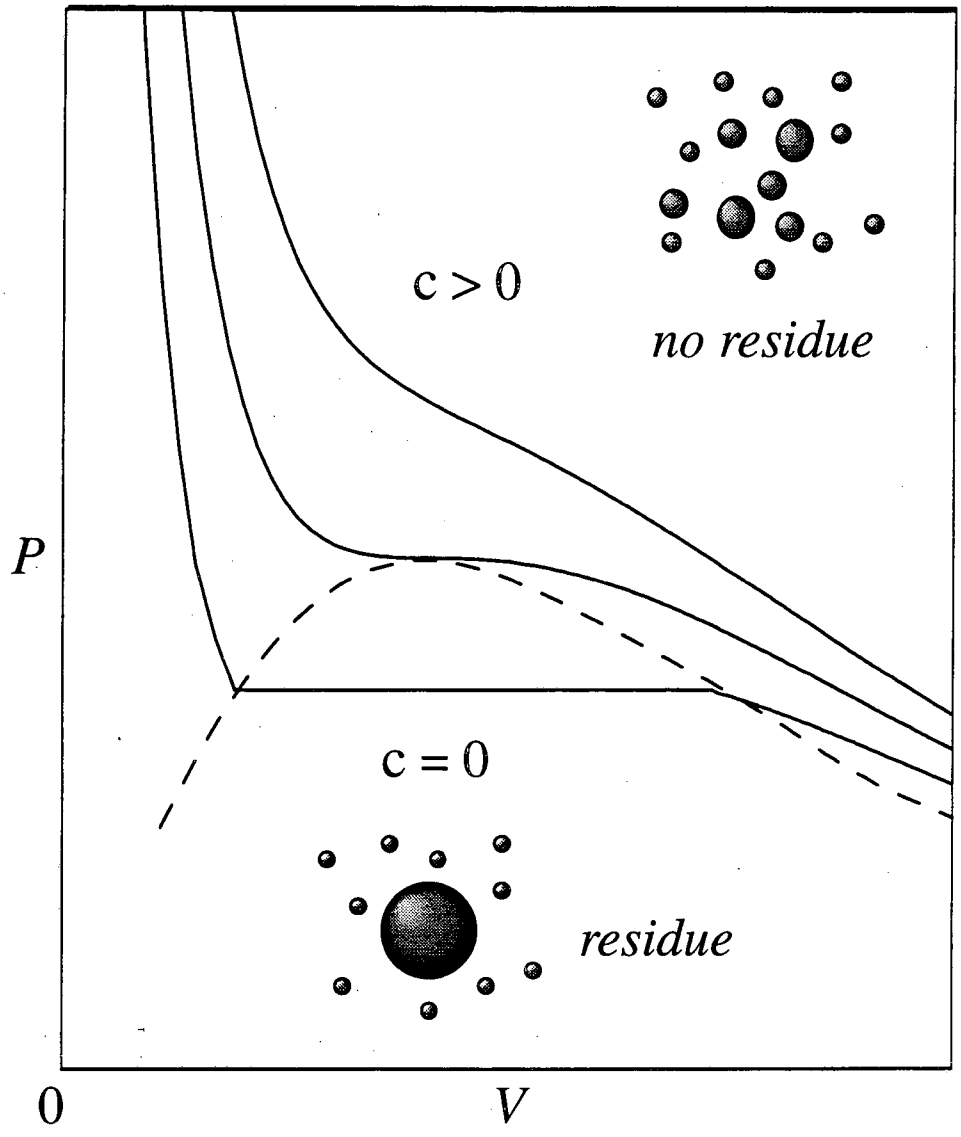

Figure 5.9 : Liquid–gas phase diagram. The top of the dashed line is the critical point. The area below the dashed line ($c = 0$) is the region where mixtures of the liquid and gas phases coexist.

This description suggests a possible physical significance of the observed energy dependence of c in terms of thermodynamics of the liquid–vapor phase coexistence. To be more precise, $c = 0$ may indicate the presence of two phases (liquid–vapor) while $c > 0$ may indicate the presence of one phase (unsaturated vapor) using the above analogy of liquid–vapor equilibrium.

5.3 $Z_{threshold}$ effect on the extraction of c

In the above analysis, the scaling factor e^{-cnZ} used to account for the n dependence of the charge distributions was shown to arise naturally in the charge distribution obtained by the least biased breaking of an integer Z_o into n integers (Euler's problem): $P(Z) = cn^2e^{-cnZ}$ (Equation 5.21). In the context of the charge distribution, n is the charged particle multiplicity and $c = 1/Z_o$, where Z_o is the total charge of the emission source.

Experimentally, it is very difficult to isolate and eliminate the pre–equilibrium contribution associated with the light charged particle emission. This contamination overestimates the value of n associated with the number of particles emitted from the thermally equilibrated source, and it also distorts the shape of the charge distribution for the light charged particles. To reduce this pre–equilibrium contamination, the charge distributions of intermediate mass fragment ($Z_{threshold} \leq Z \leq 20$) were studied as a function of fragment multiplicity (N_{IMF}) in the previous sections. The value of n in e^{-cnZ} then became N_{IMF}, and c was extracted by fitting the charge distributions of IMFs with $e^{-cN_{IMF}Z}$. If c_o is the value of c extracted from the charge distributions of all particles, it can be related to c by their common exponential fit parameters,

$$c_o \cdot n = c \cdot N_{IMF}. \tag{5.22}$$

This equation simply says that c extracted experimentally from the charge distributions of IMFs is different from c_o, since $n \neq N_{IMF}$ when a constraint is imposed on the partitioning of the source by setting a lower $Z_{threshold}$ in the IMF definition. In fact, this was one of the reason mentioned in section 5.2 for the discrepancy between $1/Z_o$ and the value of c extracted from the percolation data. In this section, the effect of $Z_{threshold}$ on the extraction of c is studied in order to obtain a constant value for c_o.

If the charge distribution $P_n(Z)$ of a given particle multiplicity n is normalized such that the total area under the curve $P_n(Z)$ is equal to n, then the number of fragments (N_{IMF}) is simply the integrated area bounded by $Z = Z_{threshold}$ and $Z = 20$. In other words, N_{IMF} can be calculated from n by integrating the charge distribution of Equation 5.21 from $Z = Z_{threshold}$ to 20:

$$N_{IMF} = \int_{Z_{threshold}}^{20} c_o n^2 e^{-c_o n Z} dZ = n \left[e^{-c_o n Z_{threshold}} - e^{-c_o n (20)} \right] \tag{5.23}$$

The exponential dependence on $Z_{threshold}$ in the above equation suggests that it can be simplified if the values of $Z_{threshold}$ are much smaller than 20. Under this condition, the above integral becomes independent on the upper limit of the IMF definition,

$$N_{IMF} \simeq \int_{Z_{threshold}}^{\infty} c_o n^2 e^{-c_o n Z} dZ = n e^{-c_o n Z_{threshold}}. \tag{5.24}$$

The above expression shows that N_{IMF} is related to n with a strong dependence on the lower $Z_{threshold}$ of the IMF definition. In the limit of small $Z_{threshold}$, the exponential term of Equation 5.24 approaches one and N_{IMF} approaches the value of n. However, as $Z_{threshold}$ increases, N_{IMF} becomes less than n and this deviation becomes progressively larger.

Since N_{IMF} can be determined experimentally, it would be more useful to express n in terms of N_{IMF}. An approximation by a Taylor expansion of Equation

5.24 up to second order yields the following expression :

$$n(N_{IMF}) = N_{IMF} + c_o Z_{threshold} N_{IMF}^2 + 1.5(c_o Z_{threshold})^2 N_{IMF}^3. \tag{5.25}$$

To study the effect of $Z_{threshold}$ on the extraction of c, the variable n in Equation 5.22 is expressed in terms of N_{IMF} according to Equation 5.25,

$$\begin{aligned} c \cdot N_{IMF} &= c_o \cdot \left[N_{IMF} + c_o Z_{threshold} N_{IMF}^2 + 1.5(c_o Z_{threshold})^2 N_{IMF}^3\right] \\ c &= c_o \cdot \left[1 + c_o Z_{threshold} N_{IMF} + 1.5(c_o Z_{threshold} N_{IMF})^2\right]. \end{aligned} \tag{5.26}$$

The above equation clearly indicates that an N_{IMF} dependence is introduced into the quantity c by setting a lower $Z_{threshold}$ in the definition of IMF. The resulting value of c will always be larger than c_o, and this deviation increases with increasing values of N_{IMF} and $Z_{threshold}$. To verify these ideas experimentally, values of c have been extracted by the χ^2 method from the charge distributions associated with different values of N_{IMF} and $Z_{threshold}$. These extracted values of c are plotted in Figure 5.10 as a function of E_t for the reaction ^{129}Xe + ^{197}Au at a bombarding energy of $E/A = 60$ MeV. In the top panel, average values of c have been extracted over several consecutive fragment multiplicities in order to minimize statistical uncertainties. Clearly, the extracted values of c associated with events of higher fragment multiplicity are larger at all values of E_t. In the bottom panel, the average value of c (over all fragment multiplicities), is found to increase with increasing $Z_{threshold}$. These results demonstrate the expected N_{IMF} and $Z_{threshold}$ dependence of c.

In an attempt to eliminate the N_{IMF} dependence of c in order to extract c_o, n of e^{-cnZ} is expressed in terms of N_{IMF} and $Z_{threshold}$ following Equation 5.25. The reduced quantity $F(Z)$ of Equation 5.10 then becomes

$$F(Z) = [\ln P_{N_{IMF}}(Z) + c_o n(N_{IMF}) Z] \sqrt{E_t}, \tag{5.27}$$

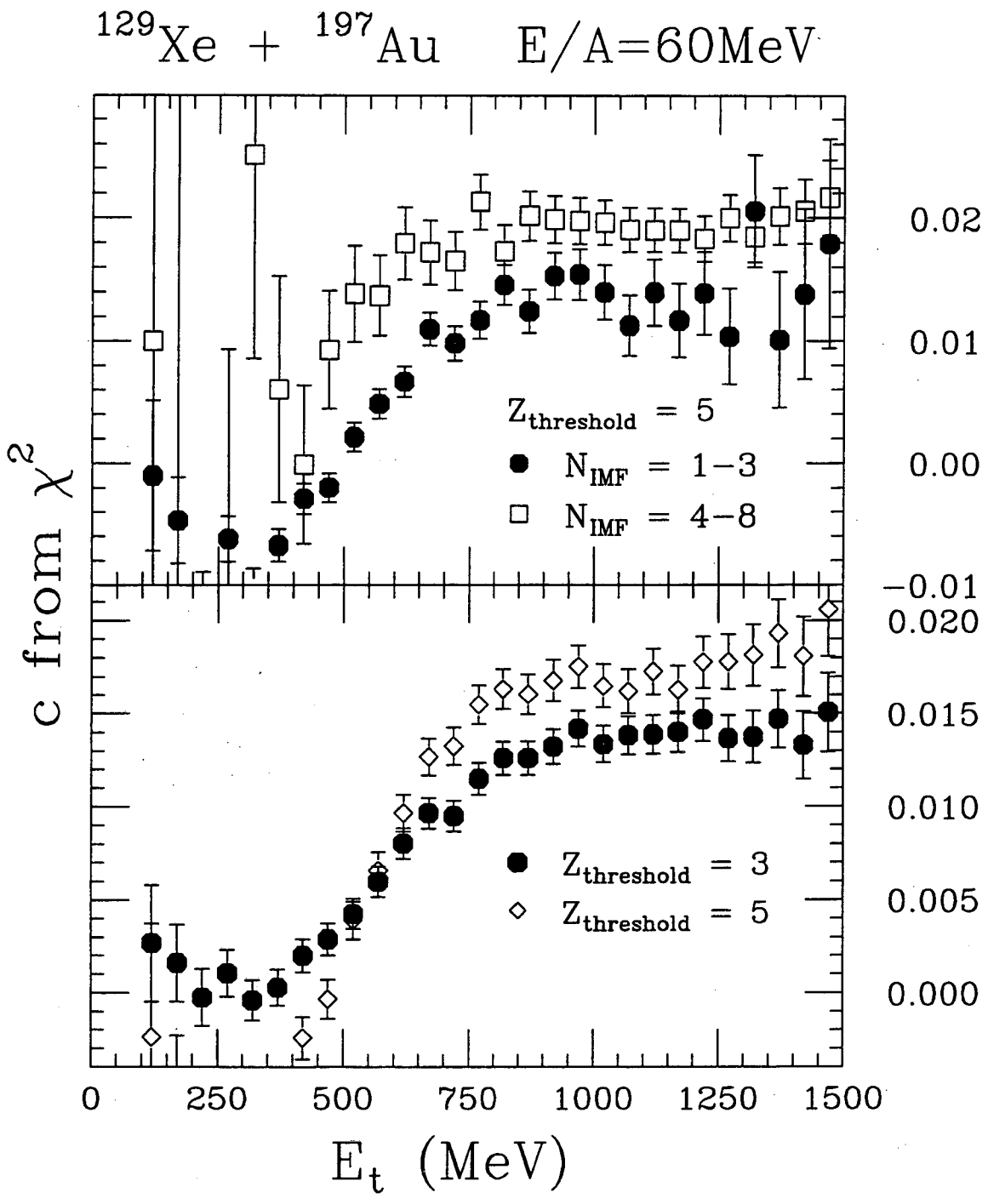

Figure 5.10 : The coefficient c extracted by the χ^2 method as a function of E_t for the reaction ^{129}Xe + ^{197}Au at a bombarding energy of $E/A = 60$ MeV. c are extracted from the charge distributions associated with indicated values of N_{IMF} (top panel) and $Z_{threshold}$ (bottom panel).

where the variable c is replaced with c_o since the $Z_{threshold}$ effect has been properly considered in the expression of n. A χ^2 is then constructed with this new functional form and c_o can be extracted using the same procedure. The top panel of Figure 5.11 shows that c_o is now independent of the various N_{IMF} cuts over a large range of measured E_t. However, a slight increase in c_o with increasing $Z_{threshold}$ is observed in the bottom panel indicating that the effect of $Z_{threshold}$ has not been completely accounted for. This residual $Z_{threshold}$ dependence may be related to the Z dependence of the detection efficiency in the experimental device which has not been accounted for. It is well known that the detection thresholds for the MSU Miniball phoswich array and the LBL silicon array depend strongly on the charge of the incident particles detected experimentally.

It is observed that the extracted values of c remain constant over a large range of E_t in Figure 5.11. Therefore, it may be statistically feasible to extract values of c associated with individual N_{IMF} if events of different E_t are binned together in this saturation region. For example, events with E_t ranged from 800 to 1500 MeV are binned together to extract c using the χ^2 method. The diamonds in Figure 5.12 show the expected N_{IMF} dependence of c for $Z_{threshold} = 3$ (upper) and 5 (lower) as well. The result also illustrates the $Z_{threshold}$ dependence since the extracted value of c is always larger for $Z_{threshold} = 5$ at a given N_{IMF}. However, when n is expressed in terms of N_{IMF} following Equation 5.25 in the χ^2 construction, the above N_{IMF} dependence is eliminated as shown by the circles in Figure 5.12. The circles scatter around the weighted average (dashed lines) of $c_o = 0.081 \pm 0.0016$ and 0.0098 ± 0.0015 for $Z_{threshold} = 3$ and 5 respectively. Similarly, the discrepancy in the values of c_o for two different $Z_{threshold}$ may be due to other residual effects that have not been considered.

Thus far, the fragment multiplicity (N_{IMF}) dependence of the charge dis-

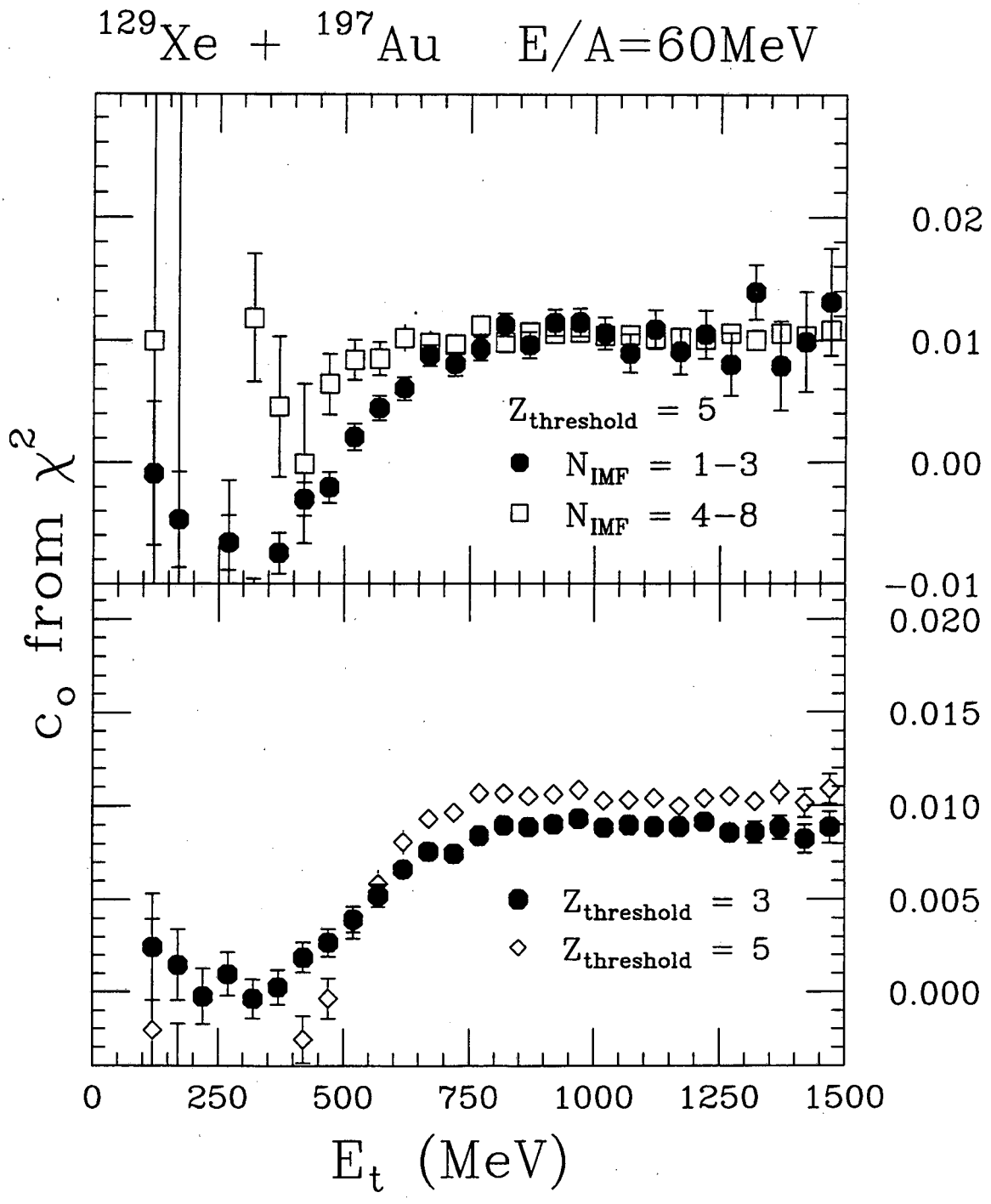

Figure 5.11 : The coefficient c_o extracted by the χ^2 method as a function of E_t for ^{129}Xe + ^{197}Au reaction at a bombarding energy of E/A = 60 MeV. In this extraction, n is expressed in terms of N_{IMF} using Equation 5.25. c_o are extracted from the charge distributions associated with indicated values of N_{IMF} (top panel) and $Z_{threshold}$ (bottom panel).

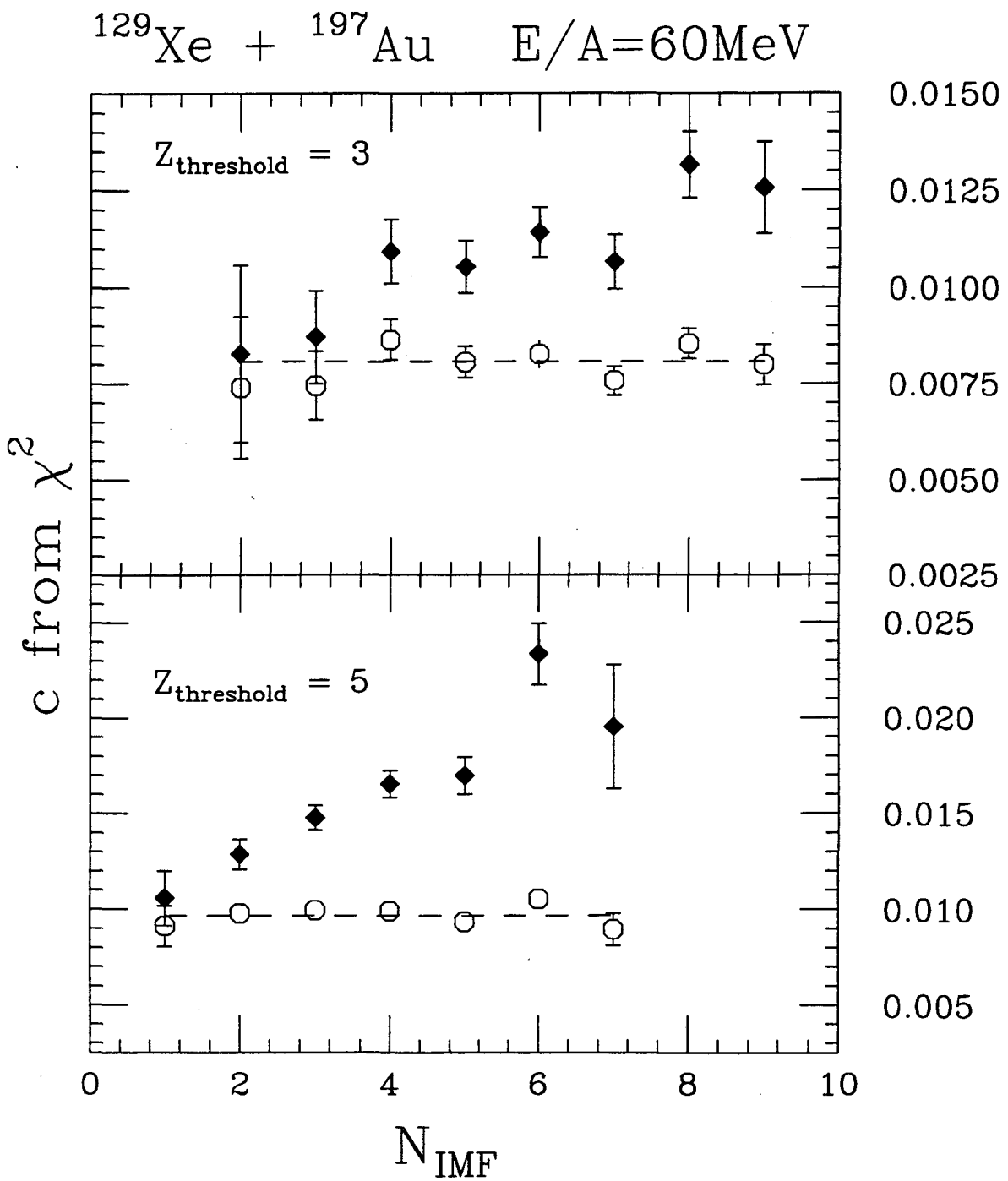

Figure 5.12 : The coefficients c (diamonds) and c_o (circles) extracted by the χ^2 method as a function of N_{IMF} for the charge distributions of $Z_{threshold} = 3$ (top panel) and $Z_{threshold} = 5$ (bottom panel).

tributions has been studied for the reaction ^{129}Xe + ^{197}Au at a bombarding energy of E/A = 60 MeV. The empirically observed N_{IMF} dependence of c is shown to be related to the lower $Z_{threshold}$ of the IMF definition. To account for the effect of $Z_{threshold}$, the number of partitioned fragments n in Euler's problem is expressed in terms of the experimental fragment multiplicity defined by $Z_{threshold}$. A constant value of c_o is then extracted independent of the fragment multiplicity. This correction for the effect of $Z_{threshold}$ may help to relate c_o extracted from the experiment to the size of the emission source.

5.4 Target Independence

In section 4.7, the observed target independence in the Arrhenius plots was shown to be consistent with an incomplete fusion picture assuming that thermal equilibration is achieved only in the vicinity of the overlapping region of the two nuclei. In this scenario, the size and the thermal properties of the emission source become independent of the specific target. When this idea is extended to the charge distribution analysis, one expects a target independence in the extraction of c. In particular, the saturated value of c, which is proportional to the size of the emission source, is expected to be a constant independent of the specific target.

In Figure 5.13, the values of c extracted by the χ^2 method (top panel) and from the ratio of $P_n(Z)/P_{n+1}(Z)$ (bottom panel) are plotted as a function of E_t for the ^{129}Xe-induced reactions on ^{nat}Cu, ^{89}Y, ^{165}Ho and ^{197}Au targets at a bombarding energy of E/A = 60 MeV. The data for the lower bombarding energy are not shown since most of their maximum values of E_t are not high enough for c to reach its saturation. At E/A = 60 MeV, both extraction procedures produce essentially the same results for all four targets, namely, the quantity c rises rapidly with increasing

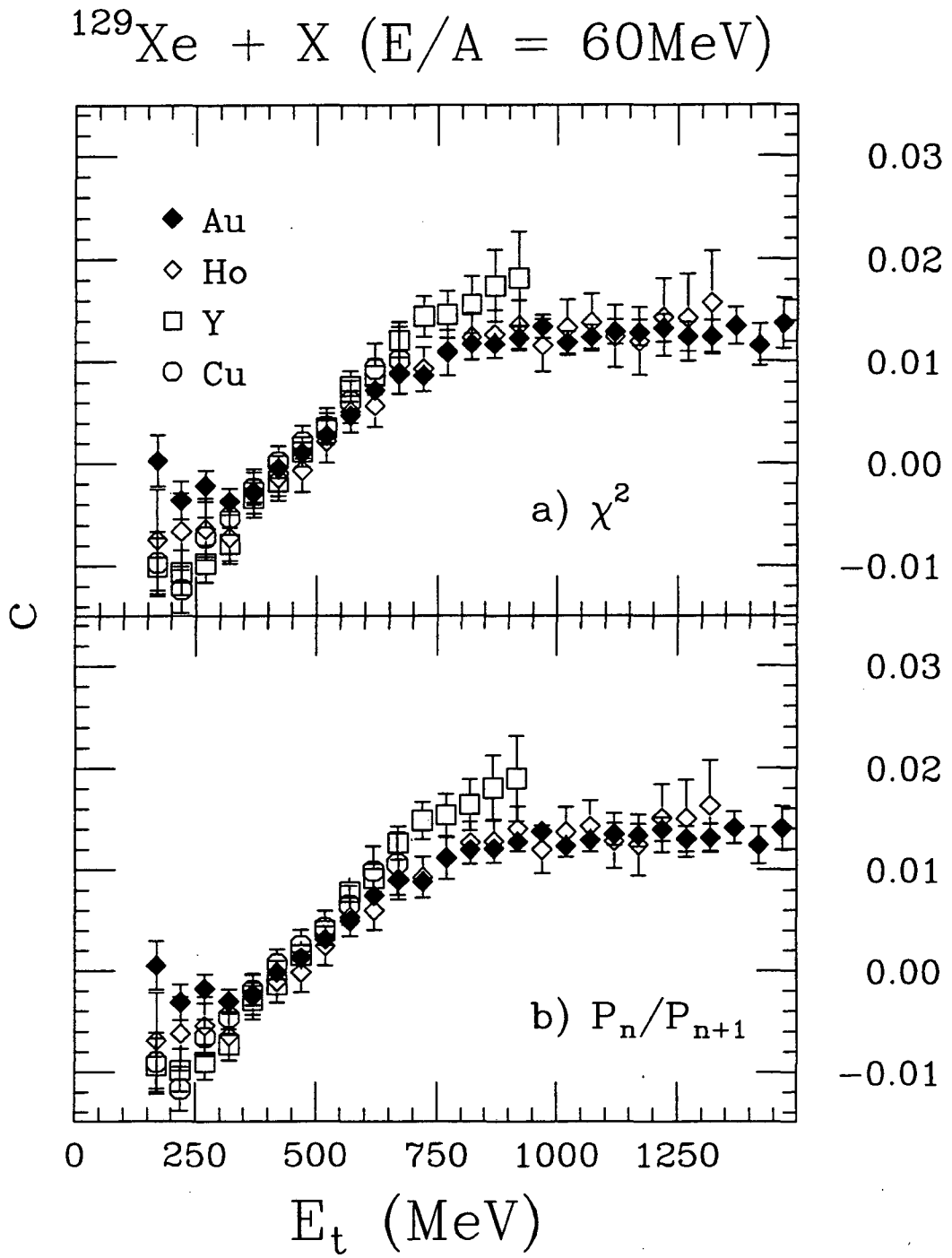

Figure 5.13 : The coefficient c extracted by the χ^2 method (top panel) and from the ratio of $P_n(Z)/P_{n+1}(Z)$ (bottom panel) as a function of E_t for the ^{129}Xe-induced reactions on ^{nat}Cu, ^{89}Y, ^{165}Ho and ^{197}Au targets at a bombarding energy of E/A = 60 MeV.

E_t until it reaches a saturation value at high E_t. The physical significance of this energy dependence has been discussed in section 5.2. A more interesting feature is that the extracted values of c are independent of the specific target over a large range of E_t. This again supports the idea that the thermal properties of the emission source are target independent. The nearly identical saturation values of c observed for the ^{165}Ho and ^{197}Au targets also reflect the similar size of the emission sources. However, the rising values of c stop at their highest E_t before they reach a saturation for the ^{nat}Cu and ^{89}Y targets. Deviations are also observed for the ^{89}Y data at the region of high E_t, and may be related to the poor statistics at the tail of the E_t distribution.

The implications of the experimental evidence presented above are far reaching. On the one hand, the thermal features observed in the n–fragment emission probabilities extend consistently to the charge distributions and strengthen the hypothesis of phase space dominance in multifragmentation. On the other hand, the reducibility of the n–fold–event charge distributions to a universal function of Z highlights the near independence of individual fragment emission, limited only by the constraint of charge conservation. Finally, the observed dependence of c on energy may have a very relevant significance on what a "1st order phase transition" might look like in a finite nuclear system.

Chapter 6

Conclusion

Nuclear multifragmentation is the most striking process observed in intermediate energy heavy–ion reactions. This work is motivated by the unsettled questions concerning the underlying mechanism of multifragment production: is the process simultaneous or sequential? Is the decay driven by dynamics or statistics? To this end, the ^{129}Xe–induced reactions on ^{nat}Cu, ^{89}Y, ^{165}Ho, and ^{197}Au at bombarding energies of E/A = 40 & 60 MeV have been studied theoretically and experimentally. The summary of the results and the conclusions will be presented in this chapter.

6.1 Theoretical Approach

To investigate the effects of dynamics on nuclear multifragmentation, the Boltzmann–Nordheim–Vlasov (BNV) reaction model has been used to simulate the ^{129}Xe–induced reactions on various targets at intermediate energies. The results of these BNV calculations for central collisions show that a "nuclear disk" develops during the collision process due to the side–squeezing of nearly incompressible nuclear matter. The disk formed at 40 MeV is relatively thick and it does not break. A thinner disk at 60 MeV shows some mottling, and eventually a thin disk at 75 MeV breaks up

into many fragments. This disk fragmentation has been analyzed in terms of the new Rayleigh–like surface instability, in which the proximity force plays an essential role. Ordinarily, a disk is at most metastable due to the energy barrier associated with the increase in the surface area of a modulated disk. When the disk becomes thin enough, the proximity potential due to the surface–surface interaction is sufficient to overcome the sharp surface barrier and trigger the surface instability. To be more precise, the system escapes from the high surface energy of a disk by breaking up into a number of spherical fragments with less overall surface. This instability is a new kind of surface instability since the Rayleigh's cylinder instability can exist with pure surface tension and does not require the proximity interaction.

In addition to nuclear disks, other exotic shapes such as bubbles have also been observed in the Boltzmann–like calculations [Baue 92]. A bubble behaves much like a sheet, and is susceptible to the surface instability when its thickness is of the order of the proximity interaction range. However, the Coulomb interaction has not been incorporated in the discussion on the surface instability. For compact shaped nuclear disks, the Coulomb contribution to the deformation energy may be small compared to the surface and proximity contributions. In the case of a nuclear bubble, the depletion of charges in the central cavity reduces the Coulomb energy significantly, and this Coulomb effect on the deformation energies should not be neglected. In fact the Coulomb energy is the driving force for the stability of "Coulomb" bubbles against monopole oscillations. In general, a more heavily charged bubble becomes stable at a thinner configuration. The vapor pressure in the central cavity of an excited bubble provides an additional force that drives the Coulomb bubbles to thinner configurations. These "Coulomb" bubbles however are susceptible to perturbations of higher order. The bubble cannot get away from the region of Coulomb instability in the case of radial modes (constant thickness), and there is always one kind of deformation or

another against which the bubble configuration is unstable. For crispation modes (modulating thickness), a bubble becomes susceptible to the surface instability when it is sufficiently thin.

In these dynamical models, the dynamics becomes dominant and drives the system into regions of instabilities. The results of these simulations suggest that the various kinds of instabilities associated with exotic shaped nuclei may conceivably be present in multifragmentation. However, the final proof must rest upon experimental verification. One feasible approach makes use of the coplanarity and sphericity of an event to discriminate between the formation of a disk or a sphere. It is expected that the trajectories of fragments broken from a spherical system tend to have an isotropic angular distribution. On the contrary, fragments broken from a disk, governed by their mutual Coulomb repulsion, will most likely lie on the plane of the disk. The orientation of this plane of the disk rotates depending upon the impact parameter. In order to analyze fragments originating from a specific plane, for example, a plane perpendicular to the beam axis in central collisions, events corresponding to a narrow range of impact parameters must be selected. Work in this direction is already in progress [Llop 95].

6.2 Experimental Investigation

Rather than dwelling solely on these complicated simulation codes, the experimental data have been analyzed and examined to search for simple regularities. In particular, the excitation functions for multifragment emission have been constructed and studied for the ^{129}Xe–induced reactions. The n–fold charge distributions of intermediate mass fragments have also been analyzed.

6.2.1 Excitation Functions

At any given transverse energy E_t, the probabilities (P_n) of detecting n fragments are observed to be binomially distributed. Empirically, an elementary one–fragment emission probability p can be extracted according to the binomial distribution. These extracted elementary probabilities have a thermal dependence of the type $p = e^{-B/T}$ as demonstrated by their linear Arrhenius plots. Indeed, a nearly universal linear Arrhenius plot is observed at each bombarding energy, independent of the specific target. In this analysis, three different procedures have been used to extract p from the fragment multiplicity distributions. The observed consistency between these various methods confirms the binomial nature of P_n and the thermal dependence of p. This observed reducibility of the n–fragment emission probability to an elementary binary decay probability implies that one can derive the probability of emitting n fragments solely from the probability of emitting one. Hence multifragmentation does not exist as an independent process. The thermal behavior of p further shows the statistical nature of the emission.

The more directly interpretable physical parameter contained in this analysis is the binary decay barrier B which is proportional to the slope of the Arrhenius plot. A single barrier suffices since the extracted average value of p is dominated by the emission of the lightest fragment ($Z_{threshold}$) with the lowest barrier in the range considered. The same analysis has been performed by progressively increasing the values of $Z_{threshold}$ from 3 to 7. A remarkable result is that the constructed excitation functions, though dramatically changed, retain their binomial reducibility. The resulting Arrhenius plots are also linear, and the slope becomes progressively steeper with increasing values of $Z_{threshold}$. The sensitivity of these slopes to $Z_{threshold}$ is consistent with the Z dependence of the emission barriers $B(Z)$, and becomes a

powerful signal for the physical meaning of p.

One possible but not unique interpretation of the reducibility is a sequential decay with constant probability at all stages. In this framework, the emission probability p is inversely proportional to the mean time separation between fragments. The observed linearity of the Arrhenius plot thus says that the emission time scale decreases exponentially with $1/\sqrt{E_t}$. In other words, the contraction of the emission time with increasing excitation energy is a natural consequence of the thermal dependence of $1/p$. The other parameter associated with a binomial distribution is m, the number of "tries" that a system has available in order to emit a fragment with fixed probability p. Empirically, the quantity $mZ_{threshold}$ is found to collapse onto a nearly universal curve. This observed $Z_{threshold}$ dependence offers a glimpse of a possible functional form for the dynamical period of a specific channel τ_o under the assumption that the overall emission time $m\tau_o$ for multifragmentation is constant.

The technical issues concerning the event–to–event fluctuations associated with the use of E_t have also been studied. The question whether these fluctuations distort a Poisson distribution into a binomial distribution is addressed by analyzing the results generated from the Poisson simulations of particle multiplicities. More specifically, Poisson distributions of the fragment, the light charged particle, and the neutron multiplicities have been generated as a function of excitation energy. The transverse energy calculated from all emitted particles is sharply correlated with the excitation energy and has no auto–correlation with the fragment and the light charged particle multiplicities. To be more realistic, neutrons are excluded from the measurement of E_t, and a strong auto–correlation between the light charged particle multiplicity and the measured transverse energy is observed. In this case, the light charged particles whose multiplicities are studied contribute extensively to the measurement of the transverse energy. This auto–correlation leads to narrower

binomial distributions of the light charged particle multiplicities at a given E_t. On the other hand, fragment yields contribute at most 20% to the measured transverse energy. Therefore, the auto–correlation between the fragment multiplicity and the measured transverse energy is not sufficient to distort a Poisson distribution into a binomial distribution. This suggests that the experimentally observed binomial fragment multiplicity distributions as a function of E_t have indeed their origin from binomial parent distributions.

To explore the effects of the finite detection efficiency on the extraction of the binomial parameters p and m, different geometric efficiency ϵ are produced by deactivating (in software) selected detectors in the measurement of the fragment multiplicity. While the number of tries m is found to be independent of the geometric efficiency ϵ, the observed probability p_{obs} is simply scaled by the geometric efficiency: $p_{obs} = \epsilon p$. Here p is the elementary probability extracted with no deactivation, and is analogous to the true probability obtained from a perfect detection system. The observed probability p_{obs} combines exactly like p in the binomial distribution. Indeed, the Arrhenius plots associated with different geometric efficiency ϵ are shown to be linear and parallel with each other. In other words, the extraction of the barrier for single fragment emission is independent of the geometric efficiency, while the absolute value of the observed elementary probability p_{obs} is modified.

The above experimental observations offer the first simplicity to be found in the rather unclear field of nuclear multifragmentation. They are direct findings that do not rely on any theory or assumption for the interpretation, but rely only on plotting the experimental data in a particularly revealing way. These findings say that multifragmentation is not a novel or special process, but is reducible to a combination of nearly independent fragment emissions. In other words, all the physics contained in the n–fragment emission probability P_n is reducible to the physical content of the

elementary binary decay probability p.

6.2.2 Charge Distributions

The reducibility observed in the fragment multiplicity distributions demands that the single fragment emission probability $p(Z)$, from which an event of n fragments is generated, is the same at every step of emission. This reducibility feature is observed for the charge distributions of the ^{129}Xe–induced reactions at relatively low transverse energies. To be more precise, the resulting fragment charge distributions for the n–fold events are the same as that for the onefold events. The thermal scaling is also shown by a thermal behavior of the Boltzmann type, $P(Z) \propto e^{-B(Z)/T}$ under the assumption that $T \propto \sqrt{E_t}$. For the charge distributions obtained at higher transverse energies, the thermal scaling is preserved but a dependence on n begins to surface. In fact, the n–fold charge distributions are well described by the following functional form:

$$P_n(Z) \propto e^{-\frac{B(Z)}{\sqrt{E_t}} - cnZ}.$$

At a given E_t, the n–fold charge distribution is thus reducible to the one–fold charge distribution through a simple scaling factor of the form e^{-cnZ}. The value of c extracted empirically is very small indicating a rather weak dependence on n. Consequently, both the thermal scaling and the reducibility feature observed in the n–fragment emission probabilities extend consistently to the charge distributions. While the thermal features strengthen the hypothesis of phase space dominance in multifragmentation, the reducibility of the charge distributions highlights the near independence of individual fragment emissions.

The above expression of the charged distribution suggests the presence of a temperature dependent enthalpy term and an entropy term that does not depend explicitly on temperature. The first term in the exponent can be interpreted as an en-

thalpy term associated with the energy barrier $B(Z)$ for the formation of a fragment. The second term that is related to the entropy points to an asymptotic combinatorial structure of the multifragmentation process in the limit of high temperature. In this framework, the quantity c is inversely proportional to the emission source size.

The energy dependence of c has also been studied. The quantity c starts at or near zero, and it rises rapidly with increasing E_t until it reaches a saturation value at high E_t. This evolution of c from zero to a non–zero quantity is compared to 1st order phase transition of a fluid that moves from the region of liquid–vapor coexistence to the region of unsaturated vapor. In the coexistence region, the presence of the liquid phase guarantees mass conservation. Hence the vapor properties, and in particular, the cluster size distributions cannot reflect the total mass of the system, and $c = 0$. On the other hand, there is no mass conserving liquid phase in the region of unsaturated vapor, and the vapor itself must take care of the conservation. The properties of the unsaturated vapor then depend on the total mass of fluid, and $c > 0$. The form e^{-cnZ} thus implies charge conservation under the constraint of n fragments.

To test these interpretations of c in finite systems, percolation calculations [Baue 88] have been performed for systems of different size. The resulting fragment charge distributions have the same n dependence of the form e^{-cnZ}. The extracted value of c starts at 0 for small bond breaking probability p_b and increases rapidly for $p_b > p_b^{crit}$. The quantity c eventually saturates at large p_b in a way similar to that observed experimentally. In fact, the saturation value of c decreases with increasing source size. The results of these percolation calculations demonstrate the sensitivity of c to the presence or absence of a charge conserving residue and reinforce the interpretations of c in two different regimes. In other words, the observed energy dependence of c may have a very relevant significance on what a "1st order phase transition" might look like in a finite nuclear system.

Appendix A

Energy Calculations

Nuclear force with a long–range attraction and a short–range repulsion behaves just like a Van Der Waals gas. This similarity suggests that nuclear matter shares the macroscopic properties of an ordinary fluid. Indeed, nuclei are treated as drops of nuclear matter in the Liquid Drop Model. In this approach, energy of a nucleus is calculated from the contributions of "volume" and "surface" terms. Also included is a Coulomb term to account for the presence of protons, and a symmetry term to correct for excessive neutrons. In the following, energies for nuclear disks and bubbles are calculated within the framework of the Liquid Drop Model.

A.1 Nuclear Disks

In nuclear disk fragmentation, the volume and the contents of the disk are conserved during the perturbation, and hence the change in volume and symmetry energies assoicated with disk deformation is essentially zero. Since a nuclear disk has a rather compact shape, the change in the Coulomb energy associated with the perturbation is small compared to the change in the surface energy. For the sake of simplicity, the Coulomb perturbation energy is assumed to be negligible in the

Table A.1 : Definition of symbols for energy calculations of a sheet of fluid.

Symbols	Definitions
d	thickness of sheet
y	width of sheet
l	length of sinusoid over one λ
λ	wavelength of perturbation
A	amplitude of perturbation
γ	surface energy coefficient
I_λ^o	surface area of an unperturbed sheet over one λ
I_λ	surface area of a perturbed sheet over one λ
S_λ^o	surface energy of an unperturbed sheet over one λ
S_λ	surface energy of a perturbed sheet over one λ
E_s^o	dimensionless surface energy of an unperturbed sheet
E_s	dimensionless surface energy of a perturbed sheet
ΔE_s	dimensionless surface energy change due to perturbation
$\Phi(s)$	dimensionless proximity potential function
E_p	dimensionless proximity energy
ΔE_p	dimensionless proximity energy change due to perturbation
ΔE	dimensionless total energy change due to perturbation

following derivations.

In these energy calculations for an ordinary fluid, surface–surface interaction is often neglected, since a disk of ordinary liquid is sufficiently thick that the skin thickness of its surface can only be measured in a microscopic scale. However, for a thin nuclear disk, this surface–surface interaction may not be negligible. In fact, nuclear surfaces interact with each other through an interaction of finite range called also the proximity force. In the following sections, expressions for both the surface and proximity perturbation energies of a disk are derived. As a reference, a list of relevant symbols and their definitions is shown in Table A.1.

To arrive at analytical expressions, a sheet of fluid instead of a finite disk is considered. To be more precise, a sheet of thickness d and width y subjected to

a perturbation of wavelength λ and small amplitude A is studied. In considering the stability of a sheet, one needs only to study the effect of small perturbations. Accordingly, one expands the relevant physical quantities in powers of A and retains only the leading terms.

A.1.1 Surface Energy

The surface energy S_λ^o of an equivalent unperturbed sheet is simply the product of the surface area and the surface energy coefficient, $S_\lambda^o = \gamma I_\lambda^o$. The surface area I_λ^o which includes the top and bottom lateral surfaces is $2\lambda y$. To express this surface energy in a dimensionless unit, it is divided by the surface energy of either the top or the bottom lateral surface ($\gamma\lambda y$). Therefore, the dimensionless surface energy of an unperturbed sheet is:

$$E_s^o = \frac{S_\lambda^o}{\gamma\lambda y} = \frac{\gamma I_\lambda^o}{\gamma\lambda y} = \frac{2\lambda y}{\lambda y} = 2. \tag{A.1}$$

Consider a simple perturbation on the sheet of the following sinusoidal form:

$$z_t = \frac{d}{2} + Asinkx, \tag{A.2}$$

where x and z_t are the horizontal and vertical coordinates of the perturbed surface (top), and $k = 2\pi/\lambda$. When the same perturbation is applied to the bottom surface, the corresponding vertical coordinates for an out of phase mode and in phase mode of perturbations are ($z_b = -d/2 - Asinkx$) and ($z_b = -d/2 + Asinkx$) respectively. Since these two modes differ only in the relative orientation of their surfaces, this does not affect the surface area. In other words, the area of the top and bottom surfaces are identical for both modes of perturbation, and the resulting total surface area is $I_\lambda = 2ly$, where l is the length of the corresponding sinusoid. An approximated

expression of l is shown below:

$$\begin{aligned} l &= \int_0^\lambda dl = \int_0^\lambda \sqrt{dx^2 + dz^2} &= \int_0^\lambda \sqrt{1 + A^2k^2cos^2kx}dx \\ &\simeq \int_0^\lambda 1 + \frac{A^2k^2}{2}cos^2kxdx &= \frac{2\pi}{k}\left(1 + \frac{A^2k^2}{4}\right). \end{aligned} \tag{A.3}$$

The corresponding surface area and energy can then be calculated:

$$S_\lambda = \gamma I_\lambda \simeq \gamma\frac{4\pi y}{k}\left(1 + \frac{A^2k^2}{4}\right) = (2\lambda\gamma y)\left(1 + \frac{A^2k^2}{4}\right), \tag{A.4}$$

$$E_s = \frac{S_\lambda}{\gamma\lambda y} \simeq 2\left(1 + \frac{A^2k^2}{4}\right). \tag{A.5}$$

The surface energy of an unperturbed sheet can also be derived by setting $A = 0$, and is simply equal to 2 identical to Equation A.1.

The dimensionless surface energy change of a sheet subjected to perturbation of wavelength λ and small amplitude A is simply the difference between E_s and E_s^o:

$$\begin{aligned} \Delta E_s &= E_s - E_s^o \simeq 2\left(1 + \frac{A^2k^2}{4}\right) - 2, \\ \Delta E_s &= A^2\frac{k^2}{2} = A^2\frac{2\pi^2}{\lambda^2}. \end{aligned} \tag{A.6}$$

The positive coefficient of A^2 simply reflects the increase in the surface area and thus energy of a modulated sheet.

A.1.2 Proximity Energy

The proximity energy is calculated from the integral of the dimensionless proximity potential $\Phi(s)$ over the area subjected to this surface–surface interaction:

$$E_p = \frac{1}{\gamma\lambda y}\int \gamma\Phi(s)2dA = \frac{1}{\gamma\lambda y}\int_0^\lambda 2\gamma\Phi(s)ydx = \frac{2}{\lambda}\int_0^\lambda \Phi(s)dx, \tag{A.7}$$

where $dA = ydx$ is the surface element of the integral and s is the separation distance between the two interacting surfaces. The denominator $\gamma\lambda y$ is used to express

the proximity energy in a standard dimensionless unit. For an in phase mode of perturbation, the separation distance is:

$$s = z_t - z_b = \left(\frac{d}{2} + Asinkx\right) - \left(-\frac{d}{2} + Asinkx\right) = d.$$

This constant value for the separation distance s indicates that an in phase mode of perturbation does not affect the thickness of the sheet, and thus the proximity energy remains unchanged. On the other hand, an out of phase mode modulates the thickness of a sheet, and the separation distance s is:

$$s = z_t - z_b = \left(\frac{d}{2} + Asinkx\right) - \left(-\frac{d}{2} - Asinkx\right) = d + 2Asinkx.$$

This A dependence for s suggests that the thinning and thickening of a sheet associated with an out of phase mode changes the proximity energy of a perturbed sheet. In the following, only this interesting out of phase mode is studied.

To evaluate the proximity energy associated with small perturbations, $\Phi(s)$ is expanded in terms of A using the out of phase mode expression for s:

$$\Phi(s) = \Phi(A, x) = \Phi_0(x) + \frac{A^2}{2}\Phi_2(x), \tag{A.8}$$

with Φ_0 and Φ_2 being the zeroth and second order coefficients of the Taylor expansion of $\Phi(A, x)$ about $A = 0$. The above integral for the proximity energy then becomes:

$$\begin{aligned} E_p &\simeq \frac{2}{\lambda}\int_0^\lambda \left[\Phi_0(x) + \frac{A^2}{2}\Phi_2(x)\right] dx, \\ E_p &\simeq \frac{2}{\lambda}\int_0^\lambda \Phi_0(x)dx + \frac{A^2}{\lambda}\int_0^\lambda \Phi_2(x)dx, \\ E_p &\simeq \frac{2}{\lambda}P(\lambda) + \frac{A^2}{\lambda}Q(\lambda). \end{aligned} \tag{A.9}$$

The proximity energy of an unperturbed sheet can be derived by setting $A = 0$, and is simply equal to $2P(\lambda)/\lambda$. Hence, the dimensionless proximity perturbation energy is:

$$\Delta E_p \simeq \frac{Q(\lambda)}{\lambda}A^2. \tag{A.10}$$

A.1.3 Overall Energy

The overall energy change of a modulated sheet can be calculated as the sum of a positive contribution from the surface energy and a negative contribution from the proximity energy:

$$\Delta E = A^2 \left[\frac{2\pi^2}{\lambda^2} + \frac{Q(\lambda)}{\lambda} \right].$$

When the coefficient of A^2 becomes zero or negative, the system becomes unstable since the perturbation decreases the overall energy. In other words, a critical wavelength can be defined by equating this coefficient to zero:

$$2\pi^2 + \lambda_c Q(\lambda_c) = 0.$$

Any perturbation with $\lambda \geq \lambda_c$ will trigger this surface instability. When the function derived from the Thomas–Fermi Nuclear Model is used for the proximity potential, the following expression for λ_c is obtained:

$$\Phi(s) = -4.5827 e^{-\frac{4s}{3b}} \quad \Rightarrow \quad \Phi_2(x) = -\frac{64}{9b^2} sin^2 kx (4.5827) e^{-\frac{4d}{3b}}$$

$$Q(\lambda) = -\frac{16.294\lambda}{b^2} e^{-\frac{4d}{3b}} \quad \Rightarrow \quad \lambda_c = 1.10 b e^{\frac{2d}{3b}}, \tag{A.11}$$

where b is the range of the proximity interaction and d is the thickness of the sheet.

A.2 Nuclear Bubbles

Energy of a nuclear bubble whose surfaces are distorted by perturbations of small amplitudes is calculated in this section within the Liquid Drop Model approach. Unlike the compact shaped nuclear disks discussed in the above section, the depletion of charges in the central cavity of a bubble reduces the Coulomb energy significantly

and this effect can no longer be neglected. Therefore, the relevant physical quantities are the surface, Coulomb and proximity energies. The kind of perturbation that is considered here preserves the azimuthal symmetry so that both the interior (R_1) and exterior radii (R_2) are functions of polar angle θ only:

$$\begin{aligned} Exterior \quad Surface \qquad R_2 &= \langle R_2 \rangle \left[1 + A_2 P_n(cos\theta)\right], \\ Interior \quad Surface \qquad R_1 &= \langle R_1 \rangle \left[1 + A_1 P_n(cos\theta)\right]. \end{aligned}$$

Here $\langle R_1 \rangle, \langle R_2 \rangle$ are mean radii of the interior and exterior surfaces; A_1, A_2 are amplitudes of the perturbations and $P_n(cos\theta)$ is Legendre Polynomial of nth order:

$$P_n(\mu) = \frac{1}{2^n n!} \frac{d^n}{d\mu^n} \left(\mu^2 - 1\right)^n, \qquad where \quad \mu = cos\theta.$$

Perturbation of this kind is called the "Spheroidal Deformation", and expressions of Legendre Polynomials for $n = 0 - 4$ are shown below:

$$\begin{aligned} P_0(cos\theta) &= 1, \\ P_1(cos\theta) &= cos\theta, \\ P_2(cos\theta) &= \frac{1}{2}(3cos^2\theta - 1), \\ P_3(cos\theta) &= \frac{1}{2}(5cos^3\theta - 3cos\theta), \\ P_4(cos\theta) &= \frac{1}{8}(35cos^4\theta - 30cos^2\theta + 3). \end{aligned}$$

Since the perturbation of each surface is independent, the ratio of their amplitudes A_1/A_2 defined as the spheroidal deformation parameter A is used to characterize the perturbation. For a perturbation of the radial mode, the distortions on both surfaces are in phase with each other and thus $A > 0$. On the contrary, $A < 0$ for a crispation mode, where the perturbations on the two surfaces are out of phase. Furthermore, to describe an unperturbed bubble formed at a given stage of expansion

Table A.2 : Definition of symbols for energy calculations of nuclear bubbles.

Symbols	Definitions
$R_1(\theta), R_2(\theta)$	radii of interior and exterior surfaces of a perturbed bubble
$\langle R_1 \rangle, \langle R_2 \rangle$	mean radii of interior and exterior surfaces of a perturbed bubble
R_{10}, R_{20}	radii of interior and exterior surfaces of an unperturbed bubble
R_0	radius of an unperturbed equivalent sphere
A_1, A_2	amplitude of perturbation to interior and exterior surfaces
$A \equiv A_1/A_2$	spheroidal deformation parameter
$P \equiv R_{10}/R_{20}$	monopole oscillation parameter
$P_n(cos\theta)$	Legendre Polynomial of nth order
γ	surface energy coefficient
$X \equiv E_c^o/2E_s^o$	Fissility parameter
E_s, E_s^o	surface energy of a bubble and an equivalent sphere
E_c, E_c^o	Coulomb energy of a bubble and an equivalent sphere
$\Delta E_s, \Delta E_c$	change in surface and Coulomb energy due to perturbation
E_p	proximity energy of a perturbed bubble
ΔE_p	change in proximity energy due to perturbation

or contraction, a monopole oscillation parameter P defined as the ratio of the two radii R_{10}/R_{20} is introduced. In the limit of $P = 0$, the central cavity vanishes, and the bubble is reduced to a sphere of equivalent volume. To determine the stability of a specific bubble configuration, the relevant energies (surface, proximity and Coulomb) must be calculated in terms of P and A. These parameters and other relevant symbols are listed in Table A.2 with their definitions.

A.2.1 Reference Energy State

For the sake of simplicity, the energy of an equivalent spherical nucleus is used as a reference energy state. Let R_0 be the radius of this equivalent sphere, E_s^o and E_c^o be their surface and Coulomb energies respectively. The relation between R_0 and the radii of a perturbed bubble can be derived from the constraint of volume

conservation. Volume of a perturbed bubble is equal to:

$$\begin{aligned} V &= \int_{r=R_1}^{R_2}\int_{\theta=0}^{\pi}\int_{\phi=0}^{2\pi} r^2 sin\theta dr d\theta d\phi \\ &= 2\pi\int_{\theta=0}^{\pi}\left(\frac{R_2^3-R_1^3}{3}\right) sin\theta d\theta \quad = \quad \frac{2\pi}{3}\int_{-1}^{1}\left(R_2^3-R_1^3\right) dcos\theta. \end{aligned}$$

To evaluate the above integral, the radii R_1 and R_2 are expanded in powers of A_1 and A_2:

$$\begin{aligned} R_1^3 = \langle R_1\rangle^3\left[1+A_1P_n(cos\theta)\right]^3 &\simeq \langle R_1\rangle^3\left[1+3A_1P_n(cos\theta)+3A_1^2\left(P_n(cos\theta)\right)^2\right], \\ R_2^3 = \langle R_2\rangle^3\left[1+A_2P_n(cos\theta)\right]^3 &\simeq \langle R_2\rangle^3\left[1+3A_2P_n(cos\theta)+3A_2^2\left(P_n(cos\theta)\right)^2\right]. \end{aligned}$$

Then, the expression for the volume of a perturbed bubble becomes:

$$V = \frac{4\pi}{3}\langle R_2\rangle^3\left[1+\frac{3A_2^2}{2n+1}\right] - \frac{4\pi}{3}\langle R_1\rangle^3\left[1+\frac{3A_1^2}{2n+1}\right]. \tag{A.12}$$

Since one is only interested in small perturbations of these spherical surfaces, an assumption is made that whatever change of shape requires only the displacement or rearrangement of the nuclear matter on the surfaces and does not involve transmission through the bulk part of the bubble nucleus. This is equivalent to the assumption that $\langle R_i\rangle$ depends on R_{i0} and A_i only, where R_{i0} is the interior ($i=1$) or exterior ($i=2$) radius of the equivalent unperturbed bubble. By identifying the terms in Equation A.12 and the terms in the following expression for the volume of an equivalent bubble,

$$V = \frac{4\pi}{3}R_{20}^3 - \frac{4\pi}{3}R_{10}^3,$$

the relations between the mean radii of a perturbed and an unperturbed bubble are obtained:

$$\begin{aligned} R_{20}^3 = \langle R_2\rangle^3\left[1+\frac{3A_2^2}{2n+1}\right] &\quad and \quad R_{10}^3 = \langle R_1\rangle^3\left[1+\frac{3A_1^2}{2n+1}\right], \\ \langle R_2\rangle = R_{20}\left[1+\frac{3A_2^2}{2n+1}\right]^{-1/3} &\quad and \quad \langle R_1\rangle = R_{10}\left[1+\frac{3A_1^2}{2n+1}\right]^{-1/3}, \\ \langle R_2\rangle \simeq R_{20}\left[1-\frac{A_2^2}{2n+1}\right] &\quad and \quad \langle R_1\rangle \simeq R_{10}\left[1-\frac{A_1^2}{2n+1}\right]. \end{aligned}$$

Moreover, R_{20} and R_{10} can further be expressed in terms of R_0 since they are also constrained by the volume conservation (i.e. $R_{20}^3 - R_{10}^3 = R_0^3$):

$$R_{20} = R_0 \left(1 - P^3\right)^{-1/3} \quad and \quad R_{10} = R_0 P \left(1 - P^3\right)^{-1/3}.$$

Consequently, the mean radii of a perturbed bubble are expressed in terms of the radius of an equivalent sphere:

$$\begin{aligned} \langle R_2 \rangle &= R_0 \left(1 - P^3\right)^{-1/3} \left[1 - \frac{A_2^2}{2n+1}\right], \\ \langle R_1 \rangle &= R_0 P \left(1 - P^3\right)^{-1/3} \left[1 - \frac{A_1^2}{2n+1}\right]. \end{aligned} \tag{A.13}$$

The above equation indicates that energies for perturbed bubbles of various configurations can be expressed in terms of P and R_0 such that they can be compared readily.

A.2.2 Surface Energy

The surface energy of a perturbed bubble is the product of the surface energy coefficient γ and the total area of the two perturbed surfaces. Since there is no spherical symmetry for a perturbed bubble, the general expression for the surface area is used:

$$S = \int_0^{2\pi} \int_0^{\pi} \sqrt{R^4 sin^2\theta + R^2 \left(\frac{dR}{d\phi}\right)^2 + R^2 sin^2\theta \left(\frac{dR}{d\theta}\right)^2} d\theta d\phi. \tag{A.14}$$

However, this integral is simplified due to the azimuthal symmetry associated with the Legendre Polynomial, and the integral for the interior surface becomes:

$$\begin{aligned} S_1 &= 2\pi \int_0^{\pi} R_1 sin\theta \sqrt{\left[R_1^2 + \left(\frac{dR_1}{d\theta}\right)^2\right]} d\theta \\ &= 2\pi \int_0^{\pi} R_1 sin\theta \langle R_1 \rangle \sqrt{\left[1 + 2A_1(P_n cos\theta) + A_1^2 (P_n cos\theta)^2 + A_1^2 sin^2\theta \left(\frac{dP_n cos\theta}{dcos\theta}\right)^2\right]} d\theta. \end{aligned}$$

Since one is interested only in perturbations of small amplitudes, this integral is further simplified by expanding the integrand in powers of A_1:

$$\begin{aligned} S_1 &\simeq 2\pi \int_0^\pi R_1 sin\theta \langle R_1 \rangle \left[1 + A_1(P_n cos\theta) + \frac{A_1^2}{2} sin^2\theta \left(\frac{dP_n cos\theta}{dcos\theta}\right)^2\right] d\theta \\ &= 2\pi \int_0^\pi \langle R_1 \rangle^2 sin\theta \left[1 + A_1(P_n cos\theta)\right] \left[1 + A_1(P_n cos\theta) + \frac{A_1^2}{2} sin^2\theta \left(\frac{dP_n cos\theta}{dcos\theta}\right)^2\right] d\theta. \end{aligned}$$

To evaluate the above integral, the following properties of Legendre Polynomials are used:

$$sin\theta \frac{dP_n cos\theta}{dcos\theta} = sin\theta \frac{dP_n cos\theta}{d\theta} \frac{d\theta}{dcos\theta} = -\frac{dP_n cos\theta}{d\theta} \qquad and \qquad \int_0^{2\pi} P_n(cos\theta) d\theta = 0.$$

Using the expression in Equation A.13 for $\langle R_1 \rangle$, the surface area of a perturbed bubble is expressed in terms of R_0, P and A_1:

$$S_1 = 4\pi R_0^2 P^2 \left(1 - P^3\right)^{-2/3} \left[1 + \frac{A_1^2(n^2 + n - 2)}{2(2n+1)}\right].$$

Similarly, the area for the exterior surface is expressed in terms of R_0, P and A_2:

$$S_2 = 4\pi R_0^2 \left(1 - P^3\right)^{-2/3} \left[1 + \frac{A_2^2(n^2 + n - 2)}{2(2n+1)}\right].$$

Therefore, the surface energy E_s of a perturbed bubble can be calculated:

$$\begin{aligned} E_s &= \gamma(S_1 + S_2) \\ &= E_s^o \left(1 - P^3\right)^{-2/3} \left[P^2 + P^2 \frac{A_1^2(n^2 + n - 2)}{2(2n+1)} + 1 + \frac{A_2^2(n^2 + n - 2)}{2(2n+1)}\right] \\ &= E_s^o \left(1 - P^3\right)^{-2/3} \left[1 + P^2 + A_2^2 \left(1 + A^2 P^2\right) \frac{n^2 + n - 2}{2(2n+1)}\right], \end{aligned} \tag{A.15}$$

where $E_s^o = \gamma 4\pi R_0^2$ is the surface energy of an equivalent sphere. The surface energy of an unperturbed bubble can be derived by setting $A_2 = 0$, and the resulting expression is identical to that derived in chapter 2. Therefore, the coefficient of A_2^2 is the change in surface energy (ΔE_s) associated with the perturbation:

$$\Delta E_s = E_s^o A_2^2 \left[\left(1 - P^3\right)^{-2/3} \left(1 + A^2 P^2\right) \frac{n^2 + n - 2}{2(2n+1)}\right]. \tag{A.16}$$

A.2.3 Coulomb Energy

The Coulomb energy E_c of a perturbed bubble with uniformed charge distribution is evaluated using the following general expression:

$$E_c = \frac{1}{2}\rho \int_{R_1}^{R_2} r_o^2 dr_o \int_0^{\pi} sin\theta_o d\theta_o \int_0^{2\pi} d\phi_o U(r_o, \theta_o, \phi_o). \tag{A.17}$$

Here ρ is a constant charge density and $U(r_o, \theta_o, \phi_o)$ is the Coulomb potential at a point (r_o, θ_o, ϕ_o) inside the bubble, whose interior and exterior radii are R_1 and R_2 respectively. To be more specific, the functional form for $U(r_o, \theta_o, \phi_o)$ is shown below:

$$U(r_o, \theta_o, \phi_o) = \rho \int_{R_1}^{R_2} r^2 dr \int_0^{2\pi} d\phi \int_0^{\pi} sin\theta d\theta \frac{1}{|\vec{r} - \vec{r_o}|}. \tag{A.18}$$

Here $\frac{1}{|\vec{r}-\vec{r_o}|}$ is the Green's Function and is expanded in spherical coordinates:

$$\frac{1}{|\vec{r} - \vec{r_o}|} = \sum_{n=0}^{\infty} \sum_{m=0}^{n} \epsilon_m \frac{(n-m)!}{(n+m)!} P_n^m(cos\theta_o) P_n^m(cos\theta) \cdot cos[m(\phi - \phi_o)] \begin{cases} r^n / r_o^{n+1}, & r < r_o \\ r_o^n / r^{n+1}, & r > r_o \end{cases}$$

where $P_n^m(cos\theta)$ is Legendre Function of the First Kind, and ϵ_m is the Neumann Factor:

$$\epsilon_0 = 1, \qquad \epsilon_m = 2 \quad (m = 1, 2, 3...).$$

The two cases for the above Green's Function show that the contribution of charges to the Coulomb potential at a point (r_o, θ_o, ϕ_o) is different for the two regions $(r < r_o)$ and $(r > r_o)$. Hence, the integral for the Coulomb potential at a point (r_o, θ_o, ϕ_o) inside the bubble must be evaluated separately for the two regions based on the boundary at r_o:

$$U(r_o, \theta_o, \phi_o) = \rho \int_0^{2\pi} d\phi \int_0^{\pi} sin\theta d\theta \left[\int_{R_1}^{r_o} \frac{r^2 dr}{|\vec{r} - \vec{r_o}|} + \int_{r_o}^{R_2} \frac{r^2 dr}{|\vec{r} - \vec{r_o}|} \right].$$

Let us consider the integral over the azimuthal angle ϕ first. Since $\int cos[m(\phi - \phi_o)]d\phi \neq 0$ only if $m = 0$, this simplify the integral tremendously as one needs

to consider only the case for $m = 0$. In fact, when $m = 0$, only the Legendre Polynomials $P_n^0(cos\theta) = P_n(cos\theta)$ are involved. Moreover the Neumann Factor $\epsilon_0 = 1$ and $\frac{(n-m)!}{(n+m)!} = 1$. The simplified integral is shown below:

$$U(r_o, \theta_o, \phi_o) = \rho 2\pi \int_0^\pi sin\theta \sum_{n=0}^{\infty} P_n(cos\theta_o) P_n(cos\theta) d\theta \left\{ \int_{R_1}^{r_o} \frac{r^{n+2}}{r_o^{n+1}} dr + \int_{r_o}^{R_2} \frac{r_o^n}{r^{n-1}} dr \right\}.$$

Then an approximation for $U(r_o, \theta_o, \phi_o)$ to the second order in A_1 or A_2 is obtained:

$$\begin{aligned} U(r_o, \theta_o, \phi_o) &= \frac{Q}{R_{20}^3 - R_{10}^3} \left\{ \left[\frac{3}{2} R_{20}^2 - \frac{1}{2} r_o^2 - \frac{R_{10}^3}{r_o} \right] \right. \\ &\left. + \frac{3P_n(cos\theta_o)}{2n+1} \left[A_2 r_o^n R_{20}^{2-n} - A_1 \frac{R_{10}^{n+3}}{r_o^{n+1}} \right] - \frac{3A_2^2 R_{20}^2}{2(2n+1)} \right\}. \end{aligned}$$

where Q is the total amount of charge in the bubble. When this functional form of $U(r_o, \theta_o, \phi_o)$ is used in Equation A.17 to evaluate the Coulomb energy for a perturbed bubble, one obtains the following result:

$$\begin{aligned} E_c &= E_c^o \left(1 - P^3\right)^{-\frac{5}{3}} \left\{ \left[1 - \frac{5}{2} P^3 + \frac{3}{2} P^5 \right] \right. \\ &\left. + \frac{5A_2^2}{2(2n+1)^2} \left[(2n+1)P^3 + 2 - 2n - 6AP^{n+3} + 3A^2 P^5 \right] \right\}. \end{aligned}$$

Here $E_c^o = 3Q^2/5R_0$ is the Coulomb energy of an equivalent sphere. When A_2 is set equal to 0, the above expression for E_c is reduced to the Coulomb energy of an equivalent unperturbed bubble. Therefore, the coefficient of A_2^2 is the change in Coulomb energy (ΔE_c) due to the perturbation:

$$\Delta E_c = E_c^o \left(1 - P^3\right)^{-\frac{5}{3}} \frac{5A_2^2}{2(2n+1)^2} \left[(2n+1)P^3 + 2 - 2n - 6AP^{n+3} + 3A^2 P^5 \right].$$

A.2.4 Proximity Energy

The proximity energy is calculated from the integral of the dimensionless proximity potential $\Phi(s)$ over the area subjected to this surface–surface interaction:

$$E_p = \int 2\gamma \Phi(s) dA, \tag{A.19}$$

where s is the separation distance between the two interacting surfaces. In the case of a thin bubble, the surface element of the above integral can be approximated by the inner surface of the bubble:

$$dA = \sqrt{\left[R_1^4 sin^2\theta + R_1^2\left(\frac{dR_1}{d\phi}\right)^2 + R_1^2 sin^2\theta\left(\frac{dR_1}{d\theta}\right)^2\right]} d\theta d\phi. \qquad (A.20)$$

Since the spheroidal deformation preserves the azimuthal symmetry, R_1 does not depend on the azimuthal angle ϕ, and the above expression for dA is simplified:

$$\begin{aligned} dA &= \sqrt{\left[R_1^4 sin^2\theta + R_1^2 sin^2\theta\left(\frac{dR_1}{d\theta}\right)^2\right]} d\theta d\phi \\ &\simeq \langle R_1\rangle^2 sin\theta\left[1 + 2A_1 P_n cos\theta + A_1^2 (P_n cos\theta)^2 + \frac{A_1^2}{2} sin^2\theta\left(\frac{dP_n cos\theta}{dcos\theta}\right)^2\right] d\theta d\phi. \end{aligned}$$

For the proximity potential, the function derived from the Thomas–Fermi Nuclear Model is used:

$$\Phi(s) = -4.5827 e^{-\frac{4s}{3b}} = -4.5827 e^{-\frac{4(R_2-R_1)}{3b}}. \qquad (A.21)$$

Here the separation distance between the two interacting surfaces is simply the difference between the two radii : $s = R_2 - R_1$.

To evaluate the proximity energy associated with small perturbations, $\Phi(s)$ is expanded in terms of A_1:

$$\Phi(s) = \Phi(A,\theta,A_1) = \Phi_0(A,\theta) + A_1\Phi_1(A,\theta) + \frac{A_1^2}{2}\Phi_2(A,\theta), \qquad (A.22)$$

where Φ_0, Φ_1 and Φ_2 are the zeroth, first and second order coefficients of the Taylor expansion of $\Phi(A,\theta,A_1)$ about $A_1 = 0$:

$$\begin{aligned} \Phi_0(A,\theta) &= -4.5827 e^{\frac{-4}{3b}(\langle R_2\rangle - \langle R_1\rangle)}, \\ \Phi_1(A,\theta) &= -4.5827 e^{\frac{-4}{3b}(\langle R_2\rangle - \langle R_1\rangle)}\left[\frac{-4}{3b}\left(\frac{\langle R_2\rangle P_n cos\theta}{A} - \langle R_1\rangle P_n cos\theta\right)\right], \\ \Phi_2(A,\theta) &= -4.5827 e^{\frac{-4}{3b}(\langle R_2\rangle - \langle R_1\rangle)}\left[\frac{-4}{3b}\left(\frac{\langle R_2\rangle P_n cos\theta}{A} - \langle R_1\rangle P_n cos\theta\right)\right]^2. \end{aligned}$$

With the above approximations for dA and $\Phi(s)$, one obtains the following expression for the proximity energy E_p:

$$E_p = E_s^o P^2 \left(1-P^3\right)^{-\frac{2}{3}} (-4.5827) e^{\frac{-4R_0}{3b}\left(1-P^3\right)^{-\frac{1}{3}}(1-P)} \left\{ 2 + \left[\frac{A_2^2}{(2n+1)} \frac{8R_0}{3b} \frac{(1-PA^2)}{(1-P^3)^{1/3}} \right] + \frac{A_2^2 A^2}{2n+1} \left[\frac{16R_0^2}{9b^2} \frac{\left(P-\frac{1}{A}\right)^2}{(1-P^3)^{2/3}} + \frac{16R_0}{3b} \frac{\left(P-\frac{1}{A}\right)}{(1-P^3)^{1/3}} + n^2 + n - 2 \right] \right\}.$$

Similarly, when A_2 is set equal to 0, the above expression for E_p is reduced to the proximity energy of an equivalent unperturbed bubble, and the coefficient of A_2^2 is the change in proximity energy (ΔE_p) associated with the perturbation:

$$\Delta E_p = E_s^o P^2 \left(1-P^3\right)^{-\frac{2}{3}} (-4.5827) e^{\frac{-4R_0}{3b}\left(1-P^3\right)^{-\frac{1}{3}}(1-P)} \left\{ \left[\frac{A_2^2}{(2n+1)} \frac{8R_0}{3b} \frac{(1-PA^2)}{(1-P^3)^{1/3}} \right] + \frac{A_2^2 A^2}{2n+1} \left[\frac{16R_0^2}{9b^2} \frac{\left(P-\frac{1}{A}\right)^2}{(1-P^3)^{2/3}} + \frac{16R_0}{3b} \frac{\left(P-\frac{1}{A}\right)}{(1-P^3)^{1/3}} + n^2 + n - 2 \right] \right\}.$$

Bibliography

[Abou 94] M. Abouffirassi, et al., LPC Caen preprint LPCC 94-02 (1994).

[Aich 91] J. Aichelin, *Quantum Molecular Dynamics: a Dynamical Microscopic n-Body Approach to Investigate Fragment Formation and the Nuclear Equation of State in Heavy Ion Collisions*, Phys. Rep. **Vol. 202**, ed. 1991), p. 233.

[Aich 84a] J. Aichelin and J. Hufner, Phys. Lett. **B136**, 15 (1984).

[Aich 87] J. Aichelin, et al., Phys. Rev. Lett. **58**, 1926 (1987).

[Aich 91] J. Aichelin, Phys. Rep. **202**, 233 (1991).

[Auge 87] F. Auger, et al., Phys. Rev. **C35**, 190 (1987).

[Ayik 88] S. Ayik and C. Gregoire, Phys. Lett. **B212**, 269 (1988).

[Ayik 90] S. Ayik and C. Gregoire, Nucl. Phys. **A513**, 187 (1990).

[Barr 80] M. Barranco and J. R. Buchler, Phys. Rev. **C22**, 1729 (1980).

[Barr 81] M. Barranco and J. R. Buchler, Phys. Rev. **C24**, 1191 (1981).

[Baue 85] W. Bauer, et al., Phys. Lett. **B150**, 53-6 (1985).

[Baue 86] W. Bauer, et al., Nucl. Phys. **A452**, 699 (1986).

[Baue 88] W. Bauer, Phys. Rev. **C38**, 1297 (1988).

[Baue 92] W. Bauer, et al., Phys. Rev. Lett. **69**, 1888-91 (1992).

[Baug 93] E. Bauge, et al., Phys. Rev. Lett. **70**, 3705 (1993).

[Bert 88] G. F. Bertsch and S. D. Gupta, *A guide to microscopic models for intermediate energy heavy ion collisions*, Phys. Rep. **Vol. 160**, ed. 1988), p. 189

[Birk 83] J. R. Birkelund and J. R. Huizenga, Annl. Rev. Nucl. Part. Phys. 33, 265 (1983).

[Bloc 77] J. Blocki, et al., Ann. Phys. (N.Y.) **105**, 427 (1977).

[Blum 91] Y. Blumenfeld, et al., Phys. Rev. Lett. **66**, 576 (1991).

[Bohr 39] N. Bohr and J. A. Wheeler, Phys. Rev. **56**, 426 (1939).

[Bohr 48] N. Bohr, Kgl. Danske Videnskab. Selskab, Mat.-fys. Medd., **XVIII**, 8 (1948).

[Bona 89] A. Bonasera, et al., Phys. Lett. **B221**, 233 (1989).

[Bona 90a] A. Bonasera, et al., Phys. Lett. **B244**, 169 (1990).

[Bona 90b] A. Bonasera, et al., Phys. Lett. **B246**, 337 (1990).

[Bond 85a] J. P. Bondorf, et al., Nucl. Phys. **A443**, 321 (1985).

[Bond 85b] J. P. Bondorf, et al., Nucl. Phys. **A444**, 460 (1985).

[Bord 84] B. Borderie et al., Z. Phys. **A318**, 315 (1984).

[Bord 90] B. Borderie, et al., *Heavy-ion Peripheral Collisions in the Fermi Energy Domain: Fragmentation Processes or Dissipative Collisions?* Ann. Phys. **Vol. 15**, ed. 1990), p. 287-392.

[Bord 92] B. Borderie, Ann. Phys. **17**, 349 (1992).

[Boug 94] R. Bougault, et al., Laboratoire de Physique Corpusculaire preprint LPCC 94- 04 (1994).

[Bowm 89] D. Bowman, Ph.D. Thesis, University of California at Berkeley, 1989.

[Bowm 91] D. Bowman, et al., Phys. Rev. Lett. **67**, 1527 (1991).

[Bowm 92] D. R. Bowman, et al., Phys. Rev. **C46**, 1834 (1992).

[Bowm 93] D. R. Bowman, et al., Phys. Rev. Lett. **70**, 3534 (1993).

[Burg 91] G. F. Burgio, et al., Nucl. Phys. **A529**, 157-89 (1991).

[Camp 85] X. Campi and J. Desbois, in XXIII Int'l Winter Meeting on Nuclear Physics, Bormio, Ital, 1985, edited by Ricerca Scientifica ed Educazione Permananente, **Vol. 47**, p. 498-511.

[Camp 86] X. Campi, J. of Phys. **A19**, L917 (1986).

[Camp 88] X. Campi, Phys. Lett. **B208**, 351 (1988).

[Char 88a] R. J. Charity, et al., Nucl. Phys. **A476**, 516 (1988).

[Char 88b] R. J. Charity, et al., Nucl. Phys. **A483**, 371 (1988).

[Chit 83] C. B. Chitwood, et al., Phys. Lett. **B131**, 289 (1983).

[Chom 91] P. Chomaz, et al., Phys. Lett. **B254**, 340 (1991).

[Colo 89] N. Colonna, et al., Phys. Rev. Lett. **62**, 1833 (1989).

[Colo 92] M. Colonna, et al., Phys. Lett. **B283**, 180 (1992).

[Colo 92a] M. Colonna, et al., Nucl. Phys. **A541**, 295 (1992).

[Davi 78] K. T. R. Davies, et al., Phys. Rev. Lett. **41**, 632 (1978).

[DelZ 95] A. D. Zoppo, et al., Phys. Rev. Lett. **75**, 2288 (1995).

[Desb 87] J. Desbois, Nucl. Phys. **A466**, 724 (1987).

[deSo 90] R. T. deSouza, et al., Nucl. Instr. and Meth. **A295**, 109 (1990).

[Ethv 93] T. Ethvignot, et al., Phys. Rev. **C48**, 618 (1993).

[Finn 82] J. E. Finn, et al., Phys. Rev. Lett. **49**, 1321 (1982).

[Fox 93] D. Fox, et al., Phys. Rev. **C47**, R421 (1993).

[Frie 90] W. A. Friedman, Phys. Rev. **C42**, 667 (1990).

[Gali 70] J. Galin, et al., Nucl. Phys. **A 159**, 461 (1970).

[Ghet 95] R. Ghetti, et al., to be published.

[Gilk 94] M. L. Gilkes, et al., Phys. Rev. Lett. **73**, 1590 (1994).

[Glas 94] T. Glasmacher, et al., Phys. Rev. **C50**, 952 (1994).

[Gong 88] W. G. Gong, et al., Nucl. Instr. and Meth. **A268**, 190 (1988).

[Gong 90] W. G. Gong, et al., Nucl. Instr. and Meth. **A287**, 639 (1990).

[Goss 77] J. Gosset, et al., Phys. Rev. **C16**, 629 (1977).

[Gros 82] D. H. E. Gross, et al., Z. Phys. **A309**, 41 (1982).

[Gros 86] D. H. E. Gross, et al., Phys. Rev. Lett. **56**, 1544 (1986).

[Gros 87] D. H. E. Gross and H. Massman, Nucl. Phys. **A471**, 339 (1987).

[Gros 90] D. H. E. Gross, *Statistical decay of very hot nuclei-the production of large clusters*, Rep. Prog. Phys. , **Vol. 53**, 1990, p. 605.

[Gros 92a] D. H. E. Gross, et al., Ann. Phys. **1**, 467-72 (1992).

[Guer 89] D. Guerreau, Formation and Decay of Hot Nuclei: The Experimental Situation ed. (Plenum Publishing Corp., 1989).

[Guer 89a] D. Guerreau, in the International School on Nuclear Physics, Les Houches, France, 1989, edited by (Grand Accelerateur National Ions Lourds)

[Gutb 89] H. H. Gutbrod, et al., Plastic Ball Experiments, Rep. Prog. Phys. , **Vol.52**, 1989, p. 1267.

[Hano 93] K. Hanold, et al., Phys. Rev. **C48**, 723 (1993).

[Helt 87] J. Heltsley, et al., MSUCl-616 (1987).

[Hufn 85] J. Hufner, Phys. Rep. **125**, 129 (1985).

[Hufn 86] J. Hufner and D. Mukhopadhyay, Phys. Lett. **B173**, 373 (1986).

[Kauf 59] R. Kaufmann, et al., Phys. Rev. Lett **3**, 232 (1959).

[Kauf 70] S. G. Kaufman, et al., Nucl. Instr. Meth. **82**, 117 (1970).

[Keho 92] W. L. Kehoe, et al., Nucl. Instr. Meth. **A311**, 258-72 (1992).

[Kim 92] Y. D. Kim, et al., Phys. Rev. **C45**, 338 (1992).

[Kort 73] R. G. Korteling, et al., Phys. Rev. **C7**, 1611 (1973).

[Lamb 81] D. Q. Lamb, et al., Nucl. Phys. **A360**, 459 (1981).

[Ller 94] A. Lleres, et al., ISN Grenoble preprint ISN 94-33 (1994).

[Llop 95] W. J. Llope, et al., Phys. Rev. **C52**, 1900 (1995).

[Louv 94] M. Louvel, et al., Phys. Lett. **B320**, 221 (1994).

[Lync 87] W. G. Lynch, Ann. Rev. Nucl. Part. Sci. **37**, 493 (1987).

[Mahi 88] M. Mahi, et al., Phys. Rev. Lett. **60**, 1936 (1988).

[McMa 85] M. A. McMahan, et al., Phys. Rev. Lett. **54**, 1995 (1985).

[McMa 86] M. A. McMahan, et al., Nucl. Instr. Meth. **A253**, 1 (1986).

[Meye 80] W. G. Meyer et al., Phys. Rev. **C22**, 179 (1980).

[More 69] L. G. Moretto, et al., Phys. Rev. **179**, 1176 (1969).

[More 72] L. G. Moretto, Phys. Lett. **B40**, 185 (1972).

[More 75] L. G. Moretto, Nucl. Phys. **A247**, 211 (1975).

[More 81] L. G. Moretto and R. P. Schmitt, Reports on Progress in Physics **44**, 533 (1981).

[More 86] L. G. Moretto and D. R. Bowman, XXIV Inter. Winter Meeting of Nucl. Phys., Bormio, Italy, 1986, edited by I. Iori (Ricerca Scientifica ed Educazione Pemanente), Vol. Supplemento N.49, p. 126.

[More 88] L. G. Moretto and G. J. Wozniak, *The Role of the Compound Nucleus in Complex Fragment Emission at Low and Intermediate Energies*, Prog. Part. & Nucl. Phys. , **Vol.21**, 1988, p. 401.

[More 92] L. G. Moretto, et al., Phys. Rev. Lett. **69**, 1884 (1992).

[More 93] L. G. Moretto and G. J. Wozniak, *Multifragmentation in Heavy-ion Processes*, Ann. Rev. Part. & Nucl. Sci , **Vol.43**, 1993, p. 379.

[More 93a] L. G. Moretto, et al., Phys. Rev. Lett. **71**, 3935 (1993).

[More 95] L. G. Moretto, et al., Phys. Rev. Lett. **74**, 1530 (1995).

[Moul 78] J. B. Moulton, et al., Nucl. Instr. and Meth. **157**, 325 (1978).

[Nege 82] J. W. Negele, Rev. Mod. Phys. , **Vol.54**, 913 (1982).

[Nord 28] W. W. Nordheim, Proc. Royal Soc. London **A119**, 689 (1928).

[Olmi 87] A. Olmi, et al., Europhys. Lett. **4**, 1121-26 (1987).

[Peas 94] G. F. Peaslee et al., Phys. Rev. **C49**, 2271 (1994).

[Peil 92] G. Peilert, et al., Phys. Rev. **C46**, 1457-73 (1992).

[Rand 81] J. Randrup and S. E. Koonin, Nucl. Phys. **A356**, 223 (1981).

[Rand 90] J. Randrup and B. Remaud, Nucl. Phys. **A514**, 339 (1990).

[Rayl 64] Lord Rayleigh, *Scientific Papers* (Dover, New York, 1964), Article 58, p. 361.

[Rayl 64a] Lord Rayleigh, *Scientific Papers* (Dover, New York, 1964), Article 60, p. 400.

[Rous 93] P. Roussel-Chomaz, et al., Nucl. Phys. **A551**, 508 (1993).

[Sang 92] T. C. Sangster, et al., Phys. Rev. **C46**, 1404-15 (1992).

[Sang 93] T. C. Sangster, et al., Phys. Rev. **C47**, R2457 (1993).

[Saue 76] G. Sauer, et al., Nucl. Phys. **A264**, 221 (1976).

[Scha 94] O. Schapiro and D. H. E. Gross, Hahn-Meitner-Institut Berlin GmbH (1994).

[Schr 77] W. U. Schroeder and J. R. Huizenga, Annual Review of Nuclear and Particle Science **27**, 465 (1977).

[Schu 89] P. Schuck, et al., Prog. Part. Nucl. Phys. , **Vol.22** 181 (1989).

[Snep 90] K. Sneppen and L. Vinet, Nucl. Phys. **A511**, 414 (1990).

[Sobo 83] L. G. Sobotka, et al., Phys. Rev. Lett. **51**, 2187 (1983).

[Sobo 84] L. G. Sobotka, et al., Phys. Rev. Lett. **53**, 2004 (1984).

[Sobo 85] L. G. Sobotka and L. G. Moretto, Phys. Rev. **C31**, 668 (1985).

[Sura 92] E. Suraud, et al., Nucl. Phys. **A542**, 141-58 (1992).

[Toke 92] J. Toke, et al., Annu. Rev. Nucl. Part. Sci. **42**, 401 (1992).

[Trau 93] W. Trautmann, et al., Z. Phys. **A344**, 447 (1993).

[Tso 95] K. Tso, et al., Phys. Lett. **B361**, 25 (1995).

[Uehl 33] E. A. Uehling and G. E. Uhlenback, Phys. Rev. **43**, 552 (1933).

[Weis 37] Weisskopf, Phys. Rev. **52**, 295 (1937).

[West 76] G. D. Westfall, et al., Phys. Rev. Lett. **37**, 1202 (1976).

[Wong 73] C. Y. Wong, Ann. Phys. **77**, 279 (1973).

[Wong 85] C. Y. Wong, Phys. Rev. Lett. **55**, 1973 (1985).

Ernest Orlando Lawrence Berkeley National Laboratory
One Cyclotron Road | Berkeley, California 94720

Prepared for the U.S. Department of Energy under Contract No. DE-AC03-76SF00098